Optimal Control-Enhanced Deconvolution of NMR Spectra: Homo- and Heteronuclear Decoupling

Zur Erlangung des akademischen Grades eines
DOKTORS DER NATURWISSENSCHAFTEN
genehmigte

DISSERTATION

von

Dipl.-Chem. Tony Reinsperger

aus Merseburg

An der Fakultät für Chemie und Biowissenschaften
Karlsruher Institut für Technologie (KIT) - Universitätsbereich
Institut für Biologische Grenzflächen 4

Dekan:	Prof. Dr. W. Klopper
Referent:	Prof. Dr. B. Luy
Koreferent:	Prof. Dr. Mirko Bunzel
Tag der mündlichen Prüfung:	22.07.2016

Karlsruher Institut für Technologie
Fakultät für Chemie und Biowissenschaften
Kaiserstraße 12
76131 Karlsruhe

Ich versichere wahrheitsgemäß, die Arbeit selbstständig angefertigt, alle benutzten Hilfsmittel vollständig und genau angegeben und alles kenntlich gemacht zu haben, was aus Arbeiten anderer unverändert oder mit Änderungen entnommen wurde. Weiterhin versichere ich, dass der Inhalt dieser Arbeit bis auf die unten angegebenen Teilpublikationen noch nicht veröffentlicht wurde und dass ich eine solche Veröffentlichung nicht vor Abschluss des Promotionsverfahrens vornehmen werde.

Karlsruhe, 08.06.2016

. . . .

(Dipl.-Chem. Tony Reinsperger)

Publikationsliste

T. Reinsperger, B. Luy, "Homonuclear BIRD-decoupled Spectra for measuring onebond couplings with highest resolution: CLIP/CLAP-RESET and constant-time-CLIP/CLAP-RESET", *J. Magn. Reson.* **2014**, *239*, 110–120.

Man kann nicht schreiben, ohne zu lügen.
Kurt Tucholsky

Abstract

High-resolution Nuclear Magnetic Resonance (NMR) spectroscopy is one of the most important analytical methods in order to study dynamic and structural aspects of molecules. It is highly complementary to X-ray diffraction and mass spectrometry. Whereas mass spectrometry excels at the detection of slightest amounts of material, NMR spectroscopy can provide atomic resolution. The latter also holds for X-ray structures, but via NMR spectroscopy molecules can be studied in solution, so that dynamic processes can be observed to a greater extent.

To improve resolution and sensitivity is the main motivation behind NMR method development. The Fourier transform (FT) technique, advances in the development of superconducting magnets with ever-increasing field strengths as well as novel probe technologies and for quite some time also hyperpolarization methods facilitated to lower the detection threshold to a few parts per million (ppm) down to a single nuclear spin. Higher static magnetic fields and the ability to spread NMR spectra across additional frequency dimensions are the main sources of increased resolution. But there is still a demand for the development of new pulse sequences to be able to measure standard NMR parameters like chemical shifts and spin couplings but also relaxation phenomena and dynamic processes with increasing reliability. The same holds for anisotropic structure parameters such as Residual Dipolar Couplings (RDCs), Residual Quadrupolar Couplings (RQCs) or Residual Chemical Shift Anisotropy (RCSA), for which molecules have to be partially aligned along a principal axis with the help of aligning media. In recent years it was shown for a multitude of examples that this methodology can address problems concerning the conformation, configuration and constitution of molecules where conventional approaches fail.

The development of radio frequency (RF) pulses, the backbone of every NMR experiment, is also subject of research. The variety of known pulse shapes is reflected in the extensive amount of design methods, extending from geometric intuition to numerical optimization algorithms. Optimal Control Theory (OCT), a gradient-based approach related to the Euler-Lagrange formalism, is highly suitable to optimize trajectories of dynamic systems with known equations of motion. For high-resolution NMR spectroscopy, it could be shown that optimal control algorithms can be used to explore the physical limits of many spin systems and that even for many thousands of independent optimization variables and a five-dimensional parameter grid, optimal solutions can be found. The basic mathematical principles of spin dynamics simulations and optimal control algorithms will be outlined in chapter 1 of this thesis.

The subject matter of this thesis is the optimization of decoupling experiments. Even if line splittings and coupling constants can hold valuable structural information, resonance lines collapsed to singlets lead to improved resolution and increased interpretability of the spectra. At the same time this can lead to higher signal intensities and therefore improved sensitivity. The main part of this thesis is organized in two parts. Chapter 2 deals

with heteronuclear decoupling which aims to suppress the interactions of different spin species, typically ^{1}H and ^{13}C. A historical overview over the most common decoupling schemes serves to introduce mechanisms to obtain spectra as artifact-free as possible and to derive criteria for optimizations. The proposed algorithms are studied with respect to the underlying mathematical formalism, generality, efficiency and convergence. The pulse sequences obtained as a result will be simulated and experimentally verified on a simple spin system. Two experimentally relevant aspects of decoupling sequences, namely the signal to artifact (S/A) ratio and the achievable resolution which is limited by restrictions of the energy deposition on the acquisition time (AQ), are investigated on examples of small organic molecules.

Chapter 3 deals with homonuclear decoupling, the suppression of couplings amongst the same spin species, whose methodology is far more complex. It is motivated by the accurate measurement of anisotropic NMR parameters, RDCs in particular. A heteronuclear correlation experiment is proposed where heteronuclear couplings can be measured without the influence of homonuclear couplings on the signal shape. It shall be determined on several examples whether the accuracy of the extracted coupling constants can be improved by homonuclear decoupling. The influence of several spin system parameters on the sensitivity of the experiments will be characterized and the identified weak spots will be compensated by optimizations of novel pulse sequence elements.

Given that both topics were subject of research by other groups in parallel to this thesis, the results obtained here will be discussed in the current framework.

Zusammenfassung

Die hochauflösende Kernmagnetresonanzspektroskopie, aus dem Englischen Nuclear Magnetic Resonance (NMR)-Spektroskopie, ist eine der wichtigsten Analysemethoden, um Dynamik- und Strukturaspekte von Molekülen zu untersuchen. Die Methode ist in hohem Maße komplementär zur Röntgenbeugung und massenspektrometrischen Analysen. Während die Massenspektrometrie für kaum zu überbietende Empfindlichkeit bei der Detektion kleinster Substanzmengen steht, kann mit der NMR-Spektroskopie atomare Auflösung erzielt werden. Letzteres gilt auch für Röntgenstrukturanalysen, jedoch erlaubt die NMR-Spektroskopie die Untersuchung von Molekülen in Lösung, so dass dynamische Prozesse in größerem Umfang messbar sind.

Die Verbesserung von Auflösung und Empfindlichkeit ist die grundlegende Motivation der NMR-Methodenentwicklung. Die Fouriertransformationstechnik, Fortschritte bei der Entwicklung supraleitender Magnete immer höherer Feldstärken sowie neuartiger Probenkopftechnologien und seit einiger Zeit auch Hyperpolarisationsmethoden trugen in großem Maße dazu bei, Detektionsschwellen von wenigen ppm bis hin zu einem einzelnen Kernspin zu erreichen. Größere statische Magnetfelder und die Auffächerung von NMR-Spektren entlang zusätzlichen Frequenzachsen gehören zu den Hauptquellen verbesserter Auflösung. Von hohem Interesse ist jedoch nach wie vor die Entwicklung neuartiger Pulssequenzen, um Standard-NMR-Strukturparameter wie chemische Verschiebungen und Kopplungen von Spins, aber auch Relaxationsphänome und dynamische Prozesse immer zuverlässiger messen zu können. Dasselbe gilt für anisotrope Strukturparameter wie dipolare oder quadrupolare Restkopplungen und residuale chemische Verschiebungsanisotropie, für deren Messung Moleküle mithilfe von Orientierungsmedien partiell entlang einer Vorzugsachse ausgerichtet werden müssen. In den letzten Jahren konnte anhand einer Vielzahl von Beispielen gezeigt werden, dass mit dieser Methodik Probleme im Bereich der Aufklärung von Konformation, Konfiguration und Konstitution von Molekülen adressiert werden können, wo konventionelle Ansätze versagen.

Auch die Entwicklung von Radiofrequenzpulsen, den fundamentalen Bestandteilen aller NMR-Experimente, ist Gegenstand aktueller Forschung. Die Vielfalt an bekannten Pulsformen steht dabei im Verhältnis zur umfangreichen Methodenpalette, die von geometrischer Intuition bis zu numerischen Optimierungsalgorithmen reicht. Die Theorie der optimalen Kontrolle, ein dem Euler-Lagrange-Formalismus verwandtes Gradientenverfahren, eignet sich in besonderem Maße dazu, Trajektorien dynamischer Systeme mit bekannten Bewegungsgleichungen zu optimieren. Im Bereich der hochauflösenden NMR-Spektroskopie konnte gezeigt werden, dass sich durch auf Kontrolltheorie basierenden Algorithmen die physikalischen Grenzen vieler Spinsysteme ausloten lassen und selbst für viele tausend unabhängige Optimierungsvariablen in bis zu fünfdimensionalen Parameterräumen optimale Lösungen gefunden werden können. Die mathematischen Grundlagen zur Simulation

der Dynamik von Spinsystemen sowie Algorithmen zur optimalen Kontrolle werden in Kapitel 1 dieser Arbeit skizziert.

Der Gegenstand dieser Arbeit ist die Optimierung von Entkopplungsexperimenten. Auch wenn Aufspaltungsmuster und Kopplungen wertvolle Strukturinformationen bergen, bedeuten zu Singuletts zusammengefallene Resonanzlinien oft eine verbesserte Auflösung und somit erhöhte Interpretierbarkeit der Spektren. Gleichzeitig kann sich die Signalintensität und somit die Empfindlichkeit steigern lassen. Der Hauptteil dieser Arbeit ist in zwei Teile gegliedert. Kapitel 2 beschäftigt sich mit heteronuklearer Entkopplung und somit der Unterdrückung von Wechselwirkungseffekten unterschiedlicher Spinspezies, typischerweise ^{1}H und ^{13}C. Ein historischer Abriss über die gängigsten Entkopplungssequenzen dient dazu, methodische Ansätze um möglichst artefaktfreie Spektren zu erhalten, aufzuzeigen und daraus Kriterien für eine Optimierung abzuleiten. Die vorgestellten Algorithmen werden untersucht im Hinblick auf den zugrundeliegenden mathematischen Formalismus, Allgemeingültigkeit, Effizienz und Konvergenzverhalten. Die als Ergebnis erhaltenen Pulssequenzen werden an einem einfachen Spinsystem simuliert und experimentell getestet. Zwei experimentell relevante Aspekte von Entkopplungssequenzen, das Signal-zu-Artefakt-Verhältnis und die zu erreichende Auflösung im Hinblick auf durch Energieeintrag begrenzte Akquisititonszeiten, werden an Beispielen kleiner organischer Moleküle untersucht.

Kapitel 3 befasst sich mit homonuklearer Entkopplung, also der Unterdrückung von Kopplungen innerhalb derselben Spinspezies, deren Methodik wesentlich komplexer ist. Als Motivation dient hier die genaue Messung von anisotropen NMR-Parametern, genauer von dipolaren Restkopplungen. Es wird ein heteronukleares Korrelationsexperiment vorgeschlagen, um heteronukleare Kopplungen ohne den Einfluss von homonuklearen Kopplungen auf die Signalform messen zu können. Dabei soll an mehreren Beispielen untersucht werden, ob die Genauigkeit der extrahierten Kopplungskonstanten durch homonukleare Entkopplung erhöht werden kann. Der Einfluss diverser Parameter der Spinsysteme auf die Empfindlichkeit der Experimente wird charakterisiert und identifizierte Schwachstellen werden durch die Optimierung neuartiger Pulssequenzbausteine ausgeglichen.

Da an beiden Themenkomplexen während der Anfertigung dieser Arbeit durch andere Arbeitsgruppen parallel geforscht wurde, werden die hier erhaltenen Ergebnisse auch im Kontext dieser Arbeiten diskutiert.

Contents

1. Theory

> Oh what is my theory that it is. [...] Well, this is what it is - my theory that I have, that is to say, which is mine, is mine. [...] This is it. My theory that belongs to me is as follows. This is how it goes. The next thing I'm going to say is my theory. Ready? [...] This theory goes as follows and begins now. [...] That is my theory, it is mine, and belongs to me and I own it, and what it is too.
>
> Anne Elk (Miss) - Monty Python's Flying Circus 31: The All-England Summarize Proust Competition

1.1. Spin Dynamics

This section deals with the introduction of all necessary concepts and formalisms which are required for a mathematical treatment of nuclear spins. They will be used to numerically evaluate NMR pulse sequences and predict spectra as well as to subject spin dynamics to optimization algorithms. Reference to most of the theory presented here can be found in comprehensive textbooks[1]. Further references are indicated.

1.1.1. Nuclear Magnetism

The origin of nuclear magnetism is not yet fully understood. Combinations of quarks with different charges and spin yield the proton and the neutron carrying a positive and neutral charge respectively. Both have half-integer spin and a magnetic moment. Their spin is a type of angular momentum that is no result of orbit or collision but an intrinsic property of the nuclear particles. The same holds for their magnetic moment which is no result of circulating currents. Nuclei can interact with magnetic fields in the same manner as electrons. In general the potential energy E_{mag} of an object exposed to a magnetic field $\boldsymbol{B}$ is given by

$$E_{\mathrm{mag}} = -\boldsymbol{\mu} \cdot \boldsymbol{B} \tag{1.1}$$

with $\boldsymbol{\mu}$ being the magnetic moment (bold symbols denote vectors). For atomic nuclei their magnetic moment is linked to the spin angular momentum via

$$-\boldsymbol{\mu} = \gamma \cdot \boldsymbol{I} \tag{1.2}$$

with $\boldsymbol{I}$ denoting the nuclear spin angular momentum operator and the proportionality constant γ corresponding to the so-called gyromagnetic ratio. The gyromagnetic ratio is one of the key figures to define the sensitivity of a given nuclear isotope towards an NMR measurement next to the natural abundance. With a natural abundance of >99.9% and γ of 42.576 MHz T^{-1}, ^{1}H, whose nucleus consists of a single proton, is among the most sensitive probes for NMR. Only ^{3}H has a higher γ than ^{1}H but is far less abundant and not a stable hydrogen isotope. The gyromagnetic ratio can assume positive and negative values. Most nuclei have $\gamma > 0$ and a magnetic moment parallel to the angular momentum. For particles with $\gamma < 0$, the magnetic moment has the opposite direction to the angular momentum.

1.1.2. Spin Precession

To understand the behavior of nuclear spins, many analogies to the quantum mechanical description of rotation and angular momentum may be drawn. For a given quantum number l there exist $2l+1$ degenerate energy levels $E_{l,m}$ which are the energy eigenstates of the system under a given Hamiltonian H and that can be described by wave functions $|\psi_{l,m}\rangle$:

$$H|\psi_{l,m}\rangle = E_{l,m}|\psi_{l,m}\rangle \tag{1.3}$$

For nuclei with a spin quantum number $I = 1/2$ such as ^{1}H (and heteronuclei such as ^{13}C, ^{15}N, ^{19}F or ^{31}P) this leads to two degenerate eigenstates. If a static magnetic field is applied, this degeneracy is broken. In NMR spectroscopy this magnetic field is aligned along the z-direction of the laboratory frame and is referred to as B_0. It induces the so-called Zeeman interaction which is described by the following Hamiltonian:

$$H_0 = -\gamma B_0 I_z \tag{1.4}$$

The solution of the time-independent Schrödinger equation yields the two eigenstates $|\alpha\rangle$ and $|\beta\rangle$ which form the Zeeman eigenbasis with the following energy levels:

$$H_0|\alpha\rangle = -\frac{1}{2}\hbar\gamma B_0|\alpha\rangle \tag{1.5}$$

$$H_0|\beta\rangle = \frac{1}{2}\hbar \underbrace{\gamma B_0}_{\omega_0} |\beta\rangle \tag{1.6}$$

The magnetic energy is minimized if the spin is in the $|\alpha\rangle$ state which means parallel alignment of the spin and the magnetic field. The less-favored $|\beta\rangle$ state corresponds to opposite alignment. The energy difference is given by $\hbar\omega_0$ with ω_0 generally being called the Larmor frequency ω_L. Since the population of these quantum states is governed by a Boltzmann distribution, a higher value of ω_L corresponds to a larger population difference of the two eigenstates at a given temperature. Therefore the macroscopic magnetization after cancellation of opposite-aligned magnetic moments, which determines the sensitivity of an NMR experiment, increases with ω_L and ultimately with B_0. The fact that spins can not all align parallel to B_0 once it is applied (turn like a compass needle in the earth's magnetic field) becomes evident if the time-dependent Schrödinger equation is solved. For simplicity H is divided by $\hbar$ to obtain the Hamiltonian $\mathcal{H}$ in natural units:

$$\frac{\partial|\psi\rangle}{\partial t} = -i\mathcal{H}|\psi\rangle \tag{1.7}$$

For time-independent Hamiltonians like the Zeeman term $\mathcal{H}_0$ this is a first-order differential equation and easily solved by an exponential:

$$|\psi\rangle(t) = \exp(-i\mathcal{H}t)|\psi\rangle(0) \tag{1.8}$$

If $|\psi\rangle$ corresponds to a Zeeman eigenstate the eigenvalues of the exponential operator can be obtained by exponentiation of the eigenvalues of the original operator. This can be done because the exponential of an operator commutes with the operator itself. For $\mathcal{H}_0$ this yields

$$\exp(-i\mathcal{H}_0 t)|\psi\rangle = \exp(-\frac{i}{2}\omega_\mathrm{L} t)|\psi\rangle. \tag{1.9}$$

This shows that the Zeeman interaction does not change the spin states but a time-dependent phase factor is introduced. These phase factors are the result of an induced motion of the spins. Without the influence of B_0 the vectors representing the angular momentum and magnetic moment point in all possible directions. In other words, the spin polarization axes are isotropically distributed. Once B_0 is applied, the spins start to move around the field on a precession cone keeping a constant angle. This precession movement happens due to the spins having an angular momentum as well as magnetic moment. There are several classical analogues to spin precession. A rotating spinning top that is given a push will start to precess rather than falling over under the effect of earth's gravitational pull. The same holds for a bicycle that will turn a corner rather than falling over once the cyclist leans to one side (although there are contributions from other forces in this particular case).

1.1.3. Nuclear Spin Hamiltonian

Typical molecules consist of multiple atoms with several protons, neutrons and electrons each. Realistically, the full Schrödinger equation of such a system can not be solved. But to a very good degree of approximation the behavior of the nuclear spins can be decoupled from all other degrees of freedom of a given molecule since the energy scale is far from being relevant to the motion of the electrons (the NMR energy scale being in the RF regime). A time-averaged contribution of electronic properties to the spin dynamics can be taken into account by modifying $\mathcal{H}_0$. For spin-1/2-nuclei, the interaction with the electrical field of the surrounding electrons is completely independent of the nucleus' orientation because its charge distribution is spherical and therefore can be compared to a point charge. This means for $I = 1/2$ there are no electric influences on the nuclear energy levels and all internal and external interactions are purely magnetic. The remarkable situation for NMR is that the spins interact more strongly with externally applied magnetic fields than with its natural environment. The by far biggest contribution to the Hamiltonian is the Zeeman interaction caused by B_0 which has been discussed in section 1.1.2.

In order to probe the spins an oscillating transverse magnetic field has to be applied. This is often referred to as B_1 and is ideally exactly perpendicular to B_0 to avoid longitudinal contributions. In order to achieve resonance and tilt the macroscopic magnetization to the transverse plane where it can be detected, B_1 has to be modulated with ω_L (it may have an additional phase ϕ; ensemble spin dynamics are discussed in section 1.1.4). In contrast to B_0, this RF field couples to the transverse components of the spin angular momentum operator:

$$\mathcal{H}_1 = -\frac{1}{2}\gamma B_1 \left\{\cos(\omega_\mathrm{ref} t + \phi) I_x + \sin(\omega_\mathrm{ref} t + \phi) I_y\right\} \tag{1.10}$$

As will be discussed further below, the actual ω_L of individual spins can deviate from γB_0. Given that the B_1 field according to equation 1.10 can only be matched to a single frequency ω_ref, the resonance condition is only fulfilled perfectly for $\omega_\mathrm{L} = \omega_\mathrm{ref}$. The product in front of the brackets of equation 1.10 is synonymously being called nutation frequency or RF amplitude ω_RF:

$$\omega_\mathrm{RF} = -\frac{1}{2}\gamma B_1 \tag{1.11}$$

The factor 1/2 is reflecting the fact that if an oscillating RF field is represented by the sum of two fields rotating in opposite directions, only one component can be in resonance with the spins precessing in only one direction.

Due to the large amplitudes of the B_0 and B_1 fields, the external magnetic fields dominate the spin dynamics and certain contributions to internal spin interactions are overcompensated or hidden. This so-called secular approximation often leads to a significant simplification of $\mathcal{H}_0$. Further, rapid molecular motion leads to the replacement of many interactions by a time-averaged value, which is often zero in gases or isotropic liquids or assumes a scalar value. This becomes evident for the chemical shift. Electrons surrounding the nuclei are also affected by B_0 and the currents that are induced in turn induce fields that perturb B_0 locally. Nuclear spins interact with these induced fields in the same way as with B_0:

$$\mathcal{H}_\mathrm{CS,full} = -\boldsymbol{\mu} \cdot \boldsymbol{\delta} \cdot \boldsymbol{B}_0 \tag{1.12}$$

The so-called chemical shift tensor $\boldsymbol{\delta}$ is a 3×3 matrix taking into account that local fields are induced in all possible directions in the laboratory frame. Given that local fields can not be measured from a reference of naked nuclei, the chemical shift has to be defined with respect to a reference shift δ_0 of a given substance, e.g. TMS for ^{1}H and ^{13}C NMR spectroscopy. Further, it is common to dissect the chemical shift tensor further into an isotropic contribution δ_iso and a contribution from Chemical Shift Anisotropy (CSA) $\boldsymbol{\Delta\delta}$. Thus, equation 1.12 can be modified according to

$$\mathcal{H}_\mathrm{CS,full} = -\boldsymbol{\mu} \cdot (\delta_0 \cdot \mathbf{1} + \delta_\mathrm{iso} \cdot \mathbf{1} + \boldsymbol{\Delta\delta}) \cdot \boldsymbol{B}_0. \tag{1.13}$$

Given that B_0 is applied along the z-axis $\boldsymbol{\Delta\delta} \cdot \boldsymbol{B}_0$ at a specific nuclear site yields

$$\begin{pmatrix} \Delta\delta_{xx} & \Delta\delta_{xy} & \Delta\delta_{xz} \\ \Delta\delta_{yx} & \Delta\delta_{yy} & \Delta\delta_{yz} \\ \Delta\delta_{zx} & \Delta\delta_{zy} & \Delta\delta_{zz} \end{pmatrix} \cdot \begin{pmatrix} 0 \\ 0 \\ B_0 \end{pmatrix} = \begin{pmatrix} \Delta\delta_{xz}B_0 \\ \Delta\delta_{yz}B_0 \\ \Delta\delta_{zz}B_0 \end{pmatrix}. \tag{1.14}$$

The matrix elements $\Delta\delta_{ij}$ generally depend on the molecule's orientation Θ and contribute to the Hamiltonian according to

$$\mathcal{H}_{\mathrm{CSA}} = -\gamma\Delta\delta_{xz}(\Theta)B_0 I_x - \gamma\Delta\delta_{yz}(\Theta)B_0 I_y - \gamma\Delta\delta_{zz}(\Theta)B_0 I_z. \tag{1.15}$$

In the secular approximation the first and second term in equation 1.15 are neglected and $\mathcal{H}_{\mathrm{CS}}$ simplifies to

$$\mathcal{H}_{\mathrm{CS}} = -\gamma\left(\delta_0 + \delta_{\mathrm{iso}} + \Delta\delta_{zz}(\Theta)\right)B_0 I_z. \tag{1.16}$$

The time-average of element $\Delta\delta_{zz}(\Theta)$ amounts to zero in liquids due to the random molecular motion and the chemical shift is thus dominated by δ_{iso}. It can be used to correct ω_{L} at each individual nuclear site to take the local chemical surrounding into account and modify $\mathcal{H}_0$ according to

$$\mathcal{H}_0 = \omega_0(\delta_0 + \delta_{\mathrm{iso}})I_z = \omega_{\mathrm{L}}^{\mathrm{local}} I_z. \tag{1.17}$$

From the considerations above, it becomes clear that the magnitude of the chemical shift is dependent on B_0. In order to unambiguously identify the position of resonance lines in NMR spectra, the ppm scale was introduced, which is also referenced to the chemical shift of a reference compound and normalized to B_0 and is then independent of the static magnetic field. Other than the exact frequency, a ppm value allows a rough conclusion about chemical moieties. Nevertheless, the ability to express the chemical shift as a frequency has advantages in the context of formulating control problems (see section 1.2).

The theoretical treatment of NMR experiments greatly benefits from a further simplification concerning the B_0 field. To separate the effects of B_0 from all other contributions to $\mathcal{H}_0$ (and most importantly from $\mathcal{H}_1$), the Hamiltonian is transformed into a coordinate system that is rotating with ω_{ref} around the z-axis of the laboratory frame. One of the immediate benefits is that $\mathcal{H}_1$ according to equation 1.10 becomes time-independent. Precession in this rotating frame can be further simplified if ω_{ref} is again subtracted from the local ω_{L} in equation 1.17 which can be rewritten as

$$\mathcal{H}_0 = \omega I_z. \tag{1.18}$$

This Hamiltonian now only contains a single frequency ω which is generally called offset frequency or resonance offset (with respect to ω_{ref}) and can also be denoted as $2\pi\nu$ with ν representing a frequency measured in Hz which will be used in the following chapters.

Spins can also mutually interact with each other via the magnetic fields generated by themselves which is referred to as coupling. The strength of a direct interaction of magnetic dipoles through space is dependent on the orientation of the spins' angular momenta with respect to a unit vector which joins the centers of the nuclei as well as their distance r_{jk}. In the secular approximation the direct dipole-dipole coupling $\mathcal{H}_{\mathrm{DD}}$ is predominantly determined by the orientation Θ_{jk} of the vector connecting the nuclei with respect to B_0 and simplifies to

$$\mathcal{H}_{\mathrm{DD}}(\Theta_{jk}) = D_{jk}(r_{jk}, \Theta_{jk}) \cdot (3I_{jz}I_{kz} - \boldsymbol{I_j} \cdot \boldsymbol{I_k}) \tag{1.19}$$

with D_{jk} being the dipolar coupling constant with a characteristic distance and orientation dependence given by

$$D_{jk}(r_{jk}, \Theta_{jk}) = -\frac{\hbar\mu_0}{4\pi} \cdot \frac{\gamma_j\gamma_k}{r_{jk}^3} \cdot \frac{1}{2}(3\cos^2\Theta_{jk} - 1). \tag{1.20}$$

The dipolar coupling constant is further defined by the gyromagnetic ratios γ_j and γ_k and the magnetic constant μ_0 ($4\pi \cdot 10^{-7}\ \mathrm{N} \cdot \mathrm{A}^{-2}$). In a heteronuclear spin system (ω_{L} of spin j and k are significantly different as a result of a different γ) even more terms are discarded to obtain

$$\mathcal{H}_{\mathrm{DD}}(\Theta_{jk}) = D_{jk}(r_{jk}, \Theta_{jk}) 2I_{jz}I_{kz}. \tag{1.21}$$

Since large parts of this thesis deal with heteronuclear two-spin systems, a common shorthand notation is used for the corresponding bilinear operators. The single-spin operators for the heteronucleus are denoted S instead of I and the operator $2I_{jz}I_{kz}$ may be rewritten as $2I_zS_z$. Equation 1.20 implies the existence of an angle Θ where D is effectively zero. This angle is called the magic angle $\Theta_{\mathrm{magic}} \approx 54.74°$ and is of major importance for solid-state NMR. Since molecules can move freely in isotropic liquids it is easily recognized that $\mathcal{H}_{\mathrm{DD}}$ has to average to zero because all angles Θ can be realized. To ensure equal probability of all orientations the factor $\sin\Theta_{jk}$ is introduced in the following integral since a portion of surface area on a sphere is proportional to $\sin\Theta_{jk}$ which leads to

$$\int_0^\pi \sin\Theta_{jk}(3\cos^2\Theta_{jk} - 1)\mathrm{d}\Theta = 0. \tag{1.22}$$

Even in isotropic liquids spins show couplings which are caused by changes in the local magnetic field at a nuclear site due to influences of neighboring spins mediated by the bonding electrons. This indirect dipole-dipole interaction is mostly called J-coupling and provides insights into molecular bonding topologies. The involvement of chemical bonds causes the manifestation of these couplings even in the presence of rapid molecular motion. The full J-coupling Hamiltonian $\mathcal{H}_{\mathrm{J}}$ is given by

$$\mathcal{H}_{\mathrm{J}} = 2\pi\boldsymbol{I_j} \cdot \boldsymbol{J_{jk}} \cdot \boldsymbol{I_k}. \tag{1.23}$$

Just like the chemical shift tensor $\boldsymbol{\delta}$, the J-coupling tensor $\boldsymbol{J_{jk}}$ is averaged to a scalar value J_{jk} (measured in Hz) if the molecules undergo motional averaging. Therefore it is also called scalar coupling and the secular $\mathcal{H}_{\mathrm{J}}$ simplifies to

$$\mathcal{H}_{\mathrm{J}} = 2\pi J_{jk}\boldsymbol{I_j} \cdot \boldsymbol{I_k}. \tag{1.24}$$

Similar to $\mathcal{H}_{\mathrm{DD}}$, $\mathcal{H}_{\mathrm{J}}$ can be further simplified for heteronuclear spin systems:

$$\mathcal{H}_{\mathrm{J}} = 2\pi J_{\mathrm{IS}}I_zS_z \tag{1.25}$$

The same simplification can be applied to homonuclear spin systems when ω_L of spin j and k differ significantly as a result of a large difference in chemical shift (weak coupling limit).

If nuclei possess $I > 1/2$ the charge distribution within the nucleus is no longer spherical which gives rise to a nuclear quadrupole moment Q. Quadrupole moments can interact with the electric field gradients generated by electrons surrounding the nucleus which are described by the electric field gradient tensor $\boldsymbol{V}(\Theta)$. The full Hamiltonian of this interaction is given by

$$\mathcal{H}_\mathrm{Q}(\Theta) = \frac{eQ}{2I(2I-1)\hbar}\boldsymbol{I}\cdot\boldsymbol{V}(\Theta)\cdot\boldsymbol{I}. \tag{1.26}$$

The magnitude of the quadrupolar coupling is often quite large compared to other interactions so the secular approximation may not be applicable to full extent and higher-order quadrupolar coupling terms have to be considered in the Hamiltonian. The first-order contribution is given by

$$\mathcal{H}_\mathrm{Q}(\Theta) = \omega_\mathrm{Q}\frac{1}{6}\left(3I_z^2 - I(I+1)\mathbf{1}\right) \tag{1.27}$$

with the first-order quadrupolar coupling ω_Q given by

$$\omega_\mathrm{Q}(\Theta) = \frac{3eQ\overline{V_{zz}(\Theta)}}{2I(2I-1)\hbar} \tag{1.28}$$

and $\overline{V_{zz}(\Theta)}$ being the motional average of the secular electric field gradient component comparable to an isotropic chemical shift with the difference being that $\overline{V_{zz}(\Theta)}$ is averaged to zero in liquids and therefore $\mathcal{H}_\mathrm{Q}$ vanishes.

All contributions to $\mathcal{H}_0$ which have been discarded so far contribute to relaxation. The remaining local magnetic fields experienced randomly by individual spins drive the ensemble back to their equilibrium state. To describe the fundamental relaxation mechanisms, the concepts of populations and coherence have to be introduced which need a formalism to depict the dynamics of spin ensembles.

1.1.4. Ensemble Dynamics

Single spin-1/2 particles can be described by a wave function that is a superposition of the two Zeeman eigenstates $|\alpha\rangle$ and $|\beta\rangle$ with complex superposition coefficients c_α and c_β:

$$|\psi\rangle = c_\alpha|\alpha\rangle + c_\beta|\beta\rangle \tag{1.29}$$

The coefficients in equation 1.29 have to fulfill the normalization condition for any given state $|\psi\rangle$. Any state $|\psi\rangle$ can be written as a two-dimensional column vector with the superposition coefficients as complex components. In this notation the Zeeman eigenstates can be written as

$$|\alpha\rangle = \begin{pmatrix}1\\0\end{pmatrix} \qquad |\beta\rangle = \begin{pmatrix}0\\1\end{pmatrix}. \tag{1.30}$$

It is now useful to look at the matrix representations of the different angular momentum operators and their effects on $|\alpha\rangle$ and $|\beta\rangle$. In analogy to regular angular momentum, shift operators can be defined for the spin which change the spin quantum number:

$$I^+ = I_x + iI_y \tag{1.31}$$

$$I^- = I_x - iI_y \tag{1.32}$$

These operators act on the Zeeman eigenstates according to

$$I^+|\alpha\rangle = 0 \qquad I^+|\beta\rangle = |\alpha\rangle \tag{1.33}$$

$$I^-|\alpha\rangle = |\beta\rangle \qquad I^-|\beta\rangle = 0. \tag{1.34}$$

Furthermore, so-called projection or polarization operators can be defined using the unity matrix and the spin angular momentum operator I_z:

$$I^\alpha = \frac{1}{2}\mathbf{1} + I_z \tag{1.35}$$

$$I^\beta = \frac{1}{2}\mathbf{1} - I_z \tag{1.36}$$

In terms of their action on the $|\alpha\rangle$ and $|\beta\rangle$ states, they have the following properties:

$$I^\alpha|\alpha\rangle = |\alpha\rangle \qquad I^\beta|\alpha\rangle = 0 \tag{1.37}$$

$$I^\alpha|\beta\rangle = 0 \qquad I^\beta|\beta\rangle = |\beta\rangle \tag{1.38}$$

The matrix representations of the aforementioned operators can be obtained by forming the direct product (or tensor product) of all possible combinations of the Zeeman eigenstates:

$$I^+ = |\alpha\rangle\langle\beta| \qquad I^- = |\beta\rangle\langle\alpha| \tag{1.39}$$

$$I^\alpha = |\alpha\rangle\langle\alpha| \qquad I^\beta = |\beta\rangle\langle\beta| \tag{1.40}$$

Equating these direct products yields

$$I^+ = \begin{pmatrix} 0 & 1 \\ 0 & 0 \end{pmatrix} \qquad I^- = \begin{pmatrix} 0 & 0 \\ 1 & 0 \end{pmatrix} \qquad I^\alpha = \begin{pmatrix} 1 & 0 \\ 0 & 0 \end{pmatrix} \qquad I^\beta = \begin{pmatrix} 0 & 0 \\ 0 & 1 \end{pmatrix}. \tag{1.41}$$

From the considerations above the matrix representations of the Cartesian components of the spin angular momentum operator and the unity matrix can be obtained from linear combinations of the direct products given above:

$$I_x = \frac{1}{2}(I^+ + I^-) \tag{1.42}$$

$$I_y = \frac{1}{2i}(I^+ - I^-) \tag{1.43}$$

$$I_z = \frac{1}{2}(I^\alpha - I^\beta) \tag{1.44}$$

$$\frac{1}{2}\mathbf{1} = \frac{1}{2}(I^\alpha + I^\beta) \tag{1.45}$$

The matrix representations of the three angular momentum operators in the Zeeman eigenbasis yield

$$I_x = \frac{1}{2}\begin{pmatrix} 0 & 1 \\ 1 & 0 \end{pmatrix} \qquad I_y = \frac{1}{2i}\begin{pmatrix} 0 & 1 \\ -1 & 0 \end{pmatrix} \qquad I_z = \frac{1}{2}\begin{pmatrix} 1 & 0 \\ 0 & -1 \end{pmatrix}. \tag{1.46}$$

In order to describe the ensemble behavior of spins, macroscopic expectation values of the angular momentum operators need to be evaluated. Expectation values of spins in a given superposition state are given by

$$\begin{aligned} \langle O \rangle &= \langle \psi | O | \psi \rangle \\ &= \begin{pmatrix} {c_\alpha}^* & {c_\beta}^* \end{pmatrix} \begin{pmatrix} O_{\alpha\alpha} & O_{\alpha\beta} \\ O_{\beta\alpha} & O_{\beta\beta} \end{pmatrix} \begin{pmatrix} c_\alpha \\ c_\beta \end{pmatrix} \\ &= c_\alpha {c_\alpha}^* O_{\alpha\alpha} + c_\alpha {c_\beta}^* O_{\alpha\beta} + c_\beta {c_\alpha}^* O_{\beta\alpha} + c_\beta {c_\beta}^* O_{\beta\beta}. \end{aligned} \tag{1.47}$$

Asterisks denote complex conjugates. To be able to describe the state of the system only by the the quadratic products of the superposition coefficients a matrix can be constructed according to the direct product

$$|\psi\rangle\langle\psi| = \begin{pmatrix} c_\alpha {c_\alpha}^* & c_\alpha {c_\beta}^* \\ c_\beta {c_\alpha}^* & c_\beta {c_\beta}^* \end{pmatrix}. \tag{1.48}$$

Expectation values of operators O can be obtained from $|\psi\rangle\langle\psi|$ via

$$\langle O \rangle = \mathrm{Tr}(O^\dagger |\psi\rangle\langle\psi|) \tag{1.49}$$

with the trace operation being the sum of the diagonal elements after a matrix multiplication. To obtain the macroscopic expectation value of Operator O for an ensemble of a massive number of spins all individual contributions have to be summed up. If the state of individual spins is denoted as $|\psi\rangle\langle\psi|$ it is sufficient to use the trace operation to project the following operator onto O:

$$\rho = \overline{|\psi\rangle\langle\psi|} = \begin{pmatrix} \overline{c_\alpha {c_\alpha}^*} & \overline{c_\alpha {c_\beta}^*} \\ \overline{c_\beta {c_\alpha}^*} & \overline{c_\beta {c_\beta}^*} \end{pmatrix} \tag{1.50}$$

with ρ being called the spin density operator and presenting the possibility to predict the outcome of macroscopic observations of quantum systems via the definition of an ensemble state which has been deduced from spin operators. The shorthand notation of $\langle O \rangle$ may be written as

$$\langle O \rangle = \mathrm{Tr}\left(O^\dagger \rho\right). \tag{1.51}$$

The matrix elements given in equation 1.50 are of fundamental importance for NMR spectroscopy. Their meaning becomes evident when ρ is rewritten using the shift and polarization operators:

$$\rho = \overline{c_\alpha {c_\alpha}^*} I^\alpha + \overline{c_\beta {c_\beta}^*} I^\beta + \overline{c_\alpha {c_\beta}^*} I^+ + \overline{c_\beta {c_\alpha}^*} I^- \tag{1.52}$$

Diagonal elements of ρ correspond to the populations of the eigenstates. For NMR only the difference of populations has a physical significance since it gives rise to a macroscopic spin polarization along the z-axis. Any state with a population of the $|\alpha\rangle$ states which is larger than the $|\beta\rangle$ states indicates polarization along B_0. If the $|\beta\rangle$ is higher populated, the polarization points against the direction of B_0. The off-diagonal elements are called coherences between states. In the simplest case of uncoupled spin-1/2-nuclei there can only exist coherence between the $|\alpha\rangle$ and $|\beta\rangle$ states. It can be classified by a quantum number defined by the difference between the I_z angular momentum eigenvalues of the interconnected states with $\overline{c_\beta c_\alpha{}^*}$ representing the most important -1 coherence which can be detected by a quadrature NMR receiver. This quantum number is called coherence order p. Coherences indicate transverse magnetization components of a given state. Therefore the spins have to be in superposition states with magnetization vectors partially aligned in the transverse plane. Otherwise no coherence will be observable.

The density operator not only allows to analyze a given state of a spin ensemble but also to predict its temporal evolution. This is in large parts facilitated by the fact that the spin systems in NMR allow for a very simple description of a thermal equilibrium state to an exceptionally good degree of approximation. Assuming that there is no coherence at thermal equilibrium the population of the Zeeman eigenstates is governed by a Boltzmann distribution:

$$\rho_{0,j} = \frac{\exp(-E_j/k_\mathrm{B}T)}{\sum\limits_k \exp(-E_k/k_\mathrm{B}T)} \tag{1.53}$$

The ratio of energy of the eigenstates (E_j) and the available thermal energy ($k_\mathrm{B}T$) can be rewritten as a Boltzmann factor

$$\mathbb{B} = \frac{\hbar\gamma B_0}{k_\mathrm{B}T} \tag{1.54}$$

and yields a very small number in the case of the NMR energy scale which indicates a very small population difference. This allows for the so-called high-temperature approximation where a power series expansion of the exponentials in equation 1.53 may be aborted after the term that is linear in $\mathbb{B}$. Due to the small values of $\mathbb{B}$ the denominator of equation 1.53 equates to two. The density operator at thermal equilibrium is therefore given by

$$\rho_0 = \frac{1}{2}\begin{pmatrix} 1+\frac{1}{2}\mathbb{B} & 0 \\ 0 & 1-\frac{1}{2}\mathbb{B} \end{pmatrix} = \frac{1}{2}(\mathbf{1} + \mathbb{B}I_z). \tag{1.55}$$

Given that the unity matrix and the value of $\mathbb{B}$ are not manipulated by any interaction described in section 1.1.3, or synonymously only the net polarization is relevant for an NMR measurement, it is sufficient to describe ρ_0 as I_z.

The equation of motion of the density operator is called the Liouville-von-Neumann equation and can be derived from the Schrödinger equation via

$$\begin{aligned} \frac{\partial\rho}{\partial t} &= \frac{\partial}{\partial t}(|\psi\rangle\langle\psi|) \\ &= \frac{\partial|\psi\rangle}{\partial t}\cdot\langle\psi| + |\psi\rangle\cdot\frac{\partial\langle\psi|}{\partial t} \\ &= -i\mathcal{H}|\psi\rangle\langle\psi| + i|\psi\rangle\langle\psi|\mathcal{H} \end{aligned} \tag{1.56}$$

$$\frac{\partial\rho}{\partial t} = -i[\mathcal{H},\rho]. \tag{1.57}$$

It can be solved by expanding the integral of the commutator in equation 1.57 in a Dyson series[2] which yields

$$\rho(t) = U(t)\rho_0 U^\dagger(t) \tag{1.58}$$

with $U(t)$ denoting the unitary propagator (and $U^\dagger$ its adjoint) given by

$$U(t) = \exp_{(\mathrm{O})}\left(-i\int\limits_0^t \mathcal{H}(\tau)\mathrm{d}\tau\right) \tag{1.59}$$

where $\exp_{(\mathrm{O})}$ indicates Dyson's time-ordered exponential. For time-independent Hamiltonians equation 1.59 simplifies to

$$U(\Delta t) = \exp(-i\mathcal{H}\Delta t). \tag{1.60}$$

The Liouville-van-Neumann equation is sufficient to describe the trajectory of density operators under any given Hamiltonian so far. However, it is not suitable to describe relaxation processes where both coherences need to be destroyed and the equilibrium state I_z has to be repopulated. Although the density operator has analogies to a macroscopic magnetization vector, unitary transformations according to equation 1.58 can not change the norm of the matrices representing density operators. This is due to their corresponding Lie algebras. Hamiltonians and density operators are defined in Hilbert space and the matrices are members of the $\mathfrak{su}(N)$ Lie algebra with $N = 2^n$ where n is the number of spins. The propagators belong to the Lie group $SU(N)$ which is connected to its Lie algebra via the exponential comparable to the connection of Hamiltonians and propagators. Therefore unitary transformations are length-preserving upon action on their vector space[3].

The traditional approach to describe macroscopic magnetization is the three-component magnetization vector whose temporal evolution is governed by the semi-classical Bloch equations which can be written in matrix form:

$$\frac{\partial}{\partial t}\begin{pmatrix} M_x \\ M_y \\ M_z \end{pmatrix} = \begin{pmatrix} 0 & -\omega & \omega_{\mathrm{RF}}\sin\phi \\ \omega & 0 & -\omega_{\mathrm{RF}}\cos\phi \\ -\omega_{\mathrm{RF}}\sin\phi & \omega_{\mathrm{RF}}\cos\phi & 0 \end{pmatrix}\begin{pmatrix} M_x \\ M_y \\ M_z \end{pmatrix} - \begin{pmatrix} M_x/T_2 \\ M_y/T_2 \\ (M_z-1)/T_1 \end{pmatrix} \tag{1.61}$$

Bloch equations are not only capable to describe the effects of RF irradiation and free precession simultaneously, but further encompass relaxation properties using only two empirically observable and measurable numbers. T_2 corresponds to the so-called transverse relaxation time and is connected to an exponential decay rate which limits the time window where coherence and hence the NMR signal may be observed. It is also referred to as spin-spin relaxation. T_1 is the so-called longitudinal relaxation time and is connected to a rate of exponential build-up of equilibrium polarization along the z-axis and therefore limits the repetition rate of NMR experiments. The shortcoming of the Bloch equations is the restriction to a three-dimensional space which is not sufficient to depict the dynamics of coupled spin systems.

The most general formalism to cover coupled many-spin dynamics in the presence of relaxation is the Liouville superoperator formalism[4]. Equation 1.57 can be transformed to yield the Liouville equation

$$\frac{\partial\hat{\rho}}{\partial t} = -i\hat{\mathcal{H}}\hat{\rho} - \hat{\Gamma}(\hat{\rho} - \hat{\rho}_0) \tag{1.62}$$

where hats denote superoperators. The relaxation superoperator $\hat{\Gamma}$ has been introduced to include all dissipative processes which contribute to T_1 and T_2 as well as chemical exchange and kinetics. Density operators in Liouville space are denoted as 2^{2n}-element vectors and are obtained by stacking the columns of the matrix representations. The matrix representation of the Hamilton superoperator (and all other angular momentum superoperators) is obtained via

$$\hat{\mathcal{H}} = \mathcal{H} \otimes \mathbf{1} - \mathbf{1} \otimes \mathcal{H}^T \tag{1.63}$$

with $\otimes$ denoting the tensor product in analogy to equation 1.48 and $\mathcal{H}^T$ being the transpose of the Hamiltonian. This yields $2^{2n} \times 2^{2n}$ matrices. Equation 1.62 can easily be solved for time-independent Hamiltonians excluding relaxation and yields

$$\hat{\rho}(\Delta t) = \hat{L}(\Delta t)\hat{\rho}_0. \tag{1.64}$$

$\hat{L}$ denotes the propagator in Liouville space and is connected to the Hamilton superoperator by exponentiation:

$$\hat{L}(\Delta t) = \exp(-i\hat{\mathcal{H}}\Delta t) \tag{1.65}$$

The matrix representation of $\hat{L}$ in the case of a unitary transformation can be derived from the corresponding unitary propagator via

$$\hat{L} = U \otimes U^*. \tag{1.66}$$

All formalisms introduced above can readily be transferred and applied in the rotating frame. Since this thesis deals with coupled spin systems in small organic molecules with comparably long relaxation times, calculations are mostly carried out in Hilbert space and relaxation is neglected. In the case of the very well conditioned spin systems in chapter 2, a reduced Liouville space is used.

1.1.5. Coupled Spin Dynamics

Section 1.1.3 already introduced Hamiltonians which describe couplings among spins and make use of products of operators to describe the corresponding interactions. The density operator formalism can serve as the basis of a depiction of coupled spin dynamics that reintroduces a part of the simplicity of the magnetization vector. This formalism is called the product operator formalism and is a common tool to analyze NMR pulse sequences without too much loss of generality. Microscopically, the state of a pair of coupled spin-1/2-nuclei can be described by a superposition of four Zeeman product states according to

$$|\psi\rangle = c_{\alpha\alpha}|\alpha\alpha\rangle + c_{\alpha\beta}|\alpha\beta\rangle + c_{\beta\alpha}|\beta\alpha\rangle + c_{\beta\beta}|\beta\beta\rangle. \tag{1.67}$$

In analogy to the formalism to derive the operator basis of uncoupled spins, the state $|\psi\rangle$ in equation 1.67 could be represented as a four-element vector and a 4×4 density operator matrix containing the 16 possible products of superposition coefficients could be formed. The corresponding density operator may be rewritten comparable to equation 1.52 using combinations of shift and polarization operators. This indicates the existence of several possible coherence orders depending on the transitions between eigenstates. A two-spin system allows for double- ($p = \pm 2$), single- ($p = \pm 1$) and zero-quantum coherences ($p = 0$).

However, the use of the Cartesian components of the spin angular momentum operator to construct an orthogonal operator basis is more advantageous due to their commutation properties:

$$\begin{aligned} [I_x, I_y] &= iI_z \\ [I_z, I_x] &= iI_y \\ [I_y, I_z] &= iI_x \end{aligned} \tag{1.68}$$

The relationship between these operators is called cyclic commutation. If any given three operators A, B and C cyclically commute, the unitary transformation of operator B under the effect of operator A is given by the so-called sandwich formula

$$\exp(-i\theta A)B\exp(i\theta A) = B\cos\theta + C\sin\theta. \tag{1.69}$$

This transformation can be understood as a rotation of B around an axis A by an angle θ. In NMR, the angles θ are always defined by products of frequencies which originate from Hamiltonians and their period of action on the spin system. The matrix representations of operators of a two-spin system can be derived from the two sets of single-spin operators according to

$$2I_{1j}I_{2k} = 2 \cdot I_{1j} \otimes I_{2k} \tag{1.70}$$

where each single-spin component may also be $\frac{1}{2}\mathbf{1}$. The 16 resulting product operators each have cyclic commutation relationships and the sandwich formula may be used to describe NMR pulse sequences consisting of a series of RF pulses and delays of free evolution with only very few assumptions. If product operators are transformed under the action of several Hamiltonians simultaneously, the corresponding transformations can be applied consecutively

$$\exp(A + B) = \exp(A) \cdot \exp(B) \qquad \text{if} \qquad [A, B] = 0 \tag{1.71}$$

holds. Therefore, for periods of free evolution where both the chemical shift and couplings are active, weak coupling has to be assumed (which is generally the case in heteronuclear spin systems) since

$$[I_{1z}, 2I_{1z}I_{2z}] = 0 \qquad \text{but} \qquad [I_{1z}, 2I_{1x}I_{2x}] \neq 0. \tag{1.72}$$

RF pulses may have arbitrary flip angles θ but must have a pure phase which corresponds to applying the pulse strictly along the x or y axis. This will lead to one of the terms in equation 1.10 vanishing which is necessary to apply the sandwich formula due to

$$[I_x, I_y] \neq 0. \tag{1.73}$$

Further, RF pulses have to be assumed to be short and strong so that the effects of resonance offsets can be neglected during the pulse. This assumption is made because of

$$[I_z, I_x] \neq 0. \tag{1.74}$$

Product operator transformations are typically written according to

$$I_z \xrightarrow{\omega_{\mathrm{RF}} I_x \tau} I_z \cos(\omega_{\mathrm{RF}}\tau) - I_y \sin(\omega_{\mathrm{RF}}\tau) \qquad \text{excitation of transverse magnetization,} \tag{1.75}$$

$$I_x \xrightarrow{\omega I_z \tau} I_x \cos(\omega\tau) + I_y \sin(\omega\tau) \qquad \text{evolution of resonance offset,} \tag{1.76}$$

$$I_x \xrightarrow{\pi J 2 I_z S_z \tau} I_x \cos(\pi J\tau) + 2 I_y S_z \sin(\pi J\tau) \qquad \text{evolution of } J\text{-couplings.} \tag{1.77}$$

It immediately follows from equation 1.75 that the flip angles $\omega_{\mathrm{RF}}\tau$ equaling $\pi/2$ (90°) and π (180°) carry significance for NMR since they correspond to the excitation of transverse magnetization from equilibrium polarization and population inversion, respectively. In general, any product operator transformation can be described by a general recipe which is referred to as the magic formula given by

$$\exp(-i\theta B) A \exp(i\theta B) = \begin{cases} A & \text{if } \; [A, B] = 0 \\ A\cos\theta + i\,[A, B]\sin\theta & \text{if } \; [A, B] \neq 0. \end{cases} \tag{1.78}$$

1.2. Optimal Control Theory

1.2.1. Definition

OCT can be seen as a generalization of the Euler-Lagrange formalism[5] to find extrema of constrained functions. In order to find an extremum of a given function $f(x, y)$ with a constraint given by $g(x, y) = c$, the Lagrangian Λ needs to be evaluated:

$$\Lambda(x, y, \lambda) = f(x, y) + \lambda\,(g(x, y) - c) \tag{1.79}$$

The Lagrange multipliers λ provide means to couple the constraints g to the function f. To find the extremum $\nabla_{x,y,\lambda}\Lambda(x, y, \lambda) = 0$ has to be fulfilled and the extremal coordinates are found by solving the system of equations formed by the partial derivatives of equation 1.79.

OCT extends this formalism to the problem of finding optimal trajectories of dynamic systems[6]. The primary objective is to find an optimal set of user-controllable parameters (controls) which are denoted by the control vector $\boldsymbol{u}(t)$, that yield an optimal trajectory which is denoted by the state vector $\boldsymbol{x}(t)$. These optimal controls and trajectories yield an extremum of a user-defined scalar quality criterion or performance index $L(\boldsymbol{x}(t), \boldsymbol{u}(t))$. A set of constraints $\boldsymbol{f}$ such as bounds for the possible values of $\boldsymbol{u}$ may be connected to L via a vector of Lagrange multipliers $\boldsymbol{\lambda}$ so that a quality criterion $\mathcal{J}$ can be defined according to

$$\mathcal{J} = L(\boldsymbol{x}(t), \boldsymbol{u}(t)) + \boldsymbol{\lambda}^T \boldsymbol{f}(\boldsymbol{x}(t), \boldsymbol{u}(t)). \tag{1.80}$$

The most apparent constraint for a dynamic system is its equation of motion which largely defines its trajectory:

$$\frac{\partial \boldsymbol{x}(t)}{\partial t} = f(\boldsymbol{x}(t), \boldsymbol{u}(t), t) \tag{1.81}$$

For a continuous system, equation 1.80 can be rewritten as

$$\mathcal{J} = h(\boldsymbol{x}(t_f), t_f) + \int\limits_{t_0}^{t_f} g(\boldsymbol{x}(t), \boldsymbol{u}(t), t)\mathrm{d}t \tag{1.82}$$

where g and h are scalar functions and h evaluates the endpoint of the trajectory at time point t_f. The second term in equation 1.82 corresponds to a running cost and judges the path how the final state $\boldsymbol{x}(t_f)$ was reached. In examples where only the final state is of interest the running cost may be dropped from $\mathcal{J}$. In general, optimality is reached when $\nabla_{\boldsymbol{u}}\mathcal{J} = 0$ which corresponds to maximum target fidelity and minimum expenditure of effort.

1.2.2. Optimal Control of Quantum Systems

This section is in large parts deduced from a comprehensive online lecture series on spin dynamics by Ilya Kuprov[7]. In order to control the trajectories of quantum systems, the solution of the Schrödinger equation (1.7) has to be known and the system has to be governed by a Hamiltonian given by

$$\mathcal{H} = \mathcal{H}_0 + \mathcal{H}_1(t) \tag{1.83}$$

where $\mathcal{H}_0$ denotes the free evolution or drift Hamiltonian and $\mathcal{H}_1$ corresponds to the control Hamiltonian given by

$$\mathcal{H}_1(t) = \sum_k u_k(t)\mathcal{H}_k \tag{1.84}$$

with a set of k time-dependent control variables which couple to their corresponding control operators $\mathcal{H}_k$. A typical problem for optimal control may be to find a set of controls which generates a unitary propagator that transforms a given state $|\psi\rangle$ to a desired target state $|\sigma\rangle$. An according cost functional may be defined such as

$$\mathcal{J} = \langle\sigma|\,\exp_{(\mathrm{O})}\left(-i\int_{t_0}^{t_f}\left[\mathcal{H}_0 + \sum_k u_k(t)\mathcal{H}_k\right]\mathrm{d}t\right)|\psi\rangle + g\left[u_k(t)\right] \tag{1.85}$$

where g denotes constraints on the admissible controls. The problem can be simplified if the controls are assumed to be discontinuous. In practice, this is often a very suitable assumption since hardware devices like NMR waveform generators can generate piecewise-constant output. Similar to equation 1.60, the unitary propagator in equation 1.85 for a time point t_j simplifies to

$$U_j = \exp\left(-i\left[\mathcal{H}_0 + \sum_k u_k(t_j)\mathcal{H}_k\right]\Delta t\right) \tag{1.86}$$

where Δt is an equal spacing on the time grid. The cost functional is now dependent on an effective propagator formed by a product of discrete propagators

$$\mathcal{J} = \langle\sigma|U_\mathrm{N}\cdots U_j\cdots U_1|\psi\rangle. \tag{1.87}$$

The penalty term has been dropped for simplicity. To approach the target as closely as possible a maximum of $\mathcal{J}$ needs to be found with respect to the controls. The evaluation of control derivatives according to

$$\frac{\partial\mathcal{J}}{\partial u_k(t_j)} = \frac{\partial}{\partial u_k(t_j)}\langle\sigma|U_\mathrm{N}\cdots U_j\cdots U_1|\psi\rangle \tag{1.88}$$

indicates that all terms in the derivative of this product vanish except

$$\frac{\partial \mathcal{J}}{\partial u_k(t_j)} = \left\langle \sigma \left| U_{\mathrm{N}} \cdots U_{j+1} \frac{\partial U_j}{\partial u_k(t_j)} U_{j-1} \cdots U_1 \right| \psi \right\rangle . \tag{1.89}$$

Therefore the main task of optimization schemes is to efficiently obtain propagator derivatives.

1.2.3. Pulse Classes

One assumption in section 1.1.5 to apply the product operator formalism to pulse sequence analysis was that RF pulses needed to be strong so that off-resonance effects could be neglected. In practice, they can not be neglected since RF energy dissipation has to be limited in order to prevent damage to the sample and the instruments. Therefore, pulses have to have a finite RF amplitude and length. This yields a rectangular amplitude profile which is why these pulses are traditionally called rectangular or simply hard pulses. The limitations of these pulses can easily be recognized from the FT. A rectangular function with finite width in the time domain will yield a *sinc* function with finite width in the frequency domain. In practice, the rotation axis of rectangular pulses is tilted as a function of the resonance offset and the effective rotation frequency is also altered[1]. This leads to decreased transfer efficiencies and is most severe in the case of spin inversion by 180° pulses where the magnetization has to pass through the transverse plane.

The first attempt to have an error-compensated 180° pulse was the $90^\circ_x 180^\circ_y 90^\circ_x$ inversion pulse (x and y denoting the phases of the individual pulses)[8]. This work prompted the term composite pulses since a self-compensated rotation was obtained by combining multiple imperfect rotations. Numerous composite pulses were developed in the following either by rational design or numerical optimization procedures[9, 10] (The significance and manifold of composite pulses is further elaborated on in chapter 2). Hence, some composite rotations are susceptible to geometric intuition whereas the mechanism of others is more intricate. Further, since different pulses may be obtained via different methods, pulses with different properties are the result. This led to a classification of the rotations which the corresponding pulses are able to generate[9] and which can also be extended to the formulation of optimal control problems.

- A: Type A composite pulses produce fully compensated rotations over a range of imperfections. Any given state of a spin system would undergo a rotation according to the desired ideal propagator. Such pulses will be referred to as universal rotation (UR) pulses in the following.

- B1: Type B1 composite pulses produce a partially compensated rotation and approach the ideal propagator up to a given phase factor

- B2: Type B2 composite pulses yield a fully compensated rotation for a single defined initial spin state and leaves the final states of other magnetization components undefined. Such pulses will be referred to as point-to-point (PP) pulses in the following.

- B3: Type B3 composite pulses act like B2 pulses but can not facilitate a uniform phase of the final state.

The design of all these types can be subject to an optimization by OCT methods if the cost functionals are defined accordingly. Type A/UR pulses aim to create an effective propagator

$$U_{\text{eff}} = \prod_{j=1}^{N} U_j = U_{\text{N}} \cdots U_j \cdots U_1 \tag{1.90}$$

that approaches a desired target propagator U_{F} as closely as possible. Any pulse which would minimize an error functional given by

$$||U_{\text{F}} - U_{\text{eff}}||^2 = ||U_{\text{F}}||^2 - 2\Re\langle U_{\text{F}}|U_{\text{eff}}\rangle + ||U_{\text{eff}}||^2 \tag{1.91}$$

can be called a UR pulse. Since the first and last term of equation 1.91 are constant, a minimum is found when the fidelity measure

$$\Phi_{\text{UR}} = \Re\langle U_{\text{F}}|U_{\text{eff}}\rangle = \Re \ \text{Tr}\left(U_{\text{F}}^{\dagger} U_{\text{eff}}\right) \tag{1.92}$$

is maximized. In fact, an arbitrary phase factor $\exp(i\phi)$ is occasionally affordable in practical NMR applications and a cost functional taking this into account can be formulated as

$$\Phi_{\text{UR}}^2 = |\langle U_{\text{F}}|U_{\text{eff}}\rangle|^2. \tag{1.93}$$

Meanwhile it is recognized that the use of Φ_{UR}^2 may seem more flexible than Φ_{UR} but it suffers hindered convergence[11, 12]. Pulses obtained by an optimization using a high Φ_{UR} as their target produce the so-called Broadband Universal Rotation By Optimized Pulses (BURBOP) family[11–18]. They have been used in a variety of NMR experiments where they are mostly applied to refocus transverse magnetization in a very robust manner to form spin echoes[19].

In analogy to B2 pulses, if a pulse is only required to transform a given initial magnetization denoted by ρ_0 into a defined target state ρ_{F} the fidelity of a PP transformation is given by

$$\Phi_{\text{PP}} = \langle \rho_{\text{F}}|\rho_{\text{N}}\rangle = \text{Tr}\left(\rho_{\text{F}}^{\dagger}\rho_{\text{N}}\right) \tag{1.94}$$

with ρ_{N} being the initial density operator after a set of N unitary transformations according to

$$\rho_{\text{N}} = U_{\text{N}} \cdots U_j \cdots U_1 \rho_0 U_1^{\dagger} \cdots U_j^{\dagger} \cdots U_{\text{N}}^{\dagger}. \tag{1.95}$$

ρ_0 and ρ_{F} are assumed to be Hermitian operators. Optimizations with Φ_{PP} as their target yield for example the Broadband Excitation By Optimized Pulses (BEBOP) and Broadband Inversion By Optimized Pulses (BIBOP) families[13, 15–18, 20–28]. They can be used to reliably excite transverse magnetization or invert the sign of longitudinal magnetization. By exploiting symmetry principles it is possible to create UR from PP pulses[29] and further relations between the pulse families are outlined in [12]. The differences between UR and PP pulses are illustrated and summarized in figure 1.1.

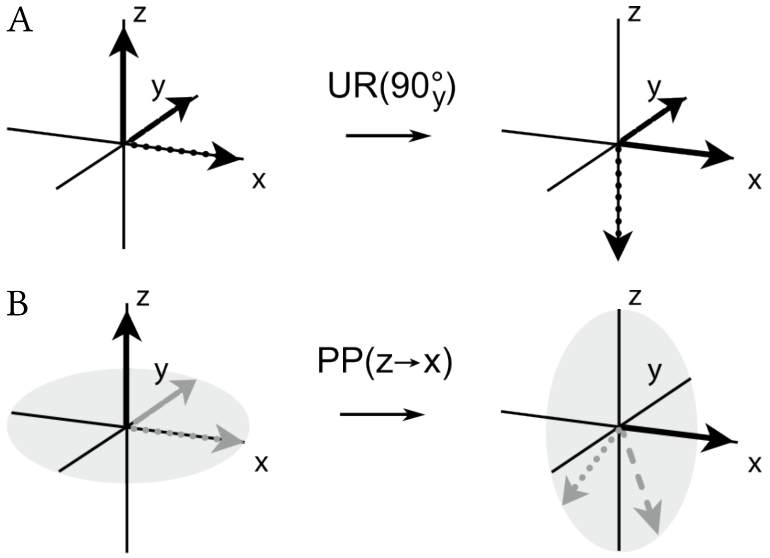

Figure 1.1.: Illustration of the difference between UR and PP pulses. A UR pulse is defined by a rotation axis and angle (here 90° around the y-axis) and will therefore transform any given magnetization components accordingly (A). A PP transformation is defined by a specific initial and final state (here the orientation of the magnetization is turned from z to x) and leaves magnetization components orthogonal to the initial state at an undefined place on the plane orthogonal to the target state. This is depicted by the gray disc (B). (Graphic taken and modified from [12])

1.2.4. The GRAPE algorithm

Gradient ascent algorithms based on principles of OCT were already proposed in the 1980s to target the problem of band-selective pulses[30–32]. These studies have been limited to the steering of the dynamics of uncoupled spin systems governed by the Bloch equations and approaches applicable to very general spin systems have been sparse for a long a time. With one exception[33], gradient-based optimizations relied largely on difference methods where control derivatives are approximated by finite differences

$$\frac{\partial \Phi}{\partial u} \approx \frac{\Phi(u + \Delta u) - \Phi(u)}{\Delta u}. \tag{1.96}$$

Here, in order to obtain gradients for N independent parameters, $2N$ evaluations of the performance index Φ are necessary. First, it has to be evaluated with the current controls, and secondly with controls modified by a slight excursion Δu.

However, the definition of quality factors in section 1.2.3 allows for a more elegant way to obtain gradients. According to the definition of inner products (compare equation 1.51) and the fact that a trace of a product does not change upon cyclic permutation of its factors, equation 1.92 can be rewritten as

$$\Phi_{\mathrm{UR}} = \mathfrak{R} \left\langle \underbrace{U_{j+1}^{\dagger} \cdots U_{\mathrm{N}}^{\dagger} U_{\mathrm{F}}}_{P_j} \middle| \underbrace{U_j \cdots U_1}_{X_j} \right\rangle . \tag{1.97}$$

X_j corresponds to the effective propagator at time t_j and P_j can be understood as an effective propagator corresponding to a rotation backwards in time starting from U_F. If the pulse was optimal, X_j and P_j would be identical at each point in time. Gradients that improve Φ_UR are therefore proportional to the overlap of these propagators and are given by

$$\begin{aligned}\frac{\partial \Phi_\mathrm{UR}}{\partial u_k(t_j)} &= \frac{\partial}{\partial u_k(t_j)} \Re\langle P_j | X_j\rangle \\ &= \Re\left\langle P_j \middle| \frac{\partial U_j}{\partial u_k(t_j)} X_{j-1}\right\rangle .\end{aligned} \tag{1.98}$$

Just as in equation 1.89, all terms except a single product vanish and the remaining task is to find the propagator derivative. These considerations can be transferred to Φ_PP. Equation 1.94 can be rewritten as

$$\Phi_\mathrm{PP} = \underbrace{\Big\langle U_{j+1}^\dagger \cdots U_\mathrm{N}^\dagger \rho_\mathrm{F} U_\mathrm{N} \cdots U_{j+1}}_{\lambda_j}\Big| \underbrace{U_j \cdots U_1 \rho_0 U_1^\dagger \cdots U_j^\dagger \Big\rangle}_{\rho_j} \tag{1.99}$$

where ρ_j is the density operator propagated forward from ρ_0 and λ_j can be imagined as the target operator ρ_F propagated backwards in time. Again, the pulse would be optimal, if ρ_j and λ_j were identical at each point in time. Hence, gradients that improve Φ_PP are proportional to the overlap of these density operators and are given by

$$\begin{aligned}\frac{\partial \Phi_\mathrm{PP}}{\partial u_k(t_j)} &= \frac{\partial}{\partial u_k(t_j)} \langle \lambda_j | \rho_j\rangle \\ &= \left\langle \lambda_j \middle| \frac{\partial}{\partial u_k(t_j)} U_j \rho_{j-1} U_j^\dagger \right\rangle .\end{aligned} \tag{1.100}$$

Evaluating the derivative of the product in equation 1.100 indicates that only propagator derivatives are non-zero:

$$\frac{\partial}{\partial u_k(t_j)} U_j \rho_{j-1} U_j^\dagger = \frac{\partial U_j}{\partial u_k(t_j)} \rho_{j-1} U_j^\dagger + U_j \rho_{j-1} \frac{\partial U_j^\dagger}{\partial u_k(t_j)} \tag{1.101}$$

The only additional effort compared to Φ_UR derivatives is therefore to find the derivatives of $U_j^\dagger$. These can be obtained by deriving the product

$$\frac{\partial (U_j U_j^\dagger)}{\partial u_k(t_j)} = \frac{\partial \mathbf{1}}{\partial u_k(t_j)} = 0 \tag{1.102}$$

which yields

$$U_j \frac{\partial U_j^\dagger}{\partial u_k(t_j)} = -\frac{\partial U_j}{\partial u_k(t_j)} U_j^\dagger \iff \frac{\partial U_j^\dagger}{\partial u_k(t_j)} = -U_j^\dagger \frac{\partial U_j}{\partial u_k(t_j)} U_j^\dagger . \tag{1.103}$$

It was shown that with the considerations above, an iterative scheme can be formulated that only needs two trajectories of the spin system to obtain gradient information for

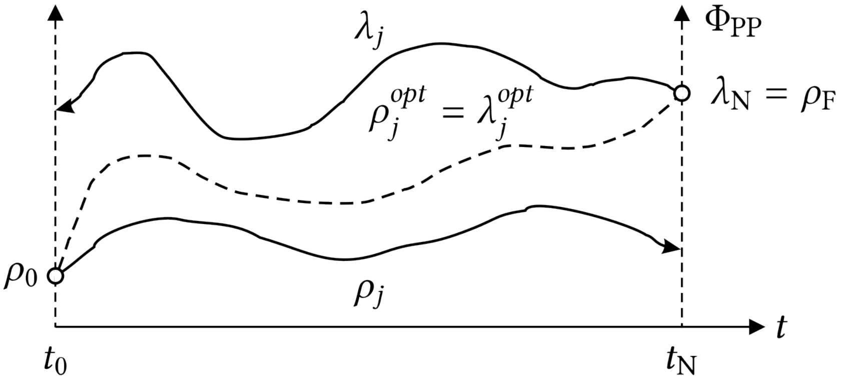

Figure 1.2.: Gradients for all control parameters are obtained by evaluating the overlap of two trajectories at each point in time. In the case of Φ_{PP}, ρ_j is obtained by a forward propagation of the initial state ρ_0. λ_j corresponds to the backward trajectory of the final state ρ_{F} (bold lines). If the pulse sequence facilitates a perfect transfer both trajectories match (dashed line).

all control parameters independent of the total number N. The concept of forward and backward propagation is further illustrated in figure 1.2. In order to achieve robustness towards a range of imperfections, these can be arranged in sets of discrete values. This way, pulses can be made robust towards a range of resonance offsets $\Delta\nu$ by choosing a reasonable number N_ν of values along this range. Deviations from an ideal B_1 field to generate the pulse can be taken into account by choosing a set of $N_{B_{1,\mathrm{rel}}}$ values for the nominal magnitude $B_{1,\mathrm{rel}}$ to scale ω_{RF}. To fit the shape of equation 1.84, equation 1.11 can be rewritten as

$$\mathcal{H}_1(t_j) = 2\pi B_{1,\mathrm{rel}}(u_x(t_j)I_x + u_y(t_j)I_y). \tag{1.104}$$

Parameter ranges can be molded into any type of quality factor by expanding it to the total average over a set of local quality factors:

$$\overline{\Phi(\nu, B_{1,\mathrm{rel}})} = \frac{1}{N_\nu N_{B_{1,\mathrm{rel}}}} \sum_{\nu} \sum_{B_{1,\mathrm{rel}}} \Phi(\nu, B_{1,\mathrm{rel}}) \tag{1.105}$$

Gradients can be generalized the same way according to

$$\overline{\nabla_{u_k(t_j)}\Phi(\nu, B_{1,\mathrm{rel}})} = \frac{1}{N_\nu N_{B_{1,\mathrm{rel}}}} \sum_{\nu} \sum_{B_{1,\mathrm{rel}}} \frac{\partial \Phi(\nu, B_{1,\mathrm{rel}})}{\partial u_k(t_j)}. \tag{1.106}$$

These mean gradients can be used to update the pulse sequence parameters in an iterative manner. The most general update rule for iteration s is given by

$$\boldsymbol{u}^{s+1} = \boldsymbol{u}^{s} + \epsilon \cdot \overline{\nabla_{\boldsymbol{u}}\Phi} \tag{1.107}$$

with ϵ being an arbitrarily chosen or optimized step length. The considerations above form the basis of the GRadient Ascent Pulse Engineering (GRAPE) algorithm[13] which in the simplest guise can be formulated as follows (The recipe is given for Φ_{PP}. For Φ_{UR} see the content in brackets):

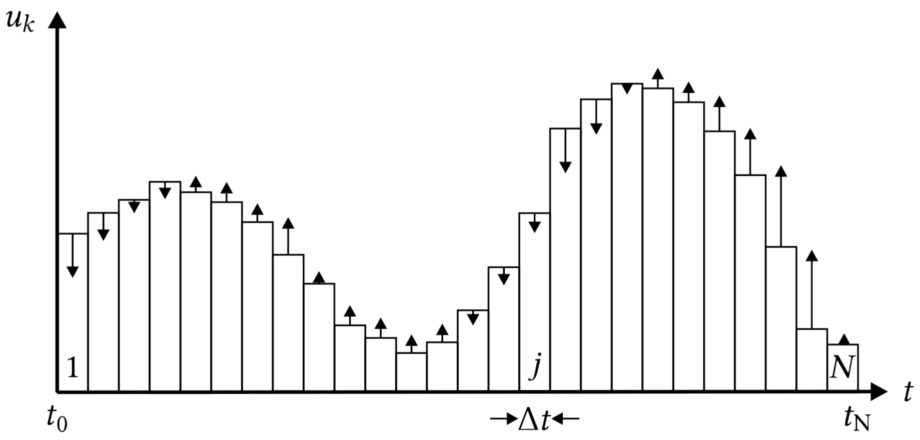

Figure 1.3.: Schematic representation of a control sequence $u_k(t_j)$, consisting of N piecewise constant steps with a duration of Δt. Vertical arrows represent the sign and magnitude of the gradients which indicate in which way individual controls need to change in order to improve the quality factor Φ.

1. Make a guess for initial controls $\boldsymbol{u}$.
2. Starting from ρ_0 (unity), compute the forward trajectory ρ_j (X_j) .
3. Starting from ρ_F (U_F), compute the backward trajectory λ_j (P_j).
4. Evaluate $\nabla_{\boldsymbol{u}}\Phi$ for all possible combinations of parameters and form the mean value.
5. Update the controls according to equation 1.107.
6. Repeat steps 2-5 until convergence.

If ϵ is chosen as one, the algorithm performs the simplest version of steepest descent (or ascent in this case) with guaranteed (but slow) convergence to the closest local optimum. More informed ways to derive a step length are given in section 1.2.8. Figure 1.3 illustrates how the controls are updated using the gradient information.

1.2.5. Optimal tracking

So far, only optimization approaches for pulse sequences were discussed where terms in the cost functional corresponding to the running cost in equation 1.82 have been discarded and only the target fidelity has been evaluated. However, for several applications in NMR, the behavior of spin systems during multi-pulse sequences is of the essence. The historically most relevant theoretical tool to describe such pulse sequences is coherent averaging or Average Hamiltonian Theory (AHT) [34], since the focus is on the effective Hamiltonian during a pulse train. Effective Hamiltonians are also achievable by means of OCT [35], but this approach does not exploit the full flexibility of the algorithms available. The general task of finding controls that facilitate a desired output trajectory can be transferred to spin dynamics, where a pulse sequence is required to steer the evolution of a density operator along a chosen trajectory. In terms of Optimal Control, this is called

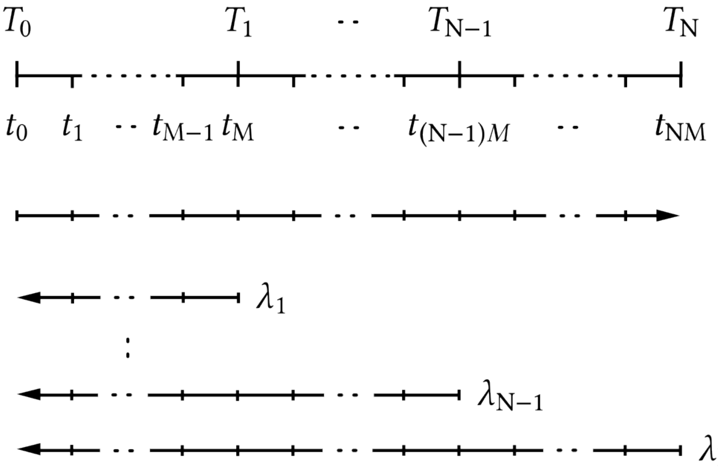

Figure 1.4.: Schematic representation of the trajectories necessary for a GRAPE tracking iteration with respect to the chosen time grid. The trajectory is digitized into N detection points T_n with M time slices of the pulse sequence, digitized into NM steps, between two subsequent detection points. As shown in equation 1.113, N backward trajectories $\lambda_j(n)$ can be combined to a single trajectory Λ_j. (Graphic taken and modified from [36])

a tracking problem[6]. A generalized version of the GRAPE algorithm, called optimal tracking, that has been tailored towards this kind of problems, was introduced in the context of low-power heteronuclear decoupling[36] (which is a main part of this thesis, see chapter 2).

The desired trajectories are no longer defined by a single target state ρ_F but by several target states spread over the time grid of the pulse sequence. In the most simple case N discrete way points would be equally distributed over the sequence with an equal spacing of ΔT. These points could correspond to data acquisition points of NMR spectra which are also recorded with an equal spacing called the dwell time (in the case of linear sampling). Typically, the digitization of a pulse sequence Δt can be chosen smaller than the digitization of the detected signal so that the number $M = \Delta T / \Delta t$ corresponds to the number of pulse sequence increments between detection points. The performance of the sequence is evaluated at each detection point via local quality factors

$$\phi_n = \langle \rho_F(T_n) | \rho(T_n) \rangle. \tag{1.108}$$

If all local quality factors are weighted equally they can be molded into a global quality factor given by

$$\Phi = \frac{1}{N} \sum_{n=1}^{N} \phi_n = \frac{1}{N} \sum_{n=1}^{N} \langle \rho_F(T_n) | \rho(T_n) \rangle. \tag{1.109}$$

In order to obtain gradients that modify the controls with respect to the improvement of each of the N local quality factors, N backward trajectories have to be evaluated alongside one forward trajectory. The propagation scheme and the according time grid is depicted in figure 1.4. The average gradients are therefore given by

$$\frac{\partial \Phi}{\partial u_k(t_j)} = \frac{1}{N}\sum_{n=1}^{N} \frac{\partial \phi_n}{\partial u_k(t_j)} = \frac{1}{N}\sum_{n=1}^{N} \frac{\partial}{\partial u_k(t_j)} \langle \lambda_j(n)|\rho_j\rangle. \tag{1.110}$$

It becomes obvious from figure 1.4 that pulse increments at early time points affect all future detection points but at the same time there is no control that can affect its past. Therefore several contributions to the sum in equation 1.110 can be dropped and a combined backward trajectory may be written as

$$\Lambda_j = \sum_{n>l} \lambda_j(n) \tag{1.111}$$

where l is an integer number given by $\lfloor j/M \rfloor$ ensuring that control derivatives at each increment j only affect detection points in the future. Therefore equation 1.110 simplifies to

$$\frac{\partial \Phi}{\partial u_k(t_j)} = \frac{1}{N}\frac{\partial}{\partial u_k(t_j)} \langle \Lambda_j|\rho_j\rangle. \tag{1.112}$$

Although this is suggested by the equations above and figure 1.4, there is no actual need to compute N backward trajectories consecutively. It is possible to replace a sum of unitary propagations by a single propagation of a sum according to

$$\sum_n U A_n U^\dagger = U\left(\sum_n A_n\right)U^\dagger \tag{1.113}$$

which allows for an extremely efficient calculation of Λ_j and retains the benefit of the GRAPE algorithm that only two full trajectories are necessary to obtain gradients for all controls. The GRAPE-based tracking algorithm for a desired density operator trajectory can be summarized as follows:

1. Make a guess for initial controls $\boldsymbol{u}$.
2. Starting from ρ_0, compute the forward trajectory ρ_j.
3. Starting from $\rho_\mathrm{F}(T_\mathrm{N})$, compute the backward trajectory Λ_j according to

$$\Lambda_{j-1} = \begin{cases} U_j^\dagger \Lambda_j U_j & \text{if } \lfloor j/M \rfloor = \lfloor (j-1)/M \rfloor \\ U_j^\dagger \Lambda_j U_j + \rho_F(T_n) & \text{if } \lfloor j/M \rfloor > \lfloor (j-1)/M \rfloor \end{cases} \tag{1.114}$$

4. Evaluate $\nabla_{\boldsymbol{u}}\Phi$ for all possible combinations of parameters and form the mean value.
5. Update the controls according to equation 1.107.
6. Repeat steps 2-5 until convergence.

1.2.6. Cooperativeness

However compensated a single RF pulse or sequence of pulses may be against experimental imperfections, each transformation will lead to small amounts of unwanted magnetization components that will not follow the desired pathway. This will give rise to spectral artifacts, diminished signal to noise (S/N) ratios and imperfect line shapes. Composite pulses or shaped pulses (SPs) in general can only compensate their own imperfections to a certain extent. Nevertheless, if NMR spectra are accumulated using several scans, unwanted magnetization components can be canceled in the averaged signal by phase cycling procedures[37]. Typically in repeated experiments, identical pulses are used but their phases are systematically altered mostly by multiples of 90°. These restrictions on the phase alteration may be lifted by designing a whole set of pulses which can compensate each others imperfections using Optimal Control methods. A cycle of such pulses can be referred to as cooperatively acting or simply COOP pulses[38]. Cooperativeness can be exploited in multiple[39] and even the same scan[40] with the focus of this thesis being on multi-scan experiments.

For a set of N_{COOP} pulses it is straightforward to define an average density operator according to

$$\overline{\rho}(t_j) = \frac{1}{N_{\mathrm{COOP}}} \sum_{m=1}^{N_{\mathrm{COOP}}} \rho^{(m)}(t_j). \tag{1.115}$$

Extensive care has to be taken on the formulation of quality factors so that cooperativeness can take effect. It has been shown by previous studies using OCT on the subject of broadband excitation with minimal phase error[23] that quality factors with quadratic terms prove advantageous. If magnetization shall be transferred from I_z to I_x, any residual I_y magnetization will be observable as a phase error in the resulting signal. This can be taken into account via

$$\Phi = 1 - (1 - \langle I_x \rangle)^2 - \langle I_y \rangle^2. \tag{1.116}$$

This quality factor will reach the maximum of $\Phi = 1$ when $\langle I_x \rangle = 1$ and $\langle I_y \rangle = 0$. The gradient with respect to the controls enforces this via

$$\nabla_{\boldsymbol{u}} \Phi = 2(1 - \langle I_x \rangle) \cdot \nabla_{\boldsymbol{u}} \langle I_x \rangle - 2 \langle I_y \rangle \cdot \nabla_{\boldsymbol{u}} \langle I_y \rangle. \tag{1.117}$$

In contrast to the simple definition of Φ_{PP}, the expectation values of the operators in question (so basically the fidelity of the transformation itself) is fed back to the gradient and acts as a scaling proportional to the transfer efficiency already reached. This principle can readily be transferred to cooperativeness. Equation 1.116 needs to be modified according to

$$\Phi_{\mathrm{COOP}} = 1 - \left(1 - \overline{\langle I_x \rangle}\right)^2 - \overline{\langle I_y \rangle}^2. \tag{1.118}$$

To adjust the controls of individual pulses $\boldsymbol{u}^{(m)}$ in order to improve Φ_{COOP}, the average density operator needs to be derived with respect to individual controls. The gradients of any Φ_{PP}-type contribution to Φ_{COOP} are given by

$$\nabla_{\boldsymbol{u}^{(m)}} \left\langle \rho_{\mathrm{F}} \middle| \overline{\rho_{\mathrm{N}}} \right\rangle = \frac{1}{N_{\mathrm{COOP}}} \sum_{m=1}^{N_{\mathrm{COOP}}} \nabla_{\boldsymbol{u}^{(m)}} \left\langle \rho_{\mathrm{F}} \middle| \rho_{\mathrm{N}}^{(m)} \right\rangle = \frac{1}{N_{\mathrm{COOP}}} \nabla_{\boldsymbol{u}^{(m)}} \left\langle \rho_{\mathrm{F}} \middle| \rho_{\mathrm{N}}^{(m)} \right\rangle. \tag{1.119}$$

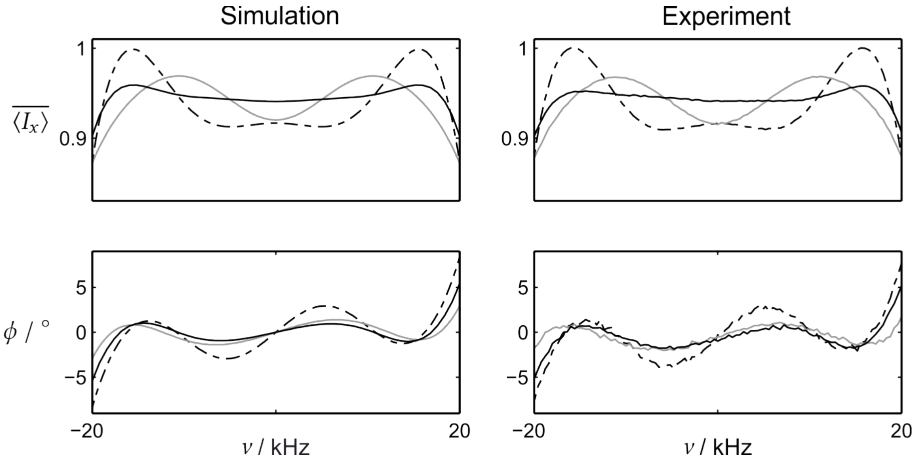

Figure 1.5.: Simulated and experimental offset profiles for the average excited magnetization $\overline{\langle I_x\rangle}$ (upper panels) and the average phase error ϕ (lower panels) for an individual pulse ($N_{\text{COOP}} = 1$, dotted and dashed line) and sets of COOP pulses with $N_{\text{COOP}} = 3$ (bold gray line) and $N_{\text{COOP}} = 6$ (bold black line). With an increasing number of pulses both the excitation and phase error homogeneously improve. Pulses were optimized for $\Delta\nu = 40$ kHz using $\omega_{\text{RF}} = 17.5$ kHz with a duration of 50 μs. (Graphic taken and modified from [39])

If the result of equation 1.119 is plugged into the derivative of equation 1.118 this yields

$$\nabla_{\boldsymbol{u}^{(\mathfrak{m})}}\Phi_{\text{COOP}} = \frac{2}{N_{\text{COOP}}}\left(\left(1-\overline{\langle I_x\rangle}\right)\cdot\nabla_{\boldsymbol{u}^{(\mathfrak{m})}}\langle I_x\rangle^{(\mathfrak{m})} - \overline{\langle I_y\rangle}\cdot\nabla_{\boldsymbol{u}^{(\mathfrak{m})}}\langle I_y\rangle^{(\mathfrak{m})}\right). \tag{1.120}$$

It becomes clear from equation 1.120 that the average fidelity of the whole set of pulses is fed back to the gradients of individual pulses. Only this way cooperativeness can take action. Apart from broadband excitation with minimal phase error, examples for total elimination of magnetization, band-selective excitation, Inherent Coherence Evolution optimized Broadband Excitation Resulting in constant phase Gradients (ICEBERG)-type pulses[26], and water suppression are given in the seminal work [39]. Excitation profiles for the former are depicted in figure 1.5. The profiles show increasing homogeneity of the intensity of the excited magnetization across the given offset range with decreasing phase errors if N_{COOP} is increased.

1.2.7. Control derivatives

It has been shown in section 1.2.4 that obtaining propagator derivatives is the key to the gradients which are the mathematical core of each iteration of the GRAPE algorithm. Derivatives of matrix exponentials with the shape of equation 1.86 are given by

$$\frac{\partial}{\partial x}e^{A+xB}\Big|_{x=0} = e^{A}\int_{0}^{1} e^{A\tau}Be^{-A\tau}\mathrm{d}\tau. \tag{1.121}$$

Applied to the unitary propagator this yields

$$\frac{\partial U_j}{\partial u_k(t_j)} = -iU_j \int_0^{\Delta t} U_j(\tau)\mathcal{H}_k U_j(-\tau)\mathrm{d}\tau. \tag{1.122}$$

If the step size Δt is sufficiently short in comparison to the period of the largest frequency component in the Hamiltonian ($\Delta t \ll \|\mathcal{H}\|^{-1}$ is fulfilled) the integral in equation 1.122 simplifies to $\mathcal{H}_k \Delta t$ and the propagator derivative to first order is given by

$$\frac{\partial U_j}{\partial u_k(t_j)} = -i\Delta t \mathcal{H}_k U_j. \tag{1.123}$$

Plugged into equation 1.98 the control derivative of Φ_{UR} to first order is given by

$$\frac{\partial \Phi_{\mathrm{UR}}}{\partial u_k(t_j)} = -\Re\langle P_j | i\Delta t \mathcal{H}_k X_j\rangle. \tag{1.124}$$

The control derivative of Φ_{PP} can be obtained by applying equation 1.123 to equation 1.101:

$$\frac{\partial \Phi_{\mathrm{PP}}}{\partial u_k(t_j)} = -\left\langle \lambda_j \middle| \, i\Delta t \left[\mathcal{H}_k, \rho_j\right]\right\rangle \tag{1.125}$$

Applying this approximation causes a convergence slowdown close to the optimum since the approximation error starts to dominate the decreasing gradients. However, equation 1.123 can be seen as the first term of the power series definition of the exponential derivative[41]. Since $\mathcal{H}$ and $\mathcal{H}_k$ often not commute the power series can be expressed more conveniently as a commutator series[42] according to

$$\begin{aligned}\frac{\partial U_j}{\partial u_k(t_j)} = U_j \Bigg(&-i\Delta t \mathcal{H}_k + \frac{\Delta t^2}{2}\left[\mathcal{H}, \mathcal{H}_k\right] + \frac{i\Delta t^3}{6}\left[\mathcal{H}, \left[\mathcal{H}, \mathcal{H}_k\right]\right] \\ &- \frac{\Delta t^4}{24}\left[\mathcal{H}, \left[\mathcal{H}, \left[\mathcal{H}, \mathcal{H}_k\right]\right]\right] + \cdots \Bigg).\end{aligned} \tag{1.126}$$

This way propagator derivatives are obtained which approach the accuracy of exact gradients up to machine precision at the computational cost of the matrix exponential. Yet a far more elegant way to obtain the exact solution for the integral in equation 1.121 exists. According to the work of van Loan[43], an augmented matrix can be constructed which yields a variety of integrals involving the matrix exponential upon exponentiation. To obtain propagator derivatives to first order with respect to the controls a triangular matrix has to be evaluated according to the following

$$\exp\begin{pmatrix} A & B \\ 0 & C \end{pmatrix} = \begin{pmatrix} e^{A} & e^{A}\int_0^1 e^{A\tau} B e^{-C\tau}\mathrm{d}\tau \\ 0 & e^{C} \end{pmatrix}. \tag{1.127}$$

Propagators and their derivatives are therefore available if the right Hamiltonians are plugged into the blocks of the augmented matrix[44]. From equation 1.127 follows

$$\exp\begin{pmatrix} -i\mathcal{H}\Delta t & -i\mathcal{H}_k \Delta t \\ 0 & -i\mathcal{H}\Delta t \end{pmatrix} = \begin{pmatrix} U_j & \frac{\partial U_j}{\partial u_k(t_j)} \\ 0 & U_j \end{pmatrix}. \tag{1.128}$$

These derivatives are exact to the same degree as the Padé approximation used to compute the matrix exponential[43]. True analytical derivatives in the context of NMR pulse sequence optimization were only used by Levante et al.[33] who made use of an eigensystem differentiation proposed by Aizu[45]. Given that exact matrix exponentiation is only possible for diagonal matrices, $\mathcal{H}$ has to be transformed to its eigenbasis by a transformation matrix V consisting of the eigenvectors $|\xi_l\rangle$ according to

$$V^{\dagger}\mathcal{H}V = \mathcal{D}. \tag{1.129}$$

The matrix $\mathcal{D}$ now only contains the eigenvalues ξ_l on its diagonal. They can be connected to the eigenvalues of the propagator ζ_l via

$$\zeta_l(j) = \exp(-i\xi_l\Delta t). \tag{1.130}$$

Although the optimization approach of Levante et al. was centered around the eigenvectors of a desired average Hamiltonian[33] it was necessary to obtain propagator eigenvalue derivatives which are related to propagator derivatives via

$$\frac{\partial\zeta_l(j)}{\partial u_k(t_j)} = \left\langle \zeta_l(j) \left| \frac{\partial U_j}{\partial u_k(t_j)} \right| \zeta_l(j) \right\rangle. \tag{1.131}$$

This can be transferred to the propagator derivative in the eigenbasis of the Hamiltonian. The general form of derivatives with the shape of equation 1.86 according to [45] is given in terms of the matrix elements by

$$\left\langle \xi_l \left| \frac{\partial}{\partial x} e^{A+xB} \right| \xi_m \right\rangle = \begin{cases} \langle \xi_l | B | \xi_m \rangle e^{\xi_l} & \text{if } \xi_l = \xi_m \\ \langle \xi_l | B | \xi_m \rangle \frac{e^{\xi_l} - e^{\xi_m}}{\xi_l - \xi_m} & \text{if } \xi_l \neq \xi_m \end{cases} \tag{1.132}$$

if $|\xi_l\rangle$ are eigenvectors and ξ_l are eigenvalues of operator A and therefore obey

$$A|\xi_l\rangle = \xi_l |\xi_l\rangle . \tag{1.133}$$

For all calculations and optimizations presented in this thesis which are performed in Hilbert space, the eigensystem differentiation approach was used.

1.2.8. Update methods

After gradients have been obtained to a desired degree of accuracy, the next crucial step in the basic GRAPE algorithm presented in section 1.2.4 is the update of the control vector according to equation 1.107. For this section, a common literature jargon is adopted that denotes the optimization problems introduced above as minimization. In order to reach a minimum of a given Φ the sign in the update rule needs to be reversed which will give physically meaningful results if all quality factors are translated from fidelities to error functionals $(1 - \Phi)$. Most of the methods discussed here are freely available as minimizers and are incorporated in the renowned spin dynamics simulation library *Spinach*[46].

As already mentioned, basic steepest descent guarantees monotonic convergence but is often slow close to the optimum. The step size ϵ can be modified by line search procedures according to

$$\epsilon_s = \arg\min_{\epsilon} \left(\Phi \left(\boldsymbol{u}^s - \epsilon \nabla_{\boldsymbol{u}} \Phi \left(\boldsymbol{u}^s \right) \right) \right) . \tag{1.134}$$

There are a variety of line search methods available which mostly differ in the way tolerances with respect to the change of Φ are applied during the search for an optimal step size. They shall not be further discussed.

Significant effort has been put in attempts to exploit the predicted quadratic convergence behavior of the Newton-Raphson method[47]. If Φ is assumed to be locally quadratic then the effect of changing controls can be approximated by a second order Taylor expansion according to

$$\Phi(\boldsymbol{u} + \Delta \boldsymbol{u}) \approx \Phi(\boldsymbol{u}) + \nabla_{\boldsymbol{u}} \Phi(\boldsymbol{u})^{\mathrm{T}} \Delta \boldsymbol{u} + \frac{1}{2} \Delta \boldsymbol{u}^{\mathrm{T}} H \Delta \boldsymbol{u} \tag{1.135}$$

with H being the Hessian matrix. The change of controls that will lead to a minimum is found by evaluating

$$\nabla_{\boldsymbol{u}} \Phi(\boldsymbol{u} + \Delta \boldsymbol{u}) \approx \nabla_{\boldsymbol{u}} \Phi(\boldsymbol{u}) + H \Delta \boldsymbol{u} \overset{!}{=} 0 \tag{1.136}$$

and yields the optimal Newton step according to

$$\boldsymbol{u}^{s+1} = \boldsymbol{u}^s - H^{-1} \nabla_{\boldsymbol{u}} \Phi(\boldsymbol{u}^s). \tag{1.137}$$

Hessians may be difficult to handle depending on the size of the control vector but an exceptional benefit of the GRAPE algorithm is that the computational effort to obtain gradients is comparable to the calculation of trajectories. In order to obtain the Hessian of $\mathcal{J}$ according to equation 1.87, $\nabla^2_{\boldsymbol{u}} \mathcal{J}$ needs to be evaluated. The (block-)diagonal elements of the Hessian are available via

$$\frac{\partial^2 \mathcal{J}}{\partial u_k(t_j) \partial u_l(t_j)} = \left\langle \sigma \left| U_{\mathrm{N}} \cdots U_{j+1} \frac{\partial^2 U_j}{\partial u_k(t_j) \partial u_l(t_j)} U_{j-1} \cdots U_1 \right| \psi \right\rangle \tag{1.138}$$

and off-diagonal elements (mixed second derivatives) are given by

$$\frac{\partial^2 \mathcal{J}}{\partial u_k(t_j) \partial u_l(t_m)} = \left\langle \sigma \left| U_{\mathrm{N}} \cdots U_{j+1} \frac{\partial U_j}{\partial u_k(t_j)} U_{j-1} \cdots U_{m+1} \frac{\partial U_m}{\partial u_l(t_m)} U_{m-1} \cdots U_1 \right| \psi \right\rangle . \tag{1.139}$$

The propagator derivatives in equation 1.138 could be obtained in the eigenbasis of U_j or the Hamiltonian[45] but a more elegant way based on auxiliary matrices has been proposed recently[44]. Propagators and derivatives to first and second order with respect to the controls can be obtained via

$$\exp \begin{pmatrix} -i\mathcal{H}\Delta t & -i\mathcal{H}_k \Delta t & 0 \\ 0 & -i\mathcal{H}\Delta t & -i\mathcal{H}_l \Delta t \\ 0 & 0 & -i\mathcal{H}\Delta t \end{pmatrix} = \begin{pmatrix} U_j & \frac{\partial U_j}{\partial u_k(t_j)} & \frac{1}{2} \cdot \frac{\partial^2 U_j}{\partial u_k(t_j) \partial u_l(t_j)} \\ 0 & U_j & \frac{\partial U_j}{\partial u_l(t_j)} \\ 0 & 0 & U_j \end{pmatrix} . \tag{1.140}$$

In the context of other non-linear optimization theories, Hessians are often too expensive to be calculated explicitly and second order derivatives are approximated from the gradient history by so-called quasi-Newton methods. A popular approach is the Broyden-Fletcher-Goldfarb-Shanno (BFGS) update[47] which has been successfully applied to the GRAPE algorithm[42]. Starting from a unity matrix, the Hessian is build up according to

$$H_{s+1}^{\mathrm{BFGS}} = H_s + \frac{\boldsymbol{g}_s \boldsymbol{g}_s^{\mathrm{T}}}{\boldsymbol{g}_s^{\mathrm{T}} \Delta \boldsymbol{u}_s} - \frac{(H_s \Delta \boldsymbol{u}_s)\,(H_s \Delta \boldsymbol{u}_s)^{\mathrm{T}}}{\Delta \boldsymbol{u}_s{}^{\mathrm{T}} H_s \Delta \boldsymbol{u}_s} \tag{1.141}$$

using the gradient history $\boldsymbol{g}_s$ given by

$$\boldsymbol{g}_s = \nabla_{\boldsymbol{u}} \Phi(\boldsymbol{u}^{s+1}) - \nabla_{\boldsymbol{u}} \Phi(\boldsymbol{u}^{s}) \tag{1.142}$$

and the history of the controls $\Delta \boldsymbol{u}_s$ given by

$$\Delta \boldsymbol{u}_s = \boldsymbol{u}^{s+1} - \boldsymbol{u}^{s}. \tag{1.143}$$

To avoid inversion, the Hessian can also be updated via its initial inverse[42]. In cases where Hessian and gradient storage are not feasible for the entire optimization (or the landscape of Φ has noisy regions) the limited-memory BFGS (L-BFGS) method can be applied where the history is erased after a given number of iterations[48]. Equation 1.135 implies that since a minimum is sought after which leaves a zero gradient, the Hessian in equation 1.137 has to be positive definite. Otherwise negative Hessian eigenvalues would invert the search direction. Modifying the Hessian in a way that the spectral decomposition is maintained but negative or small eigenvalues are avoided is the subject of so-called regularization methods, studied recently with regard to the GRAPE algorithm[49].

A good compromise between the speed of first-order and the convergence properties of second-order updates is reached by the use of conjugate gradients (CGs) [50]. It makes use of the gradient information from the past iteration to find an optimal step along a direction amongst a set of search directions which are orthogonal or conjugate to each other:

$$\boldsymbol{u}^{s+1} = \boldsymbol{u}^{s} - \epsilon_s \boldsymbol{d}_s \tag{1.144}$$

The step size ϵ_s is found by line search according to

$$\epsilon_s = \arg\min_{\epsilon} \left(\Phi\left(\boldsymbol{u}^{s} - \epsilon \boldsymbol{d}_s\right)\right) \tag{1.145}$$

and the search direction is given by

$$\boldsymbol{d}_s = \nabla_{\boldsymbol{u}} \Phi(\boldsymbol{u}^{s}) + \beta_s \boldsymbol{d}_{s-1}. \tag{1.146}$$

The initial search direction $\boldsymbol{d}_0$ is given by the gradient with respect to the initial controls and is corrected by a factor β_s which is dependent on the implementation of the CG method. Two important versions are the Fletcher-Reeves method

$$\beta_s = \frac{|\nabla_{\boldsymbol{u}} \Phi(\boldsymbol{u}^{s})|^2}{|\nabla_{\boldsymbol{u}} \Phi(\boldsymbol{u}^{s-1})|^2} \tag{1.147}$$

and the Polak-Ribière method

$$\beta_s = \frac{\left(\nabla_{\boldsymbol{u}} \Phi(\boldsymbol{u}^{s}) - \nabla_{\boldsymbol{u}} \Phi(\boldsymbol{u}^{s-1})\right)^{\mathrm{T}} \nabla_{\boldsymbol{u}} \Phi(\boldsymbol{u}^{s})}{|\nabla_{\boldsymbol{u}} \Phi(\boldsymbol{u}^{s-1})|^2} \tag{1.148}$$

which become identical if the landscape of Φ is quadratic. The convergence behavior of CGs can be compared to steepest descent far away from the optimum and a second-order method once the optimum is approached without as much slowdown as pure first-order methods and without the need to compute Hessian information. It should be noted that all second order or hybrid update methods rely on exact first-order gradients.

All optimizations described in the following chapters of this thesis are carried out using the Fortran-based *OCTOPUSSI* software package developed by Sebastian Ehni[51]. It relies on memory preallocation according to the CPU cache size for maximum speed of floating number operations. Although it is equipped with an L-BFGS module, the large number of variables necessary for the pulse sequences in chapter 2 render the handling of the according Hessians unfeasible. Hence, CGs offered the apparently best available alternative. *OCTOPUSSI* makes use of the Fletcher-Reeves-Polak-Ribière-minimization (FRPRMN) routine available for Fortran. For exhaustive details on the organization and features of *OCTOPUSSI*, the reader is referred to [51]. All modifications to the existing software that go beyond merely adding new definitions of quality factors and gradient functions (see appendix A.3) are mentioned throughout this work.

1.2.9. RF constraints

Looking at the way different flavors of the GRAPE algorithm are formulated in sections 1.2.4 and 1.2.5, one could assume that the controls may be updated to whatever extent to reach convergence. Depending on the problem at hand, this could lead to an infinite amount of RF energy being dissipated into the system. But the reality of running NMR experiments is far from it. The peak RF loading and the ratio of irradiation time and periods without irradiation (duty-cycle) is regulated to prevent damage from the coils in the probe and undue heating of the sample. Most importantly, if measurements are performed on living tissue such as humans in an Magnetic Resonance Imaging (MRI) scanner, limits of RF exposure are given by law.

Constraints on the amount of RF dissipation can be applied in different ways. They may act as penalties on the quality factor[13, 46] (see equation 1.85) or may be applied as bounds at each iteration of the algorithm after the control update. The latter is straightforward to implement and does not hinder convergence in most cases. The most immediate restriction corresponds to a local amplitude limit which applies to each increment of the pulse sequence. ω_{RF} according to equation 1.11 is connected to the Cartesian components (real and imaginary parts, see equation 1.104) of the pulse shape via

$$\omega_{\mathrm{RF}}(t_j)/2\pi = u_{\mathrm{RF}}(t_j) = \sqrt{u_x^2(t_j) + u_y^2(t_j)}. \tag{1.149}$$

A maximum amplitude $u_{\mathrm{RF}}^{\max}$ can be enforced as a bound[21, 22] via

$$u_k(t_j) \rightarrow u_k(t_j) \cdot \frac{u_{\mathrm{RF}}^{\max}}{u_{\mathrm{RF}}(t_j)} \qquad \text{if } u_{\mathrm{RF}}(t_j) > u_{\mathrm{RF}}^{\max} \tag{1.150}$$

which will leave the phase of the increment unaltered. Equation 1.150 can also be used to explicitly demand that $u_{\mathrm{RF}}^{\max}$ is used at each increment in order to obtain constant amplitude phase-modulated pulses[24]. A more flexible approach is to limit the overall power envelope given by

$$P = \frac{1}{t_\mathrm{N}} \int_{t_0}^{t_\mathrm{N}} u_\mathrm{RF}^2(t)\mathrm{d}t \tag{1.151}$$

which simplifies to a sum for piece-wise constant output according to

$$P = \frac{1}{N} \sum_{j}^{N} u_\mathrm{RF}^2(t_j). \tag{1.152}$$

Pulses with limited RF power can be compared to constant amplitude pulses using $\sqrt{P}$ as a measure which corresponds to the often used $B_{1,\mathrm{RMS}}$. Power limits P_max can be enforced as a bound via

$$u_k(t_j) \rightarrow u_k(t_j) \cdot \sqrt{\frac{P_\mathrm{max}}{P}} \qquad \text{if } P > P_\mathrm{max}. \tag{1.153}$$

Using limited RF power over limited RF amplitude can lead to increased fidelity using the same pulse length, since amplitude modulation introduces further degrees of freedom[27]. Power limits were added as a feature to *OCTOPUSSI* during the course of this thesis. To have a measure of RF exposure which is independent of time, local and overall amplitudes, the total energy of pulses can be compared. Devoid all natural constants, the energy transferred from the probe coil to the sample is given by

$$E_\mathrm{RF} \sim P \cdot t_\mathrm{N}. \tag{1.154}$$

It can be used as a bound[52] in the same way as power and amplitude according to

$$u_k(t_j) \rightarrow u_k(t_j) \cdot \frac{E_\mathrm{RF}^\mathrm{max}}{E_\mathrm{RF}} \qquad \text{if } E_\mathrm{RF} > E_\mathrm{RF}^\mathrm{max}. \tag{1.155}$$

Both power and energy limits leave the phase of the increment unaltered. Energy limits were not used in this thesis, but equation 1.154 was employed as a measure to see which combinations of $B_{1,\mathrm{RMS}}$ and AQs are feasible for experiments described in chapter 2.

1.2.10. Pulse shape analysis

The pulse shapes obtained by means of OCT can be regarded as extremely complex composite pulses. However, the trajectories describing 2^n-dimensional spin dynamics are often complicated and optimal pulses contain a seemingly arbitrary succession of flip angles due to the intricate phase and amplitude modulations which leave the user to interpret an almost noise-like pulse shape. Distinguished authors have drawn comparisons to sheep herding. Trying to understand the mode of action of optimal control pulses corresponded to watching a dog running around randomly barking and biting at the sheep whereas the sheep are steered along a trajectory rather orderly. In terms of spin dynamics the sheep may be analyzed by using projection superoperators $\hat{P}_{\mathfrak{L}_k}$ to deconstruct the state space $\mathfrak{L}$ of a given density operator according to a desired criterion[53] according to

$$p_k = \left\| \hat{P}_{\mathfrak{L}_k} \left|\rho\right\rangle \right\|. \tag{1.156}$$

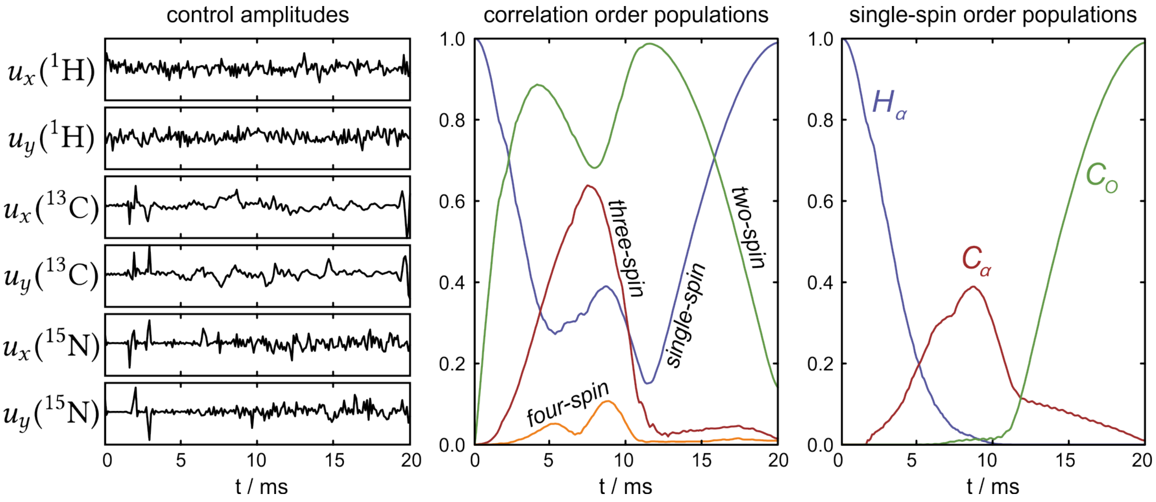

Figure 1.6.: The seemingly noise waveforms applied to ^{1}H, ^{13}C and ^{15}N (left panel, control amplitudes given as fractions of a nominal power level) steer magnetization from the H_α proton to the carbonyl carbon $\mathrm{C_O}$ of the same residue in a protein backbone. Analyzing the trajectories using the methods described in [53] with respect to correlation orders reveals that single-spin order is first depleted and via largely two-spin order and for a short period also three-spin order is regenerated at last (middle panel). Correlation orders higher than three are hardly populated. Focusing on single-spin orders (right panel) reveals a smooth transition from H_α to $\mathrm{C_O}$ via C_α. (Graphic taken and modified from [53])

The portion p_k is the part of the spin system that belongs to the subspace selected by the projection operation. Several modes of projection are proposed in [53], such as coherence order (see sections 1.1.4 and 1.1.5) or correlation order. Correlation orders can be obtained evaluating the number of non-unit spin operators contributing to a given state. Further, the single-spin correlation and coherence order is of particular interest since it can be further deconstructed to identify contributions of individual spins. An illustrative example for a noisy pulse shape creating smooth dynamics is given in figure 1.6 where magnetization is moved along a protein backbone. Note that correlation orders above three are avoided almost throughout the trajectory.

However, even pulses acting on an isolated single-spin system where trajectories can be followed on a Bloch sphere may be difficult to interpret. To solve this problem, the perspective of the dog has to be assumed. An NMR pulse shape s in the time domain is usually represented in terms of its real and imaginary parts (Cartesian components) according to

$$s(t) = u_x(t) + iu_y(t) \tag{1.157}$$

or by the temporal amplitude and phase:

$$s(t) = u_{\mathrm{RF}}(t)e^{i\phi(t)} \tag{1.158}$$

It can readily be converted to the frequency domain via the FT where the shape $S(\nu)$ is given by spectral amplitude and phase

$$S(\nu) = u_{\mathrm{RF}}(\nu)e^{i\phi(\nu)}. \tag{1.159}$$

In many cases the means of representation given above are not particularly informative given that they do not correlate irradiation time and frequency. One approach would be to evaluate the temporal frequency given by

$$\nu(t) = \frac{\partial \phi(t)}{\partial t} \tag{1.160}$$

but here the information about the intensity is lost. To accommodate these shortcomings, the short-time Fourier transform (STFT) or spectrogram representation has been applied to the analysis of optimal control pulses recently[54]. The spectrogram provides a joint time-frequency representation and is given by

$$S(t,\nu) = \int\limits_{-\infty}^{\infty} s(\tau) g(t-\tau) e^{-i2\pi\nu\tau} \mathrm{d}\tau \tag{1.161}$$

with $g(t)$ being a gate function to define the section of the pulse shape under analysis at a given time. To suppress the pulse outside the window $[t-\Delta t, t+\Delta t]$, a normalized Gaussian window function can be used according to

$$g(\tau) = \begin{cases} \frac{1}{N} e^{-\frac{\tau^2}{2\sigma^2}} & \text{for } \tau \in [-\Delta t, \Delta t] \\ 0 & \text{else} \end{cases} \tag{1.162}$$

where the variance σ is proportional to the full width at half maximum (FWHM) of the Gaussian. In order to analyze at which time the pulse deposits energy at a given frequency, the spectrogram amplitude

$$u_{\mathrm{RF}}(t,\nu) = \sqrt{\Re^2\left[S(t,\nu)\right] + \Im^2\left[S(t,\nu)\right]} \tag{1.163}$$

needs to be evaluated. Information about the time and frequency-dependent phases may also be extracted but is of minor interest for this thesis. The insights and drawbacks of different pulse sequence representations is illustrated in figure 1.7 choosing a BIBOP shape as an example which was developed as part of a bigger study[22]. Whereas the control amplitudes are not informative, the phase and amplitude representation reveal a constant amplitude shape with a smoothly swept phase. The irradiation frequency is also swept with two large swings at the beginning and end. Looking at the spectrogram however, it can be recognized that the majority of u_{RF} is deposited in the optimized region and the swings correspond to a small leakage into large frequencies due to the pulses' rectangular amplitude profile.

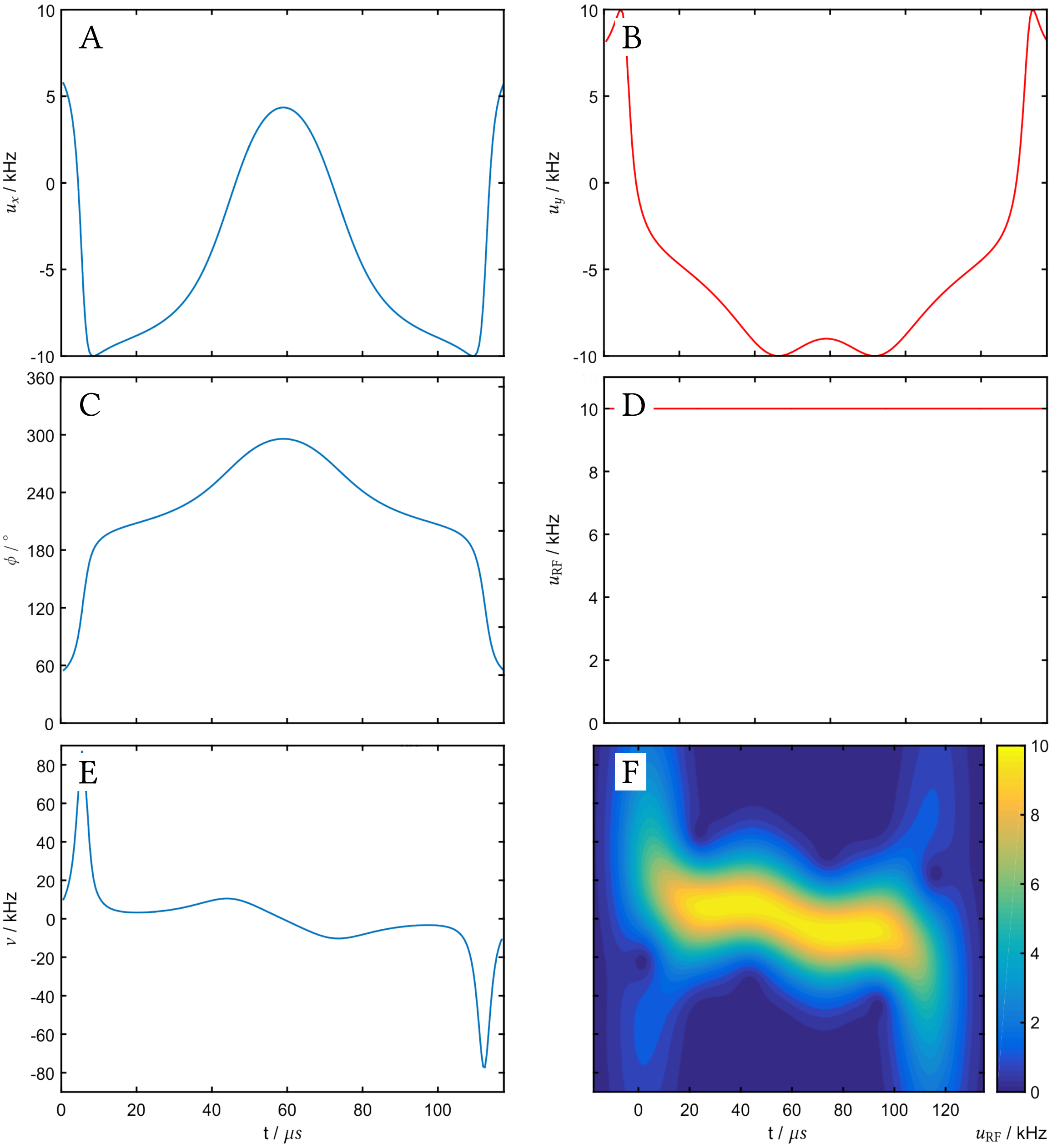

Figure 1.7.: Comparison of temporal and joint time-frequency representations of an example BIBOP shape[22]: The Cartesian control amplitudes (A and B) do not reveal the pulse's mode of action. Converting the controls to phase (C) and amplitude (D) leads to the recognition of a smooth phase modulation with constant u_{RF}. The phase derivative with respect to time (E) hints at a smooth frequency sweep with sharp swings towards high frequencies at the extremities of the shape. However, the spectrogram (F) unmasks this observation as artifacts of the rectangular amplitude profile. Parameters of the spectrogram were chosen according to the BIBOP example given in [54].

2. Heteronuclear Decoupling: The BROCODE

> Certainty of death. Small chance of success. What are we waiting for?
>
> Gimli - The Lord of the Rings: The Return of the King (Movie)

2.1. Introduction

2.1.1. Historical concepts

In a heteronuclear spin system where resonance frequencies are well-separated, the evolution of the density operator under the effect of J-coupling is governed by the Hamiltonian according to equation 1.25. If spin I is probed in an NMR experiment and is connected to spin S via a chemical bond, the Hamiltonian for spin I is given by

$$\mathcal{H}_{\mathrm{I}} = 2\pi\nu_{\mathrm{I}}I_z + \pi{}^1J_{\mathrm{IS}}2I_zS_z \tag{2.1}$$

with ν_{I} being the resonance offset of I and ${}^1J_{\mathrm{IS}}$ corresponding to the one-bond coupling constant between I and S, which is simply called J in the following. With equation 1.72 in mind, the real expectation value of the detectable I^- coherence is given by

$$\begin{aligned} \Re\left\langle I^-\right\rangle(t) &= \cos\left(2\pi\nu_{\mathrm{I}}t\right)\cos\left(\pi Jt\right) \\ &= \cos\left(2\pi\left[\nu_{\mathrm{I}} \pm \frac{J}{2}\right]t\right) \end{aligned} \tag{2.2}$$

so that the resonance line at ν_{I} will be split by the J-coupling. The wealth of information contained in these splittings will be elaborated on in chapter 3. Already in the early days of NMR spectroscopy it was recognized that these splittings may prove to be a disadvantage in terms of sensitivity and interpretability of spectra. This becomes evident for more dilute nuclei like ^{13}C with its usually large number of couplings to the abundant ^{1}H nuclei. The removal of these couplings by a second RF field (decoupling) was proposed by Bloch[55], later proved experimentally[56] and became known as double resonance[57]. If spin I is observed and assumed to be on resonance while spin S is continuously irradiated with a constant amplitude and constant phase RF field, the effective Hamiltonian is given by

$$\mathcal{H}_{\mathrm{J_{eff}}} = \pi J_{\mathrm{eff}}2I_zS_z. \tag{2.3}$$

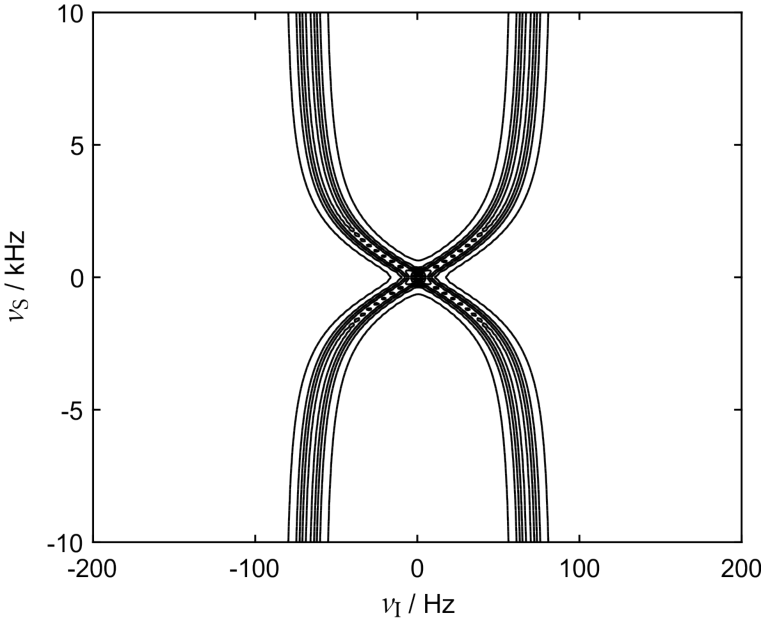

Figure 2.1.: Simulated decoupling profile for a heteronuclear two-spin system under CW irradiation with u_{RF} = 2 kHz. The coupling of J = 140 Hz is reasonably suppressed only close to $\nu_S = 0$ and is otherwise scaled according to equation 2.5. Ten contours equally spaced between 5 and 100% of the maximum achievable intensity were plotted.

The effective J-coupling J_{eff} is given by

$$J_{\text{eff}} = \lambda_{\text{CW}} J \tag{2.4}$$

where the original J-coupling is scaled by a characteristic factor for continuous-wave (CW) irradiation as a function of the spin S resonance offset ν_S and u_{RF}:

$$\lambda_{\text{CW}} = \frac{\nu_S}{\sqrt{\nu_S^2 + u_{RF}^2}} \tag{2.5}$$

Apart from offsets very close to resonance this only corresponds to a scaling since still over 70% of the total coupling are observable for equal values of ν_S and u_{RF}. The characteristic offset pattern of CW decoupling is depicted in figure 2.1. Decoupling is only achieved for S offsets close to resonance.

If not otherwise mentioned the following simulation parameters were used for the generation of the decoupling profiles in the following sections. The coupling constant was set to J = 140 Hz as a typical value for $^1J_{CH}$ in aliphatic CH_n groups of organic molecules. Theoretical spin I spectra were sampled for 128 ms with a real dwell time of 100 μs. The resulting free induction decays (FIDs) were damped according to an assumed transverse relaxation rate corresponding to a line width of 6 Hz and apodized using a cosine-squared window function. Time-domain data was zero-filled to 8192 points prior to FT and spectra were simulated using 101 offsets distributed equally over the given range.

The limited bandwidth of CW decoupling severely hampered ^{13}C NMR spectroscopy and it was realized that the RF field used for decoupling has to be modulated. Several modulation schemes have been suggested, starting with single-freqency modulation[58], pseudorandom phase modulation (noise decoupling)[59], square-wave phase modulation[60] and chirp frequency modulation[61]. However, non of these methods can be considered broadband decoupling by today's standards.

2.1.2. Composite Pulse Decoupling

A major leap towards broadband decoupling was taken by replacing continuous RF irradiation by a repeated set of 180° pulses. Decoupling is achieved when the pulses on S are applied at the midpoints between acquisition points of the I spectrum since it will lead to a refocusing of the coupling evolution:

$$\begin{aligned} I_x \xrightarrow{\pi J 2I_zS_z\tau} & I_x\cos(\pi J\tau) + 2I_yS_z\sin(\pi J\tau) \\ & \xrightarrow{\pi S_x} I_x\cos(\pi J\tau) - 2I_yS_z\sin(\pi J\tau) \xrightarrow{\pi J 2I_zS_z\tau} I_x \end{aligned} \tag{2.6}$$

Scaling can be achieved in a similar manner by a slight temporal displacement of the pulses[62]. The method is mostly limited by the inability to place reasonably short 180° pulses in between acquisition points that correspond to common spectral widths especially for ^{13}C. An inversion profile for an ordinary rectangular 180° pulse is depicted in figure 2.2. It can only provide reasonable inversion efficiency close to resonance and the nominal B_1 value. The $90^\circ_x180^\circ_y90^\circ_x$ composite pulse was already mentioned in section 1.2.3. It is obtained by splitting a conventional 180° pulse in the middle and inserting a correction 180° pulse phase-shifted by 90° [8]. The inversion profile is given in figure 2.3. Close to resonance, it excels at B_1 compensation, but at the nominal value for B_1 the offset profile within figure 2.3 is rather wavy. Given that it gets more homogeneous at higher RF amplitudes, the $90^\circ_x240^\circ_y90^\circ_x$ composite pulse was proposed, where the length of the correction pulse is simply extended[63]. The corresponding inversion profile is shown in figure 2.4. This modified composite pulse offers a more homogeneous inversion profile for the nominal B_1 value without sacrificing too much robustness against B_1 variations.

The use of Composite Pulse Decoupling (CPD) instead of spin flip decoupling using uncompensated pulses indicated that refocusing the coupling evolution at each detection point is not necessary for efficient decoupling as long as the magnetization is manipulated rapidly with respect to the magnitude of the coupling constant. Moreover, supercycles were developed to compensate imperfections of individual inversion elements. They can be obtained by recursive expansion with the MLEV series being the pioneering example[64–66]. Theoretical justification for this approach was delivered retrospectively using both AHT [34] and a more explicit spin rotation operator-based treatment[67, 68]. Practical implementations of MLEV supercycles are given in table 2.1. The effects of more and more compensated cycles is illustrated in figure 2.5 using the $90^\circ_x180^\circ_y90^\circ_x$ composite pulse. Using no or a primitive supercycle leads to a more or less direct translation of the pulses' wavy offset profile into the decoupling profile whereas higher expansions provide a homogeneous and more broadband performance. Although the $90^\circ_x240^\circ_y90^\circ_x$ composite pulse was suggested as an inversion element in the seminal work[64], the effect of its more homogeneous inversion

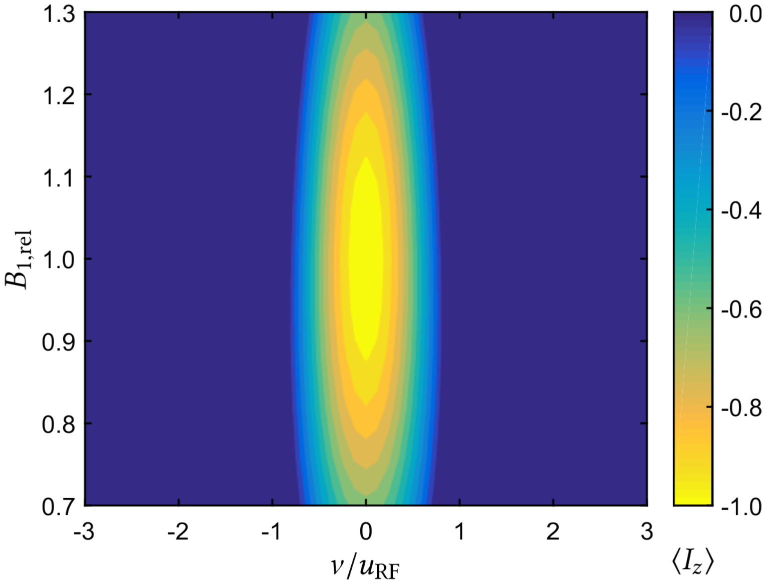

Figure 2.2.: Simulated inversion profile of a rectangular 180° pulse. Only values of $\langle I_z \rangle \leq 0$ are plotted which correspond to flip angles $\geq 90^\circ$. Optimal inversion is only facilitated for the slightest deviations from exact resonance and the nominal B_1.

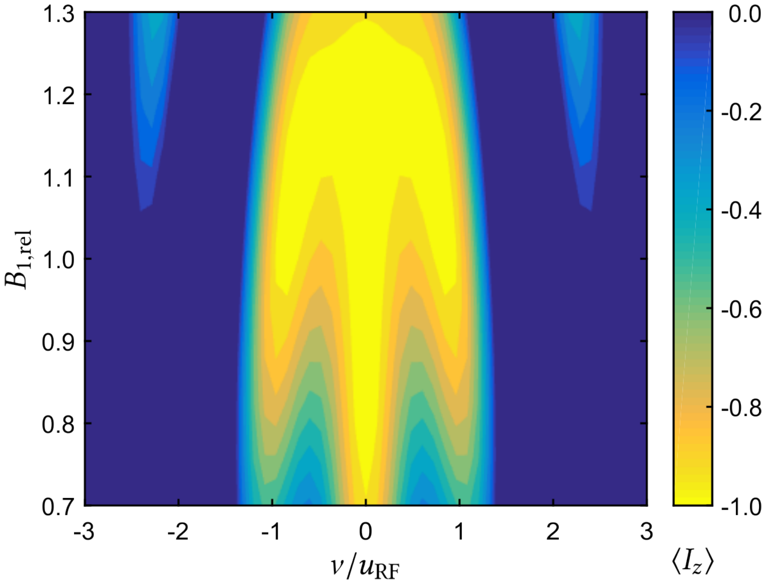

Figure 2.3.: Simulated inversion profile of a $90^\circ_x 180^\circ_y 90^\circ_x$ composite pulse. It allows for large deviations from the nominal B_1 value close to resonance and offers rudimentary compensation against resonance offset.

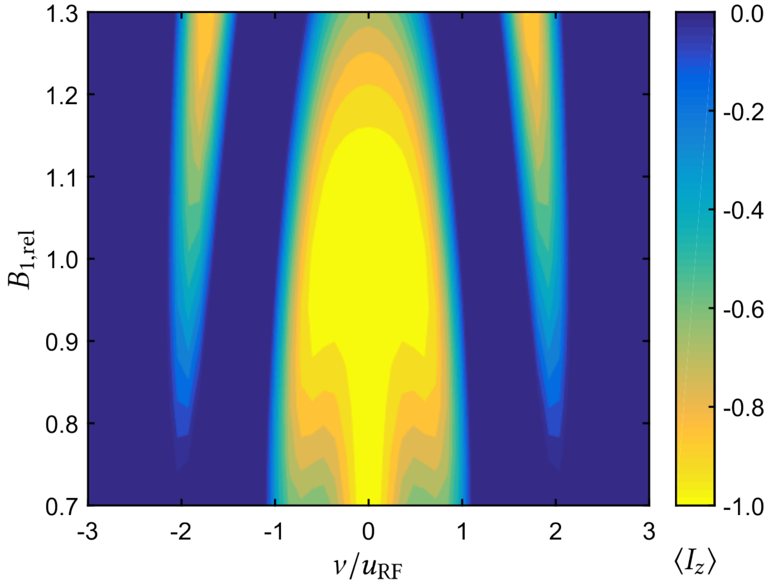

Figure 2.4.: Simulated inversion profile of a $90^\circ_x 240^\circ_y 90^\circ_x$ composite pulse. The offset profile is more homogeneous at the nominal B_1 value and compensation against B_1 inhomogeneities is maintained in particular for lower values.

Supercycle	Pulse sequence
none	R = $90^\circ_x 180^\circ_y 90^\circ_x$ or $90^\circ_x 240^\circ_y 90^\circ_x$
MLEV-4	$RR\overline{RR}$
MLEV-16	$RR\overline{RR}\ \overline{R}RR\overline{R}\ \overline{RR}RR\ R\overline{RR}R$
MLEV-64	$RR\overline{RR}\ \overline{R}RR\overline{R}\ \overline{RR}RR\ R\overline{RR}R$ $RRR\overline{R}\ \overline{RR}RR\ \overline{RRR}R\ RR\overline{RR}$ $\overline{RR}RR\ R\overline{RR}R\ RR\overline{RR}\ \overline{R}RR\overline{R}$ $\overline{RRR}R\ RR\overline{RR}\ RRR\overline{R}\ \overline{RR}RR$

Table 2.1.: Practical implementations of MLEV supercycles for CPD using different composite pulses as inversion element R. Bars indicate phase reversal.

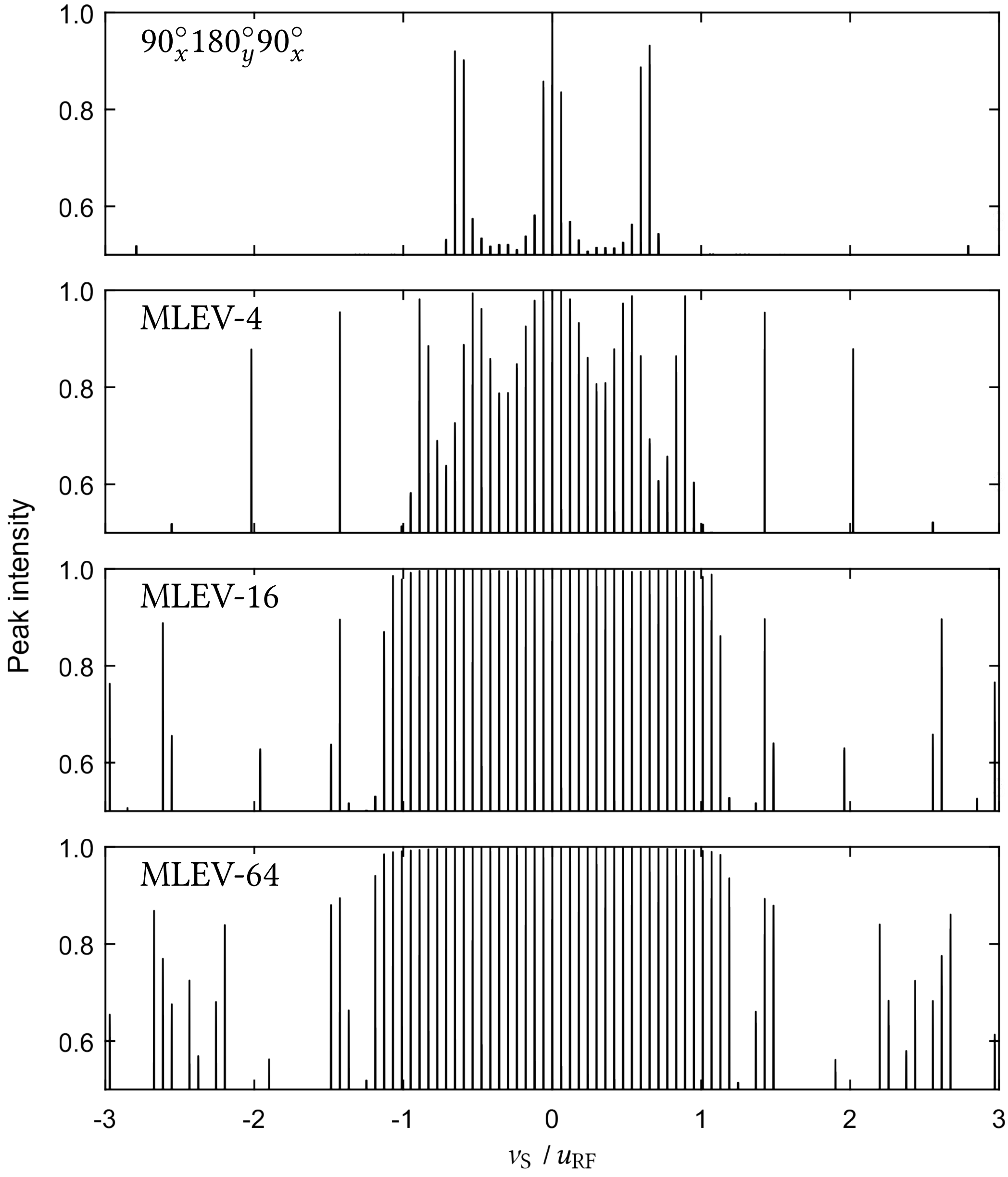

Figure 2.5.: Simulated decoupling profiles for MLEV cycles using the $90^\circ_x 180^\circ_y 90^\circ_x$ composite pulse: Using only the pulse repeatedly or in a simple cycle leads to a wavy decoupling profile comparable to the inversion profile in figure 2.3. When more compensated supercycles with more steps are used, a homogeneous decoupling profile can be obtained. Only peak intensities above 50% are plotted to indicate collapsed doublets.

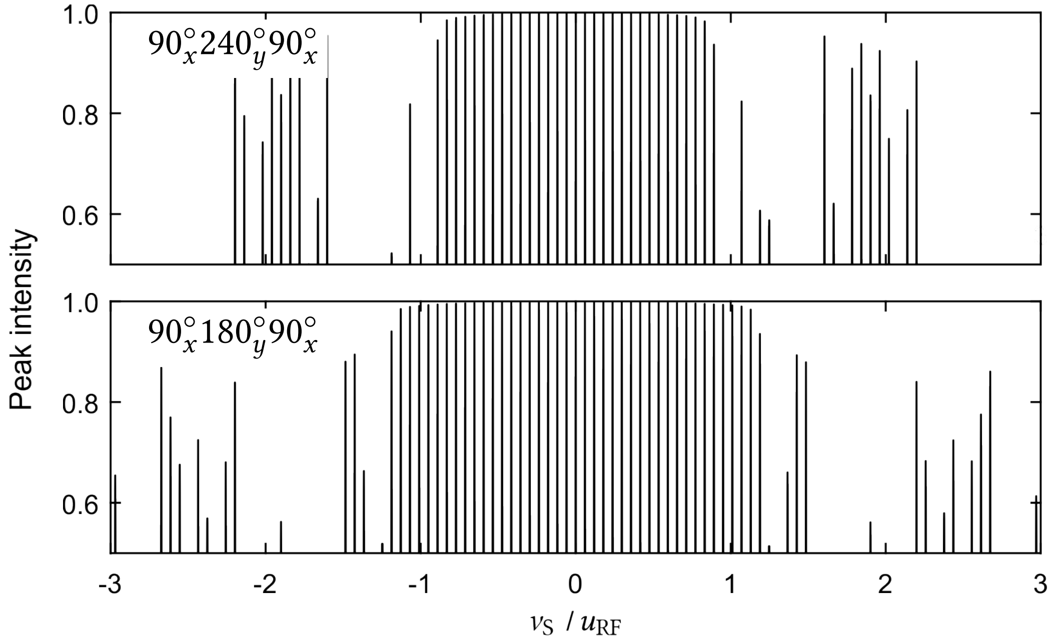

Figure 2.6.: Comparison of simulated MLEV-64 decoupling profiles using the $90^\circ_x240^\circ_y90^\circ_x$ and $90^\circ_x180^\circ_y90^\circ_x$ composite pulses: Since the irregular offset profile of the $90^\circ_x180^\circ_y90^\circ_x$ pulse is overcompensated by the MLEV-64 supercycle, it offers an about 40% broader decoupling range compared to the $90^\circ_x240^\circ_y90^\circ_x$ pulse using the same cycle.

profile (see figure 2.4) compared to the $90^\circ_x180^\circ_y90^\circ_x$ pulse is clearly overcompensated by the error correction capabilities of the supercycle as depicted in figure 2.6.

Another very important composite pulse tailored towards a broad inversion profile is the $90^\circ_x180^\circ_{-x}270^\circ_x$ or simply $1\bar{2}3$ pulse, giving rise to the Wideband, Alternating-phase, Low-power Technique for Zero-residual-splitting (WALTZ) decoupling scheme. The numbers represent the multiples of 90° pulses and the bar denotes a phase reversal[69]. Figure 2.7 shows the inversion profile of the $1\bar{2}3$ pulse, which outperforms its competitors presented so far. Several modifications to expand the WALTZ sequence have been proposed. Beyond phase reversal and recursive expansion, individual 90° pulses can be shifted to compensate net rotation errors of individual MLEV-4 portions of a supercycle[69]. More recently, adding further 90° pulses to induce a corresponding net rotation of 90° after each repetition of the cycle has been proposed along with further expansions[70]. The known cycles are given in table 2.2.

Important improvements could be achieved by pulse sequence design via numerical optimizations with the Globally optimized Alternating-phase Rectangular Pulses (GARP) sequence being the first seminal example[71]. The basic inversion element is given by

$$\begin{aligned} R = {} & 30.5\ \overline{55.2}\ 257.8\ \overline{268.3}\ 69.3\ \overline{62.2}\ 85.0\ \overline{91.8}\ 134.5\ \overline{256.1}\ 66.4\ \overline{45.9}\ 25.5 \\ & \overline{72.7}\ 119.5\ \overline{138.2}\ 258.4\ \overline{64.9}\ 70.9\ \overline{77.2}\ 98.2\ \overline{133.6}\ 255.9\ \overline{65.6}\ 53.4 \end{aligned} \tag{2.7}$$

with all numbers representing flip angles around the x-axis and bars denoting phase reversal. Expanded in a simple MLEV-4 cycle this yields the GARP-1 scheme but most commonly the GARP-4 implementation is used which has a second MLEV-4 expansion.

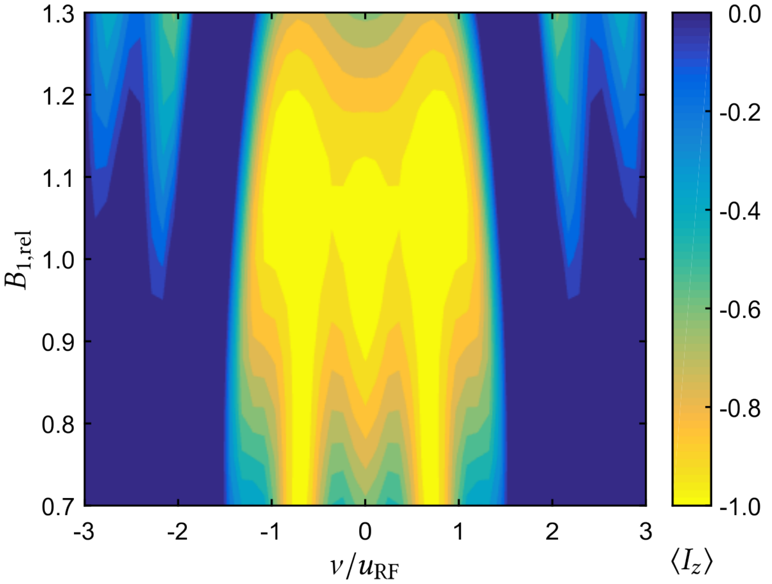

Figure 2.7.: Simulated inversion profile of a $90^\circ_x 180^\circ_{-x} 270^\circ_x$ composite pulse. A better compromise between offset and B_1 compensation is achieved compared to previous composite pulses.

Supercycle	Pulse sequence	Basic element
WALTZ-4	$RR\overline{RR}$	R = $1\overline{2}3$
WALTZ-16	$Q\overline{QQ}Q$	$Q = \overline{3}4\overline{2}3\overline{1}2\overline{4}2\overline{3}$
WALTZ-17	$Q\overline{QQ}Q\ 90^\circ_x$	
WALTZ-64	$QQ\overline{QQ}\ \overline{Q}QQ\overline{Q}\ \overline{QQ}QQ\ Q\overline{QQ}Q$	
WALTZ-65	$QQ\overline{QQ}\ \overline{Q}QQ\overline{Q}\ \overline{QQ}QQ\ Q\overline{QQ}Q\ 90^\circ_x$	

Table 2.2.: Practical implementations of WALTZ supercycles for CPD using different expansions of the $1\overline{2}3$ composite pulse as inversion element. Numbers between one and four represent multiples of 90° pulses and bars indicate phase reversal.

Pulse sequence	Flip angles
DIPSI-1	$365\ \overline{295}\ 65\ \overline{305}\ 350$
DIPSI-2	$320\ \overline{410}\ 290\ \overline{285}\ 30\ \overline{245}\ 375\ \overline{265}\ 370$
DIPSI-3	$\overline{245}\ 395\ \overline{250}\ 275\ \overline{30}\ 230\ \overline{360}\ 245\ \overline{370}$ $340\ \overline{350}\ 260\ \overline{270}\ 30\ \overline{225}\ 365\ \overline{255}\ 395$

Table 2.3.: Different DIPSI pulse sequences for CPD. All numbers represent flip angles around the x-axis and bars denote phase reversal. The pulse sequences are typically expanded in a $R\overline{RR}R$ supercycle.

Further, the Decoupling In the Presence of Scalar Interactions (DIPSI) sequences have been proposed for better quality decoupling in more complex spin system where scalar couplings among protons are involved[72]. The three known sequences are given in table 2.3 but due to their reduced decoupling bandwidth, the DIPSI sequences only gained significance as isotropic mixing sequences for TOtal Correlation SpectroscopY (TOCSY)-related experiments[73]. A bandwidth comparison for the most common implementations of relevant CPD schemes is given in figure 2.8. The reason that for high-resolution NMR of ^{13}C WALTZ is chosen over GARP is the sufficient decoupling bandwidth for ^{1}H on the one hand. On the other hand, extremely low residual splittings are necessary since very small line widths are achievable in ^{13}C NMR, where WALTZ is superior to GARP [71].

Moreover, a central issue are the cycling sidebands. The theoretical treatment of decoupling assumes synchronous sampling of the data points with respect to the pulse sequence[68]. This is impractical due to the longer supercycles or sometimes long basic inversion elements conflicting with the requirement of fast sampling for large spectral widths. Therefore sampling has to occur also during an inversion element where periods of effectively free precession may introduce a modulation of the signal depending on the magnitude of the J-coupling[74]. These artifacts appear symmetrically distributed around the decoupled center peak at frequencies which are multiples of the inverse cycle time. Example sideband profiles for the effective regions of both GARP-4 and WALTZ-65 are given in figure 2.9 where an expanded vertical scale of the spectra from figure 2.8 reveals an abundance of cycling or decoupling sidebands. In general, WALTZ-65 decoupling yields lower sideband amplitudes which is of particular interest for quantitative NMR. The increased bandwidth of GARP-4 on the other hand is exploited in ^{1}H-detected heteronuclear correlation experiments like Heteronuclear Single-Quantum Correlation (HSQC) [75] and Heteronuclear Multiple-Quantum Correlation (HMQC) [76] given that heteronuclei have larger chemical shift ranges than ^{1}H. Since decoupling schemes with a variety of origins are discussed in this thesis, these artifacts will be generally referred to as sidebands from here on. The origin of the signal modulation leading to sidebands is easily recognized looking at the spectrogram representation of the decoupling sequence. This is illustrated in figure 2.10 for the basic GARP inversion element of equation 2.7. Phase modulation in general allows for RF dissipation at different offset frequencies at different points during the pulse sequence which in turn leads to periods of effectively free precession for spins

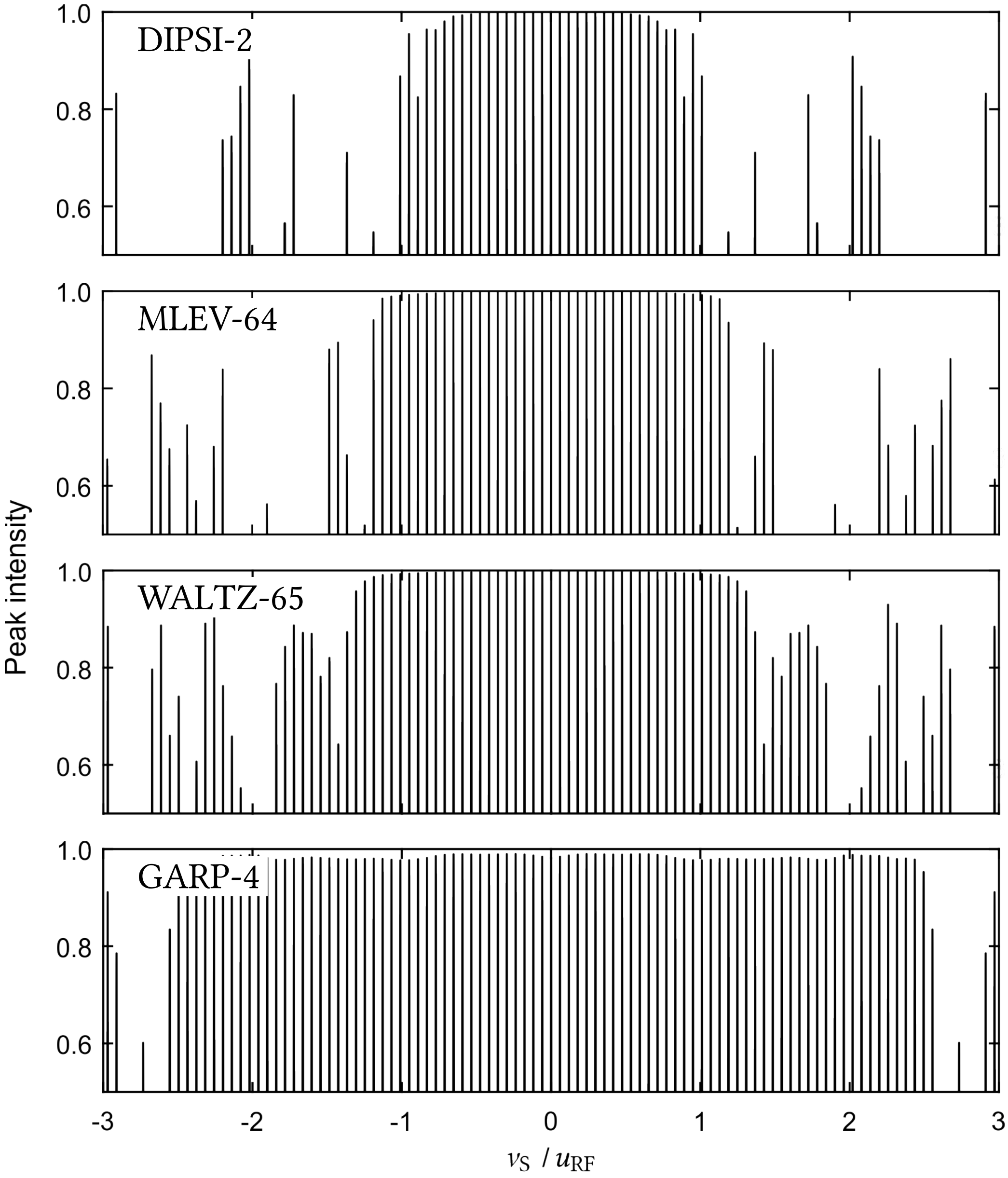

Figure 2.8.: Simulated decoupling profiles for the most common CPD schemes. WALTZ-65 presents the best compromise between the effective bandwidth and quality of decoupling for ^{13}C-detected heteronuclear NMR whereas GARP is mostly used for ^{1}H-detected experiments.

at any given frequency. These short periods lead to an unwanted signal modulation that is the cause of the spurious sidebands in the resulting spectra.

Some more decoupling schemes based on composite pulses have been proposed such as frequency-switched pulses[77, 78] or the Spin decoupling employing Ultra-broadband-inversion sequences generated via Simulated ANnealing (SUSAN) sequence[79]. But either they could not provide sideband levels as low as GARP-4 or were outperformed in terms of bandwidth by the pulses discussed in section 2.1.3.

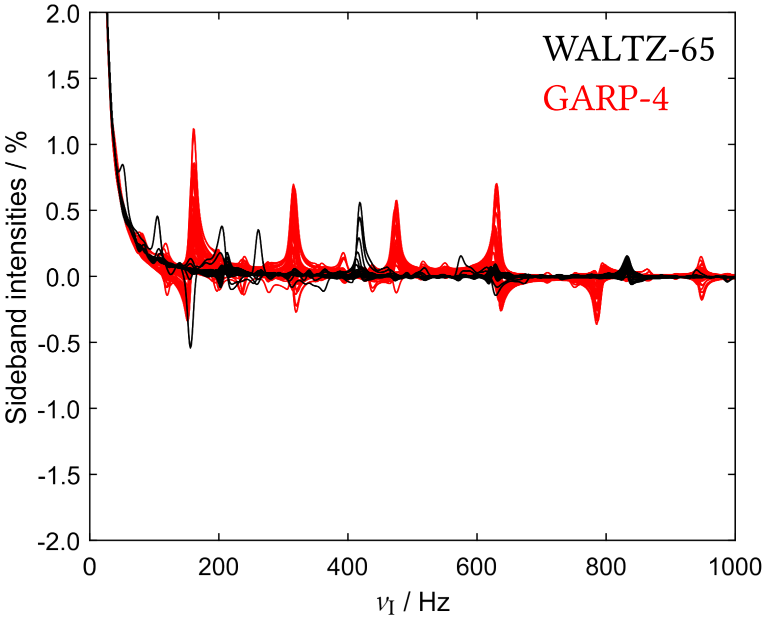

Figure 2.9.: Simulated sideband profiles for WALTZ-65 and GARP-4. Theoretical spectra for the offsets where decoupled peak intensities exceed 90% of the theoretical maximum are overlaid and expanded to 2% of the maximum achievable center peak intensity. Since the sidebands are symmetrically distributed around the center peak, only positive frequencies are plotted.

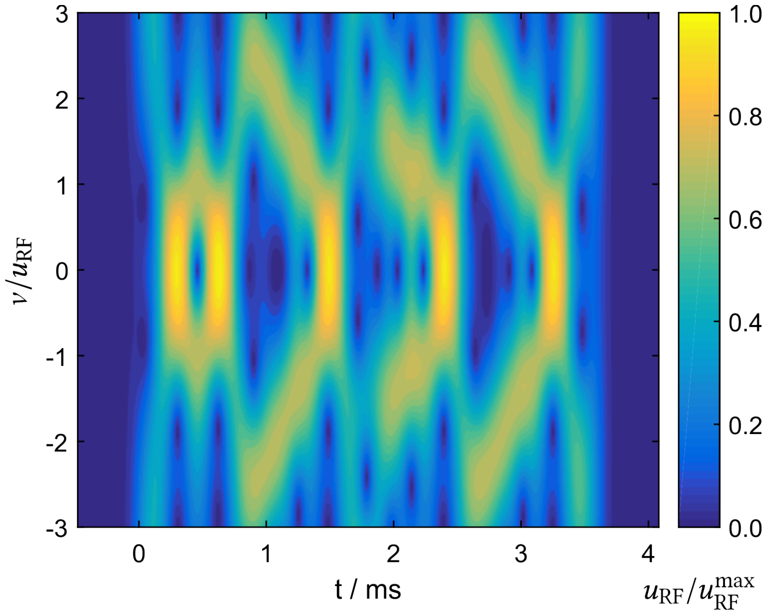

Figure 2.10.: Spectrogram representation of the GARP inversion element. Parameters of the spectrogram were chosen according to the GARP-4 example given in [54] with a 15% baseline of zeros added at the beginning and end of the pulse sequence.

2.1.3. Shaped Pulse Decoupling

With respect to the development of CPD techniques, it was realized rather early that adiabatic fast passage should be the most robust way to invert spins[80, 81]. Spin inversion can be called adiabatic if the effective field B_{eff} caused by B_1 and the resonance offset ν is tilted slow enough to fulfill the adiabatic condition given by

$$\left|\frac{\partial\theta}{\partial t}\right| \ll B_{\mathrm{eff}} \tag{2.8}$$

where θ is the angle between B_{eff} and the x-axis. This is mostly achieved by a frequency sweep which will lead to a consecutive inversion of the spins at a given frequency at a given point in time during the sweep. Mostly in parallel, competing researchers have proposed different implementations of adiabatic sweeps to be used as the inversion element for broadband decoupling. The Hyperbolic Secant (HS) pulse, originally designed for selective inversion[82–84], led to the Sech/Tanh Universal Decoupling (STUD) technique[85, 86]. Its tangential frequency sweep is given by

$$\nu(t) = \frac{\Delta\nu}{2} \cdot \tanh\ 5.3\left(\frac{2t}{T} - 1\right) \tag{2.9}$$

where $\Delta\nu$ is the swept bandwidth, T the pulse length and the factor 5.3 ensures RF truncation at the 1% level at the extremities of the sweep. Frequency sweeps are typically realized by phase-modulation which can be obtained by integrating the frequency modulation yielding

$$\phi(t) = \frac{360T}{10.6} \cdot \frac{\Delta\nu}{2} \cdot \ln\left(\cosh\ 5.3\left(\frac{2t}{T} - 1\right)\right). \tag{2.10}$$

The amplitude envelope is given by a HS function according to

$$u_{\mathrm{RF}}(t) = u_{\mathrm{RF}}^{\mathrm{max}} \cdot \mathrm{sech}\ 5.3\left(\frac{2t}{T} - 1\right). \tag{2.11}$$

A linear frequency sweep would be the most simple implementation and is represented by the (smoothed) frequency-chirped pulses[87, 88] and the method is simply referred to as CHIRP decoupling[89, 90]. Another widely-used shape for adiabatic decoupling using a linear frequency sweep which simply differs in the amplitude envelope are the Wideband, Uniform Rate, and Smooth Truncation (WURST) pulses[91, 92]. Whereas with the CHIRP pulses the first quarter of a sine wave is used to apodize a given percentage of the shape, the WURST envelope is given by

$$u_{\mathrm{RF}}(t) = u_{\mathrm{RF}}^{\mathrm{max}}\left(1 - |\sin(\beta t)|^n\right) \tag{2.12}$$

where $-\pi/2 < \beta t < \pi/2$ and the power index n indicates the steepness of the RF cutoff and can be appended to the acronym, like in WURST-40. The phase-modulation for both CHIRP and WURST is obtained by integration of a linear function and therefore resembles a parabolic profile.

The relationship between swept bandwidth, inversion bandwidth and effective decoupling bandwidth as well as the effects of RF power levels and pulse lengths on the sideband amplitudes has been studied extensively[93–96] and a fair comparison is cumbersome. There is no unifying set of parameters that could compare all three different shapes but some have proven reliable such as the adiabaticity factor Q given by

$$Q = \frac{B_{\text{eff}}}{|\partial\theta/\partial t|} = \frac{\left(u_{\text{RF}}^2 + \nu^2\right)^{\frac{3}{2}}}{u_{\text{RF}}\left(\partial\nu/\partial t\right) - \nu\left(\partial u_{\text{RF}}/\partial t\right)} \tag{2.13}$$

which should be larger than unity and is recommended as five[91]. The R-factor given by $\Delta\nu \cdot T$ can also be evaluated and should not drop below 20. Whereas Q may serve as an indicator how much energy is necessary for an efficient sweep, the R-factor becomes low if the sweep is too long to be truly adiabatic. Analysis of the different sweeping modes reveals a constant adiabaticity throughout the shape for the HS, but for linear sweeps Q has a crucial minimum at $\nu = 0$. Evaluating equation 2.13 at $\nu = 0$ yields

$$Q = \frac{u_{\text{RF}}^2}{|\partial\nu/\partial t|} \tag{2.14}$$

which led to the proposal of optimized frequency sweeps to obtain constant-adiabaticity WURST (caWURST) pulses with a desired value for Q by integrating the amplitude profile[97]. For the recommended caWURST-2 shape this corresponds to

$$\nu(t) = \frac{\left(u_{\text{RF}}^{\text{max}}\right)^2}{Q}\int \cos^4(\beta t)\mathrm{d}t = \frac{\left(u_{\text{RF}}^{\text{max}}\right)^2}{32\beta Q}\left(12\beta t + 8\sin(2\beta t) + \sin(4\beta t)\right). \tag{2.15}$$

A comparison of the different shapes and sweeping modes is given in figure 2.11. As the sweeps get increasingly non-linear, the more the frequencies are effectively swept at the center of the shape. In combination with the increased $u_{\text{RF}}^{\text{max}}$ when the pulses go through resonance, more rectangular inversion profiles are obtained going from CHIRP over caWURST-2 to HS.

Adiabatic decoupling benefited from the development of new iterative methods to obtain phase cycles[98–100]. The most common phase cycle is an MLEV-4 expansion of the 5-step phase cycle which was first presented for frequency-switched composite pulses[77] and is generally referred to as M4P5. These phase cycles follow a general recipe which is depicted in table 2.4. Different values for d are commonly used for the different phase cycles which are given in the third column of table 2.4. Decoupling profiles for the shapes depicted in figure 2.11 using a M4P5 cycle are shown in figure 2.12. The offsets used in the simulations were equally distributed over 110% of the sweep-width of the corresponding shapes. More non-linear sweeps allow for an increased translation of sweep-width into decoupling bandwidth (left panels of figure 2.12) which was obtained by evaluating the offset range where the peak intensities surpass 90% of the theoretical maximum. This way, relative decoupling bandwidths of 79.2% for a 20%-smoothed CHIRP, 94.6% for caWURST-2 and 96.8% for STUD were extracted for the given parameters. For an analysis of the sidebands, the frequency scale of the spin I spectrum was converted to multiples of the inverse pulse length T^{-1}. The sideband profiles (right panels of figure 2.12) show the most abundant and spurious sidebands at $1/T$ and $1/2T$. Going from CHIRP over caWURST-2 to STUD,

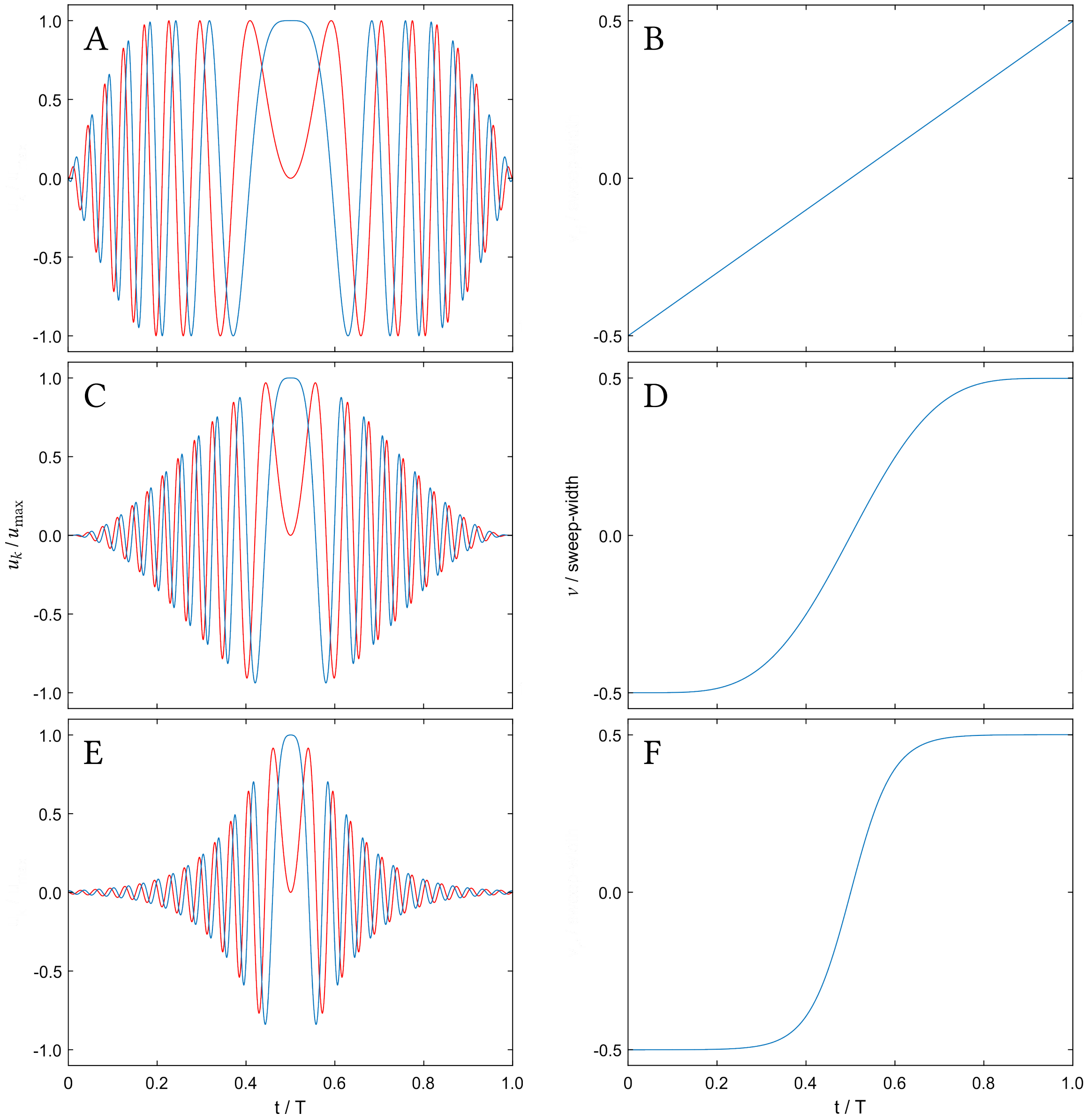

Figure 2.11.: Comparison of different adiabatic pulse shapes and sweeping modes. The Cartesian components of the pulses are given on the left and the corresponding frequency sweeps on the right. The CHIRP shape (A) is apodized at the first and final 20% and employs a linear frequency sweep (B). The caWURST shape follows a squared cosine envelope (C) and has an optimized frequency sweep according to equation 2.15 (D). The shape with the highest peak RF amplitude is the HS pulse with the amplitude envelope given by equation 2.11 (E) and a tangential frequency sweep according to equation 2.9 (F). R = 60 for all cases and the RF levels were chosen to yield Q = 5. $B_{1,\mathrm{RMS}}$ for the HS pulse was chosen to match caWURST-2. All shapes were digitized into 1000 increments.

Phase cycle	Phases / °	Recommended value for d / °
P5	0, d, 120 + 2d, 60 + 3d, 120 + 4d	150[77]
P7	0, d, 90 + 2d, 300 + 3d, 240 + 4d, 300 + 5d, 90 + 6d	none[86]
P9	0, d, 150 + 2d, 120 + 3d, 210 + 4d, 90 + 5d, 90 + 6d, 270 + 7d, 240 + 8d	15[101]

Table 2.4.: Phase cycles used in conjunction with MLEV-4. All three examples show slight variations in their performance depending on the exact value of d. M4P5, which is an MLEV-4 expansion of the five-step phase cycle P5, is most commonly used for adiabatic decoupling.

the sidebands at $1/2T$ show decreasing intensity, sidebands at $1/T$ become more in-phase and sidebands very close to the center peak become less abundant. The origin, intensity and phase behavior of sidebands caused by adiabatic decoupling is discussed extensively in section 2.1.4.

To suppress these sidebands different approaches were proposed. The authors of the STUD method tried to improve the quality of decoupling by more complex phase cycles using a single scan. A combination of M4P5 and M4P9 with cycles where the variable d in table 2.4 is incremented by 180° (shorthand notation M4P5' and M4P9') yielded the M4P5-M4P9-M4P5'-M4P9' cycle, which is referred to as STUD+[101, 102]. The potential of sideband suppression using multiple scans and a comparison with STUD+ is discussed in the following sections.

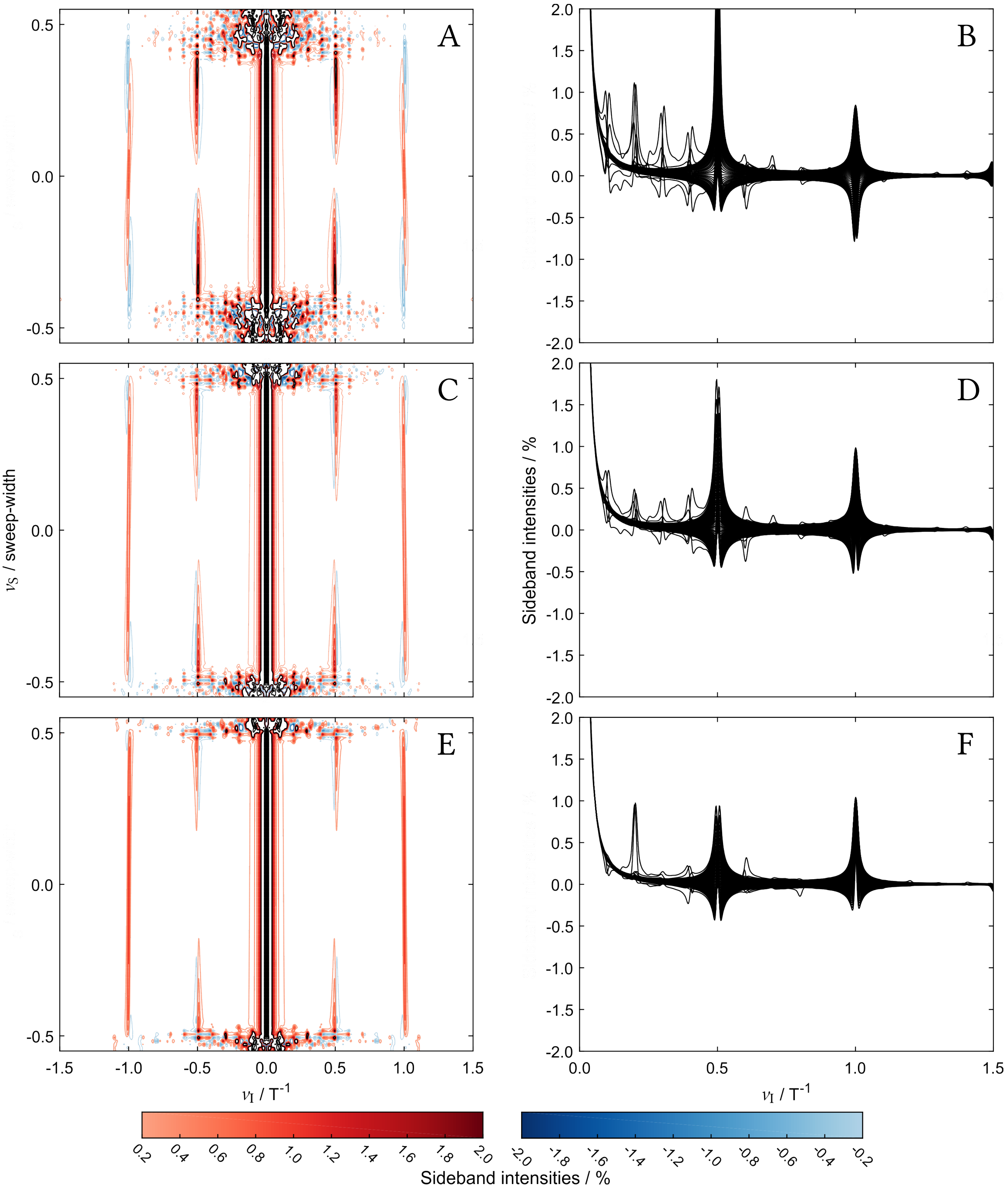

Figure 2.12.: Simulated decoupling profiles for typical adiabatic decoupling schemes. CHIRP can only provide 79.2% decoupling range with respect to the sweep-width (A) and sideband intensities above 2% can be observed (B). Using caWURST-2 the decoupling bandwidth is increased to 94.6% (C) and sidebands fall below 2% (D). STUD provides the highest effective bandwidth of 96.8% (E) and the least sidebands of about 1% (F). Ten contour levels for positive and negative sidebands were plotted distributed equally between the extreme values of ±0.2 and ±2% respectively. Peak contours were plotted using ten levels between the maximum sideband and 100% intensity.

2.1.4. Bilevel Decoupling

Sidebands in adiabatic decoupling are well understood[103]. The reason why desynchronisation-based approaches known for CPD [74, 104] can not be applied to adiabatic decoupling lies in the inversion mode of adiabatic pulses. However, the known positions and phase gradients of the sidebands allow for targeted suppression schemes. These principles are exploited in Eliminate Cycling Oscillations (ECO)-WURST decoupling[105] and the modified so-called ECHO-WURST method[106]. The advantages of both methods were molded into the standard implementation to suppress sidebands in adiabatic decoupling which will be simply referred to as bilevel decoupling and will be discussed in the following.

Looking at the left panels of figure 2.12 indicates that the only significant sidebands at decoupler offsets close to resonance of the heteronucleus appear at the frequency $1/T$. They are referred to as principal or harmonic sidebands are simply called harmonics in the following. Harmonics arise because spins close to resonance are inverted near the center of the adiabatic sweep. Up to that point the signal of spin I is modulated by the heteronuclear coupling. After inversion of the heteronucleus the coupling evolution will be refocused after T has passed, at the end of the sweep. Off-resonance, sidebands at a second frequency are introduced. Since spins far off-resonance are either inverted rather at the beginning or end of the sweep this signal modulation can only refocus after $2T$ which is why this second type of sidebands appear at $1/2T$. They are called subharmonic sidebands or simply subharmonics.

This inversion behavior also induces the phase gradients which cause the particular line shapes of the sidebands depicted in the right panels of figure 2.12. The closer spins are inverted near the middle of the sweep, the more in-phase the harmonics will appear. At the same time the intensity of the subharmonics will drop or differently put, the subharmonics will only gain significant intensity at higher frequencies. This is reflected in the progression of sideband profiles from CHIRP over caWURST-2 to STUD since the amplitude envelope in combination with the sweeping mode allows for a more focused energy disposition in the swept frequency range. The phase gradients can be turned into pure intensity gradients by averaging two scans using adiabatic pulses with opposite sweep directions[105, 106]. Then, all sidebands will appear as in-phase lines with maximum harmonic intensity near the center and maximum subharmonic intensity at the edges of the sweep, but with a sum remaining mostly constant. As a consequence, the sideband intensity can be shifted between harmonics and subharmonics[105] on the one hand or distributed over several frequencies by the frequency-unspecific accordion averaging technique[85].

However, the phase gradients are the key to efficient sideband suppression. Bilevel decoupling is based on the averaging of scans where the signal modulation leading to the sidebands has an onset to achieve a 180° phase shift between successive scans. This is facilitated by applying adiabatic pulses with a pulse length $T/2$ at the beginning of the decoupling period. To achieve reasonable adiabaticity, these pulses typically employ higher RF levels. Adding a single pulse of $T/2$ leads to a 180° phase shift of the harmonics which therefore can be canceled using two scans. In order to also cancel subharmonics the $T/2$-incrementation has to be done over four scans so an effective 180° phase shift by an onset of T is introduced. Practically, this is not achieved by averaging scans with no to three high-power pulses at the beginning of the acquisition period but one to four. These

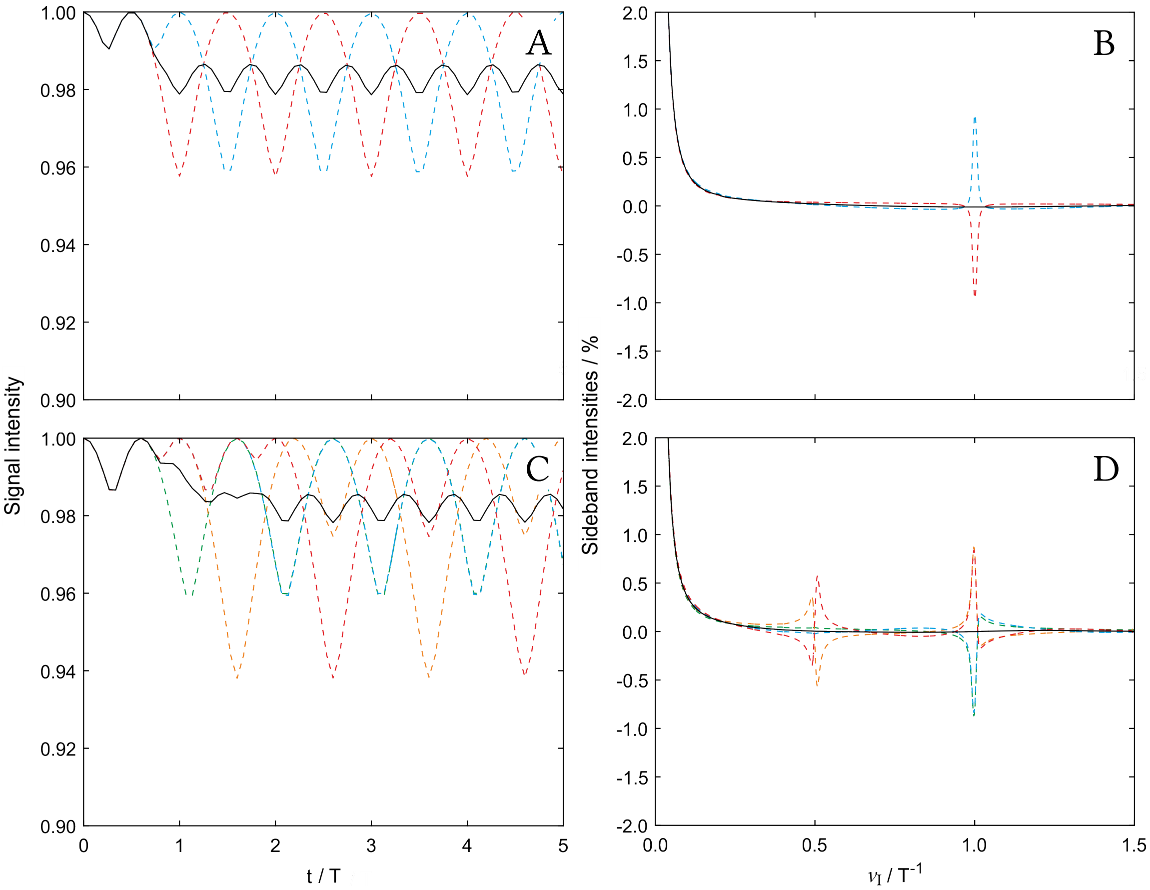

Figure 2.13.: Sideband cancelling mechanism of bilevel decoupling illustrated by simulated time- and frequency domain data for two scans on resonance and four scans off resonance bilevel decoupling. Averaging two scans where the signal modulation has an onset of $T/2$ (A) leads to cancellation of harmonic sidebands (B), $\nu_S = 0$. Using four scans with onsets of multiples of $T/2$ (C) introduces the necessary phase shifts to cancel both harmonics and subharmonics (D), $\nu_S = 1/2$ of the highest swept frequency. Individual scans are shown as colored dashed lines and the average is shown as a solid black line. caWURST-2 pulses according to figure 2.11 C and D were used. The same shape was used for the high-power pulse with pulse length $T/2$ and $u_{\mathrm{RF}}^{\max}$ was chosen to yield Q = 5.

principles are illustrated in figure 2.13 using the caWURST-2 shape. The cancellation of the sidebands is shown for an on resonance example where harmonics are the only significant sidebands and an offset half-way towards the positive edge of the sweep where both types of sidebands are present. The colored dashed lines indicate individual scans with their individual signal modulations and the resulting phase shifts of the sidebands. Solid black lines depict the averaged signal. In both cases the most obtrusive sidebands are suppressed but a residual signal modulation is left at higher frequency and lower intensity which may be negligible. The reason why the caWURST-2 shape is used here is the common notion to shy away from decoupling schemes like STUD that rely on relatively high peak RF amplitudes. A combination of bilevel decoupling and the HS shape would imply an even higher value of $u_{\mathrm{RF}}^{\max}$ if reasonable adiabaticity is required for the $T/2$ pulse. An additional reason might be that the same authors championed both the WURST shapes and the bilevel technique.

A bilevel approach to decoupling was also proposed for quantitative ^{13}C NMR. Here, CW irradiation serves as the high-power component for WALTZ decoupling using as much as 256 scans to average sidebands to a level below the detection limit so that the dynamic range in the spectrum allows for the quantitative study of polymer branching[70].

2.2. Broadband Decoupling by Optimal Control Theory

2.2.1. Motivation

Broadband decoupling by means of OCT has been the subject of work done in parallel and independently from this thesis. The Broadband Uniform Sideband Suppression (BUSS) pulse was proposed for heteronuclear decoupling in biomolecular NMR at extremely high magnetic fields[107]. In order to distinguish the motivation behind the BUSS pulse from this work the relative specifications for the decoupling schemes of the past sections has to give way to absolute numbers. The BUSS pulse was optimized to cover an offset range of 45 kHz using $B_{1,\mathrm{RMS}} = 4.4$ kHz. This corresponds to a ^{13}C chemical shift range of 150 ppm on a spectrometer operating at 28.2 T corresponding to $\omega_\mathrm{L} = 1.2$ GHz for ^{1}H. Spectrometers operating at such high magnetic fields are not yet commercially available and on the far more common 14.1 T magnets the BUSS pulse would cover 300 ppm which is more than enough for small molecule NMR. To compare different decoupling schemes it is advantageous to distill the most important figures into a single number. Figures of merit have been proposed for CPD [108] and adiabatic decoupling[91, 95] and are generally defined as simple as

$$\Xi = \frac{\Delta\nu_\mathrm{S}}{B_{1,\mathrm{RMS}}}. \tag{2.16}$$

The effective bandwidth $\Delta\nu_\mathrm{S}$ in equation 2.16 is defined as the bandwidth where 80% of the theoretically possible peak decoupled peak intensity is achieved. Using this criterion the BUSS pulse would provide $\Xi = 10.7$ since the actual $\Delta\nu_\mathrm{S}$ demanded in the optimizations was set to 47 kHz. In this work, the desired decoupling bandwidth is 40 kHz which would safely encompass 37.5 kHz that correspond to 250 ppm on a 14.1 T device ($\omega_\mathrm{L} = 600$ MHz for ^{1}H). Conversely, here the aim is set to cover this bandwidth using only $B_{1,\mathrm{RMS}} = 2$ kHz, yielding $\Xi = 20$. For the various implementations of adiabatic decoupling, figures of merit ranging from slightly above 10[91] to over 70[97] have been reported. However, all of these values neglect the important ratio $J/B_{1,\mathrm{RMS}}$ which is key for effective decoupling. The decoupling schemes given above can be reevaluated using a slightly modified figure of merit given by

$$\Xi^* = \frac{\Delta\nu_\mathrm{S} \cdot J}{B^2_{1,\mathrm{RMS}}}. \tag{2.17}$$

Values for Ξ^* for the decoupling schemes under investigation are given in table 2.5. The only reported example of a value for Ξ^* approaching the target value of 1.4 given in this thesis is a caWURST-240 implementation. Nevertheless, with $B_{1,\mathrm{RMS}}$ chosen so that the value of J corresponds to 7% of $B_{1,\mathrm{RMS}}$, the target parameters chosen here pose a more

Decoupling scheme	$B_{1,\mathrm{RMS}}$/ kHz	$\Delta\nu_\mathrm{S}$/ kHz	J/ Hz	Ξ	$J/B_{1,\mathrm{RMS}}$	Ξ^*	Citation
BUSS	4.4	47	150 (197)	10.682	0.034 (0.045)	0.364 (0.478)	[107]
STUD+	4.4	45	197	10.227	0.045	0.458	[107]
WURST-40	3.36	56	151	16.667	0.045	0.749	[91]
caWURST-2	0.92	66	11	71.739	0.012	0.858	[97]
caWURST-240	5.6	290	151	51.786	0.027	1.396	[97]
This work	2	40	140	20	0.07	1.4	-

Table 2.5.: Figures of merit for state-of-the-art decoupling techniques. In case of the BUSS pulse pairs of values concerning the magnitude of J are given since different values were used in the optimization an experimental verification (in brackets).

challenging optimization task than other reported methods. Moreover, the caWURST-240 sequence proposed in [97] operates at $B_{1,\mathrm{RMS}}$ = 5.6 kHz which is above the limit for typical cryogenically cooled probeheads of modern NMR spectrometers corresponding to 4.4 kHz for acquisition periods of about 140 ms. Further, apart from the caWURST-2 example given in table 2.5, none of the methods given above can be scaled up. By halving the digitization of all pulse increments and doubling all RF amplitudes, the frequencies and corresponding frequency ranges double as well. In table 2.5 only the caWURST-2 can be reasonably scaled up without exceeding the RF limitations of common cryo-probes. However, even up-scaling by a factor of ten would only cover J-couplings of about 110 Hz, which is below typical values of $^1J_{\mathrm{CH}}$ couplings. These couplings serve as the standard test case for broadband decoupling. However, with this scaling factor caWURST-2 would already operate at unfeasible 9.2 kHz. At the same time, none of the "high-power" methods can be scaled down to $B_{1,\mathrm{RMS}}$ = 2 kHz since the covered values for J would fall below typical values for $^1J_{\mathrm{CH}}$ couplings. Given that the aim of this work is operation at mean RF levels of 2 kHz at a target J of 140 Hz, the resulting sequences can be scaled up by a factor of 2.2 without violation of common RF constraints to yield uncompromised decoupling performance over 88 kHz for J couplings larger than 300 Hz. Since the latter is untypical for $^1J_{\mathrm{CH}}$ couplings, an improved quality of decoupling can be expected for the lower more typical values.

In order to work towards meaningful comparisons of state-of-the-art decoupling schemes with sequences developed in this thesis, the sideband suppression capabilities of the BUSS pulse and the STUD+ implementation discussed in [107] has to be reassessed with respect to bilevel decoupling each tailored towards the target parameter settings defined above. For this comparison, caWURST-2 pulses with T = 1.5 ms and $B_{1,\mathrm{RMS}}$ = 4.4 kHz digitized in 300 steps of 5 μs were used. To ensure an efficient sweep over the desired bandwidth of about 40 kHz, the total sweep was set to 42 kHz. This yields Q = 4.36 and requires $u_{\mathrm{RF}}^{\mathrm{max}}$ = 7.19 kHz. For the high-power component necessary for bilevel decoupling the caWURST-2 shape was calibrated to T = 750 μs and $u_{\mathrm{RF}}^{\mathrm{max}}$ = 10.5 kHz to obtain Q = 4.66 using the same digitization. Simulations were backed up with experiments on a sample of ^{13}C-labeled methanol ($^1J_{\mathrm{CH}}$ = 141 Hz) using the same parameters given in section 2.1.1 for the simulations except that the time-domain data was zero-filled to 16384 points to achieve a digital resolution below 1 Hz to allow for a more exact evaluation of relative intensities. The value for J has been adjusted to 141 Hz in the simulations and 101 offsets were sampled across an offset range of 60 kHz. To allow for a critical evaluation of the sideband amplitudes, all peak intensities were normalized to the maximum peak intensity which was achieved across the given offset range. Further experimental details are given in section 2.2.7. Simulated and experimental decoupling profiles for one to four scans of the bilevel implementation discussed in section 2.1.4 using the caWURST-2 shape along with a M4P5 supercycle are given in figure 2.14. Experiments agree well with the simulations in terms of position and phase gradients of the sidebands. Using two scans the harmonics appearing at $1/T$ can efficiently be suppressed whereas the subharmonics appearing at $1/2T$ cancel using four scans just in the way it is depicted in figure 2.13. For a more detailed look at the sidebands, the spectra are overlaid with an expanded vertical scale in figure 2.15. Again, experiments and simulations agree well as far as harmonics and subharmonics are concerned. The deviations are mainly posed by sidebands closer to the center peak which

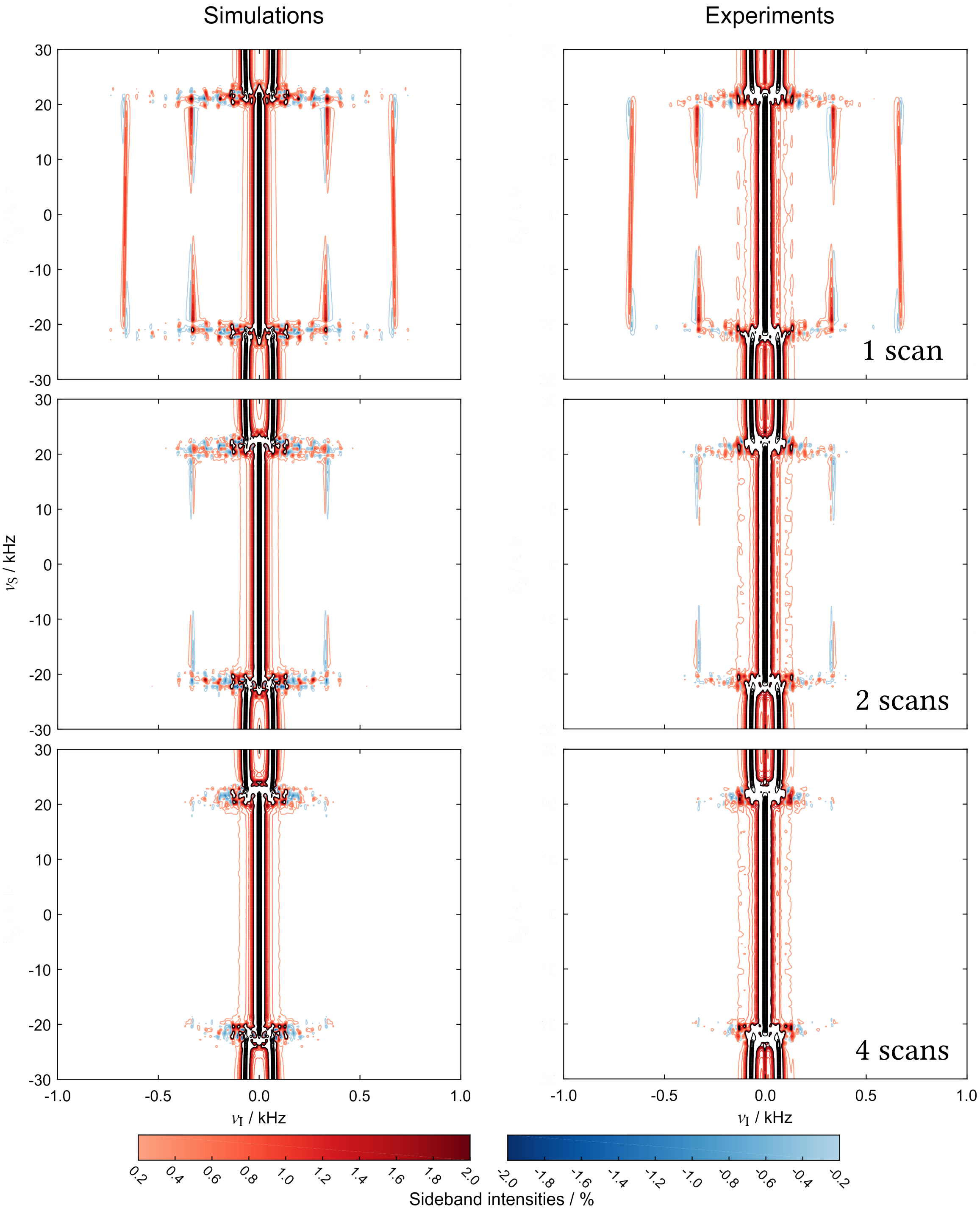

Figure 2.14.: Comparison of simulated (left panels) and experimental (right panels) offset profiles for caWURST-2 bilevel decoupling at $B_{1,\mathrm{RMS}}$ = 4.4 kHz using one to four scans. Ten contour levels for positive and negative sidebands were plotted distributed equally between the extreme values of ±0.2 and ±2% respectively. Peak contours were plotted using ten levels between the maximum sideband and 100% intensity. The number of scans are given as insets. The M4P5 cycle was used throughout.

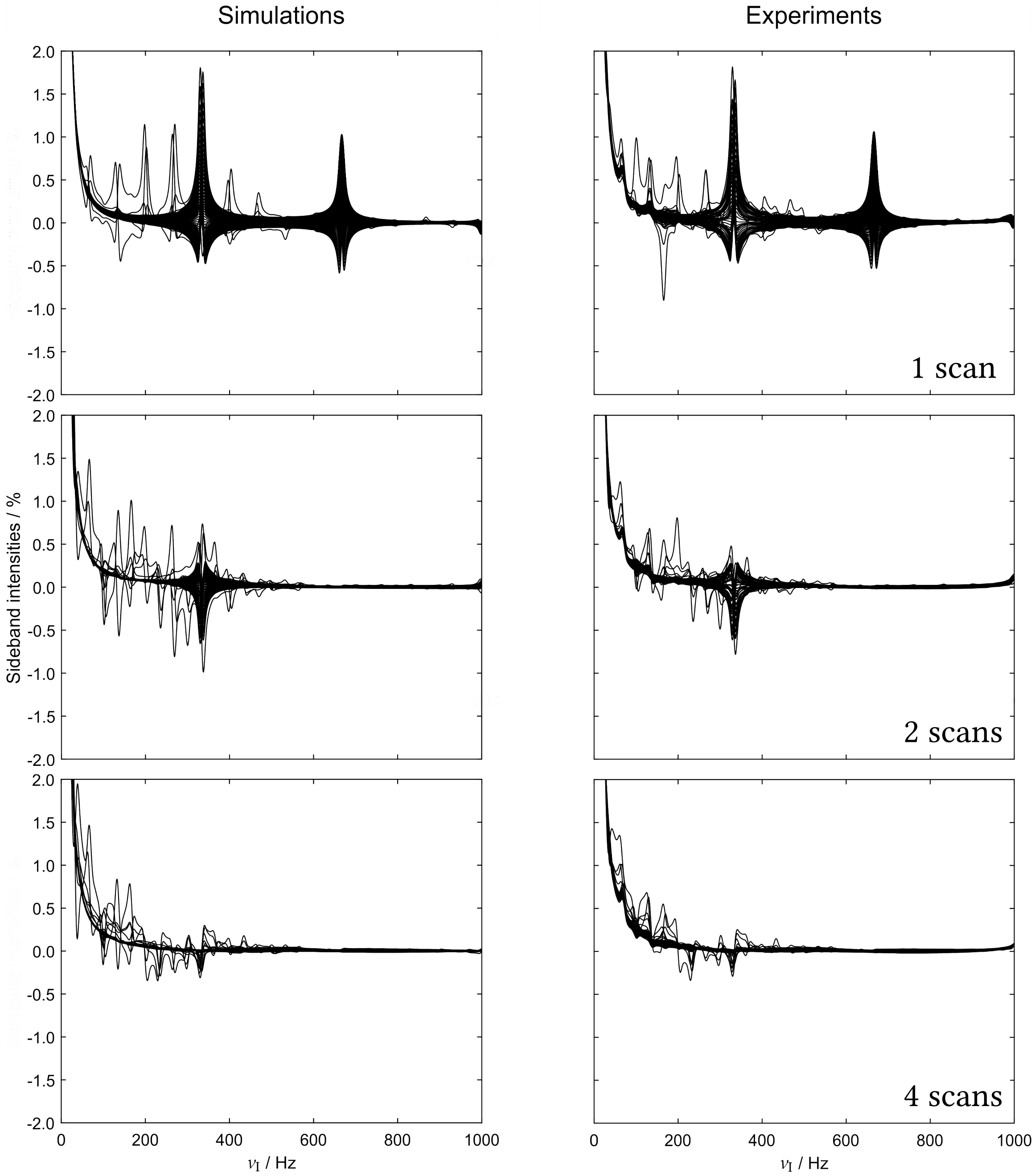

Figure 2.15.: Comparison of simulated (left panels) and experimental (right panels) sideband amplitudes for caWURST-2 bilevel decoupling at $B_{1,\mathrm{RMS}}$ = 4.4 kHz using one to four scans. Spectra are overlaid and expanded to 2% of the maximum decoupled center peak intensity across the desired offset range of 40 kHz. Since the sidebands are symmetrically distributed around the center peak, only positive frequencies are plotted. The number of scans are given as insets. The M4P5 cycle was used throughout.

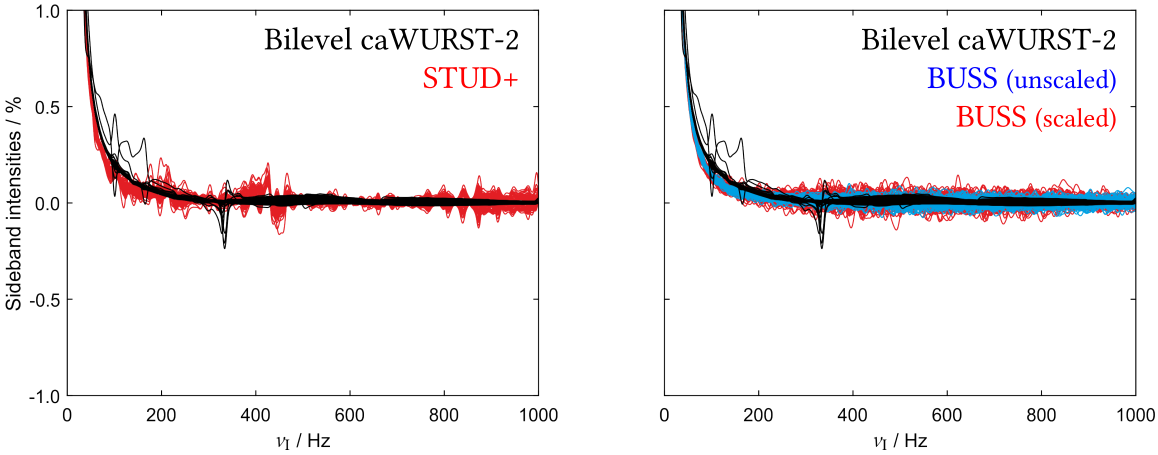

Figure 2.16.: Comparison of simulated sideband amplitudes for caWURST-2 bilevel decoupling using 4 scans with state-of-the-art single-scan methods. To further emphasize the negligible sidebands of adiabatic bilevel decoupling, spectra were expanded to 1% of the maximum decoupled center peak intensity across the experimentally relevant core offset region of 37.5 kHz where the frequency sweep is close to perfection. Bilevel decoupling (black) generally outperforms STUD+ (red, left panel) as well as scaled (red, right panel) and unscaled (blue, right panel) versions of the BUSS pulse.

differ in phase and intensity. It can be seen from looking at figure 2.14 that these sidebands only occur at the edges of the given offset range, where the decoupled peak intensity is still reasonable but an increased abundance of sidebands is observable before decoupling collapses. These sidebands are discussed further below.

The efficiency of sideband suppression using bilevel decoupling shall now be compared to STUD+ as well as scaled and unscaled versions of the BUSS pulse. For STUD+, HS pulses with $T = 500\ \mu s$ and $u_{RF}^{max} = 10.15$ kHz were used. Given that the sweep width was also set to 42 kHz, decreased adiabaticity can be expected. However, simulations and experiments show that this is overcompensated by the STUD+ supercycle[107]. The BUSS pulse is digitized in 28672 increments which are 4.3 μs long each. This allows a maximum acquisition period of about 123.3 ms. To allow a similar resolution as in the simulations above, the theoretical spin I spectra were sampled for 123.2 ms with a real dwell time of 98.9 μs and processed in the same way as given above. Scaled to the target offset range of 40 kHz, the digitization is increased to 5 μs allowing for a real dwell time of 100 μs and the BUSS pulse can be attenuated to 25600 increments necessary for a 128 ms AQ. $B_{1,RMS}$ is now reduced to 3.78 kHz. Simulated sideband profiles for the implementations given above are depicted in figure 2.16. Clearly, bilevel decoupling outperforms the single-scan methods if the corresponding offset frequency is efficiently swept by the adiabatic pulse. STUD+ suffers from residual sidebands even if no particularly spurious harmonics or subharmonics are discernible. BUSS decoupling shows no significant sidebands at a given frequency but can not provide baselines as smooth as bilevel decoupling. Therefore, the multi-scan approach has to be "gold standard" for comparisons in this thesis.

This superiority dramatically comes to a halt as soon as $B_{1,RMS}$ is reduced to 2 kHz. Simulations and experiments with the same setup as in figures 2.14 and 2.15 were repeated with $u_{\mathrm{RF}}^{\max}$ of the caWURST-2 shapes reduced to 3.27 kHz to yield $B_{1,\mathrm{RMS}}$ = 2 kHz. If the same scaling is applied to the high-power component this leaves the shorter pulses with $u_{\mathrm{RF}}^{\max}$ = 4.77 kHz. Simulated and experimental decoupling profiles for one to four scans of bilevel decoupling using the caWURST-2 shape at $B_{1,\mathrm{RMS}}$ = 2 kHz embedded in the M4P5 supercycle are given in figure 2.17. Generally, an increased abundance of sidebands can be observed in both simulations and experiments which also have a higher intensity. The range where sideband amplitudes are plotted has been increased to 0.5-5% to allow for a more dynamic representation. Additional sidebands can mostly be observed closer to the center peak with frequencies lower than $1/T$. The general sideband patterns predicted by the simulations could be reproduced experimentally although it appears as if experimental sideband amplitudes are lower than predicted. Expanded and overlaid spectra are given in figure 2.18. It can be seen that the canceling mechanism for the harmonics and subharmonics is still functional since the former can be sufficiently suppressed and all sidebands in the vicinity of $1/2T$ are largely attenuated using four scans. However, the most obtrusive sidebands remain at frequencies below $1/2T$ and cannot be eliminated. They are referred to as inner sidebands[92, 106] and appear at $1/pT$ where p are repetition elements in the supercycle. In the case of M4P5 p takes values of 4, 5 and 20. They can only gain significant intensity when the individual adiabatic spin flips suffer from substantial imperfections which become apparent upon reducing $B_{1,\mathrm{RMS}}$ to 2 kHz. Figure 2.18 indicates that the position of each sideband is reproduced correctly but the apparent intensity differences seen in figure 2.17 turn out to be differences in the phase gradients. Whereas the two most intensive and low-frequency sidebands show significant anti-phase contributions in the simulations, they appear rather in-phase in the experiments and slowly gain phase shifts upon acquiring multiple scans. As with the acquisition of all NMR signals, the phase of a resonance line at a given frequency is determined by how well the beginning of acquisition is synchronized with the beginning of the FID. As a result of modern digital data acquisition techniques, there is a transient oscillation at the beginning of each FID which has to be rectified in the processing pipeline by a so-called group delay compensation routine. Given that data is collected using oversampling in the MHz range, group delays may have a duration corresponding to a non-integer number of points on the desired final time grid. This is why it cannot be made sure that the beginning of the acquisition and hence the decoupling sequence is matching the time grid in simulations and experiments alike. The differences of the inner sidebands in figure 2.15 might therefore be caused by the same phenomenon.

From the most simple perspective, the arising of inner sidebands is rooted in a flip angle undershoot of 180° due to the dramatic reduction of $B_{1,\mathrm{RMS}}$. It can also be understood by a drop of the adiabaticity factor Q. Using equations 2.14 and 2.15, an adiabaticity map as a function of $B_{1,\mathrm{RMS}}$ and the pulse length T can be created. Q is plotted in figure 2.19 for pulse lengths between 100 μs and 5 ms and $B_{1,\mathrm{RMS}}$ ranging from 0 to 5 kHz where results higher than 5 were attenuated since no inner sidebands need to be expected at this levels of adiabaticity. As mentioned above, the caWURST-2 pulses used in figures 2.14 and 2.15 as the low-power component of bilevel decoupling reach Q = 4.36 (black circle). When $B_{1,\mathrm{RMS}}$ is reduced to 2 kHz, Q drops down to 0.9 (white circle) which is far below recommended values. Adiabaticity can be recovered using longer pulse durations but even doubling the pulse length to 3 ms can only provide Q = 1.8 (dashed white circle). Using such prolonged

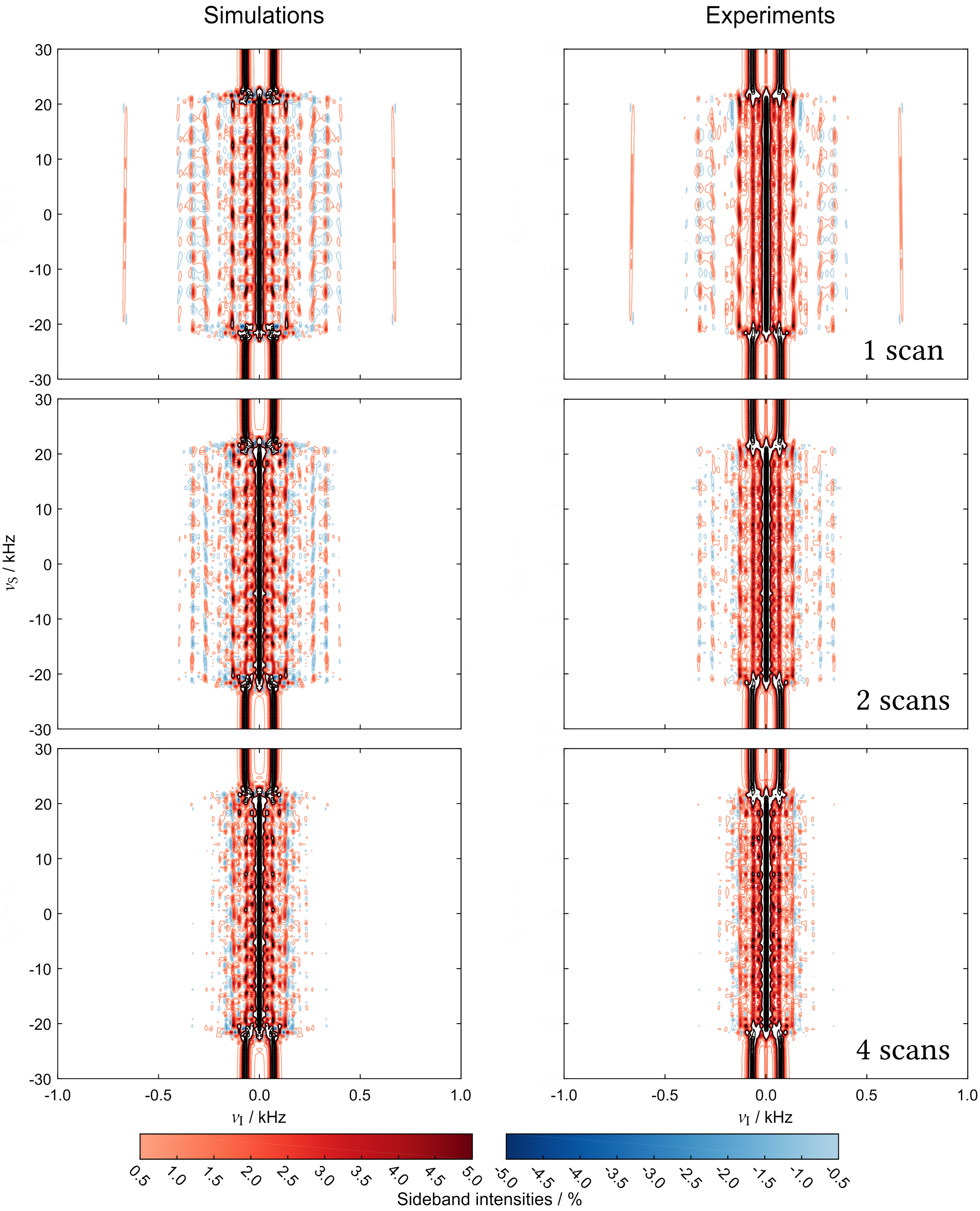

Figure 2.17.: Comparison of simulated (left panels) and experimental (right panels) offset profiles for caWURST-2 bilevel decoupling at $B_{1,\mathrm{RMS}}$ = 2 kHz using one to four scans. Ten contour levels for positive and negative sidebands were plotted distributed equally between the extreme values of ±0.5 and ±5% respectively. Peak contours were plotted using ten levels between the maximum sideband and 100% intensity. The number of scans are given as insets. The M4P5 cycle was used throughout.

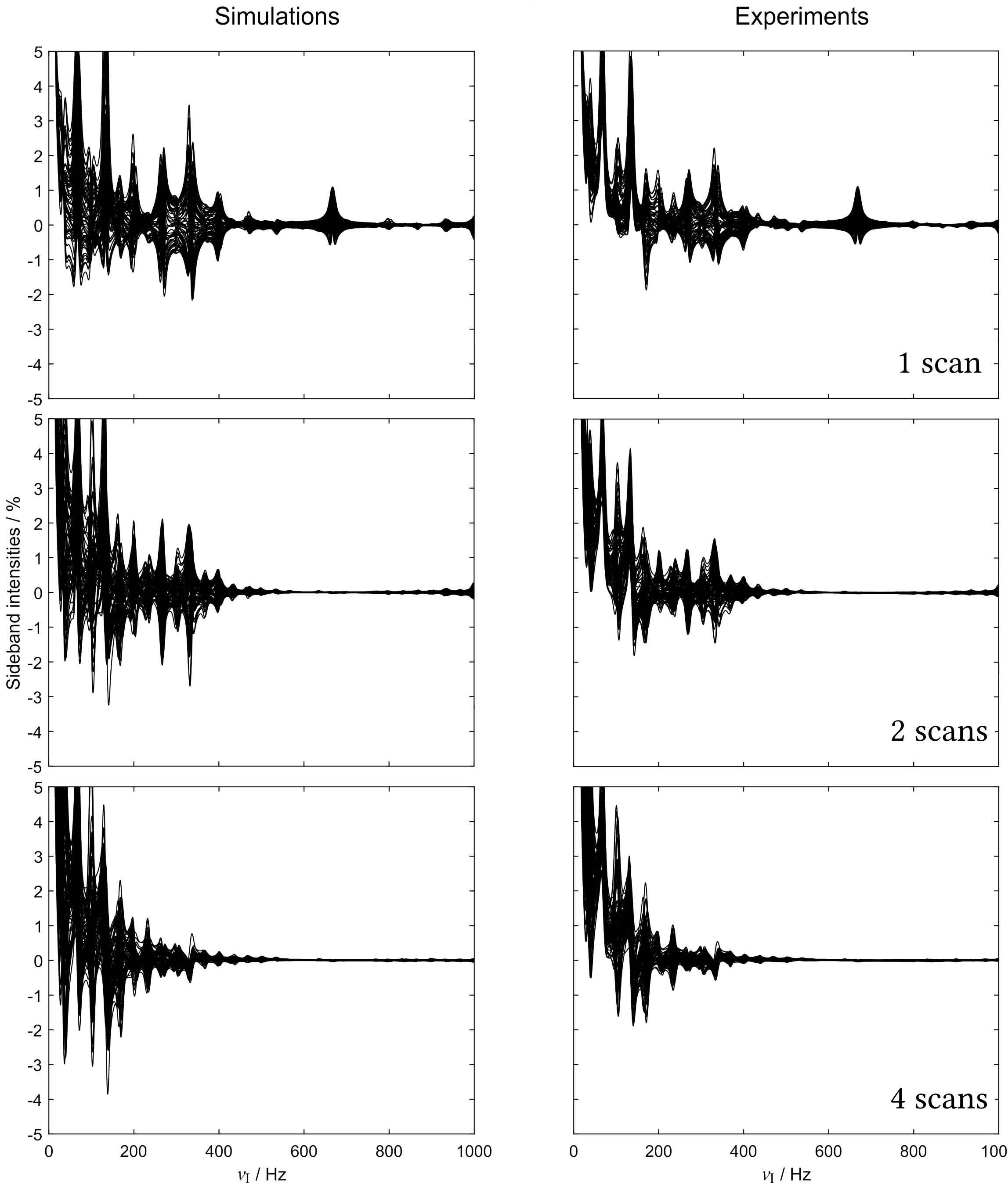

Figure 2.18.: Comparison of simulated (left panels) and experimental (right panels) sideband amplitudes for caWURST-2 bilevel decoupling at $B_{1,\mathrm{RMS}}$ = 2 kHz using one to four scans. Spectra are overlaid and expanded to 5% of the maximum decoupled center peak intensity across the desired offset range of 40 kHz. Since the sidebands are symmetrically distributed around the center peak, only positive frequencies are plotted. The number of scans are given as insets. The M4P5 cycle was used throughout.

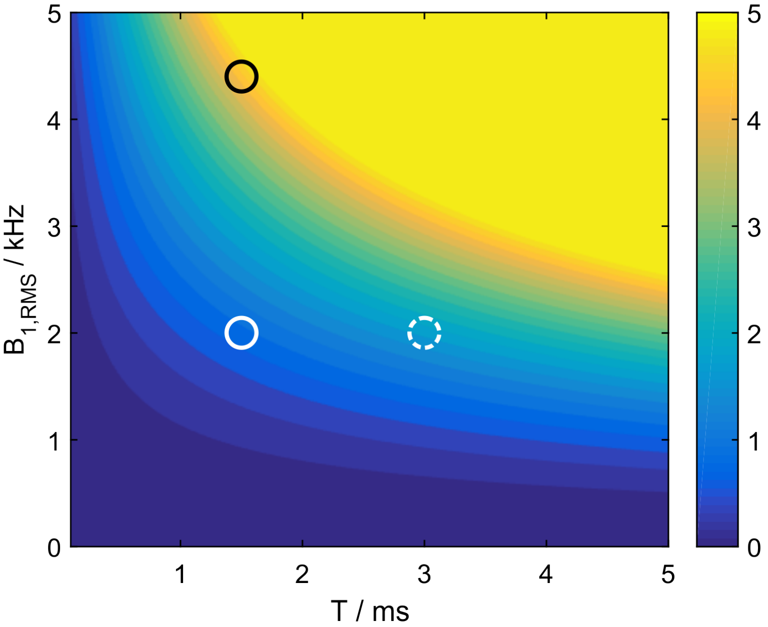

Figure 2.19.: Adiabaticity factor Q as a function of the pulse length T and $B_{1,\mathrm{RMS}}$ for the caWURST-2 shape. Values higher than 5 were attenuated. For T = 1.5 ms and $B_{1,\mathrm{RMS}}$ = 4.4 kHz, Q reaches 4.36 (black circle). Reducing $B_{1,\mathrm{RMS}}$ to 2 kHz using the same pulse length results in Q = 0.9 (white circle) which can only be recovered to 1.8 using sweeps twice as long (dashed white circle). 25 contours were plotted equally distributed between 0 and 5.

pulses poses several drawbacks for efficient (bilevel) decoupling. These drawbacks are rooted in the prolonged refocusing periods of the heteronuclear couplings. The resulting sideband patterns are depicted in figure 2.20. Using a single-scan allows for an analysis of the full variety of sidebands. Given that the pulse lengths have doubled, the frequencies of harmonics and subharmonics was halved and they can be found close to the center peak. Increased adiabaticity leads to fewer and less intensive inner sidebands. However, the first integer multiple of the harmonics can be observed as distinct sidebands at $2/T$ Hz. If bilevel decoupling was restricted to the averaging of four scans, either the harmonics and subharmonics could be suppressed using a $T/2$ incrementation of the high-power component, or the harmonics and their first integer multiple could be canceled using a $T/4$ incrementation. In order to eliminate all three types of sidebands the $T/4$ incrementation has to be expanded to eight scans. In each case, inner sidebands remain and the general picture can not be improved beyond what is given in figure 2.17. A more detailed look at the sidebands is given in figure 2.21. It can be seen that harmonics and subharmonics have greatly increased intensity. Using longer adiabatic sweeps, longer periods of free precession are introduced for each given decoupler offset leading to larger oscillations of the signal. These oscillations also lead to significant intensity losses upon averaging of the individual scans as can be seen by the wavy baselines obtained by four scans of the $T/2$ incrementation. Using four scans of the $T/4$ incrementation leaves the subharmonics uncanceled since only a 90° degree phase shift is introduced leaving the subharmonics at

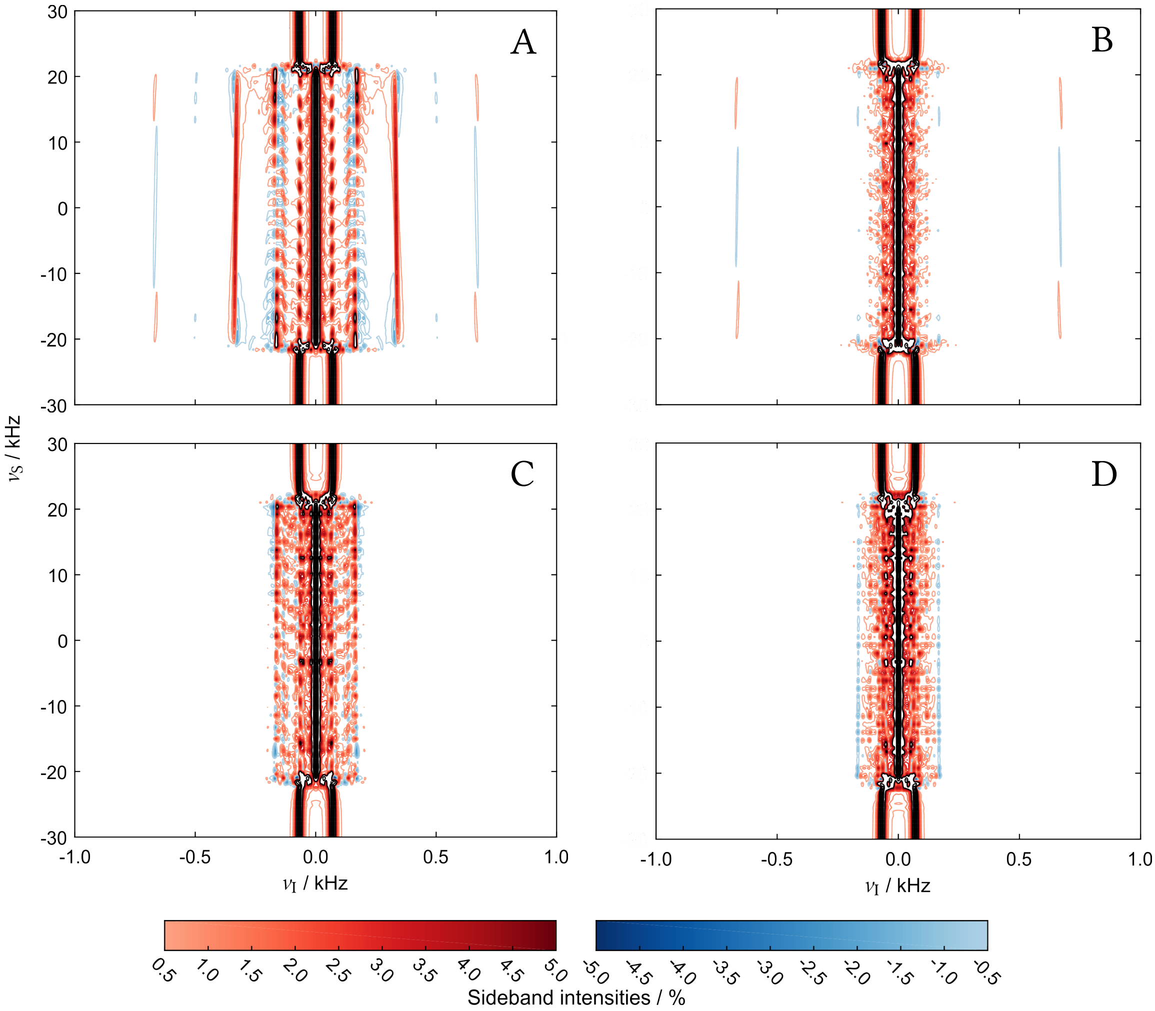

Figure 2.20.: Simulated offset profiles for caWURST-2 bilevel decoupling at $B_{1,\mathrm{RMS}} = 2$ kHz using pulses with T increased to 3 ms ($Q = 1.8$). Decoupling profiles are given for a single scan (A), four scans using a $T/2$ (B) and $T/4$ (C) incrementation of the high-power component. 8 scans using a $T/4$ incrementation are depicted in (D). Ten contour levels for positive and negative sidebands were plotted distributed equally between the extreme values of ±0.5 and ±5% respectively. Peak contours were plotted using ten levels between the maximum sideband and 100% intensity. The M4P5 cycle was used throughout.

about 5% intensity. If eight scans of the $T/4$ incrementation were to be collected, inner sidebands would still remain at the same intensity of about 5%.

It has been demonstrated that the most common and most reliable sideband suppression technique used in low-power broadband heteronuclear decoupling is mostly limited by the adiabaticity constraint of the individual inversion elements. The main task of the optimization studies of this thesis using OCT is therefore to find pulse sequences that can overcome this limit in a single or multiple scans.

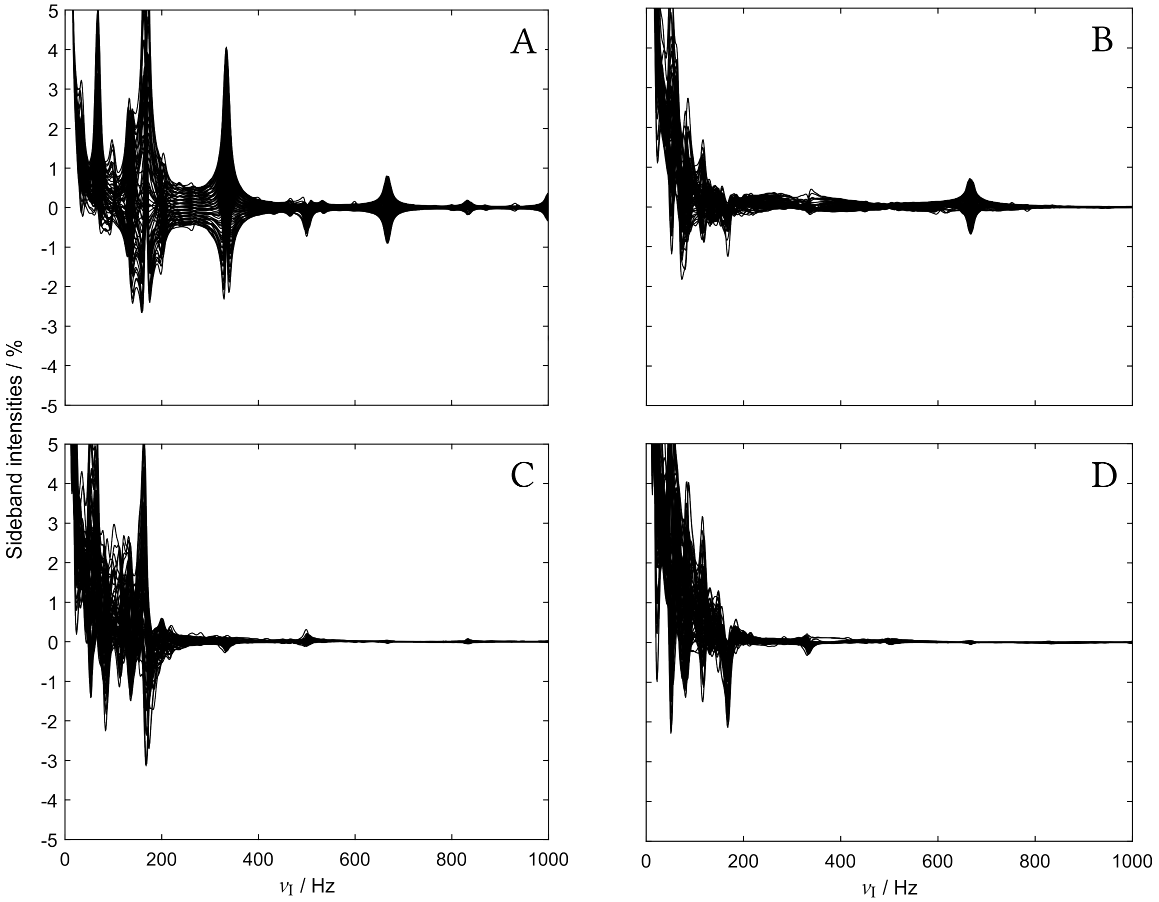

Figure 2.21.: Simulated sideband amplitudes for caWURST-2 bilevel decoupling at $B_{1,\mathrm{RMS}} = 2$ kHz using pulses with T increased to 3 ms ($Q = 1.8$). Sideband profiles are given for a single scan (A), four scans using a $T/2$ (B) and $T/4$ (C) incrementation of the high-power component. 8 scans using a $T/4$ incrementation are depicted in (D). Spectra are overlaid and expanded to 5% of the maximum decoupled center peak intensity across the desired offset range of 40 kHz. Since the sidebands are symmetrically distributed around the center peak, only positive frequencies are plotted. The M4P5 cycle was used throughout.

2.2.2. General approach

Already prior to OCT studies, pulses were known that bypass adiabaticity constraints. The Broadband Inversion Pulses (BIPs) [109] are the only reported pulse shapes that approach the physical limits established by OCT [22, 27]. Whereas BIPs are designed as rather short high-power inversion pulses, RF power-limited BIBOPs might be candidates for building blocks of periodic decoupling sequences. However, the optimal tracking algorithm introduced in section 1.2.5 poses the ultimate means to exploit the flexibility of optimal control algorithms. The application to broadband decoupling as presented in [36] shall be outlined in the following.

The Hamiltonian $\mathcal{H}$ of a heteronuclear spin system under the effect of a decoupling sequence similarly to equation 1.83 contains a drift and a control component with the decoupling sequence being the control part. The drift component of the I spin species which is sampled (see equation 2.1) is now accompanied by the chemical shift of the heteronucleus $\mathcal{H}_\mathrm{S}$. For the sake of clarity, the heteronuclear coupling term $\mathcal{H}_\mathrm{J}$ has been separated from the spin I chemical shift $\mathcal{H}_\mathrm{I}$ to yield

$$\mathcal{H}(t) = \mathcal{H}_\mathrm{I} + \mathcal{H}_\mathrm{S} + \mathcal{H}_\mathrm{J} + \mathcal{H}_\mathrm{RF}^\mathrm{S}(t) \tag{2.18}$$

with the individual components given by

$$\begin{aligned} \mathcal{H}_\mathrm{I} &= 2\pi\nu_\mathrm{I} I_z \\ \mathcal{H}_\mathrm{S} &= 2\pi\nu_\mathrm{S} S_z \\ \mathcal{H}_\mathrm{J} &= \pi J 2 I_z S_z \\ \mathcal{H}_\mathrm{RF}^\mathrm{S}(t) &= 2\pi B_{1,\mathrm{rel}}(u_x(t)S_x + u_y(t)S_y). \end{aligned} \tag{2.19}$$

Given that the I_z operator commutes with all other components of equation 2.18, decoupling performance is independent of the spin I offset and $\mathcal{H}_\mathrm{I}$ can be dropped from equation 2.18 yielding

$$\mathcal{H}(t) = 2\pi\nu_\mathrm{S} S_z + \pi J 2 I_z S_z + 2\pi B_{1,\mathrm{rel}}(u_x(t)S_x + u_y(t)S_y). \tag{2.20}$$

This means spin I can be assumed on resonance and without loss of generality the initial density operator can be assumed to be

$$\rho_0 = I_x. \tag{2.21}$$

Without the influence of the decoupling sequence the evolution of ρ_0 would solely be governed by $\mathcal{H}_\mathrm{J}$ since $\mathcal{H}_\mathrm{S}$ commutes with both $\mathcal{H}_\mathrm{J}$ and ρ_0. The free evolution density operator is given by

$$\rho(t) = I_x \cos(\pi J t) + 2 I_y S_z \sin(\pi J t). \tag{2.22}$$

Sampling the theoretical spin I spectra now requires the evaluation of expectation values of the I_x operator which are given by

$$\langle I_x \rangle (t) = \cos(\pi J t). \tag{2.23}$$

This cosine modulation causes the splitting of resonance lines after FT as decribed in section 2.1.1. Since decoupling means effectively reducing J to zero, perfect decoupling corresponds to equation 2.23 resulting in unity at all times. If the decoupling sequence is organized as outlined in section 1.2.5, the local target states are given by

$$\rho_{\mathrm{F}}(T_n) = I_x \quad \text{for } 0 \leq n \leq N \tag{2.24}$$

which would result in local quality factors according to

$$\phi_n = \langle I_x \,|\rho(T_n)\rangle \,. \tag{2.25}$$

The global quality factor would therefore yield

$$\Phi = \frac{1}{N}\sum_{n=1}^{N}\phi_n = \frac{1}{N}\sum_{n=1}^{N}\langle I_x \,|\rho(T_n)\rangle \,. \tag{2.26}$$

All considerations of section 1.2.5 still apply to the computation of gradients so that the tracking algorithm tailored towards heteronuclear decoupling can be formulated as

1. Make a guess for initial controls $\boldsymbol{u}$.
2. Starting from I_x, compute the forward trajectory ρ_j.
3. Starting from I_x, compute the backward trajectory Λ_j according to

$$\Lambda_{j-1} = \begin{cases} U_j^{\dagger}\Lambda_j U_j & \\ & \text{if } \lfloor j/M \rfloor = \lfloor (j-1)/M \rfloor \\ U_j^{\dagger}\Lambda_j U_j + I_x & \\ & \text{if } \lfloor j/M \rfloor > \lfloor (j-1)/M \rfloor \end{cases} \tag{2.27}$$

4. Evaluate $\nabla_{\boldsymbol{u}}\Phi$ for all possible combinations of parameters and form the mean value.
5. Update the controls according to equation 1.107.
6. Apply RF limits according to amplitude, power or energy.
7. Repeat steps 2-6 until convergence.

Preliminary optimizations using the algorithm above were carried out using the setup proposed in [36] for decoupling using a single scan. The pulse shape was digitized into 5120 increments with variable u_x and u_y amplitudes and 25 μs step size each (T = 128 ms using 10240 variables in total). The period between the individual tracking/detection points ΔT (corresponding to the real dwell time) was set to 1 ms. This results in a rather reduced spectral width of 1 kHz but should allow for a sufficient spin inversion in between detection points if the RF power is sufficient. All optimizations are targeted towards decoupling of spins over an offset range $\Delta\nu_{\mathrm{S}}$ = 40 kHz using J = 140 Hz. $u_{\mathrm{RF}}^{\mathrm{max}}$ was limited at each step to 2 kHz. For the optimizations described in [36], $\Delta\nu_{\mathrm{S}}$ = 1 kHz was discretized in 21 steps. If the same ratio was to be applied here, $N_{\nu_{\mathrm{S}}}$ needs to be scaled up to 801. However, it was found empirically that $N_{\nu_{\mathrm{S}}}$ = 384 can be used without significant losses.

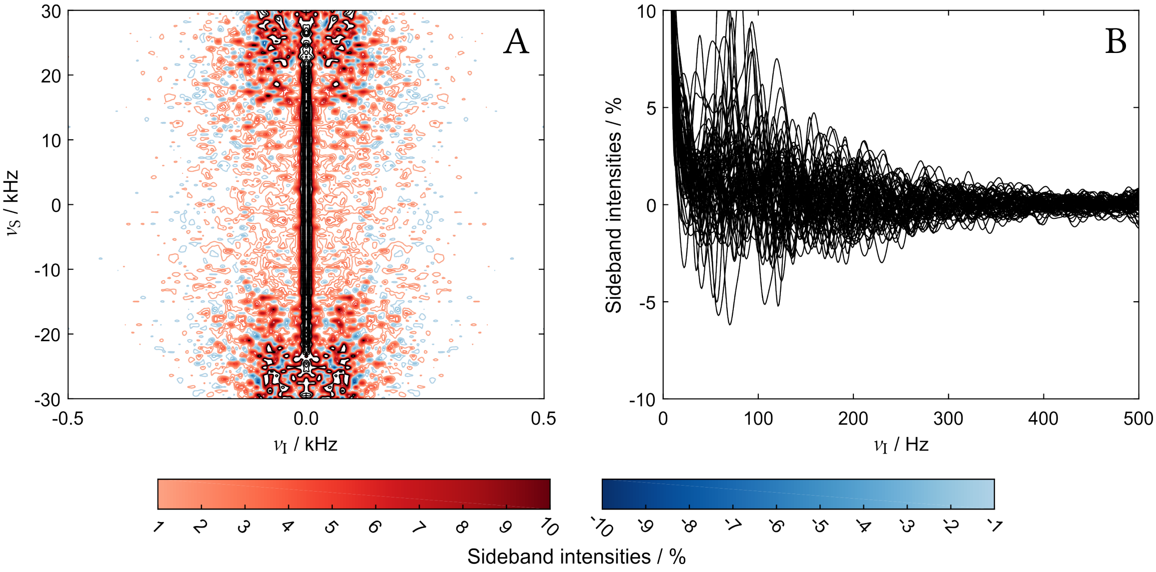

Figure 2.22.: Simulated decoupling profiles using a single optimized pulse sequence obtained by the standard tracking algorithm discussed in this section. The quality factor according to equation 2.26 was used. For the offset profile (A) ten contour levels for positive and negative sidebands were plotted distributed equally between the extreme values of ±1 and ±10% respectively. Peak contours were plotted using ten levels between the maximum sideband and 100% intensity. For the sideband profiles (B) spectra are overlaid and expanded to 10% of the maximum decoupled center peak intensity across the desired offset range of 40 kHz. Since the sidebands are symmetrically distributed around the center peak, only positive frequencies are plotted.

The converged algorithm resulted in a non-repetitive decoupling sequence which was used for the simulations depicted in figure 2.22. The simulated spectra were processed as described in section 2.1.1 apart from zero-filling only to 1024 points since this is sufficient for reasonable resolution at the reduced spectral width. Although the heteronuclear doublet could be collapsed to a single peak, the decoupled signals suffer from massive sidebands exceeding 10% at the edges of the desired offset range and even exceeding 5% below the baseline. In the following, different sources of additional degrees of freedom for the optimizations shall be explored.

2.2.3. Cooperativeness

Multi-scan cooperativeness[39] as discussed in section 1.2.6 was recently filed under a patent[38] where the application to heteronuclear decoupling and sideband suppression was hinted at. Therein, a preliminary quality factor was suggested which was found independently and developed further as a part of this thesis. It is assumed that sideband suppression can be achieved if the quality factors according to equation 1.118 and 2.26 are combined to yield

$$\Phi_{\mathrm{COOP}} = \frac{1}{N}\sum_{n=1}^{N} 1 - \left(1 - \overline{\langle I_x \rangle}(T_n)\right)^2 . \tag{2.28}$$

It can be deduced from figure 1.5 that the offset profiles of excitation pulses become increasingly homogeneous upon increasing N_COOP. However, although the values for $\overline{\langle I_x \rangle}$ are fed back to the individual pulses at each given resonance offset, there is no discernible force that drives the optimization towards low overall deviations from the average of all offsets. The same should apply to equation 2.28 in that $\overline{\langle I_x \rangle}$ for individual detection points T_n is fed back to the individual pulses but not the average over the whole pulse length T (which is given by the quality factor according to equation 2.26 which shall be referred to as Φ_mean in the following). Since these very deviations from Φ_mean are the source of the spurious sidebands, modifications of Φ_COOP shall be explored that allow for explicit sideband suppression.

The first alternative to Φ_COOP under investigation is also derived from equation 1.118. It is based on the assumption that the homogeneous profile of $\overline{\langle I_x \rangle}$ is achieved by demanding the cancellation of $\overline{\langle I_y \rangle}$. Since a single pulse can not fulfill the goals given in the optimization[39], several pulses have to produce a matching set of non-zero values for $\langle I_y \rangle$ in order to cancel it. At the same time, non-zero values for $\langle I_y \rangle$ involve values for $\langle I_x \rangle$ deviating from unity. Therefore, for Φ_COOP to reach high values, values for $\overline{\langle I_x \rangle}$ close to unity are sacrificed for effective nullification of $\overline{\langle I_y \rangle}$. The latter can be achieved rather homogeneously over the desired offset range leaving a homogeneous profile of $\overline{\langle I_x \rangle}$ as a byproduct. From the considerations in section 2.2.2 it becomes apparent that the set of operators involved in an imperfect heteronuclear decoupling scenario is rather limited. According to equation 2.22, the unperturbed evolution of the density operator only involves the I_x and $2I_yS_z$ operators since the influence of $\mathcal{H}_\text{I}$ can be neglected. Given that the decoupling sequence only acts on spin S, it can only convert the $2I_yS_z$ into the $2I_yS_x$ and $2I_yS_y$ operators, which are themselves converted into each other by $\mathcal{H}_\text{S}$. This leaves only four operators to describe the dynamics of a heteronuclear decoupling scenario with three of them needed to be suppressed. The modified Φ_COOP is therefore defined as

$$\Phi_\text{COOP} = \frac{1}{N} \sum_{n=1}^{N} 1 - \left(1 - \overline{\langle I_x \rangle}(T_n)\right)^2 - \overline{\langle 2I_yS_x \rangle}^2(T_n) - \overline{\langle 2I_yS_y \rangle}^2(T_n) - \overline{\langle 2I_yS_z \rangle}^2(T_n). \tag{2.29}$$

Gradients of Φ_COOP with respect to the controls of individual pulses can be obtained by combining equations 1.111 and 1.120 to obtain

$$\begin{aligned}\nabla_{\boldsymbol{u}^{(\mathfrak{m})}} \Phi_\text{COOP} = \frac{1}{N} \sum_{n>l} \frac{2}{N_\text{COOP}} \Big(& \left(1 - \overline{\langle I_x \rangle}(T_n)\right) \cdot \nabla_{\boldsymbol{u}^{(\mathfrak{m})}} \langle I_x \rangle^{(\mathfrak{m})}(T_n) \\ & - \overline{\langle 2I_yS_x \rangle}(T_n) \cdot \nabla_{\boldsymbol{u}^{(\mathfrak{m})}} \langle 2I_yS_x \rangle^{(\mathfrak{m})}(T_n) - \overline{\langle 2I_yS_y \rangle}(T_n) \cdot \nabla_{\boldsymbol{u}^{(\mathfrak{m})}} \langle 2I_yS_y \rangle^{(\mathfrak{m})}(T_n) \\ & - \overline{\langle 2I_yS_z \rangle}(T_n) \cdot \nabla_{\boldsymbol{u}^{(\mathfrak{m})}} \langle 2I_yS_z \rangle^{(\mathfrak{m})}(T_n) \Big). \end{aligned} \tag{2.30}$$

The tracking algorithm needs to be modified in order to concurrently optimize a set of decoupling sequences which compensate their own imperfections by maximizing Φ_COOP according to equation 2.29 which will be referred to as the full penalty approach in the following:

1. Make a guess for initial controls $\boldsymbol{u}^{(\mathfrak{m})}$.

2. Starting from I_x, compute the forward trajectories $\rho_j^{(\mathfrak{m})}$ for all pulses.
3. At each point T_n, compute $\overline{\rho}(T_n)$ and evaluate $\overline{\langle I_x \rangle}(T_n)$, $\overline{\langle 2I_yS_x \rangle}(T_n)$, $\overline{\langle 2I_yS_y \rangle}(T_n)$ and $\overline{\langle 2I_yS_z \rangle}(T_n)$
4. Starting from

$$\Lambda_{NM} = \frac{2}{N_{\mathrm{COOP}}}\left(\left(1 - \overline{\langle I_x \rangle}(T_N)\right) \cdot I_x - \overline{\langle 2I_yS_x \rangle}(T_N) \cdot 2I_yS_x \right. \\ \left. - \overline{\langle 2I_yS_y \rangle}(T_N) \cdot 2I_yS_y - \overline{\langle 2I_yS_z \rangle}(T_N) \cdot 2I_yS_z\right), \quad (2.31)$$

   compute the backward trajectory $\Lambda_j^{(\mathfrak{m})}$ for all pulses according to

$$\Lambda_{j-1}^{(\mathfrak{m})} = \begin{cases} U_j^{(\mathfrak{m})\dagger} \Lambda_j U_j^{(\mathfrak{m})} \\ \qquad\qquad\qquad\qquad \text{if } \lfloor j/M \rfloor = \lfloor (j-1)/M \rfloor \\ U_j^{(\mathfrak{m})\dagger} \Lambda_j U_j^{(\mathfrak{m})} + \dfrac{2}{N_{\mathrm{COOP}}}\left(\left(1 - \overline{\langle I_x \rangle}(T_n)\right) \cdot I_x - \overline{\langle 2I_yS_x \rangle}(T_n) \cdot 2I_yS_x \right. \\ \left. - \overline{\langle 2I_yS_y \rangle}(T_n) \cdot 2I_yS_y - \overline{\langle 2I_yS_z \rangle}(T_n) \cdot 2I_yS_z\right) \\ \qquad\qquad\qquad\qquad \text{if } \lfloor j/M \rfloor > \lfloor (j-1)/M \rfloor \end{cases} \quad (2.32)$$

5. Evaluate $\nabla_{\boldsymbol{u}^{(\mathfrak{m})}}\Phi$ for all possible combinations of parameters and form the mean value.
6. Update the controls according to equation 1.107.
7. Apply RF limits according to amplitude, power or energy.
8. Repeat steps 2-7 until convergence.

Proof-of-principle optimizations with 1000 iterations of the algorithm above were carried out for N_{COOP} = 1-6 using the parameters given in section 2.2.2. The resulting sets of decoupling sequences were subject to simulations which yielded the decoupling profiles depicted in figure 2.23. Theoretical spectra were processed as described for figure 2.22. The simulations clearly show progressive sideband reduction upon increasing N_{COOP}. First, a trend can be observed where sidebands exceeding 10% are pushed outside the desired 40 kHz bandwidth. Secondly, sidebands can in the end be suppressed well below the 5% threshold across the entire bandwidth. This is illustrated in more detail in figure 2.24. The sideband profiles confirm that going from one to two scans, even if individual sidebands may have larger amplitudes than in the single-scan case, a generally lower abundance of sidebands can be observed. However, slightly increased sidebands may occur for several reasons. Incomplete convergence may leave the pulse below its physical potential or an offset may have been sampled in the simulations which suffers decreased fidelity due to a too sparsely sampled grid in the optimization. Nevertheless, since the algorithms aim for an optimal global quality factor, decreased local quality factors can be accepted if this is overcompensated by a better overall average. Further, due to the variety of terms

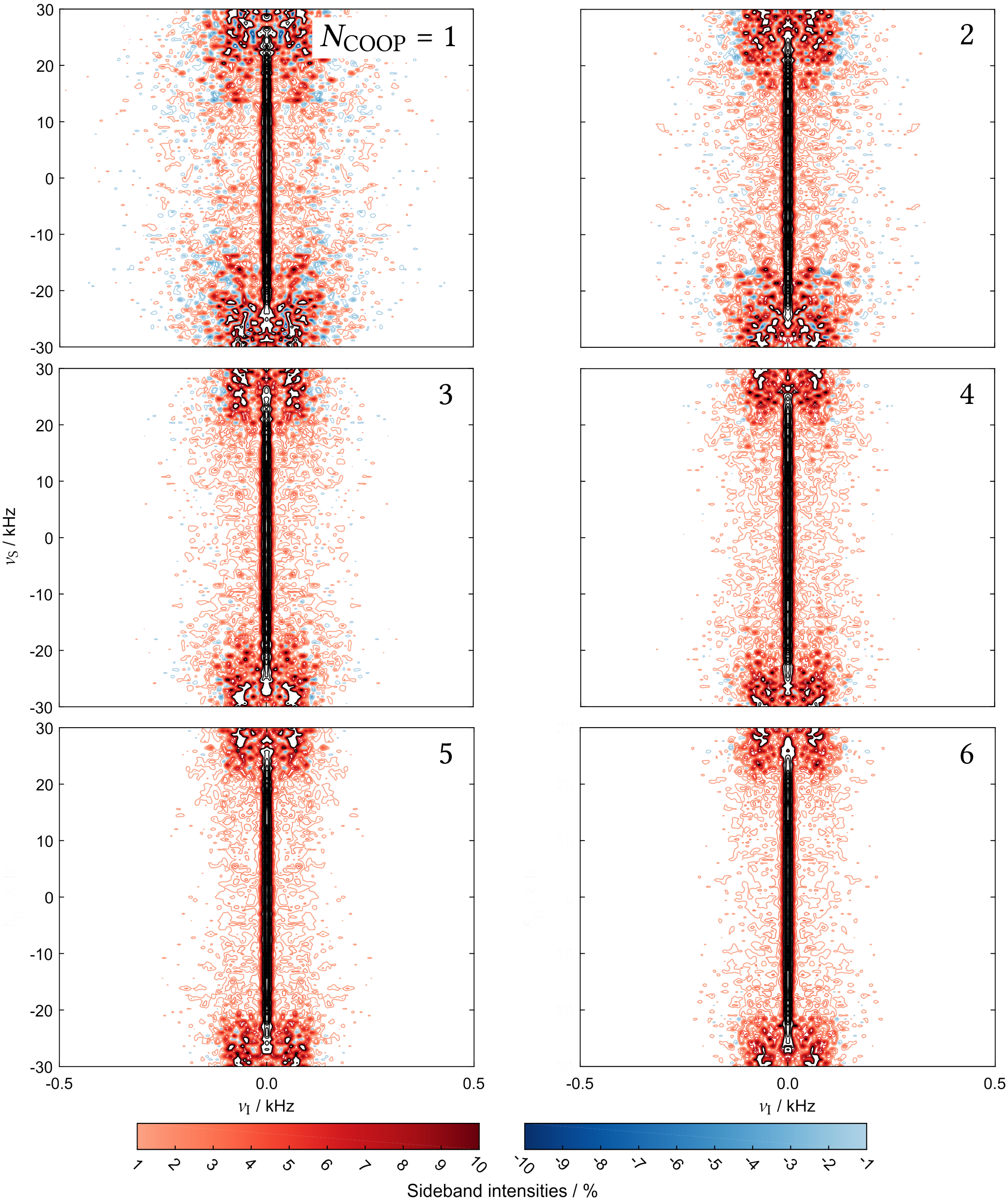

Figure 2.23.: Simulated decoupling profiles using sets of self-compensating decoupling sequences obtained by the modified tracking algorithm. The quality factor according to equation 2.29 was used (full penalty approach). Ten contour levels for positive and negative sidebands were plotted distributed equally between the extreme values of ±1 and ±10% respectively. Peak contours were plotted using ten levels between the maximum sideband and 100% intensity.

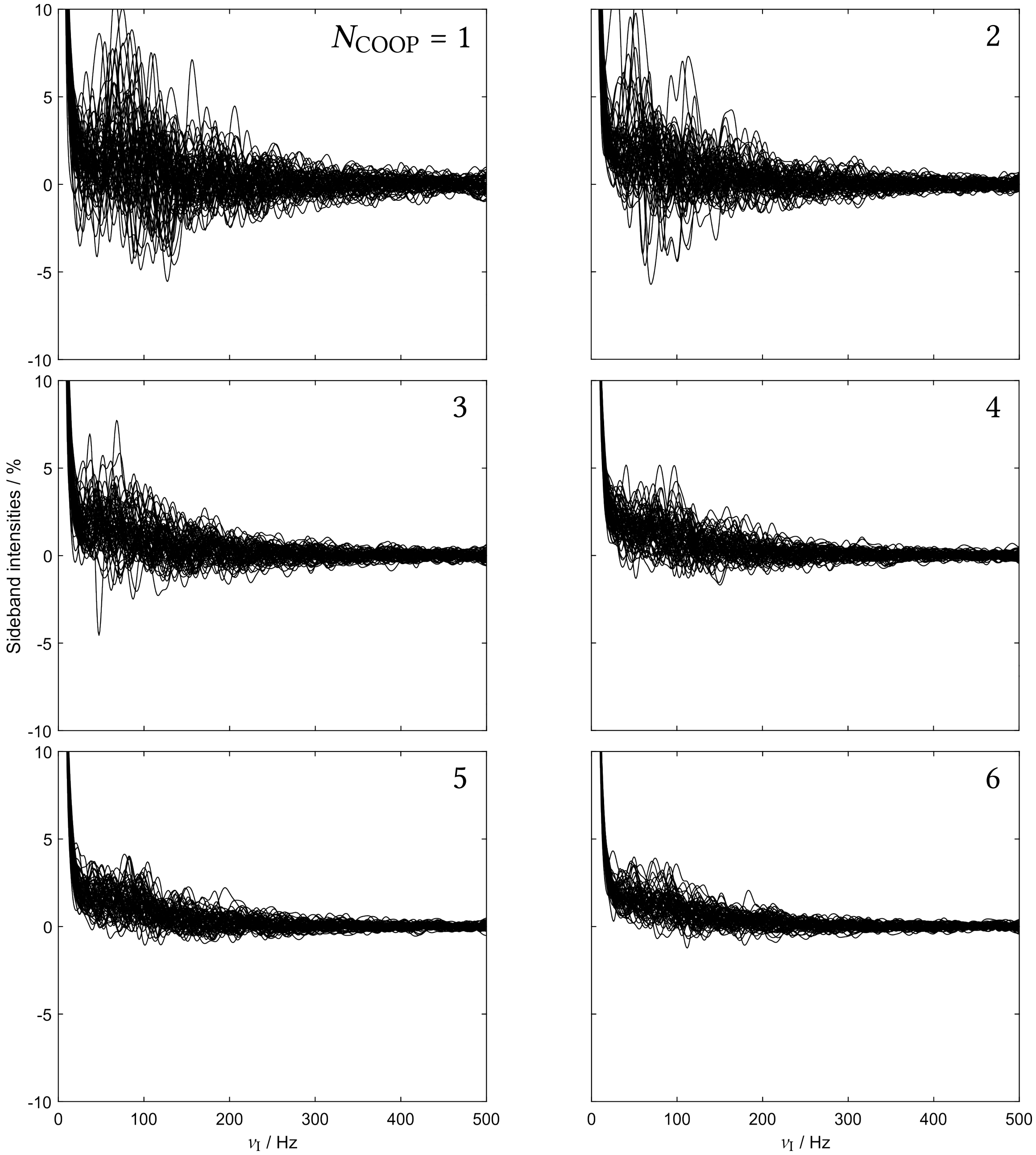

Figure 2.24.: Simulated decoupling profiles using sets of self-compensating decoupling sequences obtained by the modified tracking algorithm. The quality factor according to equation 2.29 was used (full penalty approach). Spectra are overlaid and expanded to 10% of the maximum decoupled center peak intensity across the desired offset range of 40 kHz. Since the sidebands are symmetrically distributed around the center peak, only positive frequencies are plotted.

in the quality factor for the full penalty approach, some terms can be traded off against each other. This could lead to less efficient sideband suppression in favor of higher signal intensity. Apart from that, a higher number of scans indeed corresponds to lower sideband amplitudes.

It can be argued that the sideband canceling mechanism discussed so far is rather implicit. Given that it relies on the $2I_yS_x$, $2I_yS_y$ and $2I_yS_z$ operators, which are not or only indirectly measurable, the focus is not on the main source of sidebands (oscillations of $\overline{\langle I_x \rangle}$). In order to achieve explicit sideband suppression, a suitable quality factor has to include a term that penalizes oscillations of $\overline{\langle I_x \rangle}$. A quality factor according to

$$\Phi_{\text{COOP}} = \frac{1}{N}\sum_{n=1}^{N} 1 - \left(1 - \overline{\langle I_x \rangle}(T_n)\right)^2 - \left(\Phi_{\text{mean}} - \overline{\langle I_x \rangle}(T_n)\right)^2 \tag{2.33}$$

now contains a term that penalizes excursions from the temporal average of the signal (Φ_{mean}, see above). Therefore the second term in equation 2.33 serves as an evaluation of the standard deviation of $\overline{\langle I_x \rangle}$. Ultimately, a low standard deviation of the signal should result in low sideband amplitudes. Therefore, Φ_{COOP} according to equation 2.33 should provide the means of explicit sideband suppression which shall be referred to as the homogenizing approach in the following. Gradients of Φ_{COOP} with respect to the controls of individual pulses can be obtained via

$$\begin{aligned}\nabla_{\boldsymbol{u}^{(\mathfrak{m})}}\Phi_{\text{COOP}} = \frac{1}{N}\sum_{n>l}\frac{2}{N_{\text{COOP}}}\Big(&\left(1 - \overline{\langle I_x \rangle}(T_n)\right)\cdot\nabla_{\boldsymbol{u}^{(\mathfrak{m})}}\langle I_x\rangle^{(\mathfrak{m})}(T_n)\\ &+\left(\Phi_{\text{mean}} - \overline{\langle I_x \rangle}(T_n)\right)\cdot\nabla_{\boldsymbol{u}^{(\mathfrak{m})}}\langle I_x\rangle^{(\mathfrak{m})}(T_n)\Big).\end{aligned} \tag{2.34}$$

It should be noted that Φ_{mean} itself is not subject to the formation of the gradient since it serves as a feedback value and only carries information of the past iteration. The sum within Φ_{mean} should not be mixed with the superordinate sum in equation 2.34 because Φ_{mean} has influence on each local quality factor. This is why equation 2.34 can be further simplified:

$$\nabla_{\boldsymbol{u}^{(\mathfrak{m})}}\Phi_{\text{COOP}} = \frac{1}{N}\sum_{n>l}\frac{2}{N_{\text{COOP}}}\left(1 + \Phi_{\text{mean}} - 2\overline{\langle I_x \rangle}(T_n)\right)\cdot\nabla_{\boldsymbol{u}^{(\mathfrak{m})}}\langle I_x\rangle^{(\mathfrak{m})}(T_n) \tag{2.35}$$

Now it can be directly deduced from equation 2.35 that the homogenizing approach aims at the perfect trade-off between maximum signal intensity and low deviations from Φ_{mean}. The tracking algorithm has to be further modified for the homogenizing approach according to:

1. Make a guess for initial controls $\boldsymbol{u}^{(\mathfrak{m})}$.
2. Starting from I_x, compute the forward trajectories $\rho_j^{(\mathfrak{m})}$ for all pulses.
3. At each point T_n, compute $\overline{\rho}(T_n)$ and evaluate $\overline{\langle I_x \rangle}(T_n)$.
4. Use $\overline{\langle I_x \rangle}(T_n)$ to obtain Φ_{mean} according to equation 2.26.

5. Starting from
$$\Lambda_{NM} = \frac{2}{N_{\text{COOP}}}\Big(1 + \Phi_{\text{mean}} - 2\overline{\langle I_x\rangle}(T_N)\Big)\cdot I_x, \tag{2.36}$$
compute the backward trajectory $\Lambda_j^{(\mathfrak{m})}$ for all pulses according to
$$\Lambda_{j-1}^{(\mathfrak{m})} = \begin{cases} U_j^{(\mathfrak{m})\dagger}\Lambda_j U_j^{(\mathfrak{m})} & \\ & \text{if } \lfloor j/M\rfloor = \lfloor (j-1)/M\rfloor \\ U_j^{(\mathfrak{m})\dagger}\Lambda_j U_j^{(\mathfrak{m})} + \dfrac{2}{N_{\text{COOP}}}\Big(1 + \Phi_{\text{mean}} - 2\overline{\langle I_x\rangle}(T_n)\Big)\cdot I_x & \\ & \text{if } \lfloor j/M\rfloor > \lfloor (j-1)/M\rfloor \end{cases} \tag{2.37}$$

6. Evaluate $\nabla_{\boldsymbol{u}^{(\mathfrak{m})}}\Phi$ for all possible combinations of parameters and form the mean value.

7. Update the controls according to equation 1.107.

8. Apply RF limits according to amplitude, power or energy.

9. Repeat steps 2-8 until convergence.

Another set of proof-of-principle optimizations was carried out for the homogenizing approach which used conditions identical to the full penalty approach. The decoupling profiles yielded by the different decoupling cycles are depicted in figure 2.25. The results for the homogenizing approach show a significant improvement over the full penalty approach. Even using a single scan, there are no sidebands occurring which exceed 10% intensity. In addition, sideband amplitudes well below 5% can be achieved with already four scans using the modified quality factor. It can be observed that using more than four scans, there is only slight further improvement. Nevertheless, it can be stated that the homogenizing approach offers the more promising sideband suppression capabilities. This is confirmed by the sideband profiles given in figure 2.26. It can be seen that the final improvement brought about by the homogenizing approach amounts to about 1% if a full cycle of six decoupling sequences are used. For a quantitative comparison the trend in sideband reduction upon increasing N_{COOP} is illustrated in figure 2.27 by contrasting the maximum observable sideband amplitude for the two approaches and the given number of scans. The result of the sequence individually optimized as a part of section 2.2.2 is given as a reference. It becomes obvious that a reasonable choice of the quality factor alone can result in roughly a factor of two in sideband reduction compared to using the standard Φ_{mean}. Moreover, it can be confirmed now that for each number of scans the full penalty approach is outperformed by the homogenizing approach. However, for both cases there is apparently a single occurrence of increasing sideband amplitudes when N_{COOP} is increased. This is due to singular sidebands at a given value of ν_{S} and ν_{I} which appear for reasons discussed above despite an improved overall average. These situations shall be ameliorated in the following section. The improvement of sideband suppression that can be attributed to cooperativeness can be amounted to a factor between two and three.

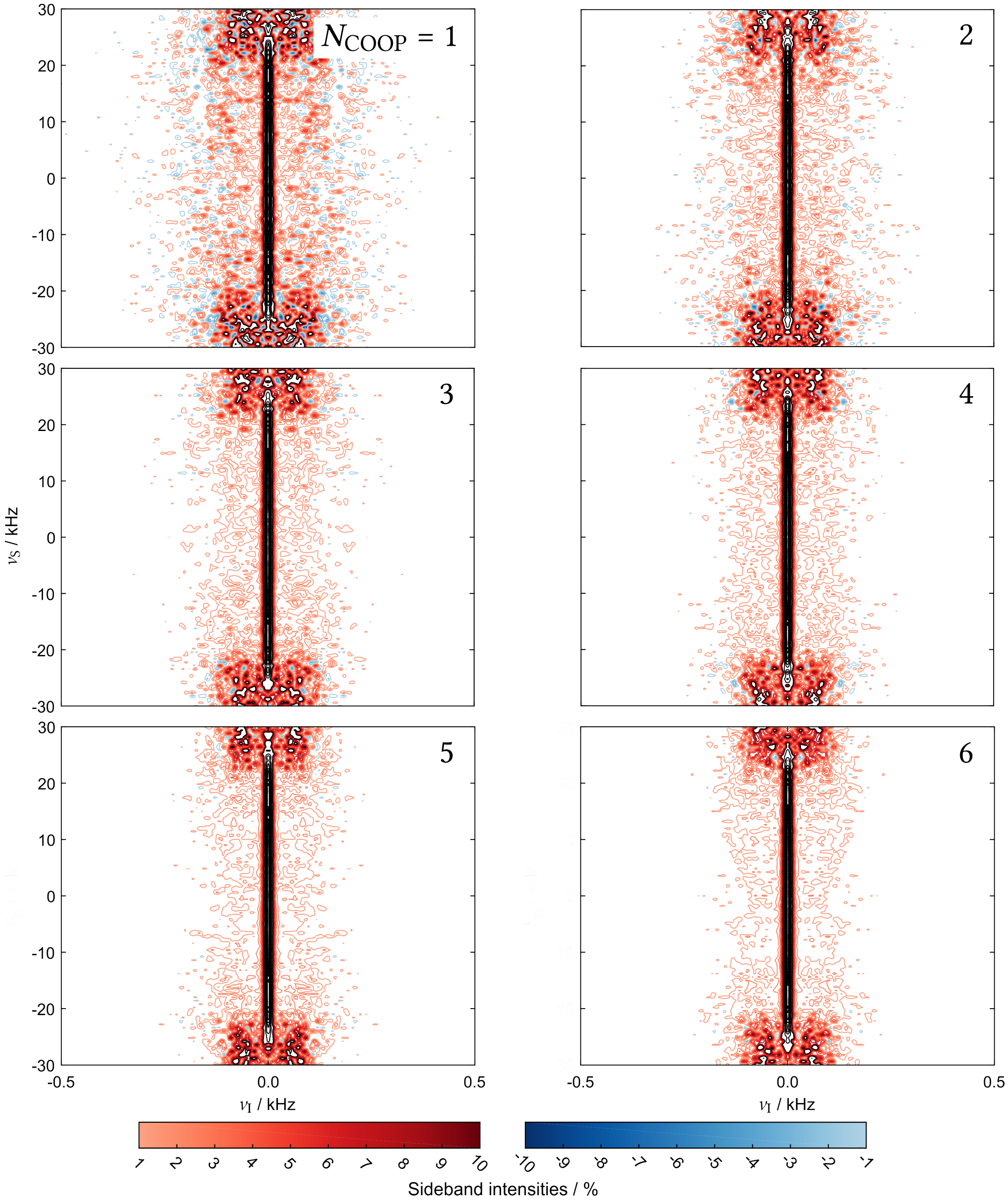

Figure 2.25.: Simulated decoupling profiles using sets of self-compensating decoupling sequences obtained by the modified tracking algorithm. The quality factor according to equation 2.33 was used (homogenizing approach). Ten contour levels for positive and negative sidebands were plotted distributed equally between the extreme values of ±1 and ±10% respectively. Peak contours were plotted using ten levels between the maximum sideband and 100% intensity.

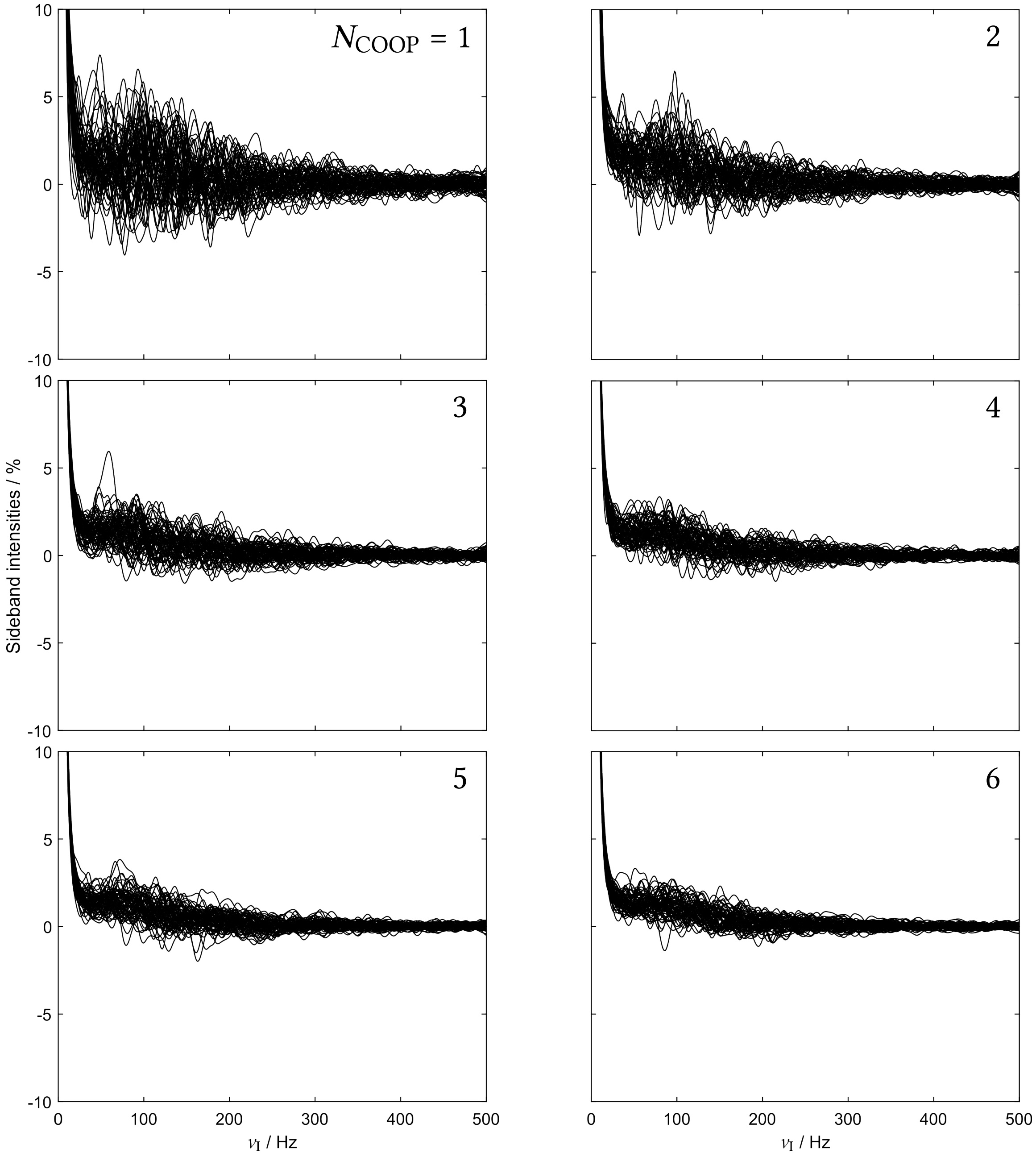

Figure 2.26.: Simulated decoupling profiles using sets of self-compensating decoupling sequences obtained by the modified tracking algorithm. The quality factor according to equation 2.33 was used (homogenizing approach). Spectra are overlaid and expanded to 10% of the maximum decoupled center peak intensity across the desired offset range of 40 kHz. Since the sidebands are symmetrically distributed around the center peak, only positive frequencies are plotted.

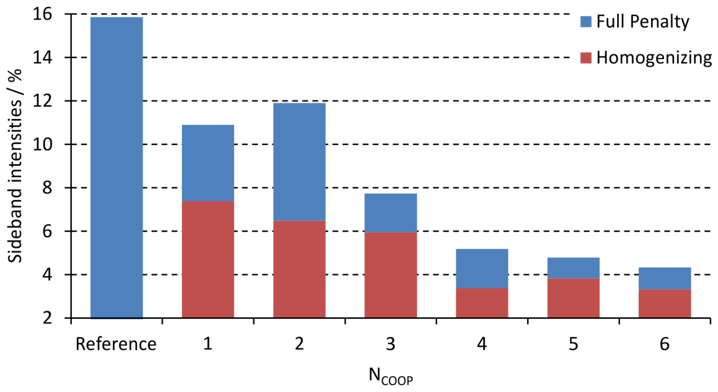

Figure 2.27.: Comparison of the maximum positive sideband amplitudes within the desired offset range $\Delta\nu_S$ = 40 kHz obtained by the sets of decoupling sequences optimized following the full penalty and homogenizing approach described in this section. The reference pulse was optimized as described in section 2.2.2.

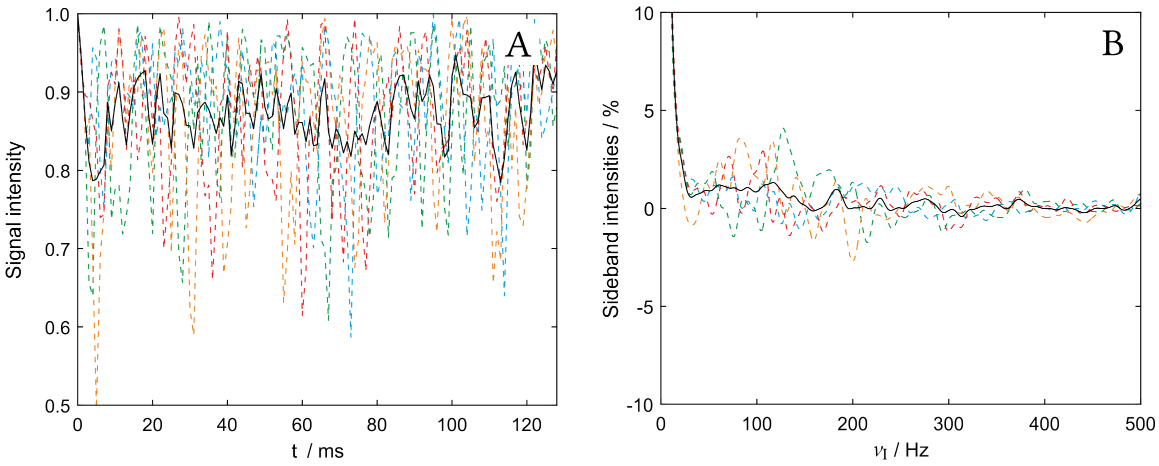

Figure 2.28.: Sideband canceling mechanism of the homogenizing approach illustrated by simulated time- (A) and frequency domain (B) data for four scans (N_{COOP} = 4) with zero decoupler offset (ν_S = 0 Hz). Individual scans are shown as colored dashed lines and the average is shown as a solid black line.

Finally, the mechanism of sideband suppression by the homogenizing approach shall be illustrated for a single value of ν_S using a decoupling cycle consisting of four self-compensating pulse sequences in figure 2.28. Individual scans now reveal massive temporal signal oscillations that would lead to severely high sideband amplitudes after FT. These oscillations are greatly reduced upon averaging so that in most cases a particularly intensive positive sideband is opposed by a negative sideband amplitude in the next scan. Moreover, in contrast to bilevel decoupling, the averaging is effective for the entire FID so that the sideband suppression is not limited to distinct frequencies ν_I. Nonetheless, the results of this section are not yet fully competitive with bilevel decoupling at the given RF constraints but the potential of cooperative decoupling was hinted at.

2.2.4. Optimizations

So far, the limiting factor of the optimizations were the computational resources. The optimization package OCTOPUSSI[51] was designed to (concurrently) optimize pulse shapes acting on two (heteronuclear) coupled spins in Hilbert space. This implies the storage of two pulse shapes and complex-numbered 16-element matrix representations of density operator trajectories. The computational limit using OCTOPUSSI was reached when six pulses with $T = 128$ ms with $\Delta t = 25\ \mu s$ were optimized using u_x and u_y controls which yields a sum of 61440 variables. Conversely, it has been discussed in the previous sections that only four operators are needed to describe a heteronuclear decoupling scenario which facilitates the use of a four-state vector representation of the density operator as an element within a reduced Liouville space[36]. The expectation values of the operators $2I_yS_x$, $2I_yS_y$, $2I_yS_z$ and I_x form the real-valued elements of the reduced state vector given by

$$\hat{\rho}(t_j) = \begin{pmatrix} \langle 2I_yS_x\rangle(t_j) \\ \langle 2I_yS_y\rangle(t_j) \\ \langle 2I_yS_z\rangle(t_j) \\ \langle I_x\rangle(t_j) \end{pmatrix} = \begin{pmatrix} \rho^{2I_yS_x}(t_j) \\ \rho^{2I_yS_y}(t_j) \\ \rho^{2I_yS_z}(t_j) \\ \rho^{I_x}(t_j) \end{pmatrix}. \tag{2.38}$$

Initial and final magnetization I_x are thus written $(0, 0, 0, 1)^{\mathrm{T}}$. Forward and backward trajectories of the density superoperator which are necessary to obtain the gradients for the GRAPE algorithm are defined as

$$\hat{\rho}_j = \hat{U}_j \cdots \hat{U}_1 \hat{\rho}_0 \tag{2.39}$$

and

$$\hat{\lambda}_j = \hat{U}_{j+1}^{\mathrm{T}} \cdots \hat{U}_{\mathrm{N}}^{\mathrm{T}} \hat{\rho}_{\mathrm{F}} \tag{2.40}$$

where $\hat{U}_j$ are the generalized rotation matrices corresponding to the unitary propagators in Hilbert space and $\hat{U}_j^{\mathrm{T}}$ is the transpose of $\hat{U}_j$. The matrix elements of these rotation superoperators are given by explicit scalar functions that no longer involve matrix exponentiation[36]. They are computed according to the following recipe:

$$\begin{aligned}
\hat{U}_{11}(j) &= a_+a_- - b_+b_- - c_+c_- + d_+d_- \\
\hat{U}_{12}(j) &= a_+b_- + b_+a_- + c_+d_- + d_+c_- \\
\hat{U}_{13}(j) &= a_+c_- - b_+d_- + c_+a_- - d_+b_- \\
\hat{U}_{14}(j) &= -a_+d_- - b_+c_- + c_+b_- + d_+a_- \\
\hat{U}_{21}(j) &= a_+b_- + b_+a_- - c_+d_- - d_+c_- \\
\hat{U}_{22}(j) &= -a_+a_- + b_+b_- - c_+c_- + d_+d_- \\
\hat{U}_{23}(j) &= a_+d_- + b_+c_- + c_+b_- + d_+a_- \\
\hat{U}_{24}(j) &= a_+c_- - b_+d_- - c_+a_- + d_+b_- \\
\hat{U}_{31}(j) &= a_+c_- + b_+d_- + c_+a_- + d_+b_- \\
\hat{U}_{32}(j) &= -a_+d_- + b_+c_- + c_+b_- - d_+a_- \\
\hat{U}_{33}(j) &= -a_+a_- - b_+b_- + c_+c_- + d_+d_-
\end{aligned} \tag{2.41}$$

$$\begin{aligned}
\hat{U}_{34}(j) &= -a_+b_- + b_+a_- - c_+d_- + d_+c_- \\
\hat{U}_{41}(j) &= a_+d_- - b_+c_- + c_+b_- - d_+a_- \\
\hat{U}_{42}(j) &= a_+c_- + b_+d_- - c_+a_- - d_+b_- \\
\hat{U}_{43}(j) &= -a_+b_- + b_+a_- + c_+d_- - d_+c_- \\
\hat{U}_{44}(j) &= a_+a_- + b_+b_- + c_+c_- + d_+d_-
\end{aligned} \tag{2.41}$$

The constituents of $\hat{U}_j$ are given by

$$a_\pm = -\frac{B_{1,\mathrm{rel}} \cdot u_x(j)}{\nu_\pm} \cdot \sin(\pi \nu_\pm \Delta t) \tag{2.42}$$

$$b_\pm = -\frac{B_{1,\mathrm{rel}} \cdot u_y(j)}{\nu_\pm} \cdot \sin(\pi \nu_\pm \Delta t) \tag{2.43}$$

$$c_\pm = -\frac{\nu_\mathrm{S} \pm J/2}{\nu_\pm} \cdot \sin(\pi \nu_\pm \Delta t) \tag{2.44}$$

$$d_\pm = \cos(\pi \nu_\pm \Delta t) \tag{2.45}$$

and

$$\nu_\pm = \sqrt{\left(B_{1,\mathrm{rel}} \cdot u_x(t_j)\right)^2 + \left(B_{1,\mathrm{rel}} \cdot u_y(t_j)\right)^2 + \left(\nu_\mathrm{S} \pm J/2\right)^2}. \tag{2.46}$$

In analogy to equation 1.125, gradients of local quality factors ϕ can be obtained to first order via

$$\frac{\partial \phi}{\partial u_x(t_j)} = 2\pi B_{1,\mathrm{rel}} \Delta t \left(\rho_j^{2I_yS_y} \lambda_j^{2I_yS_z} - \rho_j^{2I_yS_z} \lambda_j^{2I_yS_y} \right) \tag{2.47}$$

and

$$\frac{\partial \phi}{\partial u_y(t_j)} = 2\pi B_{1,\mathrm{rel}} \Delta t \left(\rho_j^{2I_yS_z} \lambda_j^{2I_yS_x} - \rho_j^{2I_yS_x} \lambda_j^{2I_yS_z} \right). \tag{2.48}$$

In order to obtain the gradients of Φ_mean in this formalism, equations 2.47 and 2.48 have to be combined with equation 1.111 to yield

$$\frac{\partial \Phi_\mathrm{mean}}{\partial u_x(t_j)} = 2\pi B_{1,\mathrm{rel}} \Delta t \cdot \frac{1}{N} \left(\rho_j^{2I_yS_y} \Lambda_j^{2I_yS_z} - \rho_j^{2I_yS_z} \Lambda_j^{2I_yS_y} \right) \tag{2.49}$$

and

$$\frac{\partial \Phi_\mathrm{mean}}{\partial u_y(t_j)} = 2\pi B_{1,\mathrm{rel}} \Delta t \cdot \frac{1}{N} \left(\rho_j^{2I_yS_z} \Lambda_j^{2I_yS_x} - \rho_j^{2I_yS_x} \Lambda_j^{2I_yS_z} \right). \tag{2.50}$$

As mentioned in section 1.2.8, to exploit the beneficial convergence behavior of second-order update methods, exact gradients are needed. Hence, exact derivatives of $\hat{U}_j$ need to be evaluated which can be done element-wise. All derivatives of the elements given in equation 2.41 can be evaluated using the sum and product rule and boil down to the derivatives of equations 2.42 to 2.45. Here, the derivatives of $c_\pm$ and $d_\pm$ with respect to u_x and u_y only vary in derivatives of $\nu_\pm$. The latter are given by

$$\frac{\partial \nu_\pm}{\partial u_x(t_j)} = \frac{B_{1,\mathrm{rel}}^2 \cdot u_x}{\nu_\pm} \tag{2.51}$$

and

$$\frac{\partial \nu_\pm}{\partial u_y(t_j)} = \frac{B^2_{1,\mathrm{rel}} \cdot u_y}{\nu_\pm} \tag{2.52}$$

so that

$$\frac{\partial d_\pm}{\partial u_k(t_j)} = -\pi \Delta t \frac{\partial \nu_\pm}{\partial u_k(t_j)} \cdot \sin(\pi \nu_\pm \Delta t) \tag{2.53}$$

and

$$\frac{\partial c_\pm}{\partial u_k(t_j)} = \frac{\nu_\mathrm{S} \pm J/2}{\nu_\pm} \cdot \frac{\partial \nu_\pm}{\partial u_k(t_j)} \left(\frac{\sin(\pi \nu_\pm \Delta t)}{\nu_\pm} - \pi \Delta t \cdot \cos(\pi \nu_\pm \Delta t) \right). \tag{2.54}$$

When it comes to $a_\pm$ and $b_\pm$, the derivatives with respect to u_x and u_y vary significantly so that

$$\frac{\partial a_\pm}{\partial u_x(t_j)} = \frac{B_{1,\mathrm{rel}}}{\nu_\pm} \left(\left[\frac{u_x}{\nu_\pm} \cdot \frac{\partial \nu_\pm}{\partial u_x(t_j)} - 1 \right] \cdot \sin(\pi \nu_\pm \Delta t) - \pi u_x \Delta t \frac{\partial \nu_\pm}{\partial u_x(t_j)} \cdot \cos(\pi \nu_\pm \Delta t) \right) \tag{2.55}$$

and

$$\frac{\partial a_\pm}{\partial u_y(t_j)} = \frac{B_{1,\mathrm{rel}} \cdot u_x}{\nu_\pm} \cdot \frac{\partial \nu_\pm}{\partial u_y(t_j)} \left(\frac{\sin(\pi \nu_\pm \Delta t)}{\nu_\pm} - \pi \Delta t \cdot \cos(\pi \nu_\pm \Delta t) \right). \tag{2.56}$$

This can be transferred to $b_\pm$ where

$$\frac{\partial b_\pm}{\partial u_x(t_j)} = \frac{B_{1,\mathrm{rel}} \cdot u_y}{\nu_\pm} \cdot \frac{\partial \nu_\pm}{\partial u_x(t_j)} \left(\frac{\sin(\pi \nu_\pm \Delta t)}{\nu_\pm} - \pi \Delta t \cdot \cos(\pi \nu_\pm \Delta t) \right) \tag{2.57}$$

and

$$\frac{\partial b_\pm}{\partial u_y(t_j)} = \frac{B_{1,\mathrm{rel}}}{\nu_\pm} \left(\left[\frac{u_y}{\nu_\pm} \cdot \frac{\partial \nu_\pm}{\partial u_y(t_j)} - 1 \right] \cdot \sin(\pi \nu_\pm \Delta t) - \pi u_y \Delta t \frac{\partial \nu_\pm}{\partial u_y(t_j)} \cdot \cos(\pi \nu_\pm \Delta t) \right). \tag{2.58}$$

These newly derived equations can be plugged into the recipe for $\hat{U}_j$ to obtain exact gradients for Φ_mean via

$$\frac{\partial \Phi_\mathrm{mean}}{\partial u_k(t_j)} = \frac{1}{N} \left\langle \hat{\Lambda}_j \middle| \frac{\partial \hat{U}_j}{\partial u_k(t_j)} \hat{\rho}_{j-1} \right\rangle. \tag{2.59}$$

Gradients $\nabla_{\boldsymbol{u}} \Phi$ can be benchmarked against a finite difference approximation $\nabla^\mathrm{FD}_{\boldsymbol{u}} \Phi$ (see equation 1.96) by evaluating

$$\sigma_\nabla = \left| 1 - \frac{\nabla^\mathrm{FD}_{\boldsymbol{u}} \Phi}{\nabla_{\boldsymbol{u}} \Phi} \right| \tag{2.60}$$

as a function of Δu. This difference was evaluated for a randomly generated pulse using gradients according to equations 2.49 and 2.50 (first order approximate) as well as equations 2.51 to 2.59 (exact). Further, a single pulse optimized comparable to as given in [36] (T = 128 ms, Δt = 25 μs, ΔT = 1 ms, J = 140 Hz, $u^\mathrm{max}_\mathrm{RF}$ = 500 Hz, $\Delta \nu_\mathrm{S}$ = 1 kHz, N_{ν_S} = 21) was also analyzed accordingly. The converged pulse yielded $\Phi_\mathrm{mean} = 0.956$ whereas the random pulse yields $\Phi_\mathrm{mean} = -0.009$. The resulting gradient errors are depicted in figure 2.29. In general, the gradient error should decrease as Δu decreases, since the finite difference approximation more and more approaches an exact gradient. Conversely, the curves

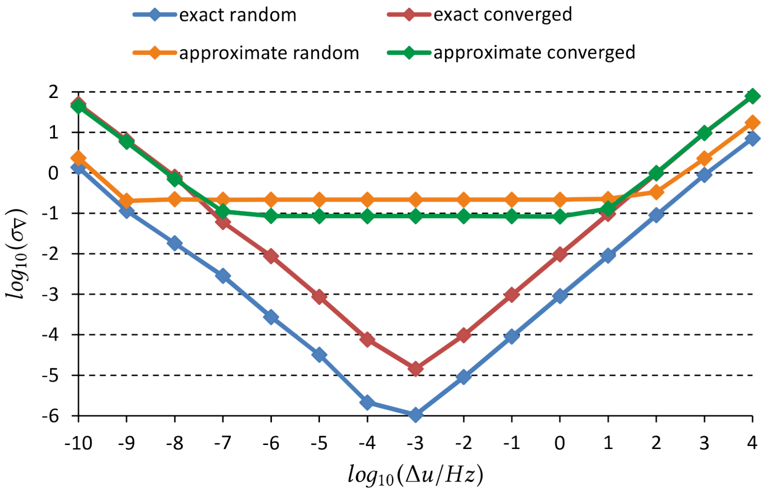

Figure 2.29.: Benchmark of first order approximate and exact gradients for Φ_{mean} against a finite difference approximation according to equation 2.60. Both gradients were applied to a randomly generated pulse ($\Phi_{\text{mean}} = -0.009$) as well as a converged sequence ($\Phi_{\text{mean}} = 0.956$).

for the exact gradients in figure 2.29 show a distinct dip. This is due to a threshold in machine number precision. At some point, the change of control amplitudes Δu becomes too insignificant to cause a substantial change in the quality factors so that the finite differences in equation 1.96 become very small. In terms of machine number precision, there are increasingly less places after the decimal point which can contribute to a meaningful difference. This source of numerical noise causes the gradient error to increase if Δu decreases below a certain threshold. The dip is more pronounced for the randomly generated pulse since closer to the optimum the same change in control amplitude causes less response in fidelity. At the same time, a $\Phi_{\text{mean}} > 0.9$ also takes away one significant digit for the finite difference. For each case of the first order approximate gradient the gradient accuracy is by orders of magnitude worse and shows a flat region where the exact gradients show the dip.

With access to exact gradients in the reduced state space formalism, a feasibility study of optimal single and cycles of decoupling sequences is now possible. Given that there is no more need to store complex numbers and far less arrays of matrices have to be stored, the newly available memory can be invested in a more finely digitized time grid of the pulse shapes. In addition, depending on the particular optimization problem and whether the computation is performed in parallel or not, a gain in speed between 5 and 20 can be accomplished (see appendix figure A.1). To give an overview about the computational resources and to be able to correlate the feasibility of optimizations with the hardware configuration, the available machines for this work are listed in table 2.6. Prior to a systematic study of the problem outlined in section 2.2.1, possibilities to boost convergence were explored. The most important second order update methods discussed in section 1.2.8 assume at least locally quadratic behavior of the quality factor landscape. Since this assumption can not be made a priori, a periodical refreshment of the CGs comparable to the limited gradient history in the L-BFGS update has been tested on the optimization procedure given in section 2.2.2. The CG reinitialization can be performed

Pet name	CPU vendor	CPU model	Clock frequency / GHz	Cores	CPU cache / MHz
Ork	Intel®	Pentium® 4	2.66	1	0.5
Sodom	AMD	Athlon™MP 2800+	2.13	2	0.5
Goblin	AMD	Athlon™II X2 240e	2.8	2	1
Uff	Intel®	Core™2 Quad Q8200	2.33	4	2
Cybershot	Intel®	Core™2 Quad Q6600	2.4	4	4
Sandstone	Intel®	Core™2 Quad Q6600	2.4	4	4
Server	Intel®	Core™2 Quad Q9650	3	4	6
Wanderlust	Intel®	Core™i7 950	3.07	4	8
JP	Intel®	Xeon®E5-2470	2.3	16	20

Table 2.6.: Overview of the computational resources available in this thesis. All machines are Linux-based except for Goblin, which is a Windows® workstation which was not used for optimizing pulse sequences.

when a convergence criterion is met to avert premature termination or at fixed intervals as depicted in figure 2.30. Here the quality factor as a function of the iteration number is given as an error functional (deviation from unity) on a logarithmic scale which leads to this representation infamously being called spaghetti plots. For ten different starting pulses spaghetti plots are given for CG reinitialization after 500, 250, 100 and 50 iterations as well as no refreshment. Each optimization ran for 1000 iterations. It can clearly be seen that without reinitialization, after 1000 iterations almost full convergence is reached whereas each additional instance of CG refreshment results in consecutively improved overall convergence rates. It can be deduced from the slope at the final iteration that further improvements can be expected for CG reinitialization after 50 iterations which was found to be an optimal value for this problem. Resetting the CG trajectory after 25 and 10 iterations leads to impaired convergence (see appendix figure A.2). Looking at the spread of results, the variance within one group of optimizations is markedly marginal leading to hardly any overlap between the different groups. Therefore it can be stated that CG reinitialization at a given interval allows access to a whole set of new (or better) solutions which are out of reach for a conventional unperturbed search.

To affirm the results obtained so far, a series of optimizations was performed to find the best possible individual decoupling sequence. For a single sequence, the smallest possible digitization Δt was found to be 2 μs which was still feasible on Ork on a single CPU as well on Uff in parallel. For $T = 128\ ms$ this amounts to 128000 variables. Ten optimizations with 1000 iterations each were performed using both Φ_{mean} and Φ_{COOP} (homogenizing approach) as a quality factor for Δt = 25, 20, 10, 5, 4 and 2 μs. Further, the effect of applying and omitting CG reinitialization after 50 iterations was examined for each setting so that a total of 240 optimizations contribute to this study. In order to provide a more reasonable spectral width, ΔT was reduced to 100 μs. Otherwise, all parameters were kept the same

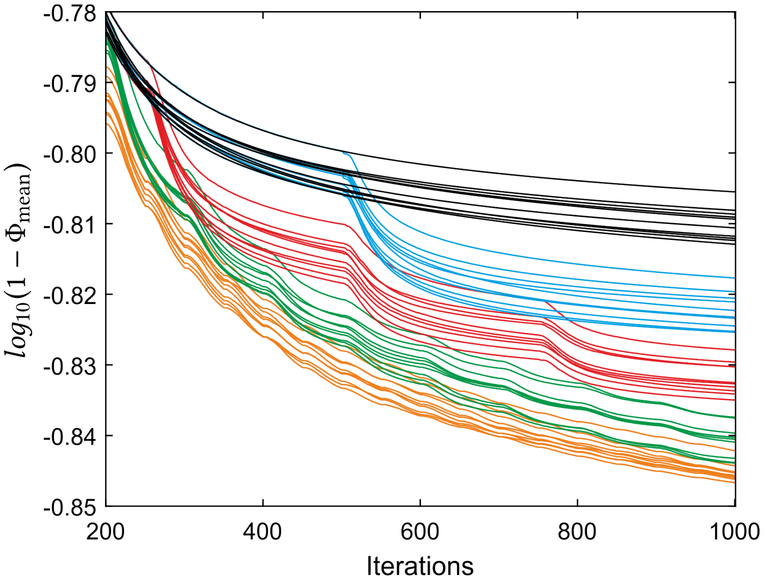

Figure 2.30.: Convergence benchmark (spaghetti plots) for different frequencies of CG reinitialization during optimizations of pulse sequences as described in section 2.2.2. The CG trajectory was refreshed after 500 (blue), 250 (red), 100 (green) and 50 (orange) and compared to the reference (black). The plot was expanded to the region with the most significant differences.

as described in the previous sections. The decoupling sequences thus obtained were analyzed with respect to the maximum positive and negative as well as the root mean square (RMS) sideband amplitudes within the desired offset range $\Delta\nu_S$ = 40 kHz. For each digitization, the average sideband amplitudes of the four possible settings are illustrated in figure 2.31. All three modes of evaluation share common trends. It is globally affirmed that the homogenizing approach provides reduced sideband amplitudes compared to relying on Φ_{mean} alone. In addition, CG reinitialization proves beneficial in each case so that further sideband suppression can be achieved compared to using no convergence boost. The quality factor landscape is thus seemingly not locally quadratic. It can be observed that there is no significant improvement beneath 5 μs. Therefore it can be assumed that the physical limits are approached rather than a speed limit in terms of phase modulation due to the coarse digitization. In particular for cases where no CG reinitialization is applied there are instances where the error bars or even the mean values indicate that the sideband amplitudes increase for a finer digitization. This could be attributed to the convergence behavior which is illustrated for the case of Φ_{COOP} and CG reinitialization in figure 2.32. Two influences can be deduced from the two subplots. First, at the initial steps a finer digitization results in slightly impaired convergence due to a larger space of possibilities given that there are more variables (there is only one outlier for Δt = 2 μs with drastically faster convergence but with a worse result than the rest of the set). This will later largely be compensated for by the fact that overall better solutions can be achieved which leads to the sets of Δt < 20 μs to overtake the optimizations with a more coarse time grid after about 50 iterations. After about 100 iterations, the sets of Δt < 10 μs overtake the latter. Secondly, the spread between the individual sets of optimizations still increases between iteration

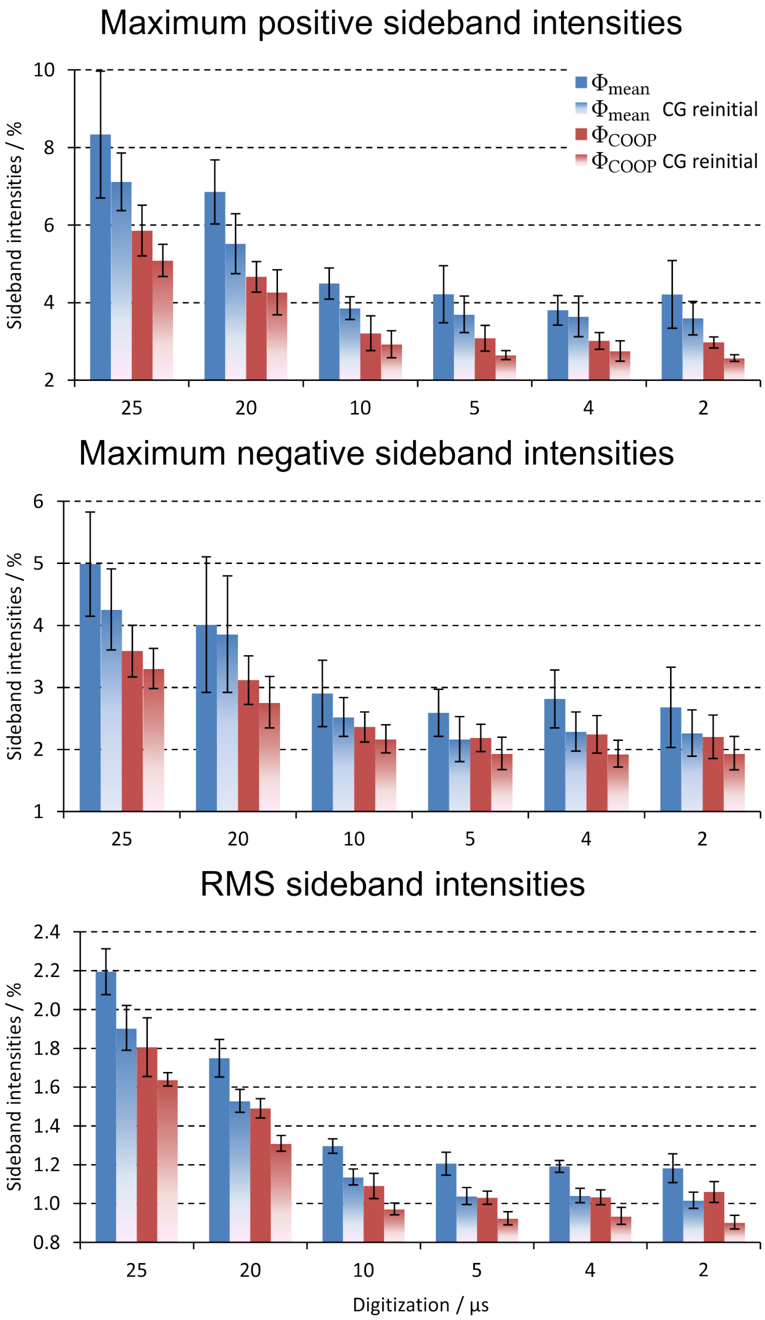

Figure 2.31.: Sideband statistics for individual decoupling sequences with varying digitization. Sideband amplitudes are given for Φ_{mean} and Φ_{COOP} (homogenizing approach) as well as with and without CG reinitialization. The bars indicate the mean value and error bars correspond to the standard deviation. The legend applies to all graphs.

200 and 1000 so that the state of convergence is not guaranteed to be reached within the frame of these optimizations, which can lead to occasionally increased sidebands for a finer digitization. These fluctuations are almost exclusively observed when the positive and negative sideband amplitudes are evaluated. The trend can be rectified if the sideband amplitudes are averaged over $\Delta\nu_{\text{S}}$ at each frequency ν_{I} within the observed window of

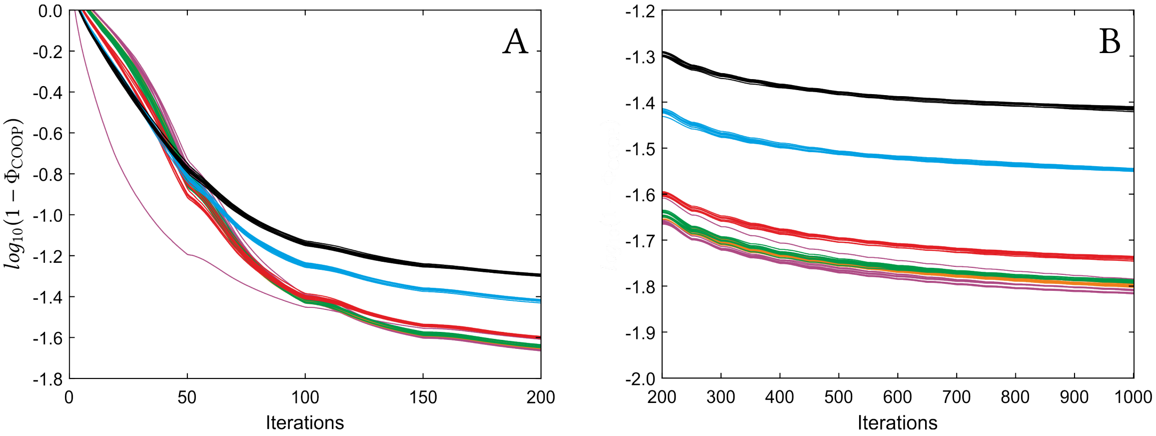

Figure 2.32.: Spaghetti plots for different digitizations of pulse shapes using Φ_{COOP} and CG reinitialization. Optimizations were logged for Δt = 25 (black), 20 (blue), 10 (red), 5 (green), 4 (orange) and 2 μs (purple). The plots were expanded to bring the regions of the initial 200 (A) and the final 800 iterations (B) into focus.

1 kHz. Although the RMS sideband intensities carry less physical meaning, they appear to confirm the statements derived from the data obtained so far. Although the RMS sidebands can be suppressed below 1%, the real sidebands which would be apparent in the measured spectra would still be in range of 2-3%. The decoupling sequences obtained in this part of the study are therefore only on the cusp of being competitive with bilevel decoupling.

In the second part of the study, COOP decoupling sequences were optimized to find the best possible tradeoff between N_{COOP} and Δt with regard to the computational resources given in table 2.6. The most exhaustive combinations which could be achieved were $N_{\text{COOP}} = 6$ for $\Delta t = 10\ \mu s$ (153600 variables), $N_{\text{COOP}} = 4$ for $\Delta t = 5\ \mu s$ (204800 variables) and $N_{\text{COOP}} = 3$ for $\Delta t = 4\ \mu s$ (192000 variables). These optimizations were only feasible on Wanderlust and JP. The 256000 variables necessary for $N_{\text{COOP}} = 2$ and $\Delta t = 2\ \mu s$ could not be handled on any of the available machines. Again, ten optimizations were carried out until the maximum ratio between N_{COOP} and Δt was reached for every digitization using CG reinitialization after every 50 of the 1000 iterations. The resulting cycles of decoupling sequences were analyzed according to figure 2.31 and compared with individual sequences which is shown in figure 2.33. Here, an increase in N_{COOP} consistently provides an improvement in the sideband suppression capabilities of the decoupling cycle at a given digitization for all three modes of evaluation. Most strikingly, decoupling cycles with a rather coarse digitization but higher number of pulses can outperform individual pulses with a finer digitization, which can be understood quantitatively be evaluating the ratios $N_{\text{COOP}}/\Delta t$. This quotient can be imagined as a pseudo-digitization which can be inversely correlated with the degrees of freedom for the optimization. For the ratios given above it equates from coarse to fine to 1.67, 1.34 and 1.25 for 153600, 192000 and 204800 variables, respectively. This can in parts explain the drastic improvements of COOP cycles over individual pulses with $\Delta t = 2\ \mu s$ as well as allow for a guess which setting may yield the optimal result. Indeed, the three sets of decoupling sequences only vary by nuances in terms of the resulting sideband amplitudes. However, by absolute numbers $N_{\text{COOP}} = 6$ for

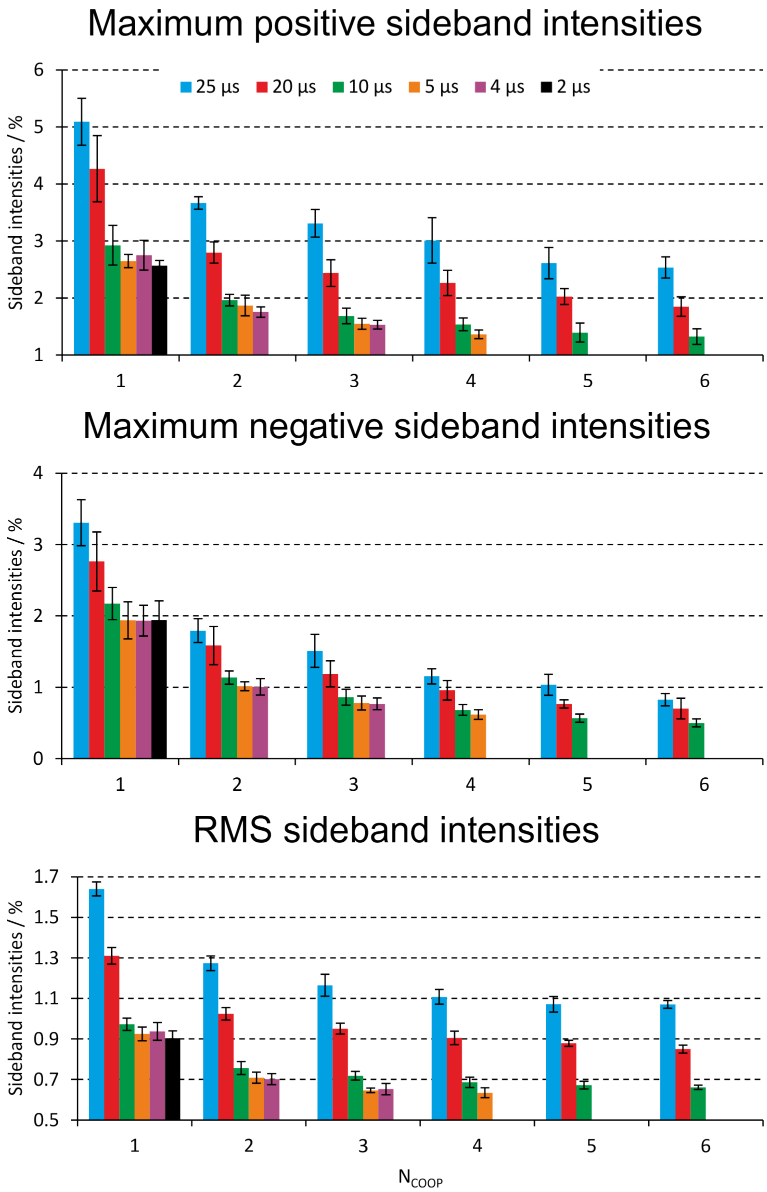

Figure 2.33.: Sideband statistics for COOP decoupling sequences with varying ratios of N_{COOP} and the digitization Δt. Φ_{COOP} (homogenizing approach) and CG reinitialization after 50 iterations were used for all optimizations. The bars indicate average sideband amplitudes of ten optimizations and error bars denote the standard deviation. The legend applies to all graphs.

$\Delta t = 10\ \mu s$ and $N_{\text{COOP}} = 4$ for $\Delta t = 5\ \mu s$ offer a slight advantage with the latter providing the lowest RMS sideband intensities. At best, average sideband amplitudes of about 0.6% with apparent maximum sidebands of 1.5% can be achieved so that $N_{\text{COOP}} = 4$ and $\Delta t = 5\ \mu s$ is chosen to be developed further in the following sections since it not only poses the most promising but also the most reasonable and fair comparison to the bilevel implementation discussed in section 2.2.1.

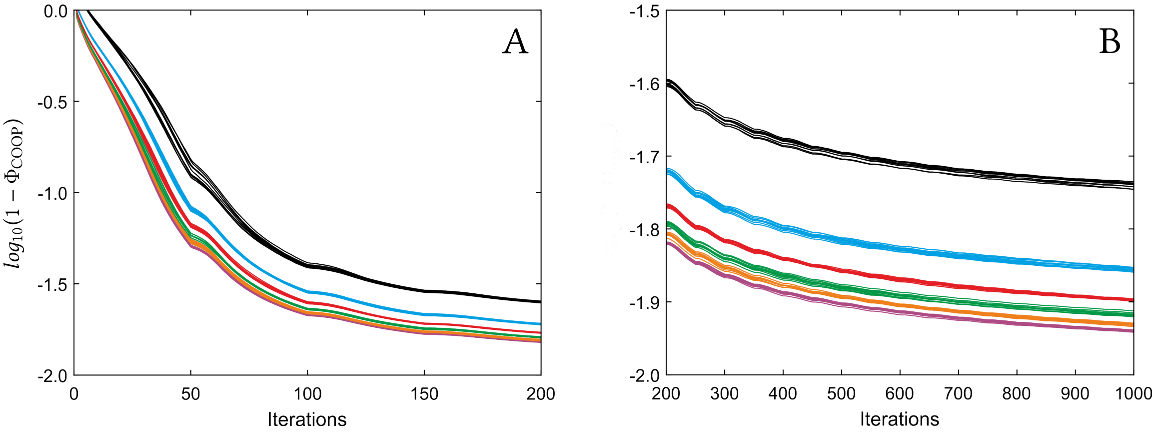

Figure 2.34.: Spaghetti plots for different COOP decoupling sequences using the homogenizing approach and CG reinitialization. Optimizations were logged for Δt = 10 μs and N_{COOP} = 1 (black), 2 (blue), 3 (red), 4 (green), 5 (orange) and 6 (purple). The plots were expanded to bring the regions of the initial 200 (A) and the final 800 iterations (B) into focus.

Cooperativeness is also reflected in the convergence behavior. This is illustrated for Δt = 10 μs going from N_{COOP} = 1 to 6 in figure 2.34. In contrast to figure 2.32, already from the initial state of the optimizations, cycles with more pulses (and therefore more degrees of freedom) show improved convergence and fidelities compared to individual pulses or cycles with fewer members. This is due to fact that the average trajectory has the same complexity for each value of N_{COOP} given that the additional degrees of freedom are condensed in the same increment. This is why at each step the available solutions improve with increasing N_{COOP}. Moreover, in the later stages of the optimizations, the spread between the different sets remains rather constant so that it can be assumed that all sets of optimizations reach a similar state of convergence.

2.2.5. The BROCODE

Now the search for the best possible comparison to the bilevel implementation discussed in section 2.2.1 is going to be further refined. This section therefore solely focuses on cycles of decoupling sequences with Δt = 5 μs and N_{COOP} = 1, 2 and 4. From the sets optimized so far, the best candidate in terms of the value of Φ_{COOP} was chosen to be optimized until full convergence was reached. The dwell time ΔT was set to be equal to Δt just as proposed for the BUSS pulse[107]. This practically demands a refocusing of the coupling evolution after each of the 5 μs increments. Although this is physically impossible, the algorithm will be forced to find a solution that approximates the demanded behavior to the best of its capabilities. In practice, performance in terms of continuous decoupling throughout the grid was already generally satisfactory for all pulses which were optimized for Δt = 100 μs beforehand. Thus, a sufficient robustness against different dwell times can be expected. The offset grid was discretized in 501 increments rather than 384 to make sure that the on resonance case is sampled as well as spurious oscillations in the offset behavior of the sequences are avoided. To make sure that the pulse sequences make use of the available $u_{\mathrm{RF}}^{\max} = 2$ kHz at each increment, the individual control amplitudes were adjusted to the maximum value after each iteration according to equation 1.150. CG reinitialization was only applied when the difference in Φ_{COOP} between two iterations was below 10^{-7}. Convergence in each case was generally reached within 10000 iterations. Simulated decoupling profiles are given in figure 2.35. Simulation parameters were chosen as in figures 2.14 and 2.17 to be set up for a later comparison with experiments. The profiles clearly show a reduction in maximum sideband intensities from about 3% to below 2% going from $N_{\mathrm{COOP}} = 1$ to 4. However, the average 1.5% sideband amplitudes given in figure 2.33 could not be retained. On the one hand, given that Φ_{COOP} has multiple terms, it is not guaranteed that the pulse sequences with the highest numerical quality factor provide the lowest sideband amplitudes. On the other hand the offset grid was more dense than for the preliminary optimizations in section 2.2.4, so that the fidelity at some offsets might slightly suffer from the fact that individual frequencies which were off the grid before have to be significantly improved in order to yield a more homogeneous broadband behavior for the new grid.

Although the sequences obtained so far are already competitive with bilevel decoupling, there are still degrees of freedom available to be exploited. In a final set of optimizations, RF amplitude modulation was allowed by restricting the overall RF power according to equation 1.153 to ensure that $B_{1,\mathrm{RMS}} = 2$ kHz is not exceeded. Sets of 10 optimizations were carried out for $N_{\mathrm{COOP}} = 1$, 2 and 4 using $\Delta t = 5\ \mu s$. Continuous decoupling was demanded throughout all shapes. 384 equally spaced checks across the offset grid with $\Delta \nu_{\mathrm{S}} = 40$ kHz were used and CG reinitialization was applied after every 50 of the initial 1000 iterations. Subsequently, the best candidate according to the value of Φ_{COOP} was chosen for further optimizing with 501 offset checks and resetting the CG trajectory only when the change in Φ_{COOP} between two iterations was less than 10^{-7}. The converged algorithm resulted in a family of self-compensating decoupling sequences with the best performance achieved in this work. Simulations and experiments on a sample of ^{13}C-labeled methanol were performed according to the protocol used for figures 2.14 and 2.17. Decoupling profiles are given in figure 2.36. It is easily recognizable that allowing for amplitude modulation alone provides a boost in sideband reduction comparable to cooperativeness. Upon increasing N_{COOP} up to 4, sidebands can with few exceptions be suppressed down to 0.5%. The general sideband pattern of the simulations can be reproduced rather reasonably in the experiments. Apparently the differences seem to focus very close to the center peak. The sideband profiles given in figure 2.37 confirm that already a single RF power-limited decoupling sequence is competitive with a cycle of four purely phase-modulated sequences. Differences between simulations and experiments entail a signal systematically appearing at about 70 Hz right of the center peak. This peak appears throughout all experiments and can be attributed to an impurity in the purchased methanol which was not further purified. Further, it appears that at a specific range of frequencies (namely right of the impurity signal and up to 500 Hz), sideband intensities and the overall spread from maximum positive to maximum negative sideband amplitudes is smaller in the experiments than predicted by the simulations. At the same time, at frequencies left of the impurity signal (maybe due to it) the sideband intensities exceed those of the simulations. These deviations amount to 0.1 to 0.4% of absolute sideband intensity so that the spread between positive and negative sidebands varies by up to 0.5%. Sources of systematic errors may be RF

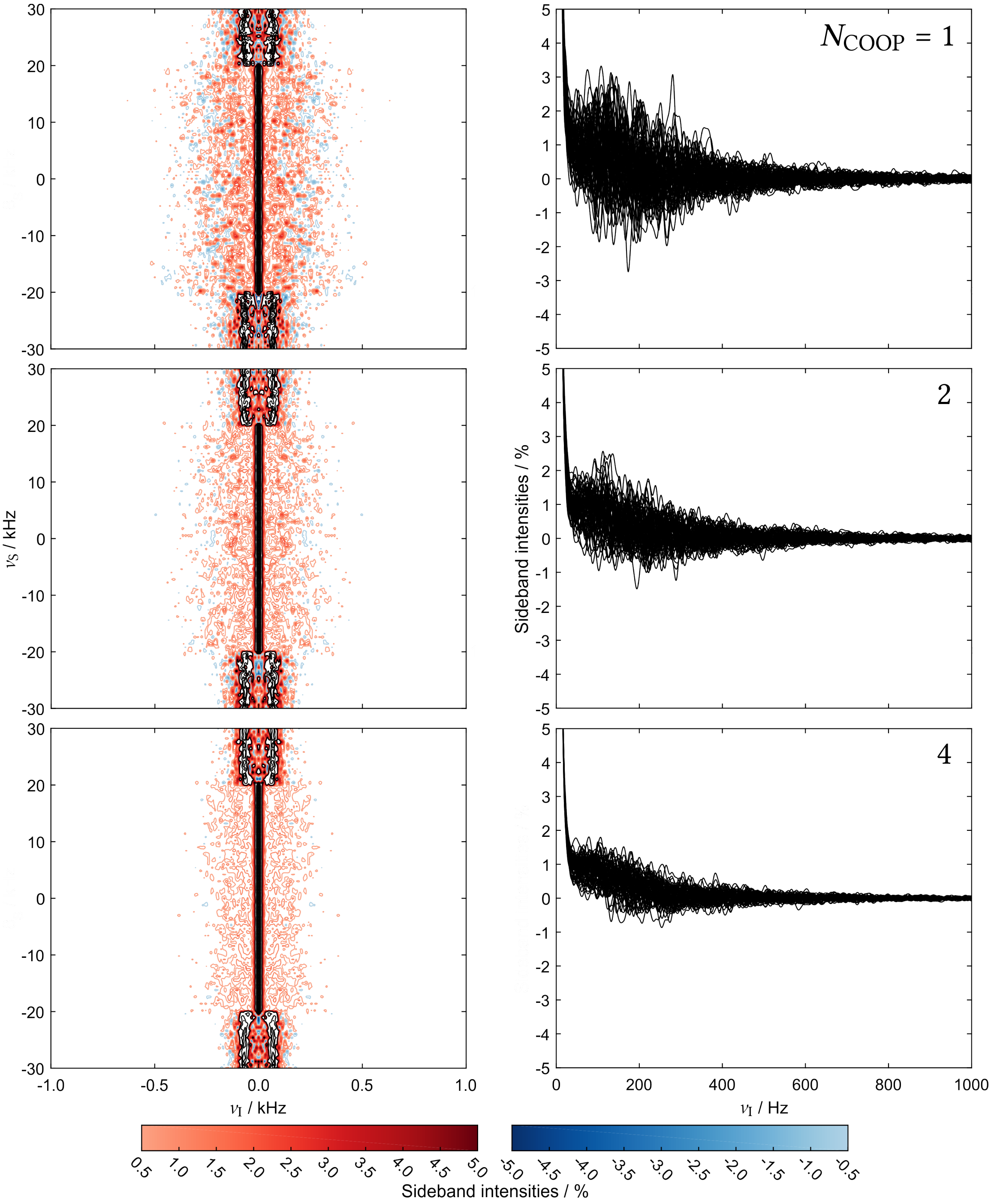

Figure 2.35.: Simulated decoupling profiles using the fully converged constant amplitude COOP decoupling sequences (Δt = 5 μs). For the offset profiles (left panels) ten contour levels for positive and negative sidebands were plotted distributed equally between the extreme values of ±0.5 and ±5% respectively. Peak contours were plotted using ten levels between the maximum sideband and 100% intensity. For the sideband profiles (right columns) spectra are overlaid and expanded to 5% of the maximum decoupled center peak intensity across the desired offset range of 40 kHz. Since the sidebands are symmetrically distributed around the center peak, only positive frequencies are plotted.

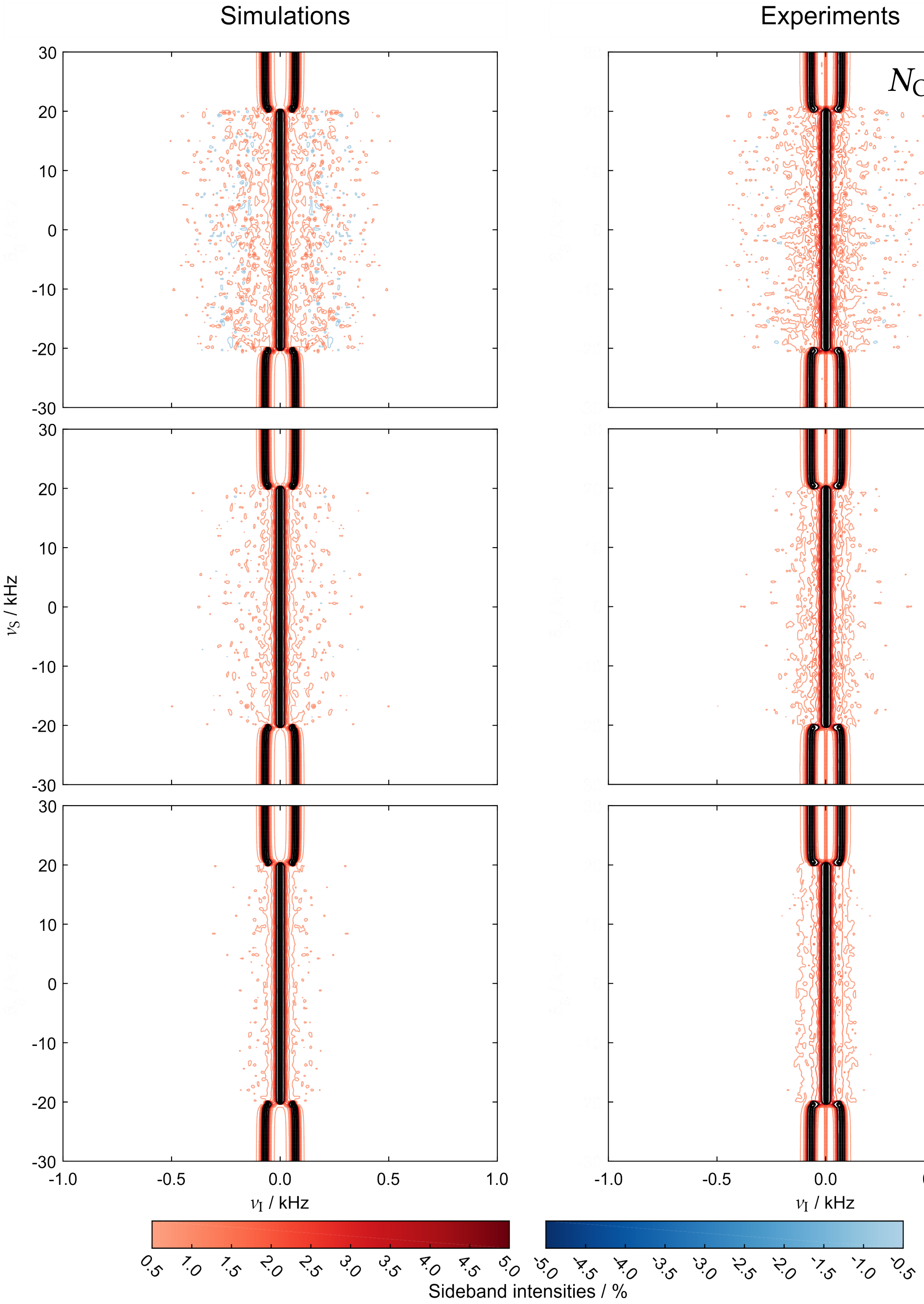

Figure 2.36.: Comparison of simulated (left panels) and experimental (right panels) offset profiles using the fully converged power-limited COOP decoupling sequences ($\Delta t = 5\ \mu s$). Ten contour levels for positive and negative sidebands were plotted distributed equally between the extreme values of ±0.5 and ±5% respectively. Peak contours were plotted using ten levels between the maximum sideband and 100% intensity.

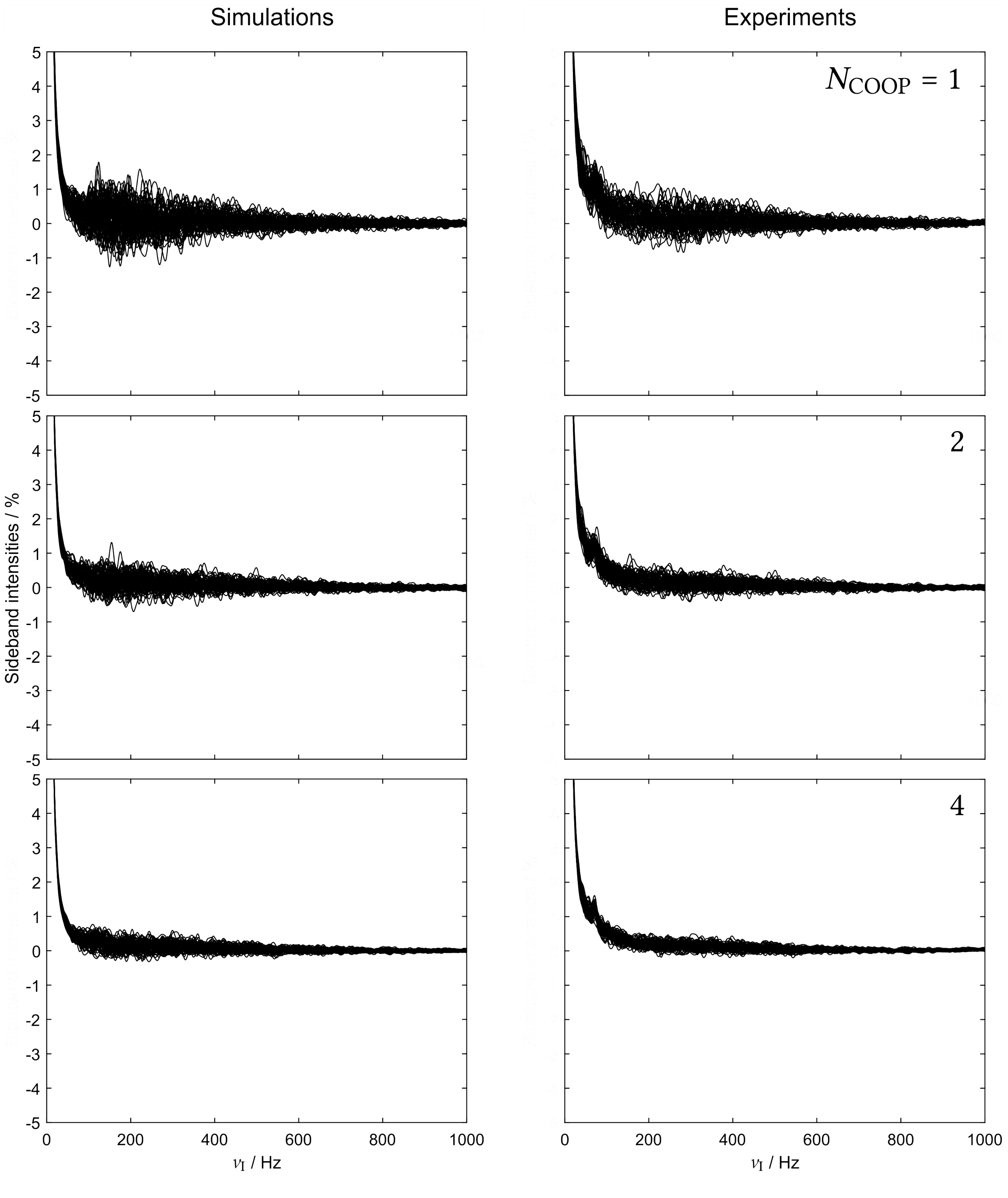

Figure 2.37.: Comparison of simulated (left panels) and experimental (right panels) sideband amplitudes using the fully converged power-limited COOP decoupling sequences ($\Delta t = 5\ \mu s$). Spectra are overlaid and expanded to 5% of the maximum decoupled center peak intensity across the desired offset range of 40 kHz. Since the sidebands are symmetrically distributed around the center peak, only positive frequencies are plotted.

inhomogeneity or miscalibration which can theoretically affect heteronuclear decoupling favourably in cases of overshooting the nominal $u_{\mathrm{RF}}^{\mathrm{max}}$ or at least not be detrimental[107]. Since all experiments for figures 2.36 and 2.37 were performed using a single calibration (see section 2.2.7), they would all be affected equally. Another experimental imperfection that might work in favor of decoupling performance are smoothing effects on the pulse shapes since the amplitude and phase modulation happens on a 5 μs grid which is rather coarse compared to other OCT studies (see the references in section 1.2.3). From the statistics given in figure 2.31, there might be slight improvements to be expected from an even smoother modulation, but these effects are hard to predict and to measure. In addition to these subtle effects, it has to be mentioned that the signal of residual ^{12}C-bound protons was not suppressed so that it can add up to the total signal intensity but it should only add a relative 1-2% and therefore be rather negligible. Moreover, effects from digital filtering and group delay compensation have already been discussed in section 2.2.1 and may have a strong influence if particularly severe oscillations appear at the beginning of the FIDs which might hence get retouched. Probably the most profound source of deviations between simulations, given that basically the course of the baseline is analyzed, are the differences in the signal processing procedure. Due to the fact that the experimental data is processed by TopSpin© software, the effects of elaborate digital filter functions and baseline correction algorithms on the line shape can not be reproduced in the simulations so that this could be a viable contribution to the observed differences.

Even with the decoupling profiles at hand, it has to be proven that COOP decoupling sequences outperform sets of randomly assorted sequences which were optimized individually. Hence, simulations were performed for sets of individually optimized decoupling sequences obtained during the series of optimizations discussed above and compared with the results for the COOP sequences. Figure 2.38 contains the data for both amplitude- and power-limited sequences evaluated using the same criteria as in figures 2.31 and 2.33. The data clearly show how in each case power-limited pulse sequences outperform their purely phase-modulated counterparts for each value of N_{COOP}. Moreover, by whatever metric the sideband amplitudes are evaluated, a set of randomly compiled decoupling sequences never reaches the sideband levels of specifically optimized COOP cycles. The effect is more pronounced with amplitude-modulated pulses than with their exclusively phase-modulated counterparts as well as more pronounced with four instead of two pulses. The differences are the least significant for the RMS sideband intensities which is due to the fact that at the frequencies where the sideband levels are extracted, obviously a limit set by the line shape is approached which amounts to about 0.3%. Quantitatively, in terms of positive and negative sidebands, the absolute improvement ranges from 0.3-0.6% which corresponds to a relative gain of 14-64%. This proves that cooperativeness can by design benefit from additional degrees of freedom provided by more pulses or amplitude modulation beyond mere statistical averaging.

As a final aspect of this study, the effect of the amplitude-modulation on the drastic improvement of decoupling performance shall be elucidated. Figure 2.39 depicts amplitude and phase profiles as well as a spectrogram representation of the first 5 ms of a single constant amplitude and an amplitude modulated decoupling sequence. Whereas the phase profiles are rather similar in showing a rather noise-like modulations the amplitude profiles clearly resemble the different mechanisms by which constraints are applied to the RF

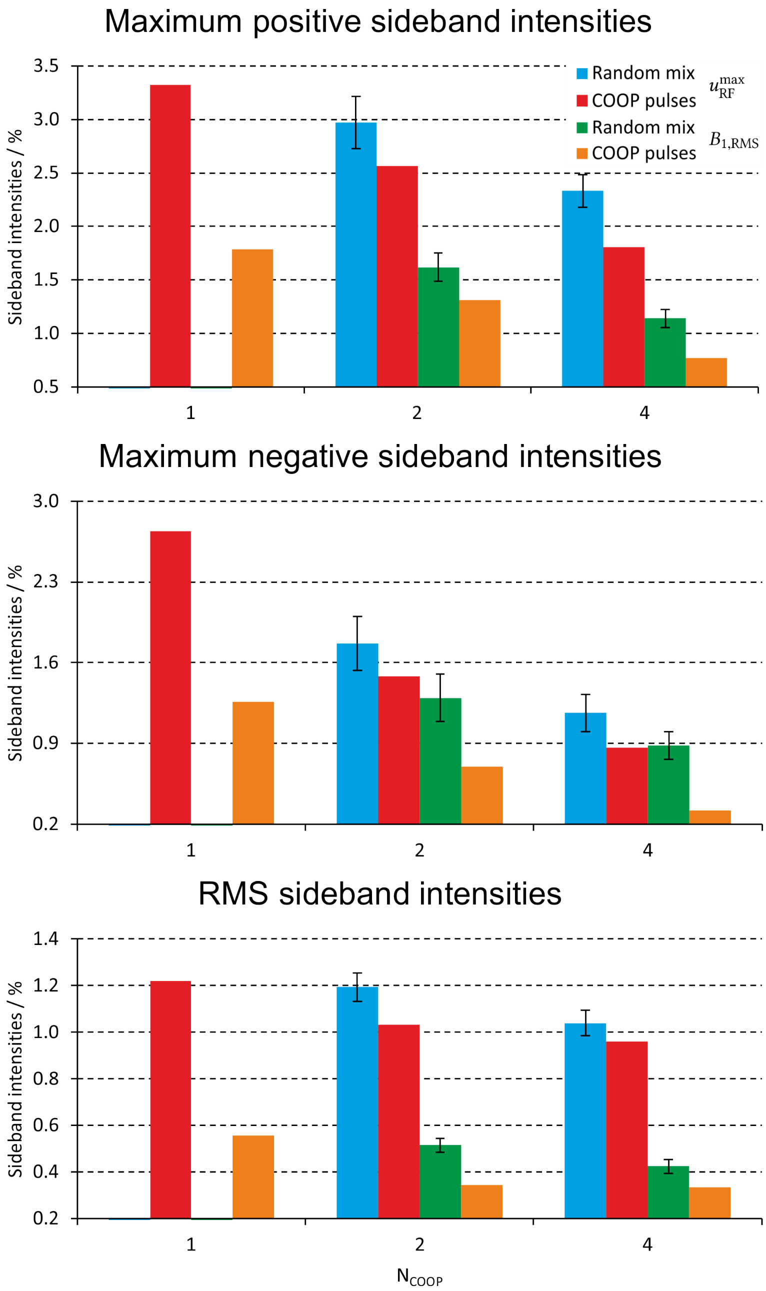

Figure 2.38.: Sideband statistics for COOP decoupling sequences versus sets of individually optimized sequences as a function of N_{COOP}. Decoupling sequences with limited RF amplitude are marked with $u_{\mathrm{RF}}^{\max}$ and pulses with limited RF power are marked with $B_{1,\mathrm{RMS}}$. The bars for individually optimized sequences indicate the mean value and error bars correspond to the standard deviation. The legend applies to all graphs.

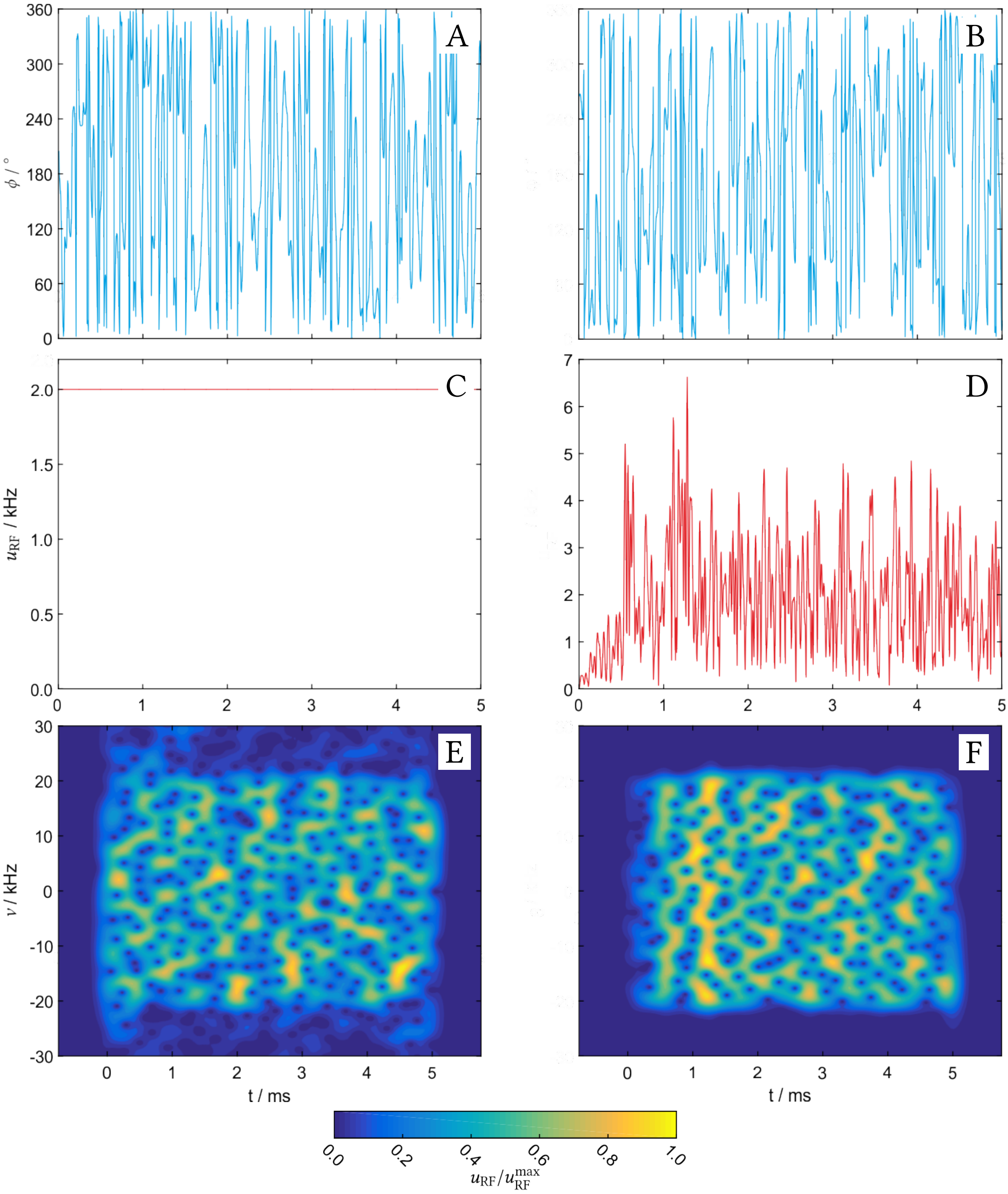

Figure 2.39.: Visual representation of differently modulated pulse shapes for decoupling. Phase, amplitude and spectrogram representations of a single optimized pure-phase modulated decoupling sequence (A, C and E respectively) and an amplitude-modulated sequence (B, D and F respectively). Parameters of the spectrogram were chosen according to the BUSS example given in [54] with a 15% baseline of zeros added at the beginning and end of the shape.

control amplitudes. It can be deduced from figure 2.39 D that for several hundred μs at the beginning of the sequence the RF amplitude slowly builds up since heteronuclear coupling evolution on this timescale does not necessitate significant RF expenditure. Nevertheless, prior to oscillating again seemingly chaotic around $B_{1,\mathrm{RMS}}$ = 2 kHz there are bursts of more than 6.5 kHz which can compensate for such a build-up behavior (further experimental details of the individual pulses are given in section 2.2.7). It has been shown in [54] that the apparently random modulation of the pulse sequence serves a distinct purpose which is revealed by the spectrogram. For the power-limited sequence (figure 2.39 F) it is easily shown that all the RF energy is being dissipated in the desired range of offsets $\Delta\nu_\mathrm{S}$ = 40 kHz with rapidly changing frequency ranges of RF deposition. Conversely, the purely phase-modulated sequence has a spillover outside the desired offset range for the same reason as discussed with the BIBOP shape of figure 1.7. As can be seen by the corresponding contour levels, this leaves less energy available to span a dense web of RF irradiation over the desired frequency range and over the timescale of the sequence. This causes more abundant periods of effectively free coupling evolution which gives rise to more pronounced sidebands as discussed for the GARP inversion element (see figure 2.10). Another more phenomenological evidence for the RF spillover can be found at the edges of the offset profiles in figure 2.35 (left side) where there is no visible transition from a singlet (inside the optimized region) to a doublet (outside the optimized region) as can be observed in figure 2.36. The RF energy deposition at these frequencies leads to a diffuse and distorted doublet with an abundance of sidebands.

In summary, it has been shown that the seemingly noise-like but apparently highly-orchestrated RF modulation scheme in combination with multi-scan cooperativeness as introduced in section 2.2.3 does in principle provide the ultimate sideband canceling mechanism for broadband heteronuclear decoupling. Given that the decoupling scheme is non-repetitive, there is no predetermined or dominant signal modulation which will lead to a dominant sideband at a given frequency which makes the method more attractive in the low-power regime as it is not subject to adiabaticity constraints. This is proven by the very homogeneous sideband profiles in figure 2.37. At the same time broadband operation is maintained beyond the capabilities of CPD methods. The sideband canceling mechanism as depicted in figure 2.28 is more general and straight-forward than any frequency-unspecific desynchronisation[74, 104] or averaging techniques[85] and is independent of a minimum required number of scans (or maximum for that matter). It is therefore nearby to refer to this method in the most general way as BROadband COoperative DEcoupling (BROCODE) [110] in the following.

2.2.6. Experiments

Finally, two experimental aspects of the BROCODE shall be elucidated. First, the confidence levels given in terms of the maximum sideband amplitudes in section 2.2.5 shall be tested with regard to the dynamic ratio that is defined by the signal and the corresponding sidebands. Therefore, a sample of imidacloprid, a widely-used insecticide[111] was doped with its synthetic precursor 2-chloro-5-chloromethyl-pyridine as an impurity (referred to simply as pyridine precursor in the following) to approximately yield a concentration ratio of 100:1. The synthetic pathway to imidacloprid which employs the pyridine precursor is one of the two common methods to obtain the insecticide[112] and is depicted in figure 2.40. To characterize the compounds for decoupling experiments, one-dimensional ^1H and ^{13}C as well as two-dimensional CLean In-Phase-HSQC (CLIP-HSQC) [113] experiments were recorded to obtain relevant information about the labeled atoms in figure 2.40. Chemical shifts of ^1H and ^{13}C nuclei and their corresponding $^1J_{CH}$ couplings are given in table 2.7. Decoupled two-dimensional HSQC spectra of the aforementioned 100:1 compound mixture were recorded with AQs of 128 ms using the BROCODE pulses ($B_{1,RMS}$ = 2 kHz) and bilevel decoupling employing caWURST-2 pulses at $B_{1,RMS}$ = 4.4 kHz as well as 2 kHz. Further, following equation 1.154 the RF energy scales quadratically with $B_{1,RMS}$ so that a reduction of the latter by more than 50% (as is the case for BROCODE) affords an AQ prolonged by a factor more than four. Therefore, additional spectra were recorded with AQs of 512 ms using the BROCODE pulses and bilevel decoupling employing caWURST-2 pulses at $B_{1,RMS}$ = 2 kHz. Four scans have been averaged in each case. For the first comparison, spectra using the BROCODE and caWURST-2 bilevel decoupling (both with AQ = 128 ms, the latter with $B_{1,RMS}$ = 4.4 kHz) were evaluated with regard to whether the impurity can be identified. In all experiments stated above, position 1 is very easily discerned in the mixture (see figure 2.40 B for atom numbering). On the contrary, position 4 poses several problems. The spectral regions of 6 ppm for the ^1H and 125 ppm for the ^{13}C dimension are sampled with a resolution of 7.8 and 294 Hz, respectively. This is sufficient for the pure compounds, but given that the chemical shift differences for position 4 amount to 18 Hz for both dimensions, a significant challenge has to be met. At the given resolution, the $^3J_{HH}$ coupling to position 3a is not resolved so the line width achieved after apodization using a cosine-squared window function also amounts to about 18 Hz. This is why several line

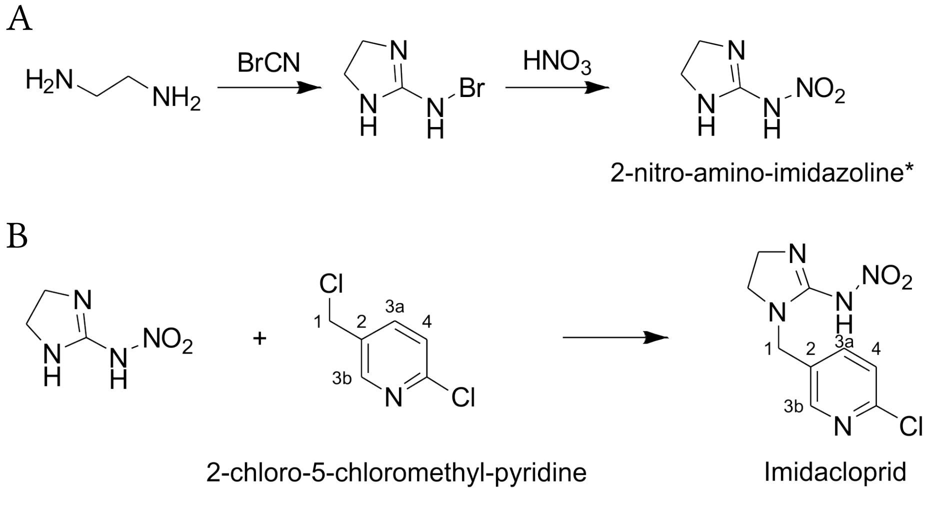

Figure 2.40.: Reaction schemes of the synthetic pathway to obtain imidacloprid using the pyridine precursor. The necessary substrate 2-nitro-amino-imidazoline (*the tautomeric form would be called 2-nitroimine-imidazolidine) is obtained starting from ethylene diamine (A). The reaction with the pyridine precursor yields the desired compound with the atom numbering corresponding to the number of bonds between the given carbon atom and the moiety which distinguishes the compounds from each other (B).

Imidacloprid position	$\delta(^1H)$ / ppm	$\delta(^{13}C)$ / ppm	$^1J_{CH}$/ Hz	-
1	4.48	44.94	141.0	-
3a	7.80	139.85	164.9	-
3b	8.37	149.78	182.1	-
4	7.53	124.79	172.5	-
Pyridine position	$\delta(^1H)$ / ppm	$\delta(^{13}C)$ / ppm	$^1J_{CH}$/ Hz	-
1	4.83	42.61	154.3	-
3a	7.95	140.77	166.0	-
3b	8.50	150.37	183.2	-
4	7.56	124.91	173.1	-
Chemical shift differences	$\Delta\delta(^1H)$ / ppm	$\Delta\delta(^1H)$ / Hz	$\Delta\delta(^{13}C)$ / ppm	$\Delta\delta(^{13}C)$ / Hz
1	0.35	210	2.33	349.5
3a	0.15	90	0.92	138
3b	0.13	78	0.59	88.5
4	0.03	18	0.12	18

Table 2.7.: Characterization of imidacloprid and the pyridine precursor. Chemical shifts were determined for both compounds in order to calculate the corresponding differences for each position which yields an HSQC cross peak (position 2 is a quaternary carbon). The values in Hz are calculated for a ^{1}H resonance frequency corresponding to 600 MHz.

shape distortions overlap with the signal of the impurity component. These are the wiggles due to incomplete nullification of the FID at its end as well as residual distortions due to lock phase misadjustment. It is hard to judge if these distortions are symmetric around the main signal since bilevel decoupling introduces a baseline wave due to the intensity drop at the beginning of each FID upon averaging of the individual scans (see figure 2.13) which makes it hard to thoroughly phase the signal to the necessary accuracy at the given intensity levels. This baseline wave can be observed in the simulations depicted in figure 2.16. The spectra using the BROCODE can be phased more reliably and reveal asymmetric line shape distortions which may be caused by the signal of the impurity component. However, given that such statements involve a fair amount of speculation, position 4 shall not be further discussed and positions 3a and 3b shall be further elucidated. Excerpts of the HSQC spectra showing signals for position 3a and 3b for both compounds are depicted in figure 2.41. A highly-resolved one-dimensional ^{1}H spectrum was added on top of the spectrum to pinpoint the position where the impurity signals can be expected. Integration of the signals reveals a concentration ratio between 100:1.3 and 100:1.4. Errors during the sample preparation happen most likely due to difficulties with the handling

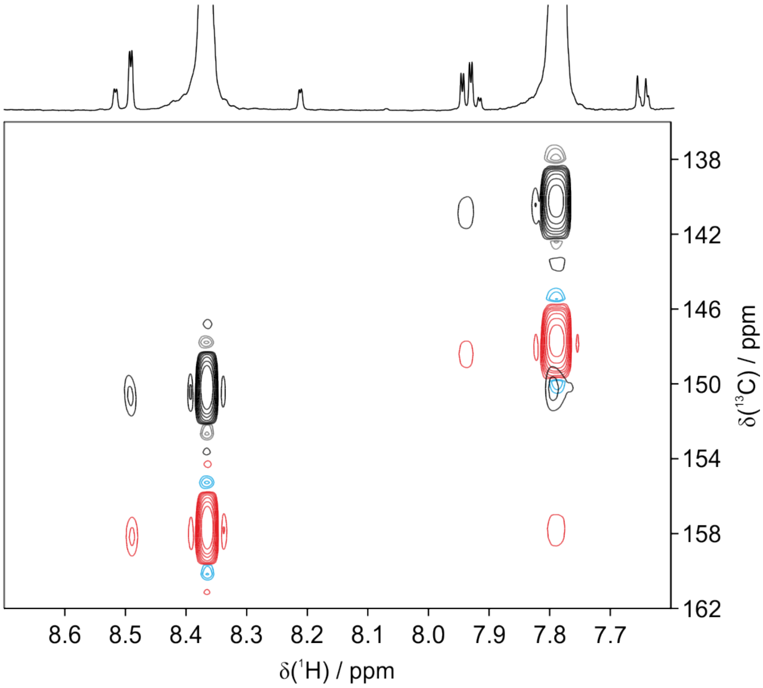

Figure 2.41.: HSQC comparison for signals 3a and 3b of the imidacloprid/pyridine precursor mixture. Experiments using the BROCODE pulses (black and gray contours) and caWURST-2 bilevel decoupling ($B_{1,\mathrm{RMS}}$ = 4.4 kHz, red and blue contours) were collected for 128 ms. Eight positive and negative contour levels are plotted with an 1.8-fold incrementation starting at 1% of the maximum intensity of signal 3a at 7.8 ppm belonging to imidacloprid. This corresponds to 0.6% of the maximum intensity of signal 3b at 8.37 ppm. A highly-resolved one-dimensional ^{1}H spectrum was added on top of the spectrum.

of the solid substances at the given dynamic ratio in terms of mass, particularly given that the pyridine precursor is hygroscopic. However, the contour levels were plotted with an 1.8-fold incrementation starting from 1% of the maximum intensity of signal 3a of imidacloprid, so that the representation of the spectra is not substantially affected. The first contour level of signal 3b corresponds to 0.6% of the maximum intensity. As expected, bilevel decoupling with $B_{1,\mathrm{RMS}}$ = 4.4 kHz allows for the identification of cross peaks for positions 3a and 3b. Additionally, an artifact due to long-range transfer between the 3b carbon to the 3a proton yields a further cross peak. All this information content is retained when the BROCODE is used despite the drastically reduced RF levels of 2 kHz. Sidebands remain below 1% for signal 3a and 0.6% for signal 3b despite the fact that the $^1J_{\mathrm{CH}}$ couplings for the aromatic moieties exceed 140 Hz which is the value used in the optimizations and despite the fact that the RF levels were calibrated by automated routines. Nevertheless, the poor resolution in the ^{1}H dimension does not allow for a discrimination of impurity signals and typical HSQC artifacts at a first glance. Therefore, longer AQs are desirable.

The experiments described above were repeated with AQ = 512 ms where $B_{1,\mathrm{RMS}}$ for caWURST-2 bilevel decoupling had to be reduced to 2 kHz according to probehead specifications. Due to the extended AQ the resolution could be boosted to 1.95 Hz. Even so, this did not lead to the unambiguous identification of an impurity signal at position 4 for several reasons. The prolonged AQ requires a repetition of the BROCODE sequences. Since the sequences are non-cyclic and according to the categorization of section 1.2.3 behave like PP pulses, each repetition impairs the decoupling performance, which can lead to a slight increase in sideband intensities and the introduction of distinct sidebands very close to the center peak. Enhanced resolution also may affect sideband intensities such that the individual sidebands are better resolved and may have increased intensity at the given frequency. Another method to boost resolution is linear forward-prediction (LFP). The full FID can in principle be used to predict another chunk of data up to the same amount as the FID itself. For the spectra presented in this section, LFP worked more reliably with the spectra which provided an already increased resolution due to 512 ms AQ. At the same time, slightly higher sideband amplitudes may be a spurious byproduct. Nevertheless, LFP is attractive in this context since it can lead to resolved resonance line splittings due to $^3J_{\mathrm{HH}}$ couplings and occasionally even $^4J_{\mathrm{HH}}$ couplings (another example will be discussed further below). Resolved line splittings are in principle beneficial in order to distinguish impurity signals from sidebands, but in the case of position 4 did not help to resolve the signal belonging to the pyridine precursor. Excerpts of the HSQC spectra showing signals for position 3a and 3b for both compounds are depicted in figure 2.42. With the help of LFP, the time-domain data corresponds to an experiment with more than 1 s of AQ yielding a resolution below 1 Hz. Again, eight positive and negative contour levels were plotted with an 1.8-fold incrementation but this time starting from 1.2% of the maximum intensity of signal 3a of imidacloprid. Obviously the intensity threshold where only the signal of the pyridine precursor is observable had to be lifted in the higher resolved spectra using the BROCODE. The same contour levels correspond to about 0.7% of the maximum intensity at position 3b of imidacloprid where the impurity signal would be hidden among the sidebands which is why the contours in the lower panel of figure 2.42 had to be raised to 1% to identify the pyridine precursor. When caWURST-2 bilevel decoupling is used, sidebands are more abundant and obtrusive so that the impurity signals have to be sought after among the sidebands.

For a more detailed analysis, 1D slices were extracted for signals 3a and 3b for both resolutions. The digital resolution of the ^{13}C dimension was increased to about 74 Hz using a zero-filling factor of four so that 1D slices can be extracted closer to the actual ^{13}C chemical shift of the impurity signal. This facilitates a more reliable identification of impurity resonances. Slices of signal 3a extracted from the spectra acquired with the different decoupling schemes as well as different resolutions are given in figure 2.43. At the resolution achieved by AQ = 128 ms, no J-couplings can be resolved so that the impurity signal at position 3a can only be distinguished from the long-range transfer artifact at the chemical shift of position 4 on a closer look. Nevertheless, using only $B_{1,\mathrm{RMS}}$ = 2 kHz also the BROCODE can provide sideband amplitudes which are marginal enough to identify signals of the impurity component. Upon increasing the resolution by applying LFP to datasets acquired with AQ = 512 ms, both the $^3J_{\mathrm{HH}}$ and the $^4J_{\mathrm{HH}}$ couplings of the signals at position 3a can be resolved. Unluckily, this also applies to the sidebands caused by the bilevel method, which are still spurious at the ^{13}C chemical shift of the impurity signals such that they equal the latter. However, it is now easily possible to at least discern transfer artifacts from all other signals appearing in the spectrum. This is particularly beneficial when the BROCODE is used at this resolution, since now the only relevant signal is easily

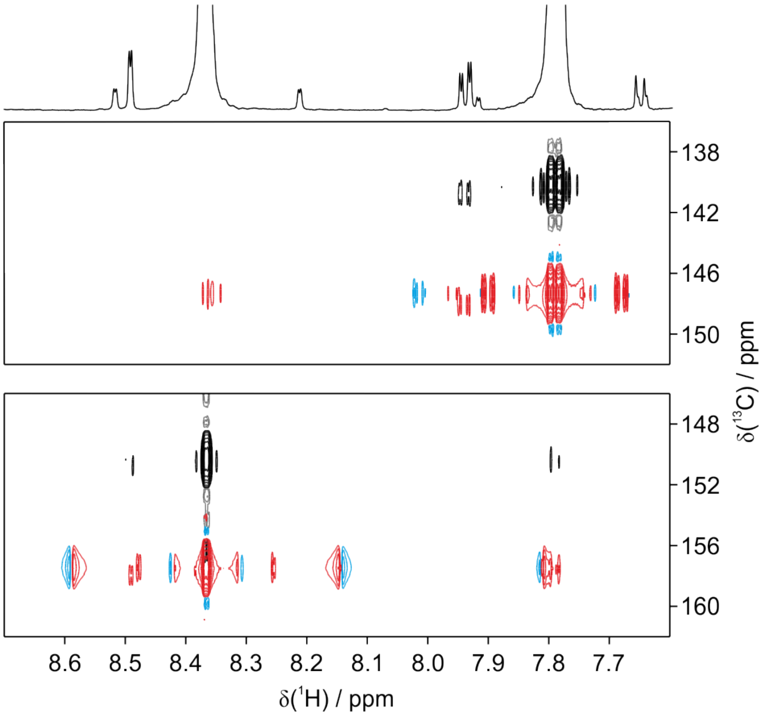

Figure 2.42.: HSQC comparison for signals 3a and 3b of the imidacloprid/pyridine precursor mixture. Experiments using the BROCODE pulses (black and gray contours) and caWURST-2 bilevel decoupling (red and blue contours) were collected for 512 ms ($B_{1,\mathrm{RMS}}$ = 2 kHz in both cases). Eight positive and negative contour levels are plotted with an 1.8-fold incrementation starting at 1.2% of the maximum intensity of signal 3a at 7.8 ppm belonging to imidacloprid (upper panel) and 1% of the maximum intensity of signal 3b at 8.37 ppm (lower panel). A highly-resolved one-dimensional ^{1}H spectrum was added on top of the spectrum.

identifiable due to its line shape defined by J-couplings. The most significant remaining sidebands are directly next to the center peak which are most likely due to the repetition of the BROCODE sequences. This appears plausible since these sidebands are found about 8 Hz away from the center peak which corresponds to 1/128 ms. A similar trend can be observed for position 3b. 1D Slices of signal 3b extracted from the same spectra are given in figure 2.44. Again, looking at the spectra recorded with AQ = 128 ms, the information content of the experiment using bilevel decoupling at $B_{1,\mathrm{RMS}}$ = 4.4 kHz can be retained when the BROCODE is employed at the much reduced RF power levels. At the higher resolution and equal RF power as the BROCODE, bilevel decoupling suffers from very obtrusive sidebands which exceed the intensity of the impurity signal by far. Using the BROCODE however, the signal of position 3b of the pyridine precursor can be identified with the $^{4}J_{\mathrm{HH}}$ coupling moderately resolved.

The aspect of increased ^{1}H resolution in decoupled HSQC spectra due to extended AQ facilitated by the extremely low-power BROCODE sequences and the possible synergy with LFP was further studied on a sample of (+)-borneol. The compound class of bornanes and norbonanes is well studied[114] and is a good example for molecules that have cyclic

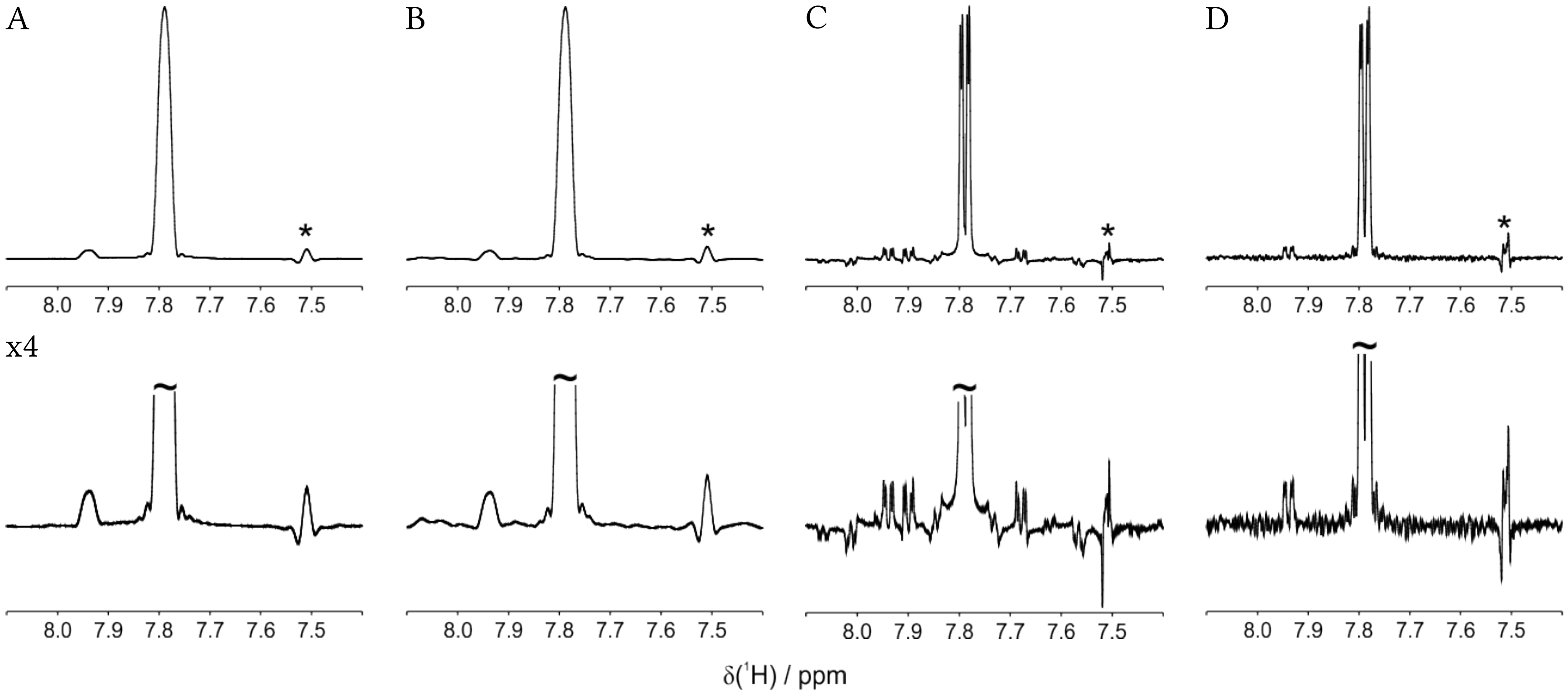

Figure 2.43.: 1D HSQC slices for signals 3a of the imidacloprid/pyridine precursor mixture. Excerpts of spectra (top panels) and four-fold magnifications (bottom panels) are shown with AQ = 128 ms using bilevel decoupling ($B_{1,\mathrm{RMS}}$ = 4.4 kHz, A) and the BROCODE (B) as well as AQ = 512 ms using bilevel decoupling ($B_{1,\mathrm{RMS}}$ = 2 kHz, C) and the BROCODE (D). Datasets recorded for the latter two were subject to LFP. All spectra were normalized to the same maximum intensity. The long-range transfer artifact at the chemical shift of position 4 is indicated by an asterisk.

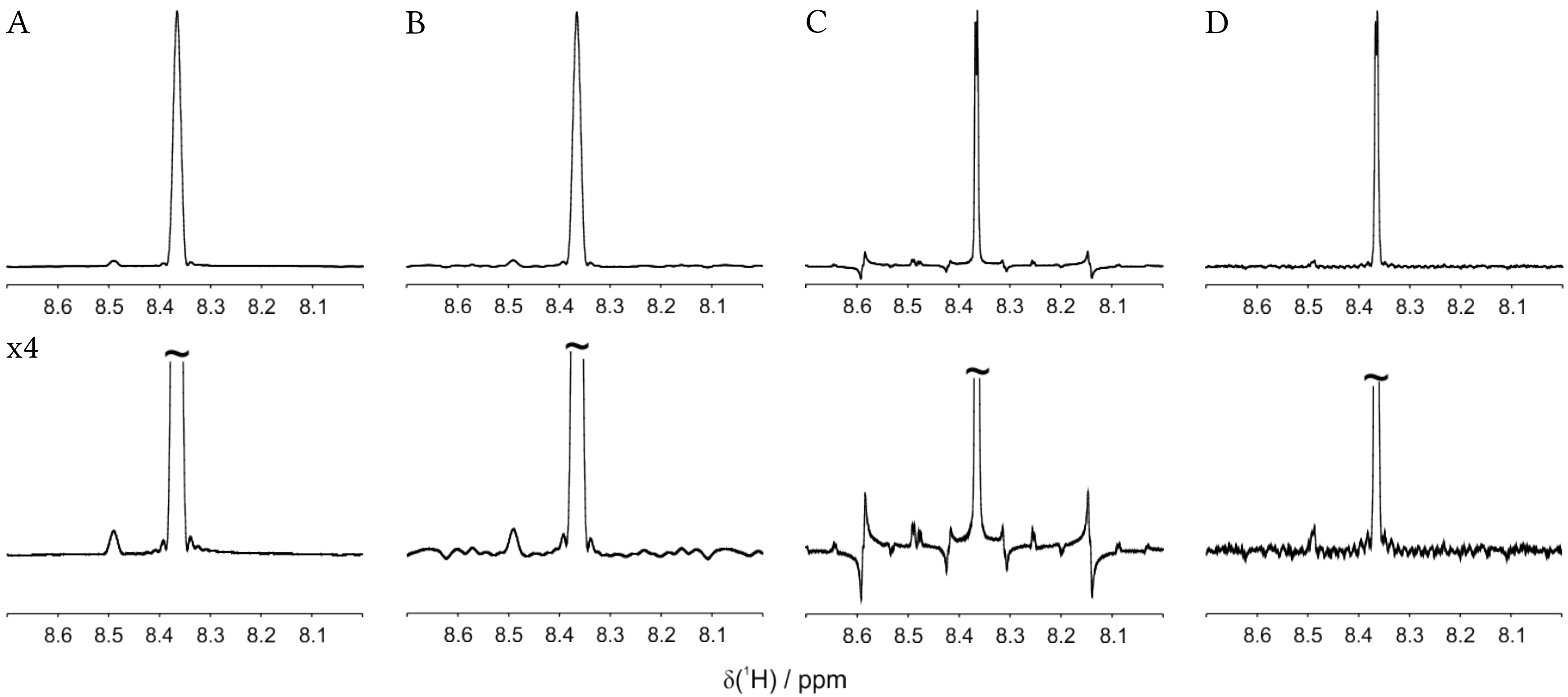

Figure 2.44.: 1D HSQC slices for signals 3b of the imidacloprid/pyridine precursor mixture. Excerpts of spectra (top panels) and four-fold magnifications (bottom panels) are shown with AQ = 128 ms using bilevel decoupling ($B_{1,\mathrm{RMS}}$ = 4.4 kHz, A) and the BROCODE (B) as well as AQ = 512 ms using bilevel decoupling ($B_{1,\mathrm{RMS}}$ = 2 kHz, C) and the BROCODE (D). Datasets recorded for the latter two were subject to LFP. All spectra were normalized to the same maximum intensity.

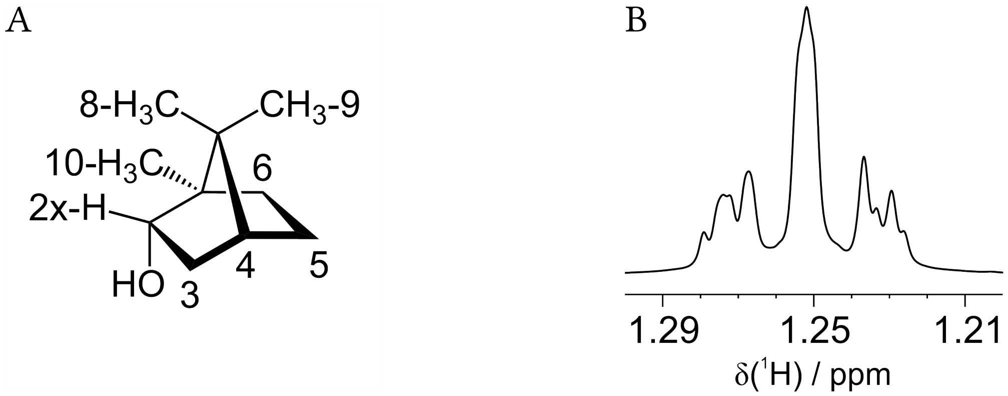

Figure 2.45.: Structure (A) and overlapping signals 5n and 6x (B) of (+)-borneol. Atom numbering was chosen according to [114].

moieties or aliphatic chains which are either not highly- or not diversely substituted so that CH_2 groups can form rather complex spin systems. In the case of (+)-borneol, proton 5-*endo* (here denoted 5n) and 6-*exo* (here denoted 6x) both resonate at 1.25 ppm and are coupled which results in a higher order spectrum. The atom numbering and particular ^1H signal are shown in figure 2.45. Such multiplets can not be deconvolved by homonuclear correlation spectra such as COrrelation SpectroscopY (COSY) [115] or TOCSY. Figure 2.46 shows a Double-Quantum-Filtered COSY (DQF-COSY) [116] spectrum (methyl groups were excluded) of (+)-borneol with annotated 1D ^1H spectra used as projections. The assignment of the resonances was adopted from [114]. The signal at about 2 ppm stems from the hydroxyl group. The diagonal peak of protons 5n and 6x shows only three correlations to signals 2x, 5x, and 6n. Without knowing the structure, it can not be said *a priori* if these cross peaks are due to $^2J_{\mathrm{HH}}$, $^3J_{\mathrm{HH}}$ or even $^4J_{\mathrm{HH}}$ couplings and which of the two protons in question gives rise to these correlations. An HSQC spectrum reveals that the two protons at 1.25 ppm are not attached to the same carbon atom, so they can in principle be deconvolved using the ^{13}C dimension in heteronuclear correlation experiments. The signals of position 3 are assigned rather easily. With the help of COSY and HSQC correlations as well as some values for homonuclear J-couplings, signals 5n and 6x can be solved indirectly as soon as the signals for 5x and 6n are unambiguously assigned. Nevertheless, in complex spectra (regardless whether the complexity is caused by the structure of a single compound or overlap is caused by a mixture of compounds) it might be necessary to directly solve multiplets such as 5n and 6x. Given that due to the use of heteronuclear decoupling, the resolution in the ^1H dimension is usually very limited, several spectra using the BROCODE were recorded. Experiments were conducted with AQ = 128 ms and 512 ms both with and without the use of LFP so that datasets with effective AQs of 128, 256, 512 and 1024 ms were obtained. For the ^1H spectral width of 4 ppm this yielded resolutions of 7.84, 3.92, 1.95 and 0.98 Hz, respectively. Corresponding spectra for the former and the latter showing the CH_2 region of (+)-borneol is depicted in figure 2.47. It is easily recognizable from the contours that the spectrum reveals a lot more fine structure of the individual cross peaks upon the fourfold increase brought about using the BROCODE and LFP. A more detailed analysis of the cross peaks was performed by a

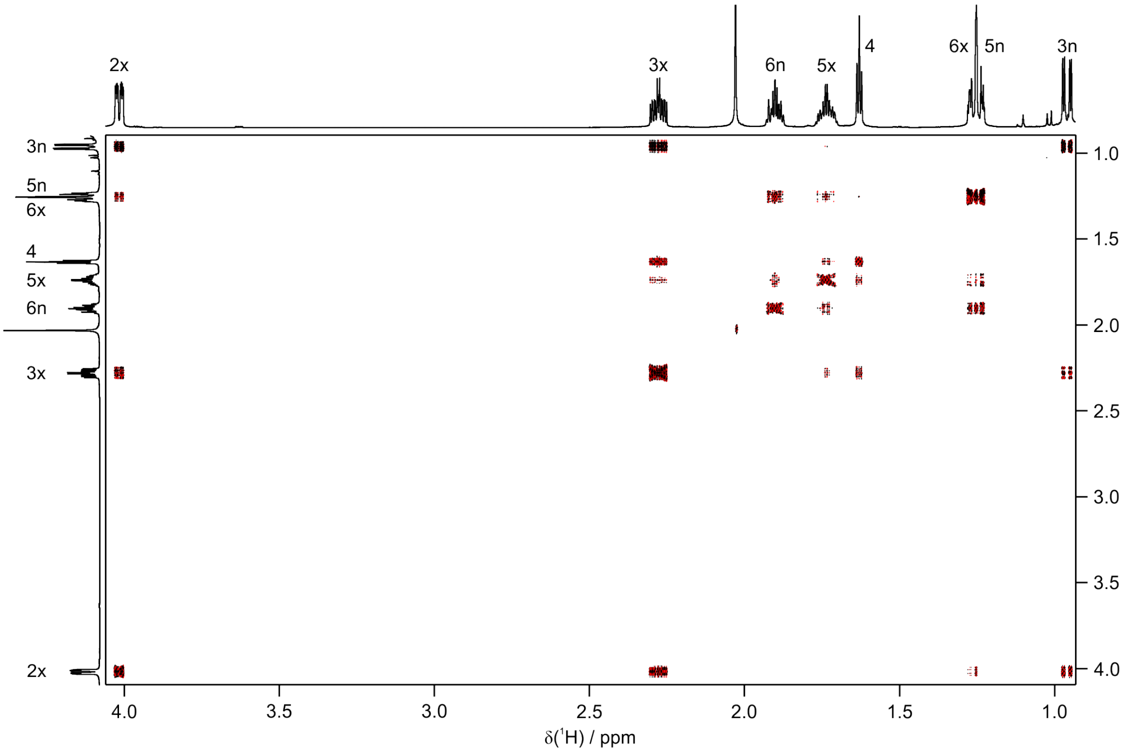

Figure 2.46.: Two-dimensional DQF-COSY for (+)-borneol. A highly-resolved 1D ^{1}H spectrum was used for the projections. Resonance assignment was adopted from [114].

comparison with simulations of simple spin systems. 1D slices of the HSQC spectra for all four resolutions as well as simulated spectra of signals 5n and 6x are given in figure 2.48. The experiments with AQ = 128 ms show no discernible fine structure and the cross peaks obtained by LFP only reveal a triplet-like envelope. Even the extended AQ of 512 ms only reveals a quantitative difference between both signals which can be explained by different magnitudes of the $^2J_{\mathrm{HH}}$ coupling within the CH_2 groups, the $^3J_{\mathrm{HH}}$ couplings between 5n and 6x themselves and the $^3J_{\mathrm{HH}}$ couplings to 5x and 6n, respectively. When LFP is applied to the experiment with AQ = 512 ms, a qualitative difference is revealed as the signal of proton 6x shows a further fine structure which can only be explained by an additional coupling. The COSY correlation to proton 2x therefore must be due to a $^4J_{\mathrm{HH}}$ coupling between the former and proton 6x. The four protons at positions 5 and 6 were plugged into the simulation for signal 5n using their respective chemical shifts and $^2J_{5n5x} = -12.2$ Hz, $^3J_{5n6x} = 4.6$ Hz and $^3J_{5n6n} = 9.4$ Hz. For signal 6x, a five-spin system using the protons at positions 5 and 6 as well as 2x was simulated using the respective chemical shifts and $^2J_{6n6x} = -12.7$ Hz, $^3J_{5n6x} = 4.6$ Hz, $^3J_{5x6x} = 12.4$ Hz and $^4J_{2x6x} = 1.9$ Hz. The assignment of the overlapping resonances 5n and 6x is thus also more directly possible. Resolving the full multiplet structure of overlapping signals is not only useful for strongly coupled spin systems but can also facilitate a direct multiplet analysis in weakly coupled spin systems. More importantly, it is highly desirable to exploit the simplicity of HSQC spectra to the highest possible extent in terms of extraction of homonuclear coupling constants as it

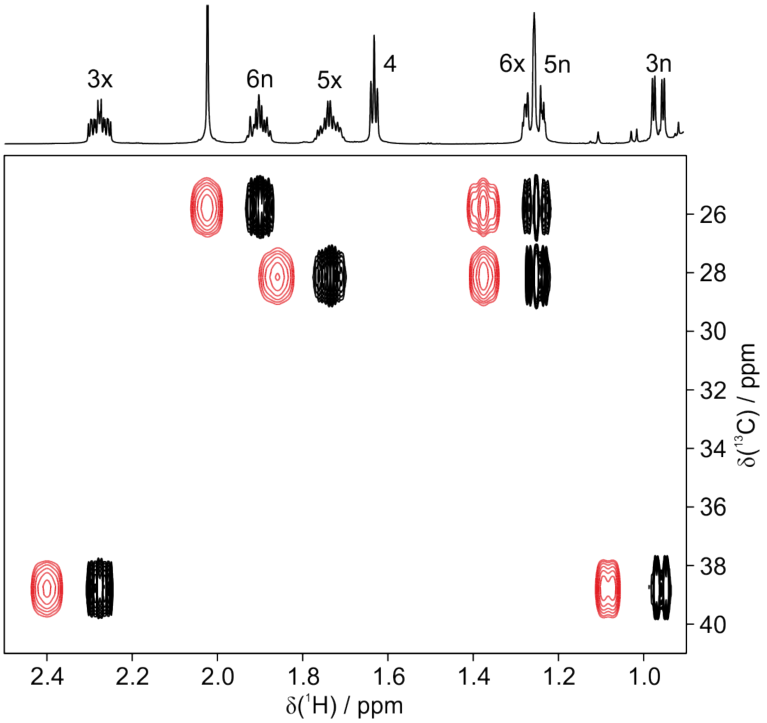

Figure 2.47.: Two-dimensional HSQC spectra showing the CH_2 region of (+)-borneol. Experiments are given for AQ = 128 ms (red contours) and 512 ms using LFP (black contours). A highly-resolved 1D ^{1}H spectrum was used for the projection. Resonance assignment was adopted from [114].

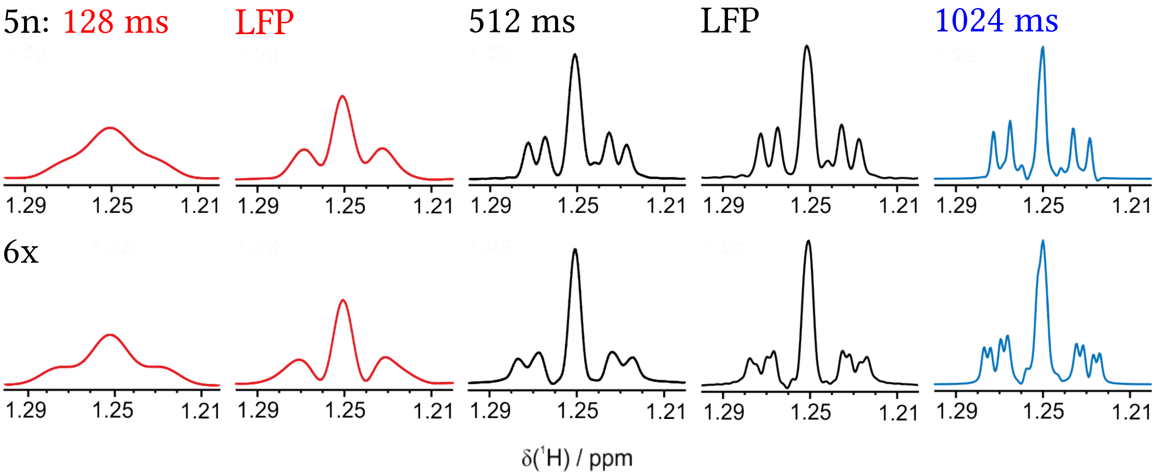

Figure 2.48.: 1D HSQC slices for signals 5n (upper panels) and 6x (lower panels) of (+)-borneol. Signals obtained from experiments with AQ = 128 ms and 512 ms are given in red and black, respectively. Simulations of spectra with AQ = 1024 ms are shown in blue. The values for AQ and the use of LFP are indicated as insets.

may render in terms of information theory more complex experiments like Heteronuclear Multiple-Bond Correlation (HMBC) [117] or HSQC-TOCSY [118] expendable.

In summary, the BROCODE was presented as the possibly most general and universal approach for sideband suppression in low-power broadband heteronuclear decoupling. Within the established confidence limits of residual sideband amplitudes, the information content of the decoupled HSQC spectra can be retained using the lower levels of RF energy dissipation. By using the BROCODE repetitively in experiments with AQ = 512 ms (and LFP), homonuclear J-couplings could be extracted which increased the information content of the HSQC spectra discussed in this section. This was not possible using adiabatic bilevel decoupling within usual adiabaticity constraints ($B_{1,\mathrm{RMS}}$ = 4.4 kHz) given that the same net RF energy dissipation according to equation 1.154 ensues much shorter AQs.

2.2.7. Materials & methods

Simulations were performed using the MATLAB® software package with either self-written scripts and functions (see appendix A.2.1) or code developed during the theses of Sebastian Ehni[51] and Martin Koos as well as modifications of the latter with the following exceptions: Spectrograms[54] shown in figures 1.7, 2.10 and 2.39 were obtained from a software package provided by Thomas Heydenreich, Technical University Munich. The data for the experimental decoupling profiles given in figures 2.14, 2.15, 2.17, 2.18, 2.36 and 2.37 was processed using a MATLAB® Metabolomics toolbox provided by the Bruker Biospin GmbH. Adiabatic shapes used in the simulations discussed in sections 2.1.3, 2.1.4 and 2.2.1 as well as in corresponding experiments in section 2.2.1 were generated using the Shapetool of the Bruker TopSpin® software package. The BUSS shape[107] used in the simulations of figure 2.16 was provided by Dr. Franz Schilling, Technical University Munich.

Experimental decoupling profiles shown in the figures referenced above were obtained from spectra recorded on a 600 MHz Bruker Avance III spectrometer equipped with an inversely detected ^{1}H,^{13}C,^{15}N-triple-resonance cryogenically cooled TCI probehead using a 500 mM sample of ^{13}C-enriched methanol dissolved in $CDCl_3$. 1D ^{1}H spectra with synchronized inverse gated ^{13}C decoupling were acquired with spectral widths of 10 kHz corresponding to 16.7 ppm with the carrier frequency set to the methyl resonance at 3.49 ppm. The ^{13}C resonance at about 50.75 ppm which served as the zero decoupler offset for the decoupling experiments was determined individually for each series of experiments within 0.01 Hz accuracy from a highly-resolved 1D ^{13}C spectrum. Data was collected for 128 ms corresponding to 2560 complex data points which were zero-filled to 16384 points. Time-domain data was apodized using a cosine-squared window function and an exponential line broadening of 6 Hz prior to FT. The frequency-domain data was then phased and subject to an automated baseline correction procedure. Four dummy scans were used in each series of experiments with a recovery delay of 30 s. Experiments using bilevel decoupling with two or four scans made use of the CPD program *bi_p5m4sp_4sp* whereas for the single-scan experiments the *p5m4sp180* program was used as implemented in Bruker TopSpin® 3.0 (and above). Measurements using the BROCODE required self-written CPD programs using bilevel syntax (see appendix A.5). The temperature was set to 300 K. RF levels for the decoupler channel were calibrated using the off-resonance scaling of the $^1J_{\mathrm{CH}}$ coupling of methanol under CW irradiation according to equation 2.5. The coupling constant of about 141 Hz was determined individually for each series of experiments within 0.6 Hz accuracy from a non-decoupled 1D ^{1}H spectrum. Off-resonance scaling was used to determine the power levels corresponding to u_{RF} = 4 kHz (62.5 μs pulse length) within ±1% accuracy. For experiments using caWURST-2 pulses at $B_{1,\mathrm{RMS}}$ = 4.4 kHz, the shapes had to be calibrated to $u_{\mathrm{RF}}^{\mathrm{max}}$ = 7.19 kHz (34.77 μs pulse length) for the low-power component and 10.5 kHz (23.81 μs pulse length) for the high-power component. The shapes had to be calibrated to $u_{\mathrm{RF}}^{\mathrm{max}}$ = 3.27 kHz (76.45 μs pulse length) for the low-power component and 4.77 kHz (52.41 μs pulse length) for the high-power component to achieve equal scaling for operation at $B_{1,\mathrm{RMS}}$ = 2 kHz. The optimization of the BROCODE pulses resulted in shapes with different values for $u_{\mathrm{RF}}^{\mathrm{max}}$. Upon conversion from the three-column u_x, u_y, Δt into the two-column amplitude/phase format of Bruker shapes, the amplitudes which will serve as the 100% reference in the Bruker format were determined from rounding $u_{\mathrm{RF}}^{\mathrm{max}}$ up to the nearest multiple of 0.5 kHz. These values and the corresponding pulse lengths were then used to calibrate the actual power levels. The individual pulse requires $u_{\mathrm{RF}}^{\mathrm{max}}$ = 6623.50 Hz which was referenced to 7 kHz (35.71 μs pulse length). The two-step BROCODE pulses require $u_{\mathrm{RF}}^{\mathrm{max}}$ = 6192.08 and 7049.91 Hz which were referenced to 6.5 and 7.5 kHz, respectively (38.46 and 33.33 μs pulse length, respectively). For the four-step BROCODE cycle, pulses were obtained with $u_{\mathrm{RF}}^{\mathrm{max}}$ = 6478.45, 6578.45, 5977.50 and 5759.49 Hz which were referenced to 6.5, 7, 6 and 6 kHz, respectively (38.46, 35.71, 41.67 and 41.67 μs pulse length, respectively). Power levels for ^{1}H pulses were calibrated by automated routines.

Experiments to obtain the spectral information about imidacloprid and the pyridine precursor given in table 2.7 were recorded on a 500 MHz Bruker Avance III HD spectrometer equipped with a CryoProbe Prodigy™using 100 mM samples of imidacloprid and 2-chloro-5-chloromethyl-pyridine dissolved in DMSO-d_6. ^{1}H chemical shifts were extracted from 1D spectra acquired with spectral widths of 4 kHz corresponding to 8 ppm with the carrier frequency set to 6 ppm. Data was collected for 1024 ms corresponding to 8192 complex data points which were zero-filled to 16384 points. Experiments were recorded using a single scan. ^{13}C chemical shifts were extracted from 1D spectra using WALTZ-65 ^{1}H decoupling at u_{RF} = 2.5 kHz (100 μs pulse length) throughout the experiments which were collected from 16 scans using four dummy scans and a recovery delay of 1.5 s. Spectral widths of 17.5 kHz corresponding to 140 ppm with the carrier frequency set to 100 ppm were used. Data was collected for 1.87 s corresponding to 65536 complex data points which were zero-filled to 131072 points. Time-domain data for all experiments was apodized using an exponential line broadening of 0.3 Hz prior to FT and phase correction. RF levels were calibrated automatically. The temperature was set to 298 K. $^1J_{\mathrm{CH}}$ couplings were determined according to the method described in [119] from two-dimensional CLIP-HSQC [113] spectra. Spectral widths were adopted from the corresponding 1D spectra and data matrices of 8192 × 512 complex data points were collected. Time-domain data was zero-filled to 16384 × 1024 points and apodized using a cosine-squared window function prior to FT and phase correction. Experiments were recorded using two scans and 16 dummy scans with a recovery delay of 1 s. Delays for magnetization transfer via $^1J_{\mathrm{CH}}$ couplings were set for a 145 Hz coupling constant. The pulse sequence was adopted from the *hsqcetgpsp.2* sequence provided in the standard Bruker library and uses SPs for inversion and refocusing of ^{13}C spins. OCT-derived pulses were used for these purposes. The pulse parameters of the corresponding BIBOP and BURBOP shapes such as bandwidth ($\Delta\nu$), RF levels ($u_{\mathrm{RF}}^{\max}$), pulse length (T), compensation of B_1 variations (ϑ) and the number of pulse increments are given in accordance to the nomenclature introduced in [12] such as BURBOP-α($\Delta\nu$, $u_{\mathrm{RF}}^{\max}$, T, ϑ, #points). The 180° pulses acting on ^{13}C were replaced by BIBOP (37.5 kHz, 10 kHz, 600 μs, ±5%, 1200) for inversion and BURBOP-180(37.5 kHz, 10 kHz, 1100 μs, ±5%, 2200) for refocusing. Both were introduced in [15].

Decoupled HSQC experiments on the imidacloprid/pyridine precursor mixture were recorded on a 600 MHz Bruker Avance III spectrometer equipped with an inversely detected ^{1}H,^{13}C,^{15}N-triple-resonance cryogenically cooled TCI probehead using a sample of the compound mixture dissolved in DMSO-d_6 at a concentration ratio of 500/5 mM. Spectra were acquired with spectral widths of 3.6 and 18.9 kHz for ^{1}H and ^{13}C, respectively, corresponding to 6 and 125 ppm with the carrier frequencies set to 6 and 97 ppm. For the spectra shown in figure 2.41, data was collected for 127.9 ms and 3.40 ms in the ^{1}H and ^{13}C dimension, respectively. This corresponds to a data matrix of 920 × 128 complex data points which was zero-filled to 16384 × 256 points and apodized using a cosine-squared window function prior to FT and phase correction. Experiments were recorded using four scans and 16 dummy scans with a recovery delay of 3 s. Delays for magnetization transfer via $^{1}J_{\mathrm{CH}}$ couplings were set for a 145 Hz coupling constant. The pulse sequence was adopted from the *hsqcetgpsp.2* sequence provided in the standard Bruker library using the same pulse shapes for inversion and refocusing as given above. RF levels were calibrated automatically and the temperature was set to 300 K. The shapes for bilevel decoupling at $B_{1,\mathrm{RMS}}$ = 4.4 kHz and the four-step BROCODE cycle were calibrated according to the specifications given above. The spectra shown in figure 2.42 employed bilevel decoupling at $B_{1,\mathrm{RMS}}$ = 2 kHz and the BROCODE using the same parameters as given for figure 2.41 except as follows: Data was collected for 511.80 ms in the ^{1}H dimension (the same 3.40 ms were recorded in the ^{13}C dimension) which resulted in a data matrix of 3682 × 128 complex data points. LFP in the ^{1}H dimension was applied using 18 coefficients to obtain a data matrix of effectively 7364 × 128 complex data points which were zero-filled to 16384 × 256 points. For repetitive application of the BROCODE it was necessary to acquire a series of single-scan experiments and add up the time-domain data afterward. This is due to memory limitations of the spectrometer hardware and strongly depends on the console but can in principle be automated. The projection of both figures was taken from a highly-resolved 1D ^{1}H spectrum acquired using a spectral width of 4.8 kHz corresponding to 8 ppm with the carrier frequency set to 6 ppm. Data was collected in a single scan for 1.7 s corresponding to 16384 complex data points which were zero-filled to 32768 points. The time-domain data was apodized using an exponential line broadening of 0.3 Hz prior to FT and phase correction.

Experiments on (+)-borneol were also recorded on a 600 MHz Bruker Avance III spectrometer equipped with an inversely detected ^{1}H,^{13}C,^{15}N-triple-resonance cryogenically cooled TCI probehead using a sample dissolved in CDCl$_3$ at a 500 mM concentration. The DQF-COSY shown in figure 2.46 was acquired with spectral widths of 2.4 kHz in both ^{1}H dimensions corresponding to 4 ppm with the carrier frequency set to 2.5 ppm. Data was collected for 1.71 s and 106.75 ms in the direct and indirect dimensions, corresponding to a data matrix of 8192 × 512 complex data points which was zero-filled to 16384 × 1024.

Time-domain data was apodized using a sine-squared window function prior to FT. The spectrum was recorded using eight scans and 16 dummy scans with a recovery delay of 1 s. The *cosydfetgp.2* sequence provided in the standard Bruker library was employed. RF levels were calibrated automatically and the temperature was set to 300 K.

Decoupled HSQC experiments on (+)-borneol shown in figures 2.47 and 2.48 used spectral widths of 2.4 and 11.3 kHz for ^{1}H and ^{13}C, respectively, corresponding to 4 and 75 ppm with the carrier frequencies set to 2.5 and 45 ppm. Data was collected for 127.6 ms (red contours and slices), 511.66 ms (black contours and slices) in the ^{1}H and 3.40 ms in the ^{13}C dimensions, respectively. This corresponds to data matrices of 612 × 128 (red contours and slices) and 2454 × 128 (black contours and slices) complex data points which were zero-filled to 8192 × 256 points. Time-domain data was apodized using a cosine-squared window function prior to FT and phase correction. Experiments were recorded using four scans and 16 dummy scans with a recovery delay of 3 s. Delays for magnetization transfer via $^{1}J_{\mathrm{CH}}$ couplings were set for a 145 Hz coupling constant. The pulse sequence was adopted from the *hsqcetgpsp.2* sequence provided in the standard Bruker library using the same pulse shapes for inversion and refocusing as given above. The Insensitive Nuclei Enhanced by Polarization Transfer (INEPT) transfer element[120] prior to acquisition was replaced by a perfect echo INEPT (PE-INEPT) element to remove the effects of homonuclear J-couplings during heteronuclear magnetization transfer[121]. RF levels were calibrated automatically and the temperature was set to 300 K. The shapes for the four-step BROCODE cycle were calibrated according to the specifications given above. In cases where LFP in the ^{1}H dimension was applied, 33 coefficients were used to obtain data matrices of effectively 1224 × 128 (red contours and slices) and 4908 × 128 (black contours and slices) complex data points which were zero-filled to 8192 × 256 points. For repetitive application of the BROCODE a series of single-scan experiments was acquired and added up in the time-domain afterward. The projection of both the COSY and HSQC spectra was taken from a highly-resolved 1D ^{1}H spectrum acquired using the same spectral width as in the two-dimensional experiments. Data was collected in a single scan for 3.4 s corresponding to 16384 complex data points which were zero-filled to 32768 points. The time-domain data was apodized using an exponential line broadening of −0.1 Hz and a Gaussian multiplier with a maximum position at 0.6 relative to the FID prior to FT and phase correction. The same spectrum was used for figure 2.45 B.

Imidacloprid, 2-chloro-5-chloromethyl-pyridine and (+)-borneol were purchased from Sigma-Aldrich®. Deuterated solvents and ^{13}C-enriched methanol were purchased from Eurisotop®. All compounds were used without further purification.

3. Homonuclear Decoupling: RESET experiments

> I want us to face the shape we're in
> A world of confusion awaits our sons and kin
> Let's reset it all
>
> Karnivool - We Are (Asymmetry)

3.1. Introduction

3.1.1. Motivation

NMR structure parameters accessible in isotropic media such as chemical shifts, J-couplings and Nuclear Overhauser Enhancement (NOE) distances have their limits as far as the elucidation and verification of structure models of small to medium-sized organic molecules is concerned given that they are rather short-ranged. Therefore, high-resolution NMR spectroscopy experienced a major boost when weakly-orienting media were introduced to induce partial alignment upon the analyte molecule so that anisotropic structure parameters become available. Contributions to the Hamiltonian which exhibit an orientation dependence (see equations 1.16, 1.20 and 1.28) resurface to a small extent and become observable as RCSA [122], RQCs [123] and RDCs [124–128] in NMR spectra. The latter proved to be especially potent for solving structural problems. For small molecules in particular, heteronuclear one-bond RDCs, notably $^1D_{\mathrm{CH}}$ couplings, are highly interesting since they can correlate C-H vectors (the most basic spin systems in organic compounds) over longer distances than the NOE by using the B_0 field as an external orientational reference.

Already in isotropic liquids, $^1J_{\mathrm{CH}}$ couplings carry a wealth of information. They indicate the degree of hybridization of carbon atoms[129], serve as a measure of the configuration-relevant anomeric effect in saccharides[130] and can be used for the conformational refinement of peptides[131]. Together with $^1D_{\mathrm{CH}}$ couplings however, challenges with the structural elucidation of many different kinds of molecules in terms of conformation[132–136], relative configuration[119, 137–142] and constitution[143] could be met. Using chiral alignment media, enantiomers show differences in alignment so that questions concerning enantiomeric excess and absolute configuration of molecules can be addressed[144–147].

RDCs in general are obtained by evaluating the differences between isotropic J-couplings and the total couplings under anisotropic conditions given by

$$T = J + 2D. \tag{3.1}$$

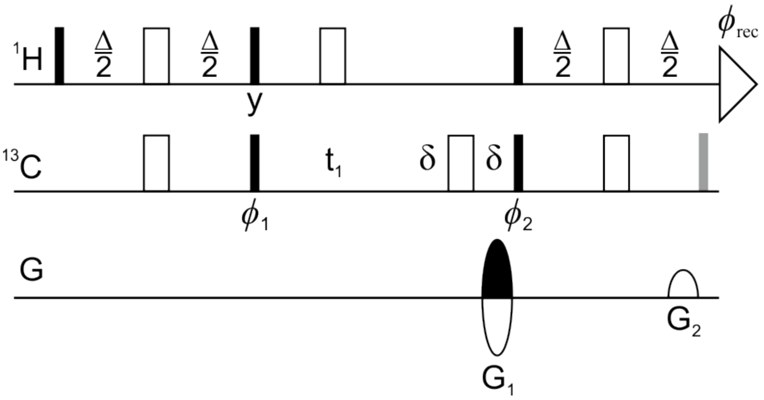

Figure 3.1.: Pulse sequence of the CLIP-HSQC. Narrow and wide bars correspond to 90° and 180° pulses, respectively. Phases are x unless indicated otherwise. Transfer delays are calibrated to match $\Delta = 1/(2^1J_{CH})$. Phases are $\phi_1 = x, -x$; $\phi_2 = x, x, -x, -x$ and $\phi_{rec} = x, -x, -x, x$. The narrow gray rectangle indicates a 90° pulse to ensure anti-phase removal which can be cycled according to ϕ_1. Delays δ accommodate for the applications of PFGs. Coherence order selection is applied with the gradients of ratio G_1:G_2 = 80:20.1 for ^{13}C as the heteronucleus. Phase-sensitive detection in the ^{13}C dimension is achieved by using an Echo/antiEcho-TPPI protocol.

In the case of $^1D_{CH}$ couplings, a massive interest in ^{1}H,^{13}C-HSQC-type experiments emerged, from which $^1J_{CH}$ and $^1T_{CH}$ couplings could be reliably extracted either from the direct[15, 113, 148–153] or indirect dimension[154–157]. All these experiments have shifted their emphases between sensitivity, resolution, robustness, line shape, speed and the multiplet structure of often notorious diastereotopic CH_2 groups. A good compromise between all those aspects and probably the most-widely used experiment is the CLIP-HSQC [113]. The pulse sequence is depicted in figure 3.1. The 90° pulse acting on ^{13}C prior to acquisition (indicated by a gray bar in figure 3.1) is meant to convert residual anti-phase magnetization (e.g. $2I_yS_z$) from incomplete INEPT back transfer to non-detectable multiple-quantum coherence (e.g. $2I_yS_y$) to prevent the former to introduce a dispersive contribution to the heteronuclear doublet. This yields purely absorptive signals with respect to the $^1J_{CH}$ coupling which can readily be extracted from in-phase doublets.

The most significant drawback of all HSQC experiments where couplings are obtained from the ^{1}H dimension are the abundant $^nJ_{HH}$ and $^nD_{HH}$ couplings which can cause overlap and asymmetric doublets due to line shape distortions arising from strong coupling. Both can impair an accurate determination of $^1J_{CH}$ and $^1T_{CH}$ couplings. In aligned samples in particular, ^{1}H nuclei can form highly complex networks due to $^nD_{HH}$ couplings which lead to a decrease in sensitivity and resolution. This effect is illustrated in figure 3.2. The gray contours indicate that under anisotropic conditions, resolution is lost. Therefore, possibilities to apply homonuclear ^{1}H decoupling to HSQC experiments in order to enable a more accurate extraction of one-bond couplings are explored in the following. It has to be noted that an approach based on dipolar decoupling was proposed some time ago[158]. However, it has not found as widespread applications and is far less general as the methods which will be discussed in section 3.1.2.

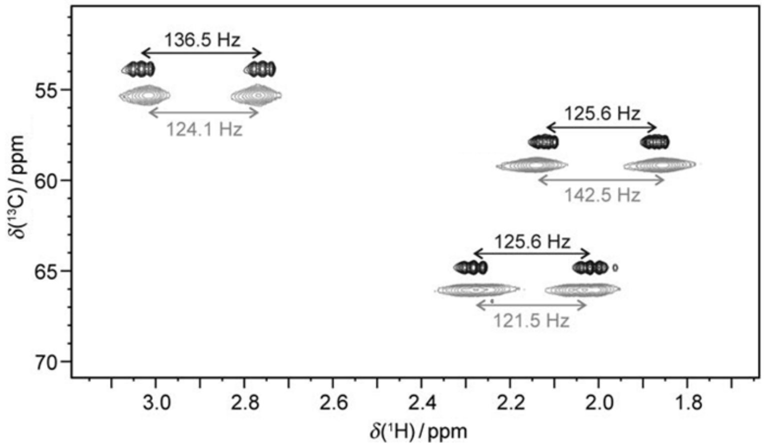

Figure 3.2.: Excerpts of an annotated CLIP-HSQC spectrum presented in [139] illustrating the effects on the line shape going from an isotropic environment (black contours) to an anisotropic environment (gray contours). ${}^1T_{\mathrm{CH}}$ couplings can either be increased or decreased by the dipolar contribution compared to the ${}^1J_{\mathrm{CH}}$ coupling. (Graphic taken and modified from [139])

3.1.2. Broadband Homonuclear Decoupling

Sensitivity and resolution are main concerns of NMR method and instrumentation developments. Higher static magnetic fields and novel probe technologies significantly boosted sensitivity but despite the increased chemical shift dispersion due to higher field strengths and the possibility to spread resonance lines across multiple dimensions, the resolution in ^{1}H spectroscopy poses a challenge in terms of signal overlap. Therefore, methods that collapse homonuclear multiplets to singlets have been pursued almost from the get go. Homonuclear decoupling approaches can be grouped in several categories. One of the oldest methods is a projection from a 2D J-resolved spectrum tilted by 45° in frequency space[159]. Unluckily, due to the phase-twist line shape of the traditional J-resolved experiment, the projection has to be taken from an absolute-value spectrum which limits the final resolution because of large feet next to the signals caused by the dispersive contributions. Apart from processing techniques (e.g. [160] and references therein), several experimental approaches towards absorptive line shapes have been proposed. Dispersive contributions can be removed from the spectrum by zero-quantum filtering[161] followed by the application of a multiplet reduction algorithm[162]. Alternatively, a conventional J-spectrum can be combined with a so-called *anti-J*-spectrum of same intensity that has a reversed tilt and is mirrored along the J-dimension in order to cancel dispersive signal components and yield the desired line shape[163]. The possibility to remove homonuclear splittings via J-evolution periods was exploited in Diffusion-Ordered SpectroscopY (DOSY) where reduced signal overlap facilitates more reliable extraction of diffusion coefficients[164, 165].

In general, phase-sensitive homonuclear decoupled spectra can be obtained in various ways. The effect of homonuclear J couplings during evolution periods can either be kept constant (and therefore practically hidden) or be refocused. A constant-time (CT) period allows for the evolution of chemical shifts for a variable period while the evolution of *J* couplings is kept constant by shifting a 180° pulse in an indirect dimension of a multi-dimensional NMR experiment[166, 167]. In addition to homonuclear decoupled 1D ^{1}H spectra, CT evolution is the only possibility to obtain COSY spectra with homonuclear decoupling in the indirect dimension[168, 169]. Direct *J*-refocusing approaches fail for COSY as they would collapse the anti-phase multiplets to zero intensity (unless an experiment is chosen that produces in-phase cross peaks[170]). CT experiments are widely used in biomolecular NMR to suppress homonuclear couplings among heteronuclei in isotopically enriched materials[171].

The most relevant methods to achieve broadband homonuclear ^{1}H decoupling employ *J*-refocusing elements using RF pulses. Since decoupling among the abundant ^{1}H nuclei can not be achieved by RF irradiation in the sense of chapter 2, the pulse sequences are based on the selection of sub-ensembles of spins. The result is an inherent sensitivity penalty given that a small set of active spins has to be selected which can then be decoupled from a larger set of passive spins to afford the decoupling and therefore increased resolution. This methodology became known as pure shift (PS) NMR and exploded into a plethora of experiments during the course of this thesis and which has already been extensively reviewed[172–174]. The fundamental principles at the core of all those experiments, however, are rather old. The first of the reported building blocks which can serve as what can be referred to as a single-spin inversion (SSI) element is the BIlinear Rotation Decoupling (BIRD) isotope filter element[175]. It acts as an effective 180° rotation on protons directly bound to a heteronucleus (e.g. ^{13}C) while leaving more remotely connected protons unaffected. Since the discrimination is facilitated by a difference of the magnitudes of heteronuclear *J*-couplings, the ^{13}C spin can be regarded as a local decoupling field. If ^{13}C-bound ^{1}H magnetization is selected, broadband homonuclear decoupling is achieved by the combination of the BIRD filter with a hard 180° pulse in the middle of a free evolution period as it will allow the chemical shift evolution of the active spins while refocusing the homonuclear *J*-couplings to the remotely-bound passive spins. By incrementing this evolution period and concatenating the first points of the resulting FIDs, a PS FID can be obtained. The sensitivity of this experiment depends on the natural abundance of the heteronucleus which is 1.1% in the case of ^{13}C. Although the BIRD element was introduced as a PS method, up until recently it was mostly used as a building block in heteronuclear correlation experiments[154–157, 176, 177].

A second pulse sequence building block that can be used in a PS context (although not necessarily a SSI element) is a succession of two small-flip-angle pulses ($\beta < 90°$). The fact that the efficiency of different coherence transfer pathways (CTPs) depends on the flip angle of a mixing pulse was first presented for the Exclusice COrrelation SpectroscopY (E.COSY) experiment[178], where cross peaks are simplified and appear as if COSY spectra with different selected coherence orders were combined. The same effect can be achieved by two successive 90° pulses, phase-shifted by β, which was also the basis of the less-used time-reversal method[179]. However, if a small-flip-angle pulse pair is used instead of a 90° mixing pulse, COSY peaks are simplified in a way that is more suitable to obtain PS ^{1}H spectra. In the z-COSY experiment[180], diagonal and cross peaks of the active spins only retain those multiplet components where the passive spins have the same spin state in both the direct and indirect dimension and the remaining transitions are suppressed if β is sufficiently small. The resulting diagonal peaks therefore completely lie along the diagonal. The *anti*-z-COSY provides diagonal peaks where all multiplet components lie perpendicular to the diagonal by inserting an additional 180° rotation prior to the β pulse pair. Now only multiplet components are retained in which the spin states of passive spins in the indirect dimension was different from the direct dimension. Therefore the spectrum can be tilted by 45° just as a J-resolved spectrum and the diagonal peaks can be used to obtain an absorption-mode PS spectrum from a projection[181]. Also the possibilities to decouple via small-flip-angle pulses has not been taken up again until recently.

Certainly the most significant approach was presented by Zangger and Sterk[182] and their seminal work of 1997 introduced two major concepts at once. First, the sub-ensemble selection can be achieved by spatial frequency encoding. A combination of a band-selective 90° pulse with a PFG leads to broadband excitation of each resonance at a given sample volume. J-refocusing is achieved by the combination of a hard and selective 180° pulse while a PFG is applied simultaneously so that the active spins of a given slice of the sample experience a 360° rotation and are decoupled from all passive spins by the hard 180° pulse. This Zangger-Sterk (ZS) SSI also sits in the middle of an indirect ^{1}H chemical shift evolution period but the second novelty that was introduced concerns the data acquisition. It is not mandatory to restrict the collection of data to the single point in time where homonuclear couplings are refocused. Chunks of data can be recorded for as long as $\mathrm{AQ} \ll J^{-1}$ is fulfilled, which corresponds to several ms in the case of $^{\mathrm{n}}J_{\mathrm{HH}}$ couplings which are typically below 20 Hz. The result is a reduced time requirement to obtain a PS FID since it can be concatenated from usually only a few dozen chunks which is why this and related methods are referred to as interferogram-based or pseudo-2D experiments. Now that only a few increments of an indirect dimension are needed, PS spectra can be acquired in minutes rather than hours. The sensitivity is clearly reduced since only a small portion of spins contribute to the signal at a given resonance frequency. More specifically, this depends on the minimum chemical shift difference of spins that need to be decoupled as it defines the necessary selectivity $\Delta\nu$ of the selective pulse which in turn defines the slice thickness Δz in combination with the slice selection gradient G_s via

$$\Delta z = \frac{\Delta\nu}{\gamma} \cdot G_s. \tag{3.2}$$

The ZS element resurfaced in the context of DOSY experiments where signal overlap is a significant impediment for the determination of diffusion coefficients[183]. Several modifications to the original pulse sequence were proposed and the term PS NMR was established[184]. A modified ZS pulse sequence is depicted in figure 3.3 A. For simplicity, slice-selective excitation was replaced by a hard 90° pulse. This necessitates selection of the active spins by CTP gradients to obtain clean spectra. Further, the newly-introduced delays τ not only accommodate for PFGs and recovery delays. The additional echo time around the hard 180° pulse can delay the refocusing of homonuclear couplings optimally until the center of the data chunk while chemical shifts are refocused at the beginning of data acquisition. In terms of the PS trajectory, now not only the very flat initial region of the cosine wave but also the flat region of the terminal sine build-up can be monitored, effectively doubling the tolerable chunk length[184]. Such a ZS-based PS pseudo-dimension can readily be appended to two-dimensional experiments. The PS information of the direct dimension obtained from such pseudo-3D experiments can readily be transferred to the indirect dimension of the final spectrum by means of covariance processing[185], as was proposed for 2D-TOCSY [186, 187] and Nuclear Overhauser Enhancement SpectroscopY (NOESY) [188]. As mentioned above, SSI elements fail for COSY but covariance processing can be used to transfer the PS information of the indirect dimension of a CT-COSY spectrum to the direct dimension[188]. The general shortcoming of the ZS method is that the sensitivity is connected to the slice thickness. An improved version has been proposed, where the offsets of the band-selective pulses are shifted after each scan, so that fresh reservoirs of polarization are available and relaxation delays can be shortened[189].

The improved ZS data sampling scheme could successfully be applied to the BIRD method[190]. The pulse sequence is depicted in figure 3.3 B. Again, a combination of a hard 180° pulse and an SSI, here a BIRD filter, facilitates the decoupling. Many different BIRD filters were proposed[191], using the spin species they affect with a 180° rotation as a superscript. This can be either combination of protons directly (d) or remotely (r) bound to the heteronucleus (X). The BIRD element in the gray box of figure 3.3 B corresponds to a $\text{BIRD}^{\text{d,X}}$ filter which refocuses chemical shifts and homonuclear couplings but not heteronuclear couplings for the directly coupled CH group. Given that ^{13}C-bound protons are selected by a stimulated echo and omitting the first ^{13}C pulse on alternate transients, the ^{1}H 180° pulse has to be timed so that heteronuclear couplings are refocused at the beginning of acquisition, homonuclear couplings 2τ later, and chemical shifts have evolved for t_1. Since ^{13}C-bound protons are observed, heteronuclear decoupling has to be applied during acquisition. The correct CTP is enforced by PFGs. A major advantage of the BIRD method is that it can bypass strong coupling (where the ZS-based experiment would fail) if the ^{13}C satellite of a given signal is only weakly coupled to the passive proton. The downside is that geminal couplings within a diastereotopic CH_2 group can not be suppressed because both ^{1}H nuclei are attached to the same ^{13}C atom. It would further fail for isotopically enriched compounds. A BIRD pseudo-dimension is predestined to be incorporated into heteronuclear correlation experiments, where the sensitivity penalty has already been paid and only a loss of S/N per unit time has to be condoned. A similar approach has been pursued with the Reducing nuclEar Spin multiplicitiEs to singuleTs (RESET) HSQC [192], although the data sampling scheme is different in a way that a full 3D dataset is recorded and each FID acquired contributes to the final S/N. Any BIRD-based PS approach to long-range correlation experiments also has to fail since BIRD filters can not distinguish between different remotely-bound protons. A PS HMBC experiment was proposed using a J-resolved dimension[193].

From all PS methods discussed in this thesis, the double-β pulses were the latest bloomer. The approach was revived by the Pure Shift Yielded by CHirp Excitation (PSYCHE) experiment[194]. Figure 3.3 C illustrates the pulse sequence. Hard β pulses were replaced by swept-frequency pulses in the presence of a weak PFG. The sub-ensemble of active spins that is refocused by this stimulated echo and selected for the PS trajectory statistically depends on $\sin^2 \beta$ while the signal contribution of the passive spins depends on $\cos^2 \beta$ and needs to be suppressed. Since frequency sweeps are used instead of hard pulses, CTPs which would lead to cross peaks in a corresponding *anti*-z-COSY experiment as well as zero-quantum coherence evolution are blocked. Signals with different zero-quantum coherence evolution times can be superimposed across the sample just as described by Keeler[161]. Spurious signals from cross peak pathways are also dephased since the corre-

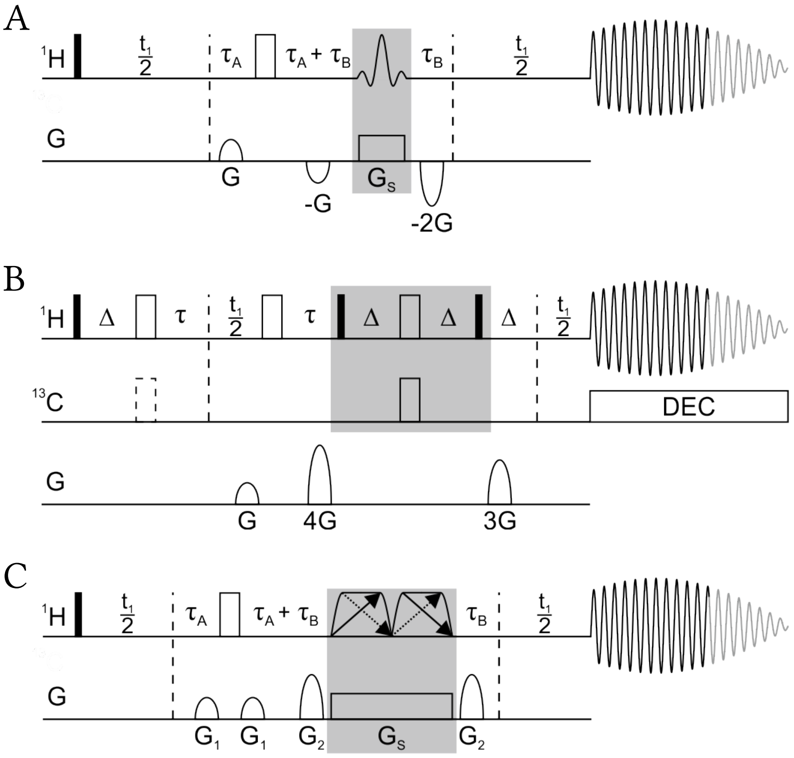

Figure 3.3.: Interferogram-based pulse sequences for PS 1D ^{1}H NMR. Narrow and wide bars correspond to hard 90° and 180° pulses, respectively. Phases are uniformly x. The SSI in each sequence is indicated by a gray box. The sinc shape corresponds to a band-selective 180° pulse which facilitates J-refocusing in the ZS sequence (A). Heteronuclear transfer delays in the BIRD sequence (B) are calibrated to match $\Delta = 1/(2^1 J_{\mathrm{CH}})$. The dashed 180° pulse is omitted in alternate transients. Trapezoids with diagonal arrows indicate low-power frequency-swept CHIRP pulses with low flip angles used in the PSYCHE sequence (C). They can be replaced by pulses which sweep frequencies in opposite directions simultaneously as indicated by dotted arrows. Delays τ accommodate for the applications of CTP gradients and allow for prolonged data chunks if τ_A (A, C) and τ (B) are chosen as AQ/4n with n being the number of data chunks.

sponding spins are on resonance at different times during the two sweeps. A unique feature of the PSYCHE element is that spectral purity can be tuned according to the choice of β since the intensity of the PS signals depends on $\sin^2 \beta$ whereas the intensity of spurious signals depends on $\sin^4 \beta$. PSYCHE shares almost none of the weaknesses of other PS methods and is far less prone to strong coupling. S/N can be further improved when double frequency sweeps are used as indicated by dotted arrows in figure 3.3 C. The PSYCHE element can be incorporated in the indirect dimension of a TOCSY sequence so that the resulting spectrum can be subjected to covariance processing to yield a PS TOCSY without a penalty in S/N per unit time[195] (apart from having to record enough t_1 increments to benefit from decoupling). Further, it can be used to remove dispersive signal components in J-resolved spectra[196] or to specifically reintroduce couplings to a chosen spin in a related experiment[197].

In parallel to the interferogram-based experiments, methods were proposed that circumvent the biggest disadvantage of PS techniques so far, which is the increased time consumption a pseudo-dimension ensues. The first experiment that incorporated real-time (RT) broadband homonuclear decoupling was based on BIRD elements in the middle of short acquisition windows[198]. RT PS acquisition relies on stopping the acquisition and internal spectrometer clock, inserting an SSI to achieve homonuclear J-refocusing, leaving the chemical shift trajectory in the same state as it has been when acquisition was stopped and then resume the collection of data points. These acquisition windows should be reasonably short to fulfill the condition $\mathrm{AQ}/n \ll J^{-1}$ just as in interferogram-based experiments with n being the number of acquisition windows. All FID segments can be stitched together on the fly by the spectrometer software afterwards and do not require additional processing. The original pulse sequence to obtain BIRD-based RT PS 1D ^{1}H spectra is depicted in figure 3.4 A. This sequence also relies on selecting ^{13}C-bound ^{1}H magnetization and on an efficient suppression of ^{12}C-bound ^{1}H signals. This is achieved by purging heteronuclear spin states $2I_zS_z$ by a PFG and inverting these states in alternate transients by omitting the dashed ^{13}C 180° pulse in figure 3.4 A. Further, a BIRD element flanked by gradients ensures that solely $2I_zS_z$ states are excited. XY-supercycling[199] can be used to increase the tolerance of BIRD filters towards a variation of $^1J_{\mathrm{CH}}$ couplings. To benefit from the improved data-chunking introduced in [184], the first acquisition period has to be half as long as all subsequent ones. The replacement of such a homospoil-sequence with a traditional HSQC-sequence creates an unrivaled situation among PS experiments. Given that the sensitivity penalty is paid by the selection of dilute heteronuclei via the HSQC transfer, RT homonuclear decoupling increases resolution and sensitivity at the same time due to the collapse of homonuclear multiplets[200]. Doublets within diastereotopic CH_2 groups remain as an irreducible multiplicity and are the only drawback that is specific to this method. A general downside that can be observed in all RT PS experiments is a loss in resolution due to broadened lines. Since acquisition is stopped but relaxation remains in effect, an artificial source of damping is introduced which causes the line broadening. Just recently, RT BIRD acquisition and ^{13}C-editing was proposed to replace the multiplet reduction algorithm (see [162]) in zero-quantum-filtered J-resolved spectroscopy[201].

RT acquisition was soon after proposed for the ZS approach[202]. Selection of the active spins resembles the original experiment and is achieved by slice-selective excitation. The FID is then periodically interrupted to apply the ZS SSI as described above. The corresponding pulse sequence is depicted in figure 3.4 B. This sequence affords ZS-based PS spectra in a reduced amount of time although sensitivity is still lost due to the slice-selection procedure. RT ZS acquisition can readily replace conventional acquisition in two-dimensional experiments as has been demonstrated for TOCSY [202], DOSY [203] and Rotating frame nuclear Overhauser Enhancement SpectroscopY (ROESY) [204]. A drawback which is specific to RT ZS decoupling is that the length of the selective 180° pulse has to be limited in order to prevent severe discontinuities in the resulting FID, so that the selectivity can be hampered. Several modifications to the RT ZS acquisition scheme have been proposed. Couplings with respect to a single spin can be reintroduced by adding an additional selective pulse to the ZS SSI, which removes the signal of the corresponding spin from the spectrum[205, 206]. Given that very small splittings may be hidden due to the

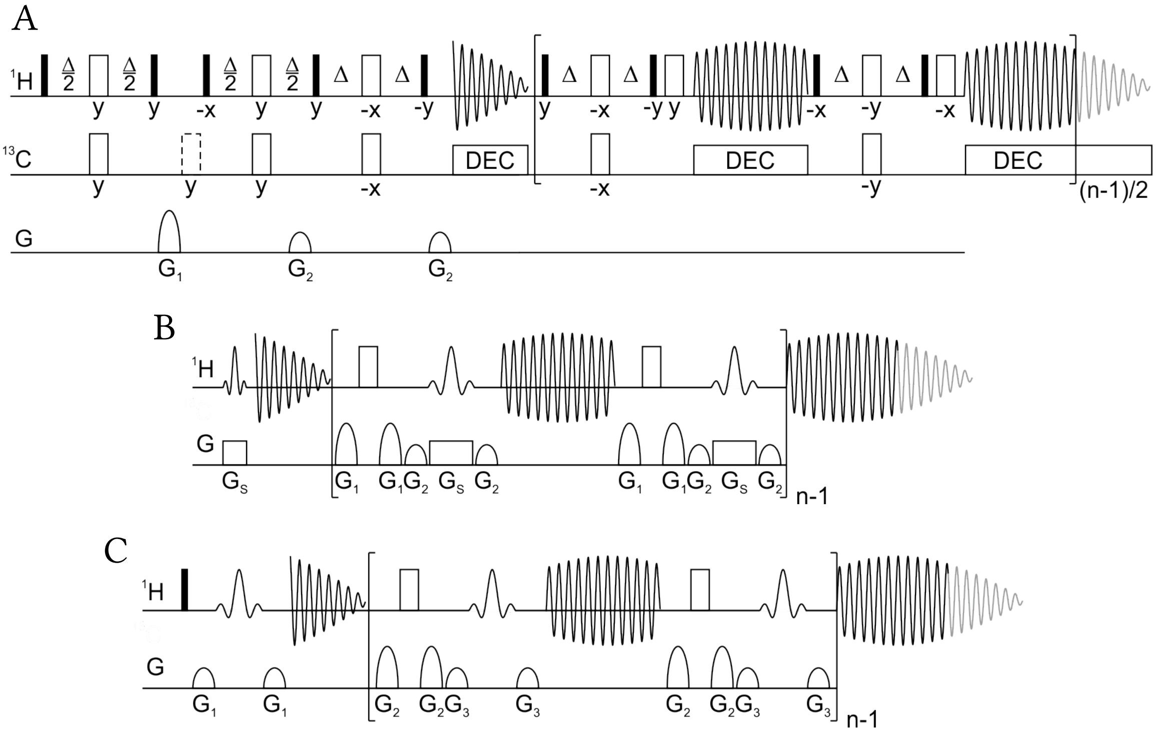

Figure 3.4.: Pulse sequences for RT PS 1D ^{1}H NMR. Narrow and wide bars correspond to hard 90° and 180° pulses, respectively. Phases are x unless indicated otherwise. Heteronuclear transfer delays in the BIRD sequence (A) are calibrated to match $\Delta = 1/(2^1J_{\mathrm{CH}})$. The dashed 180° pulse is omitted on alternate transients. Narrow and wide sinc shapes respectively correspond to band-selective 90° and 180° pulse in the ZS sequence (B). To obtain the HOBS sequence (C), the slice-selection gradient G_s has to be omitted and slice-selective excitation is replaced by broadband excitation of the whole sample before refocusing only the frequency region which shall contribute to the final spectrum.

line broadening introduced by RT ZS decoupling, an interferogram-based version of the same experiment was proposed soon after[207].

A very important offspring of RT ZS decoupling (although it can not be considered broadband) are the Homodecoupled Band-Selective (HOBS) experiments, sometimes referred to as Band-Selective Homonuclear (BASH) decoupling[208–210]. Here, the subset of active spins is a whole frequency region, which is decoupled from all spins outside that region by region-selective pulses. Unique to all PS methods, the active spins can be observed with the full sensitivity but mutual couplings within the selected frequency region can not be decoupled. Further, passive spins are completely removed from the spectrum, so that it might be necessary to acquire several spectra in succession. Therefore the method lends itself to be applied to types of molecules where the spectra can be easily divided in distinct regions such as peptides and proteins[208, 209]. The pulse sequence is shown in figure 3.4 C. By omitting the slice-selection gradient G_s, observation is restricted to spins which are refocused by the band-selective pulses, which may be far less selective now. The HOBS approach could be applied to TOCSY [208], NOESY [209], ROESY [204] and HSQC experiments[208, 209] as well as measurements of relaxation times[211]. The sensitivity and resolution achieved in the selected regions of HOBS experiments is competitive to PSYCHE although the method is not as general. However, the SSI of the PSYCHE experiment is too long to be applied in RT experiments so that HOBS experiments are unrivaled with respect to the S/N per unit time ratios for the decoupled spins.

3.2. RESET Experiments

3.2.1. Basic principle

The most promising starting point to work towards broadband homonuclear decoupled CLIP-HSQC spectra is the RESET HSQC [192]. According to the nomenclature introduced in [191], it uses a $\mathrm{BIRD}^{\mathrm{r,X}}$ filter to refocus all homonuclear couplings to ^{12}C-bound protons and $^{1}J_{\mathrm{CH}}$ couplings, while the chemical shift evolution of ^{13}C-bound ^{1}H nuclei is monitored during an indirect evolution period. If a $\mathrm{BIRD}^{\mathrm{r}}$ filter was inserted, the ^{13}C nuclei would remain effectively unperturbed and $^{1}J_{\mathrm{CH}}$ couplings can freely evolve as only ^{12}C-bound protons experience a 180° rotation. To benefit from the improved ZS data-chunking proposed in [184], the $\mathrm{BIRD}^{\mathrm{r}}$ element can be replaced by a combination of a hard 180° pulse and a $\mathrm{BIRD}^{\mathrm{d}}$ element with according delays as described in [190]. The resulting pulse sequence, which is referred to as CLIP-RESET HSQC in the following is depicted in figure 3.5. It differs from the conventional RESET HSQC as follows: the 90° pulse, indicated by the narrow gray rectangle, removes anti-phase coherences after incomplete heteronuclear transfer. It can be omitted alongside the 180° pulse in the gray box to obtain CLean Anti-Phase-HSQC (CLAP-HSQC)-type spectra[113]. These can be combined with their CLIP-RESET counterparts to allow the extraction of couplings from overlapping signals in an In-Phase Anti-Phase (IPAP) fashion[213]. After this, n FID chunks are collected in a PS pseudo-dimension which is incremented by AQ/n. Delays τ are chosen so that chemical shifts and $^{1}J_{\mathrm{CH}}$ couplings evolve for t_2 and the refocusing of homonuclear couplings is delayed for AQ/2n until the middle of each chunk. The FID chunks are then concatenated by the use of processing software[214]. This enables the user to drop points from the beginning of each data chunk to avoid distortions from digital signal processing and digital-to-analogue conversion[184]. The delay τ^* can be used to compensate for this in the pulse sequence. The correct CTP during the pseudo-dimension is enforced by PFGs. If HSQC spectra fully-decoupled in all frequency dimensions are desired, the dashed 180° pulse and a heteronuclear decoupling sequence during acquisition can be applied to obtain RESET-type spectra by the ZS data sampling scheme.

A CLIP-RESET HSQC spectrum obtained by using the experiment from figure 3.5 on a sample of (−)-menthol dissolved in $\mathrm{CDCl_3}$ is shown in comparison with a conventional CLIP-HSQC spectrum in figure 3.6. A gain in resolution due to a collapse of homonuclear multiplets can be seen for practically all cross peaks. However, on a closer look it can be seen that a PS heteronuclear doublet is only achieved for CH and $\mathrm{CH_3}$ moieties. The homonuclear doublets due to $^{2}J_{\mathrm{HH}}$ couplings within diastereotopic $\mathrm{CH_2}$ groups are retained as an irreducible multiplicity. Figure 3.7 compares slices extracted from the two-dimensional spectra for all carbon multiplicities and also shows examples for failed

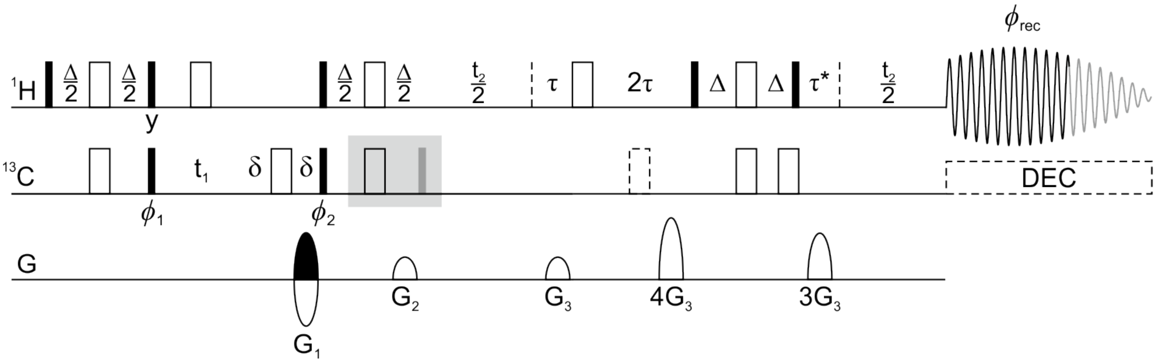

Figure 3.5.: Pulse sequence for the CLIP-RESET HSQC. Narrow and wide bars correspond to hard 90° and 180° pulses, respectively. Phases are x unless indicated otherwise. Heteronuclear transfer delays are calibrated to match $\Delta = 1/(2^1J_{CH})$. Phases are $\phi_1 = x, -x$; $\phi_2 = x, x, -x, -x$ and $\phi_{rec} = x, -x, -x, x$. The narrow gray rectangle indicates a 90° pulse to ensure anti-phase removal which can be cycled according to ϕ_1. Pulses in the gray box can be omitted to obtain CLAP-HSQC-type spectra. For the acquisition of CLAP spectra, ϕ_{rec} has to be changed to $y, -y, -y, y$. If only the 90° pulse in the gray box is omitted and the dashed 180° pulse is applied along with broadband heteronuclear decoupling during acquisition, fully decoupled RESET HSQC-type spectra can be obtained in a more time-efficient manner. The delay τ is set to AQ/4n with n being the number of data chunks. AQ/n corresponds to the length of each FID chunk and therefore corresponds to the t_2 increment. Delay τ^* allows for the compensation of phase distortions introduced by dropping points at the beginning of each FID chunk (see text). Delays δ accommodate for the applications of PFGs. Coherence order selection is applied with the gradients of ratio G_1:G_2:G_3 = 80:20.1:20 for ^{13}C as the heteronucleus. Phase-sensitive detection in the ^{13}C dimension is achieved by using an Echo/antiEcho-TPPI protocol. Graphic taken and modified from [212].

decoupling due to strong coupling. Whereas CH_3 and CH moieties can be fully homonuclear decoupled, diastereotopic CH_2 groups show the above-mentioned doublet-structure. The latter also display dispersive lineshapes given that $^2J_{HH}$ couplings do not evolve in synchronicity with chemical shifts because homonuclear couplings are active during all heteronuclear transfer delays and delays τ. The result of strong coupling can be observed for the cross peaks obtained for position 4 (figure 3.7 D). Signals show severe line shape distortions so that the heteronuclear doublets become asymmetric.

The S/N ratios of CLIP-RESET HSQC spectra can improve compared to the conventional CLIP-HSQC as far as the final data matrix is concerned. This gain as well as the gain in resolution comes at the cost of the time required to build up the final spectrum from the initial interferogram. So the S/N per unit time ratios drop by $\sqrt{n}$ and improve at best by the original multiplicity of the fully-coupled resonance line. In practice, slightly more moderate drops can be expected since the AQ in the detection dimension can be drastically reduced. Since the final FIDs are concatenated from chunks of length AQ/n, CLIP-RESET HSQC spectra show weak artifacts similar to decoupling sidebands at frequency multiples of n/AQ distributed around the signals. This is due to the modulation of each FID chunk by

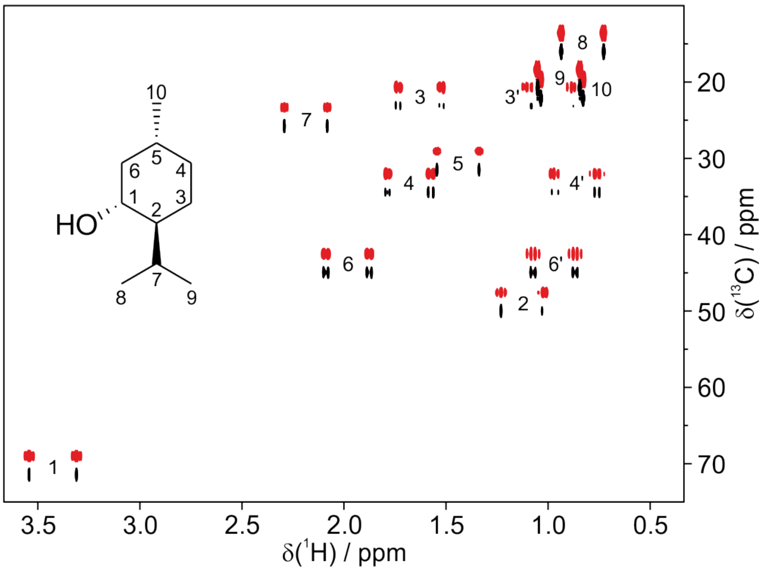

Figure 3.6.: Comparison of CLIP (red contours) and CLIP-RESET HSQC spectra (black contours) of (–)-menthol. The structure of (–)-menthol and atom numbering is given as an inset. Graphic taken and modified from [212].

signal evolution under the influence of $\cos(\pi^n J_{HH} t)$ terms. These discontinuities give rise to artifacts which in favorable cases stay at about 1-2% intensity if AQ/n is chosen so that $\cos(\pi^n J_{HH} AQ/n)$ does not significantly drop below 0.9 for representative $^nJ_{HH}$ couplings. As far as the extraction of $^1J_{CH}$ coupling constants is concerned, these sidebands do not hamper the accuracy of the extracted couplings as long as the overall line shape is unaffected. The measurement of couplings is easily possible for all weakly coupled spins. This also holds for CH_2 groups if all relevant homonuclear couplings lie in the weak coupling limit as the resulting heteronuclear doublets are symmetric and $^1J_{CH}$ couplings can reliably be extracted. For strongly coupled spins however, the line shape distortions render the measurement of coupling constants erroneous just as in conventional CLIP-HSQC spectra. On the other hand, CLIP-RESET HSQC spectra are simplified in a way that at least allows unambiguous identification of higher-order spectra from deviations from expected line shapes. The reliability of the extracted couplings will be further elaborated on in the following sections.

An experiment closely related to the one discussed in this section was developed in parallel and independently from this thesis[215].

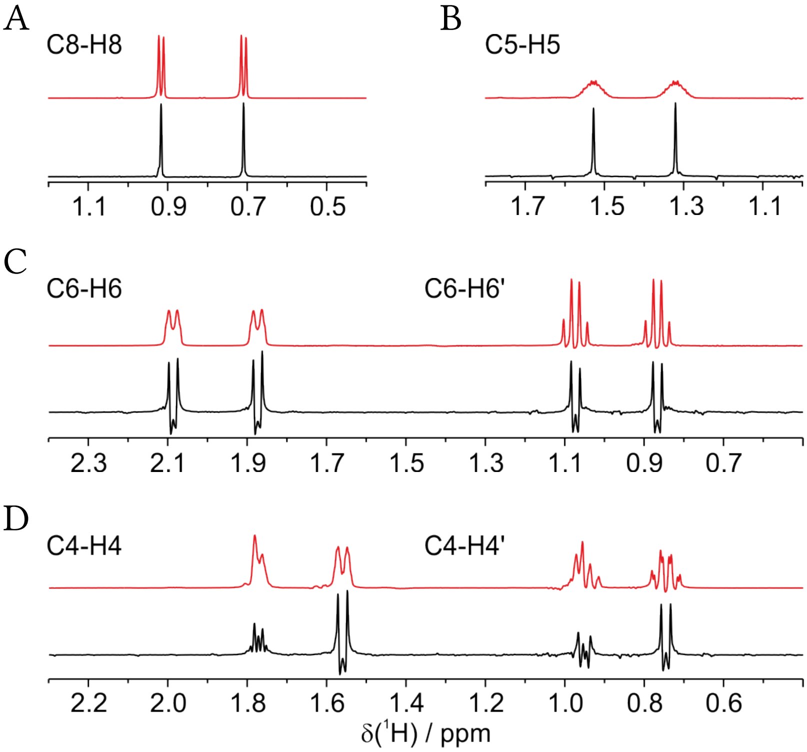

Figure 3.7.: Slices from CLIP (red) and CLIP-RESET HSQC spectra (black) of (−)-menthol. Heteronuclear doublet components can be reduced to single resonance lines for CH_3 (A) and CH (B) moieties. Weakly coupled diastereotopic CH_2 groups show a remaining splitting and dispersive lineshapes due to non-refocused ${}^2J_{HH}$ couplings (C). Strong couplings can not be suppressed by a single BIRD filter and lead to line shape distortions and asymmetric heteronuclear doublets (D). These allow for the immediate identification of strongly-coupled spins. Atoms are numbered according to figure 3.6. Graphic taken and modified from [212].

3.2.2. CT-RESET Experiments

As already discussed, BIRD-based PS methods fail to refocus the coupling evolution within CH_n groups. This retains the coupling evolution due to $^2J_{HH}$ couplings for CH_2 but also for CH_3 groups under anisotropic conditions. In order to suppress couplings within CH_n groups in RESET-type experiments, the BIRD element has to be combined with an additional source of decoupling from the ones discussed in section 3.1.2. Given that the CLIP/CLAP-RESET HSQC experiments rely on a pseudo-dimension to achieve J-refocusing, the t_2 evolution period can readily be replaced by a CT version. The PS acquisition scheme depicted in figure 3.5 can be replaced by the pulse sequence shown in figure 3.8 to yield CT-CLIP/CLAP-RESET HSQC experiments. Several subtleties had to be taken into account for the design of CT-RESET experiments. An echo period of AQ/2n had to be introduced to delay the refocusing of all $^nJ_{HH}$ couplings (n>2) until the middle of each FID chunk. Chemical shifts and heteronuclear couplings have to evolve for $t_2/2$ on either side of the BIRD element and finally, the total flip angle of ^{13}C-bound and ^{12}C-bound has to differ by 180° so that homonuclear decoupling is achieved. The sequence depicted in figure 3.8 is a possible solution that addresses all these issues. Given that it contains an even number of non-selective 180° pulses, a BIRD^r elements has to be used. Ideally, if strong coupling can be neglected, the maximum signal intensity for a CH_2 group should be reached if the CT evolution period T is set according to

$$T = \frac{m}{^2J_{HH} + {}^2D_{HH}} = \frac{m}{^2T_{HH}}. \tag{3.3}$$

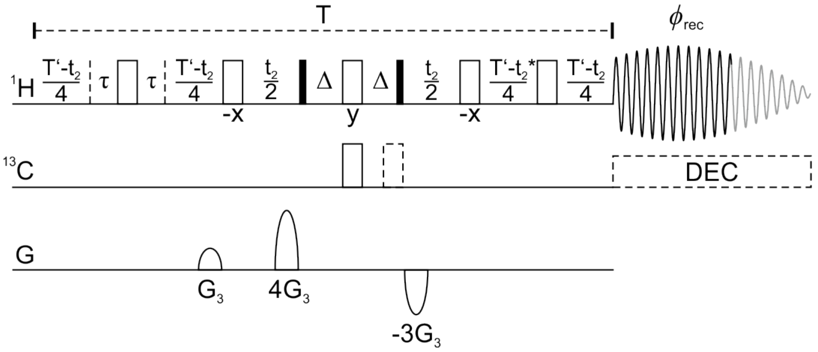

Figure 3.8.: Pulse sequence for a CT pseudo-dimension of CLIP/CLAP-RESET HSQC experiments. Narrow and wide bars correspond to hard 90° and 180° pulses, respectively. Phases are x unless indicated otherwise. For the acquisition of CLAP spectra, ϕ_{rec} has to be changed to $y, -y, -y, y$. Heteronuclear transfer delays are calibrated to match $\Delta = 1/(2^1J_{CH})$. If the dashed 180° pulse is omitted and broadband heteronuclear decoupling is applied during acquisition, CT versions of the fully decoupled RESET HSQC experiment can be obtained in a more time-efficient manner. The delay τ is set to AQ/4n with n being the number of data chunks. Decremented CT delays have to be corrected from the overall evolution period T according to equation 3.4. Delays marked with an asterisk allow for the compensation of phase distortions introduced by dropping points at the beginning of each FID chunk. Graphic taken and modified from [212].

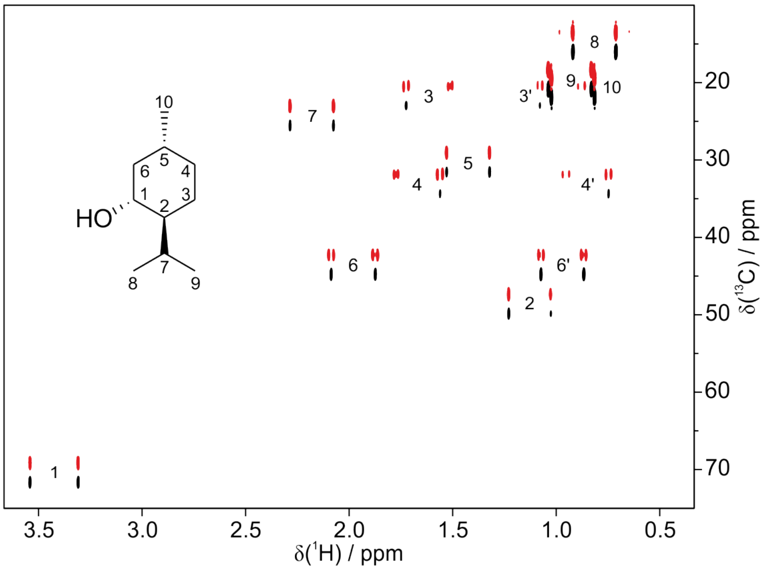

Figure 3.9.: Comparison of conventional (red contours) and CT-CLIP-RESET HSQC spectra (black contours) of (−)-menthol. The structure of (−)-menthol and atom numbering is given as an inset. Graphic taken and modified from [212].

Odd integers m will lead to negative cross peaks while even integers m will lead to positive cross peaks for CH_2 groups. The actual delays T' that have to be decremented in the pulse sequence shown in figure 3.8 have to be corrected from the overall evolution period according to

$$T' = \frac{1}{4} \cdot \left(T - 2\Delta - 2\tau - \sum t_p\right) \tag{3.4}$$

since all couplings which can not be refocused by BIRD elements are active during all heteronuclear transfer periods Δ, delays τ and the lengths of all individual pulses t_p. The cross peak intensities for CH_2 groups therefore no longer primarily depend on weakly coupled remote protons but are governed by their corresponding $\cos(\pi^2 T_{HH} T)$ terms, so that it might be necessary to record a number of experiments with different times T to cover a possible distribution of $^2J_{HH}$ couplings within CH_2 groups.

A CT-CLIP-RESET HSQC spectrum acquired on a sample of (−)-menthol dissolved in $CDCl_3$ is shown in figure 3.9 together with a reference conventional CLIP-RESET spectrum. The comparison clearly shows the additional decoupling of CH_2 groups in the case of position 6. However, several cross peaks only show one heteronuclear doublet component at the chosen contour levels. Figure 3.10 compares slices extracted from the two-dimensional spectra for the same cross peaks as in figure 3.7. In this example, the CT evolution period T was set to 333 ms, accommodating geminal coupling constants $^2J_{HH} = -12$ Hz for $m = 4$. This period defines the relaxation losses which are visibly suffered for the CH_3 and CH cross peaks depicted in figure 3.10 A and B. These losses can be overcompensated (or at least ameliorated) in cases where the doublets within CH_2 groups can be collapsed to singlets provided that the condition of equation 3.3 is met. This could be achieved for the weakly coupled CH_2 group at position 6 of (−)-menthol (see figure 3.10 C). However, CT incrementation can not prevent the dissipation

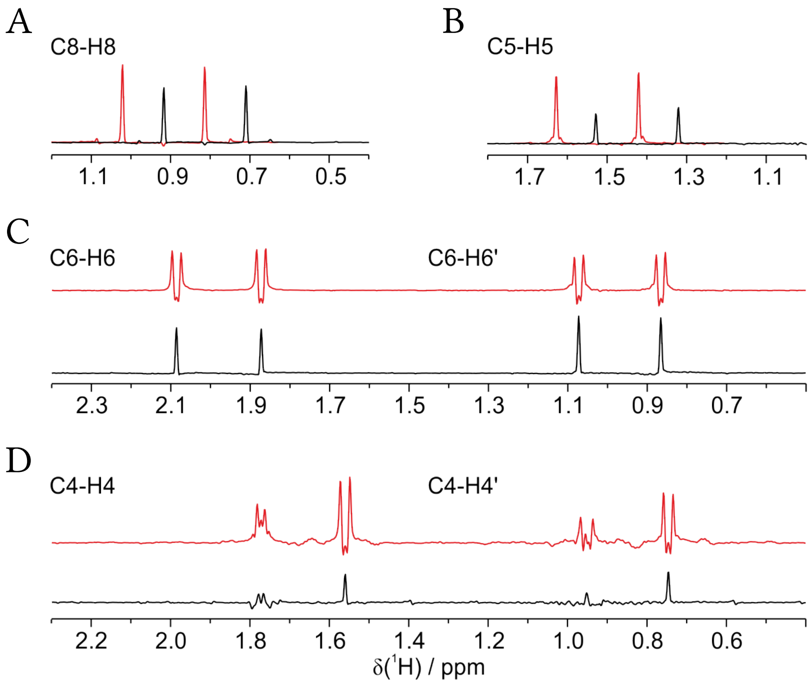

Figure 3.10.: Slices from conventional (red) and CT-CLIP-RESET HSQC spectra (black) of (−)-menthol. Collapse of heteronuclear doublet components to single resonance lines can now be achieved for CH_3 (A), CH (B) and weakly coupled diastereotopic CH_2 groups (C). As in conventional CLIP-RESET HSQC experiments, strong couplings can not be circumvented and lead to line shape distortions and asymmetric heteronuclear doublets (D). These allow for the immediate identification of strongly-coupled spins. Atoms are numbered according to figure 3.9. Graphic taken and modified from [212].

of magnetization due to strong coupling. Again, for position 4 (see figure 3.10 D), only one of the heteronuclear doublet components for each proton can be reduced to a single resonance line. Here, the decoupling can not compensate for the relaxation losses and the line shape distortions of the respective other doublet components clearly indicate that the simple extraction of one-bond couplings will not lead to reliable data. Hypothetically, if absorptive line shapes were obtained in fully decoupled CT-RESET HSQC spectra, they could be used together with one absorptive heteronuclear doublet component obtained in CT-CLIP-RESET HSQC spectra to extract the corresponding $^1J_{CH}$ coupling constant.

Table 3.1 compiles $^1J_{CH}$ coupling constants for (−)-menthol extracted from the spectra shown so far. The accuracy of the measured couplings is determined by a maximum error estimate as described in [119]. Generally, the values for $^1J_{CH}$ couplings can become more accurate upon homonuclear decoupling in the case of weakly coupled spins systems. The doublet C6-H6’ belongs to a weakly coupled CH_2 group and serves as an example where the accuracy is progressively improved going from conventional CLIP to CLIP-RESET and CT-CLIP-RESET HSQC experiments. For strongly coupled spin systems, it is far from trivial to predict the outcome of a manipulation by BIRD elements. For (−)-menthol, both a decrease as well as an increase of the widths of heteronuclear doublet components can be observed. This holds in particular among the spin systems containing CH_2 groups. For

Group	$^{1}J_{CH}$ / Hz (CLIP)	$^{1}J_{CH}$ / Hz (CLIP-RESET)	$^{1}J_{CH}$ / Hz (CT-CLIP-RESET)
C1-H1	139.2	139.1	139.1
C2-H2*	126.2 ± 1.6	124.8 ± 3.5	126.6 ± 4.1
C3-H3*	128.4 ± 3.6	126.8 ± 0.8	128.0 ± 6.3
C3-H3'*	124.4 ± 0.4	124.8 ± 0.8	123.2 ± 1.8
C4-H4*	125.8 ± 2.0	126.9 ± 0.9	126.9 ± 15.3
C4-H4'*	118.6 ± 4.9	122.9 ± 1.1	122.8 ± 0.5
C5-H5	123.6 ± 0.3	124.0 ± 0.1	124.2 ± 0.2
C6-H6	127.6 ± 0.1	127.5 ± 0.2	127.7
C6-H6'	123.4 ± 0.9	123.2 ± 0.6	124.0
C7-H7	127.2 ± 1.2	126.1 ± 0.1	126.1
C8-H8	124.9 ± 0.6	124.5	124.3
C9-H9	124.5	124.4	124.5 ± 0.1
C10-H10	124.5 ± 0.1	124.4	124.5

Table 3.1.: Comparison of $^{1}J_{CH}$ couplings for (−)-menthol extracted out of conventional CLIP-HSQC spectra and spectra obtained by the RESET-type experiments developed in this thesis. Groups marked with an asterisk are affected by strong coupling and the values for the coupling constants are not fully reliable. In cases where no maximum error estimate for the couplings is given, it was below 0.1 Hz.

group C3-H3', the maximum error estimate shows a gradual increase whereas for group C4-H4' a gradual decrease can be observed. In the extreme case of group C4-H4 the error estimate varies by an order of magnitude.

If this source of bias could be bypassed by the PSYCHE method, would be the topic of subsequent work. The possible advantages of CH_n decoupling and suppression of strong couplings would meet the disadvantage of an additional sensitivity penalty since the statistical sub-ensemble selection would further subdivide the portion of spins contributing to the signal. Very recently, a method based on indirect covariance has been proposed[216] that is completely insensitive to carbon multiplicity but depends on *a priori* PS input. It still has to be proven if this approach can generate CLIP-HSQC-type spectra. In parallel to this thesis, the perfectBIRD method was proposed[217] which makes use of the fact that once the protons of a CH_2 group have been reduced to an AX spin system, they are susceptible to a perfect echo sequence[218]. Although the perfectBIRD experiment allows for a distribution of $^{2}J_{HH}$ couplings, it usually fails for higher spin systems such as CH_3 groups under anisotropic conditions. The latter can in principle be adressed by CT-CLIP-RESET HSQC experiments. The lack of generality of the perfect echo is the reason why it is not *per se* considered a PS method but is limited to very specific applications such as Carr-Purcell-Meiboom-Gill (CPMG) sequences[219], HMQC experiments[220] and INEPT building blocks[121]. Finally, it has to be stated that both the perfectBIRD and the

CT-RESET approach fail for strong coupling and can either due to their complexity or inherently not be applied to RT BIRD acquisition.

3.2.3. Robustness

The experiments discussed so far are not compensated against a variation in $^1J_{\mathrm{CH}}$ couplings, resonance offsets or B_1-inhomogeneities. Standard experiments nowadays contain at least broadband inversion and refocusing pulses on the heteronucleus instead of rectangular 180° pulses. Further improvements can be expected if also 90° pulses are replaced by broadband excitation pulses. Additional slight improvements of spectral quality can be achieved if offset- and B_1-compensated pulses are also applied on ^{1}H. The classification along with the graphical representation of the required pulse shapes is introduced in figure 3.11 A. Broadband excitation requires a PP 90 transfer facilitated by BEBOP shapes. Broadband inversion and refocusing require PP 180 and UR 180 transfers facilitated by BIBOP and BURBOP-180 shapes, respectively (see section 1.2.3). 90° pulses used in the BIRD$^{\mathrm{d}}$ elements require UR 90 transfers and were replaced by BURBOP-90 shapes. In cases where RF pulses are applied simultaneously on both channels, J-compensated pulses for concurrent excitation and time-reversed excitation (PP 90$^{\mathrm{tr}}$) and vice versa are used. The corresponding pulse sandwiches are referred to as Broadband Excitation and time-reversed Broadband Excitation (BEBE$^{\mathrm{tr}}$) and time-reversed Broadband Excitation and Broadband Excitation (BE$^{\mathrm{tr}}$BE), respectively[17]. For concurrent refocusing of ^{1}H and inversion of ^{13}C, the J-compensated Broadband Universal Broadband Inversion (BUBI) pulse sandwich is used[17]. Both types of pulse pairs aim at avoiding losses of magnetization due to the evolution of $^1J_{\mathrm{CH}}$ couplings during the pulses. If the rectangular 90° and 180° pulses are replaced by the corresponding shapes, the SP-CLIP/CLAP-RESET HSQC experiments depicted in figure 3.11 B are obtained. These experiments efficiently address experimental issues such as large offset effects and B_1-inhomogeneities. To compensate the experiments against a variation of $^1J_{\mathrm{CH}}$ couplings, conventional INEPT transfer elements have to be replaced with the more robust Couplings, Offsets, B_1-deviation (COB)-INEPT building block[15]. It uses odd-flip angle pulses (UR α) and a series of transfer delays to facilitate uniform heteronuclear magnetization transfer spanning $^1J_{\mathrm{CH}}$ = 120-250 Hz. If plugged into the SP-CLIP/CLAP-RESET HSQC sequences, the COB-CLIP/CLAP-RESET HSQC experiments depicted in 3.11 C are obtained. It has to be noted that a COB-BIRD element is not yet known and will therefore become a topic in this thesis (see section 3.3). The pulse shapes required to carry out the experiments described in this section were introduced as part of [15] and [17] with the exception of the BURBOP-90 pulses required for the BIRD$^{\mathrm{d}}$ filters. The optimization procedure for this particular pulse shape as well as all experimental parameters for all other pulses are outlined in section 3.4. The newly-designed ^{1}H BURBOP-90 pulse is applied concurrently with a BIBOP shape on ^{13}C and was not matched according to the procedure described in [17]. This has to be kept in mind when experimental imperfections are discussed in the following. Further, a rectangular 90° pulse is still used for anti-phase removal after INEPT steps, since preliminary experiments indicated that the application of shaped CLIP pulses leaves the trajectory of the desired ^{1}H magnetization undefined during the pulse and leads to signal losses. The latter are kept

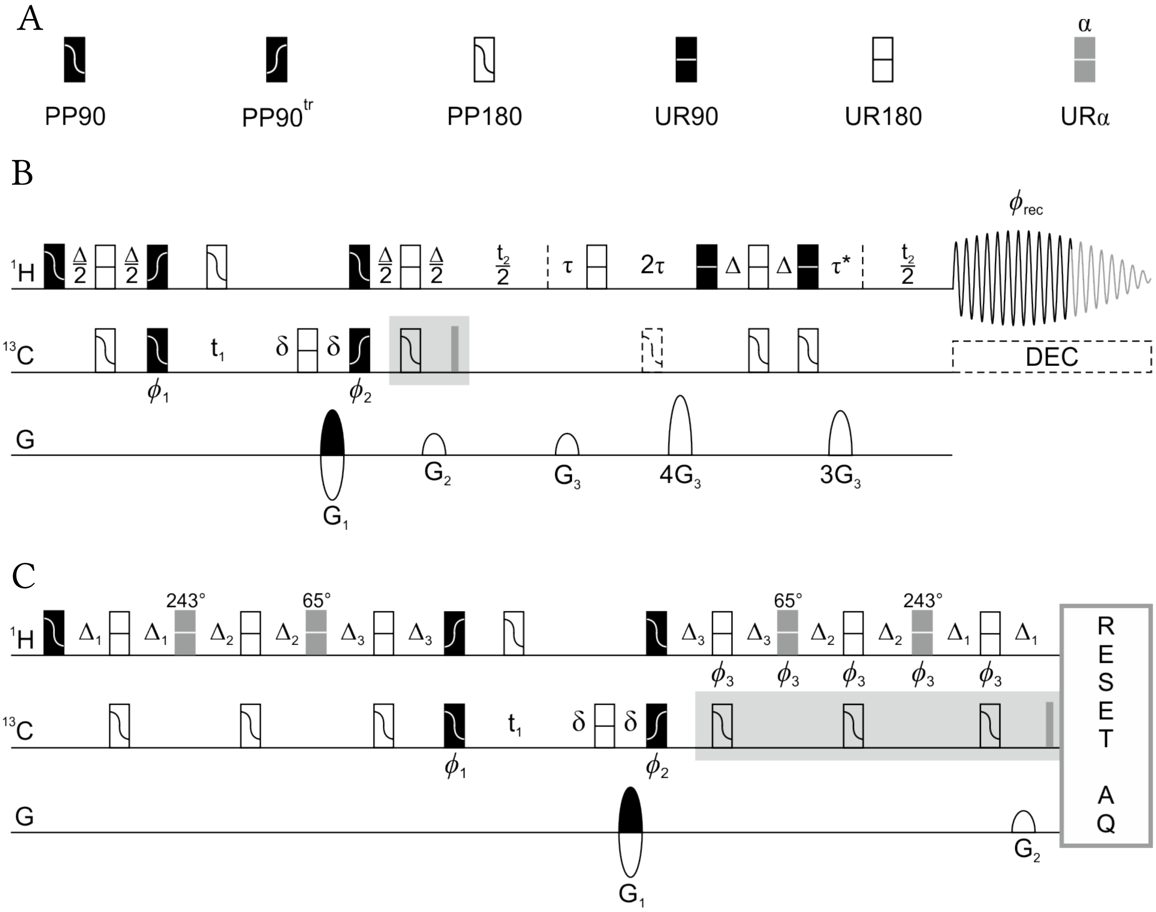

Figure 3.11.: Pulse sequences for compensated CLIP/CLAP-RESET HSQC experiments. Rectangular 90° and 180° pulses have been replaced by SPs according to their function depicted in the legend (A) and as described in the text. In SP-CLIP/CLAP-RESET HSQC experiments (B), heteronuclear transfer delays are calibrated to match $\Delta = 1/(2^1 J_{CH})$. In COB-CLIP/CLAP-RESET HSQC experiments (C), transfer delays are set according to $\Delta_1 = 1.469$ ms, $\Delta_2 = 2.135$ ms and $\Delta_3 = 0.394$ ms to facilitate uniform INEPT-type transfer spanning values for $^1J_{CH}$ of 120-250 Hz. Phases are x unless indicated otherwise and are cycled according to $\phi_1 = x, -x$; $\phi_2 = x, x, -x, -x$ and $\phi_{rec} = x, -x, -x, x$. The narrow gray rectangle indicates a hard 90° pulse to ensure anti-phase removal which can be cycled according to ϕ_1. Pulses in the gray box can be omitted to obtain CLAP-HSQC-type spectra. For the acquisition of CLAP spectra, ϕ_{rec} has to be changed to $y, -y, -y, y$ and for COB-CLAP-RESET experiments ϕ_3 has to be set to y. If only the 90° pulse in the gray box is omitted and the dashed 180° pulse is applied along with broadband heteronuclear decoupling during acquisition, fully decoupled RESET HSQC-type spectra can be obtained. The delay τ is set to AQ/4n with n being the number of data chunks. Delay τ^* allows for the compensation of phase distortions introduced by dropping points at the beginning of each FID chunk (see text). Delays δ accommodate for the applications of PFGs. Coherence order selection is applied with the gradients of ratio G_1:G_2:G_3 = 80:20.1:20 for ^{13}C as the heteronucleus. Phase-sensitive detection in the ^{13}C dimension is achieved by using an Echo/antiEcho-TPPI protocol. Graphic taken and modified from [212].

to a minimum if the CLIP pulse is kept as short as possible. The pulse sequence for a CT RESET acquisition scheme using SPs is given in appendix A.4.

To evaluate the performance of the experiments discussed so far, a compound mixture that provides a particularly wide range of offsets and $^1J_{\mathrm{CH}}$ couplings was prepared. Ethylvanillin, methylpropiolate and triethyl orthoformate were dissolved in DMSO-d_6 and used as a test sample in the following. Triethyl orthoformate can easily decompose into ethyl formate and ethanol and therefore gives rise to additional signals. Figure 3.12 shows example spectra obtained using the COB-CLIP/CLAP-RESET HSQC in comparison to reference COB-CLIP/CLAP experiments. Already in this representation, it can be deduced from signals of methylpropiolate (b2) and ethyl formate (d1), which display high $^1J_{\mathrm{CH}}$ values, that significant intensity losses are observable in RESET experiments. Those can be attributed to the BIRD elements which are not yet compensated for a large variation in $^1J_{\mathrm{CH}}$ couplings. To further break down the individual sources of signal losses, also conventional as well as SP-CLIP/CLAP-RESET experiments were collected for the compound mixture and compared to the reference spectra in figure 3.12. Thus figure 3.13 contains 1D slices from four different experiments. Fully-coupled COB-CLIP/CLAP-HSQC experiments provide 98% overall transfer with respect to the defined ranges of resonance offsets, B_1-inhomogeneities and $^1J_{\mathrm{CH}}$ couplings[15] and therefore define the maximum intensity achievable in the experiments under discussion. Whereas the signals shown in figure 3.13 A and A' are examples for possible gains in sensitivity due to the collapse of homonuclear multiplets, the subspectra B-E and B'-E' *per se* show no homonuclear splittings but allow for the examination of the different influences of uncompensated pulses and transfer elements on apparent intensity losses. Given that signals a1, a6 and c3 appear at the edges of the corresponding spectra, the sensitivity primarily benefits from the application of broadband pulses. Signal c1 lies rather in the center of the observed frequency ranges and shows the steadiest progression from conventional over SP to COB-CLIP/CLAP-RESET experiments. As expected, signals that benefit the most from the application of COB-INEPT elements, like d1 and in particular b2 of methyl propiolate ($^1J_{\mathrm{CH}}$ = 258 Hz), suffer the most severe intensity losses in RESET experiments which can be ascribed to uncompensated BIRD[d] elements. Further, anti-phase contributions to the heteronuclear doublets can be observed for b2 which is most likely caused by the BURBOP-90/BIBOP pulse pair that has not been matched with respect to the evolution of $^1J_{\mathrm{CH}}$ couplings. In total, sensitivity losses greater than 90% can be expected if completely uncompensated experiments are used on realistic natural abundance samples.

Another feature of the more robust COB-INEPT is the improved cancellation of heteronuclear doublet components when CLIP/CLAP-spectra are combined following the IPAP procedure[213]. In order to completely suppress one of the multiplet components, CLIP and CLAP spectra have to have identical signal magnitudes. Given that CLAP spectra do not require a second INEPT-type magnetization transfer, they always provide maximum cross peak intensities. In CLIP spectra however, J-mismatch leads to incomplete back-transfer of magnetization during the second INEPT step. This is illustrated in figure 3.14 where subsprectra from adding and substracting CLIP/CLAP-RESET experiments on (−)-menthol and the compound mixture from above using conventional and COB-INEPT are compared. Incomplete cancellation of heteronuclear doublet components can be observed where the heteronuclear coupling deviates from the nominal $^1J_{\mathrm{CH}}$ = 145 Hz as can be seen for the

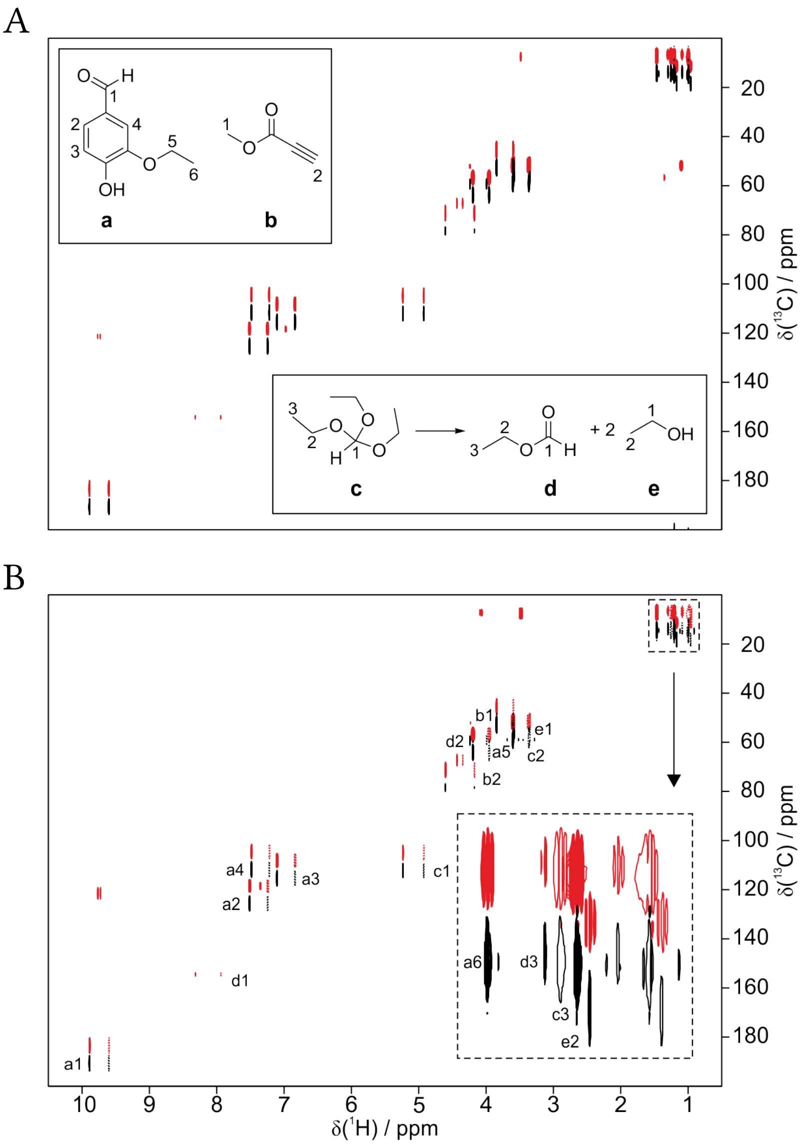

Figure 3.12.: Comparison of 2D COB-CLIP/CLAP- and COB-CLIP/CLAP-RESET HSQC spectra recorded on a mixture of ethylvanillin (a), methylpropiolate (b) and triethyl orthoformate (c) in DMSO-d_6. The impurities ethyl formate (d) and ethanol (e) are the result of the decomposition of (c). A reference COB-CLIP (red contours) and a COB-CLIP-RESET HSQC spectrum (black contours) are compared in (A). Chemical structures as well as labelling of the compounds and respective atom numbering are given as insets. The labels are applied to the corresponding COB-CLAP (red contours) and COB-CLAP-RESET HSQC spectra (black contours) shown in (B). The crowded region of the methyl groups inside the dashed box is magnified and shown as an inset. Negative contours are indicated by single contour lines (inset) or dashed lines (overview spectra). Graphic taken and modified from [212].

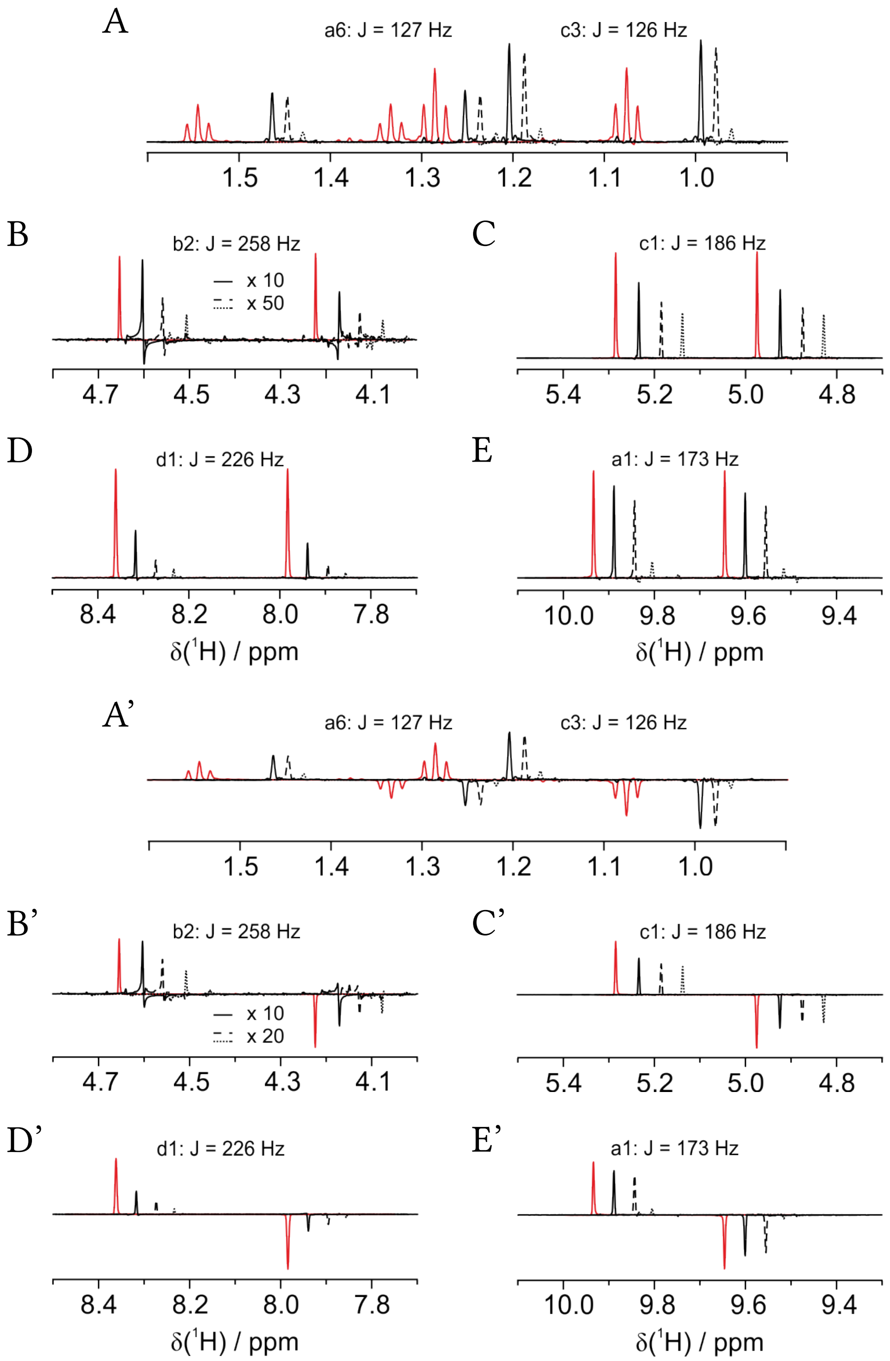

Figure 3.13.: Slices from altogether four spectra collected on the compound mixture depicted in figure 3.12 are shown: the fully-coupled COB-CLIP-HSQC (red solid lines) serves as a reference for the COB-CLIP-RESET (black solid lines), the SP-CLIP-RESET (black dashed lines) and the conventional hard pulse CLIP-RESET HSQC (black dotted lines). Compound and atom labels as introduced in figure 3.12 are added to subspectra A-E as insets next to the value of $^{1}J_{\mathrm{CH}}$. The traces of corresponding CLAP experiments (A'-E') are indicated by a prime. Note the magnification of subspectra B and B' given by the legend shown as an inset. Graphic taken and modified from [212].

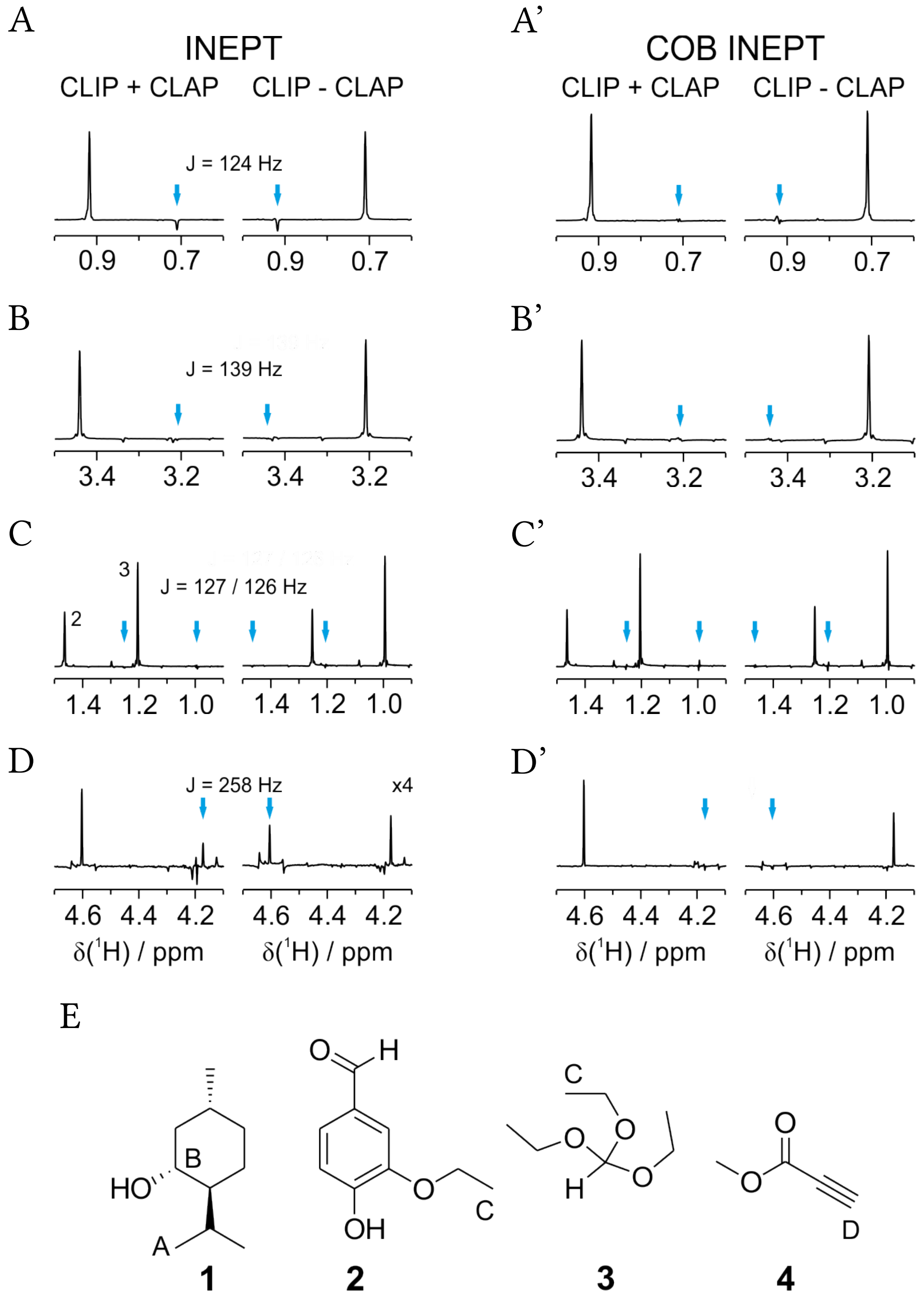

Figure 3.14.: Comparison of subspectra from addition and substraction of CLIP/CLAP-RESET experiments using (−)-menthol (1) and a mixture of ethylvanillin (2), triethyl orthoformate (3) and methylpropiolate (4). Spectra shown in the left column were recorded using conventional INEPT (A-D) and delays set to $\Delta = 1/(2 \cdot 145\text{ Hz})$ while the traces in the right column employ COB-INEPT (A'-D'). Blue arrows indicate the positions of the canceled heteronuclear doublet components. The values for $^1J_{CH}$ are given as insets. A phase correction had to be applied to the signals in (D) and (D') with the former being magnified by a factor of four. The structures of the compounds and peak annotations are given in (E). Graphic taken and modified from [212].

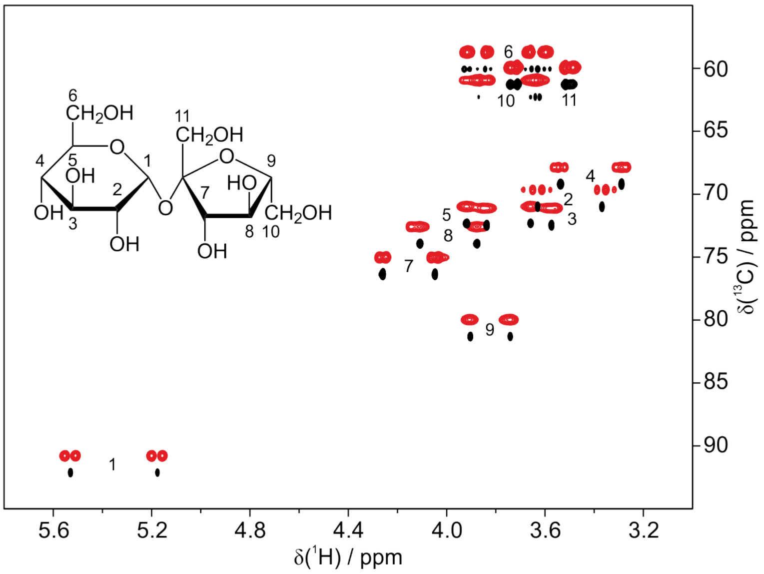

Figure 3.15.: Comparison of COB-CLIP (red contours) and COB-CLIP-RESET HSQC spectra (black contours) of sucrose in a stretched gelatin/D_2O gel 30% (w/v) for a resulting quadrupolar ^{2}H splitting of the solvent of $\Delta\nu_Q$ = 271 Hz. The structure of sucrose and atom numbering is given as an inset. Graphic taken and modified from [212].

CH_3 group of (−)-menthol (see figure 3.14 A) and even more pronounced for the CH group of methylpropiolate (see figure 3.14 D). If the coupling is closer to the nominal value for INEPT or the COB-INEPT is used, which tolerates couplings between 120 and 250 Hz, only very small artifacts remain adjacent to the positions of the canceled multiplet components (see figure 3.14 A'-D'). These appear most likely due to residual phase misadjustments or correspond to sidebands caused by the PS acquisition scheme.

So far it has been shown that homonuclear decoupling can strongly improve the resolution for conventional isotropic samples. Partially aligned samples on the other hand experience a multitude of homonuclear RDCs which result in complex coupling networks among the spins such that hardly any homonuclear multiplet structure can be resolved. To investigate the applicability of the PS methodology on RDC measurements, COB-CLIP-RESET HSQC spectra were recorded on a sample of sucrose in gelatin/D_2O (30% w/v)[154] stretched to an extension corresponding to a quadrupolar ^{2}H splitting of the solvent of $\Delta\nu_Q$ = 271 Hz. A comparison with a conventional COB-CLIP-HSQC spectrum is given in figure 3.15. In general it can be recognized that a significant line narrowing could be achieved due to the partial refocusing of the homonuclear dipolar interactions. The multiplicity of all CH cross peaks could be reduced to heteronuclear doublets whereas the resolution could not be improved for the CH_2 moieties. Figure 3.16 compares slices extracted from the two-dimensional spectra for different CH and CH_2 groups. Whereas the cross peak of the anomeric center (C1-H1) displays a symmetric shape and only a homonuclear doublet need to be decoupled, the heteronuclear doublet components of signal C2-H2 are distorted and result in an asymmetric doublet in the conventional COB-CLIP-HSQC spectrum (see figure 3.16 B). Here, BIRD-based homonuclear decoupling can circumvent these effects as described in [190] and singlets are obtained for each component of the

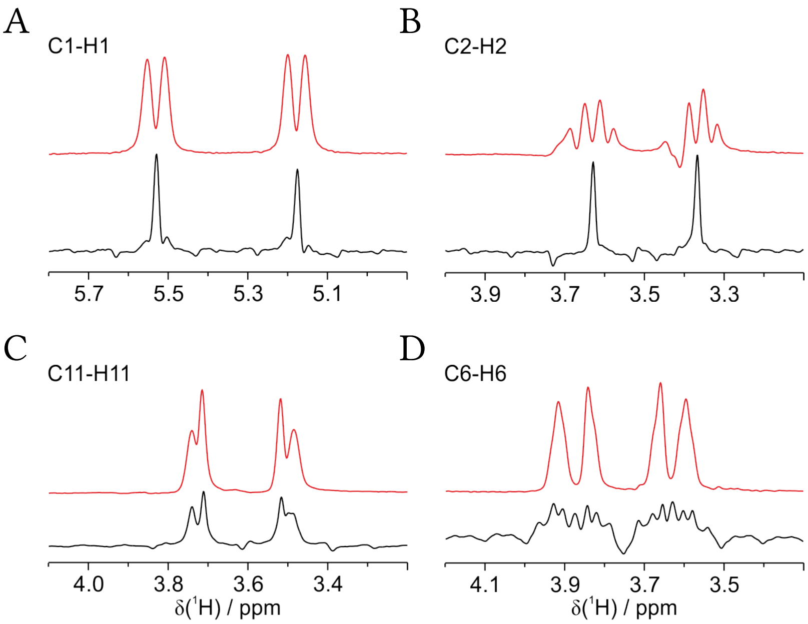

Figure 3.16.: Slices from COB-CLIP (red) and COB-CLIP-RESET HSQC spectra (black) of partially aligned sucrose. Heteronuclear doublet components can be reduced to single resonance lines for CH moieties (A) even in cases where distortions due to strong or longe-range heteronuclear couplings are observable (B). Cross peaks of CH_2 groups can not be further simplified (C) or even lead to highly distorted signals (D) which indicate strong coupling networks. Atoms are numbered according to figure 3.15. Graphic taken and modified from [212].

symmetric heteronuclear doublet. For CH_2 groups, however, no simplification of any cross peaks can be observed. On the contrary, rather than discernable dispersive doublets, highly distorted signals are obtained for the C6-H6 resonance (see figure 3.16). Obviously, complex coupling networks are formed which can not be deconvolved by the methods presented in this work, including CT-RESET experiments. Values for $^1T_{CH}$ couplings could therefore not reliably extracted for these moieties. The RESET experiments on sucrose suffer from significantly increased sideband amplitudes. These are introduced since each FID chunk more severely deviates from a PS trajectory due to the more pronounced modulation by a multitude of $\cos(\pi^n T_{HH} t)$ terms. At a given degree of alignment, this can only to a limited extent be ameliorated by shorter FID chunks. So the experiments presented here suffer more from a reduced S/A rather than S/N ratio. The effect on the accuracy of the extracted one-bond couplings will be discussed further below.

Another feature of BIRD-based homonuclear decoupling is the possibility to suppress artifacts from long-range correlations. Figure 3.17 illustrates this effect for signal C8-H8 of sucrose. In conventional CLIP-HSQC spectra, the signal at position 8 is affected by long-range correlations to position 7 and 9, which is easily recognized in the isotropic case (see figure 3.17 A). The effect is even more pronounced in the aligned sample (see figure 3.17 B) but not as easily discerned *a priori.* In RESET-type spectra, these artifacts can be suppressed so that symmetric heteronuclear doublets can be obtained. In the case

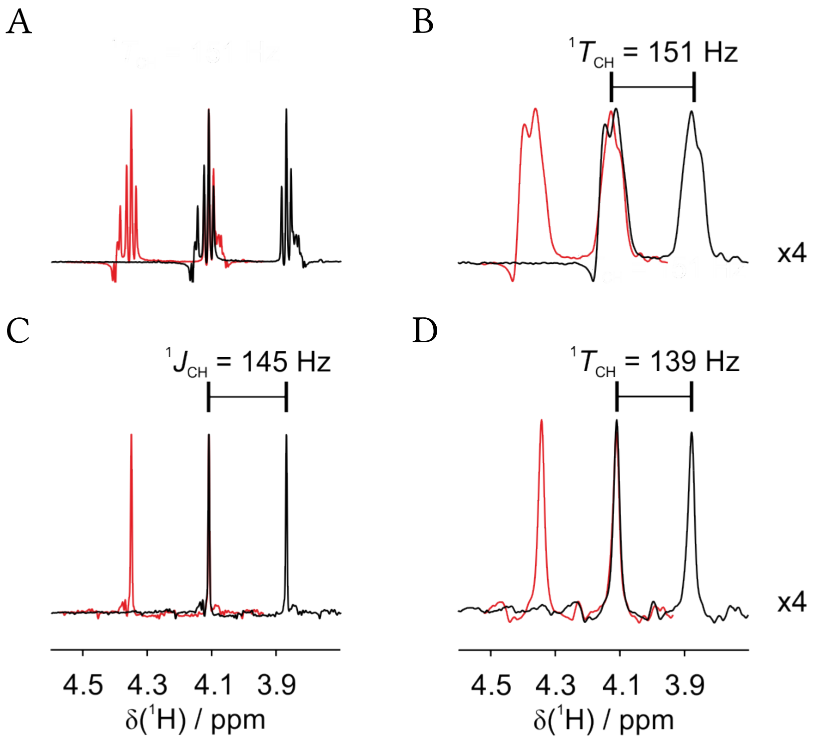

Figure 3.17.: Comparison of slices along the chemical shift of C8 of sucrose for the spectra shown in figure 3.15 and their isotropic counterparts. Couplings are extracted from the original slices (black) by determination of the maximum overlap between the doublet components with the help of a copy (red) as described in [119]. In conventional CLIP-HSQC spectra artifacts due to long-range correlations may be introduced which is clearly visible in the isotropic case (A). The effect is more dominant but less simple to recognize in the partially aligned sample (B). These artifacts can be removed by the BIRD filter (C and D), which can benefit the accuracy of the determined coupling as indicated by the insets. Note that the subspectra shown in (B) and (D) are scaled by a factor of four. Graphic taken and modified from [212].

of position 8 of sucrose this means that the measurement of a ${}^1D_{\mathrm{CH}}$ coupling with a wrong sign is prevented. In general, apart from the anomeric center, no symmetric heteronuclear doublets are obtained for sucrose under partially aligned conditions so that homonuclear decoupling improves the line shapes for almost all signals. This leads to improved accuracy of the extracted ${}^1D_{\mathrm{CH}}$ couplings in many cases and in particular when the spectral quality is affected already under isotropic conditions. Table 3.2 compiles ${}^1J_{\mathrm{CH}}$, ${}^1T_{\mathrm{CH}}$ and thereby derived ${}^1D_{\mathrm{CH}}$ couplings for sucrose obtained from conventional and homonuclear decoupled CLIP-HSQC spectra. Generally, the accuracy of the obtained one-bond RDCs is at least similar if not improved by CLIP-RESET-HSQC-type experiments at the cost of no anisotropic information about the $\mathrm{CH_2}$ moieties in the case of sucrose. This holds in particular for signals like position 7-9 where heteronuclear doublets appear asymmetric due to being affected by long-range correlations or strong coupling also under isotropic conditions. In summary, the family of CLIP/CLAP-RESET HSQC experiments developed

	CLIP			CLIP-RESET		
Group	$^1J_{\mathrm{CH}}$ / Hz	$^1T_{\mathrm{CH}}$ / Hz	$^1D_{\mathrm{CH}}$ / Hz	$^1J_{\mathrm{CH}}$ / Hz	$^1T_{\mathrm{CH}}$ / Hz	$^1D_{\mathrm{CH}}$ / Hz
C1-H1	169.7	212.0 ± 0.3	21.2 ± 0.2	169.7 ± 0.1	212.1 ± 0.6	21.2 ± 0.3
C2-H2	144.4	156.7 ± 0.5	6.2 ± 0.3	144.3 ± 0.1	156.8 ± 0.4	6.3 ± 0.2
C3-H3	145.3 ± 0.1	159.9 ± 0.4	7.3 ± 0.2	145.3 ± 0.2	158.0 ± 0.3	6.4 ± 0.2
C4-H4	144.5 ± 0.1	146.2 ± 5.0	0.9 ± 2.5	144.2	148.9 ± 0.8	2.4 ± 0.4
C5-H5	144.4 ± 0.1	154.2 ± 1.1	4.9 ± 0.6	144.3	155.9 ± 1.0	5.8 ± 0.5
C6-H6	144.0 ± 0.2	-	-	143.8 ± 0.1	-	-
C7-H7*	144.5 ± 0.1	128.7 ± 1.3	-7.9 ± 0.7	144.4 ± 0.3	127.0 ± 0.5	-8.7 ± 0.3
C8-H8*	144.8 ± 0.2	151.0 ± 6.6	3.1 ± 3.3	144.5	139.2 ± 0.4	-2.7 ± 0.2
C9-H9*	146.2 ± 2.4	96.3 ± 2.2	-25.0 ± 1.6	148.2 ± 0.4	97.4 ± 0.5	-25.4 ± 0.3
C10-H10	144.3 ± 2.4	-	-	143.3 ± 0.6	-	-
C11-H11	144.6	-	-	144.6	-	-

Table 3.2.: Comparison of heteronuclear one-bond couplings for sucrose obtained from conventional and homonuclear decoupled CLIP-HSQC spectra. $^1D_{\mathrm{CH}}$ couplings were calculated from $^1T_{\mathrm{CH}}$ and $^1J_{\mathrm{CH}}$ couplings according to equation 3.1 and maximum error estimates have been propagated accordingly. Groups marked with an asterisk are affected by long-range correlations due to strong coupling already under isotropic conditions which could be suppressed in RESET experiments. In cases where no values are given in the table, the multiplet pattern of the CH_2 groups did not allow for a reliable extraction of coupling constants. In cases where no maximum error estimate for the couplings is given, it was below 0.1 Hz.

in this thesis present a rather robust method to obtain one-bond heteronuclear couplings from reduced multiplets in a more simple and often more accurate manner. Strong coupling effects can occasionally be bypassed and at least be identified in a straightforward way by deviations from expected line shapes.

The measurement of heteronuclear coupling constants employing PS methods has been the subject of investigations in parallel and independently from this thesis (although not exclusively focused on ${}^1J_{\mathrm{CH}}$ couplings). The interferogram-based approaches to obtain PS 1D ^{1}H spectra have been used to identify remote couplings to abundant heteronuclei that would be otherwise hidden in complex ^{1}H multiplets. The BIRD sequence (see figure 3.3 B) was used to extract ${}^{\mathrm{n}}J_{\mathrm{HF}}$ couplings for fluorinated organic compounds[221] and a comparable ZS example (see figure 3.3 A) was given for ${}^{\mathrm{n}}J_{\mathrm{HX}}$ (X = ^{19}F, ^{31}P) couplings[222]. It has to be noted that such experiments primarily aim at identifying heteronuclei. They can not provide the same information content as multi-dimensional correlation experiments. As mentioned in section 3.1.2, BIRD-based PS methods fail for heteronuclear long-range correlation experiments. Alternatively, a CPMG-Heteronuclear Single-Quantum Multiple-Bond Correlation (HSQMBC) experiment employing ZS decoupling in a pseudo-dimension was proposed to obtain ${}^{\mathrm{n}}J_{\mathrm{HX}}$ (X = ^{13}C, ^{31}P, ^{77}Se) couplings from simplified anti-phase doublets[223]. PSYCHE can readily be applied to this experiment[224].

It was further attempted in this thesis to combine CLIP-HSQC experiments with RT BIRD-based homonuclear decoupling as in [200] but with only marginal success. The extracted couplings deviate from those obtained via CLIP or CLIP-RESET HSQC experiments by several %. It can only be speculated upon that periodical losses of magnetization due to J-mismatch of individual BIRD filters or the data acquisition scheme itself induce some modulation of the FIDs so that frequency errors are introduced that render the measurement of coupling constants erroneous. While it was reported that passive ${}^{\mathrm{n}}J_{\mathrm{HX}}$ and ${}^{\mathrm{n}}J_{\mathrm{CX}}$ (X = ^{2}H, ^{19}F, ^{31}P) couplings can be extracted from E.COSY-type cross peaks of RT BIRD-decoupled ^{1}H,^{13}C-HSQC spectra[225], it is now general consensus among the NMR community that the extraction of ${}^1J_{\mathrm{CH}}$ couplings from simplified multiplets depends on an interferogram-based PS acquisition[226]. However, HOBS-HSQMBC experiments apparently seem unaffected by such errors given that also values for ${}^1J_{\mathrm{CH}}$ couplings were reported[227]. As mentioned before, HOBS-experiments are less general, since mutual couplings within a selected region are not suppressed and only a part of the whole spectrum can be recorded at a time.

3.3. Optimal BIRD filters

3.3.1. General considerations

The original BIRD filter was introduced as a means to use the ^{13}C spin (or other heteronuclei) as a local decoupler field to achieve homonuclear ^{1}H decoupling[175]. This manipulation on a spin system can be described as a bilinear π-rotation on a heteronuclear two-spin system, hence the acronym BIRD. With both spins on resonance, the heteronuclear coupling Hamiltonian sandwiched between two 90° pulses yields a propagator of the

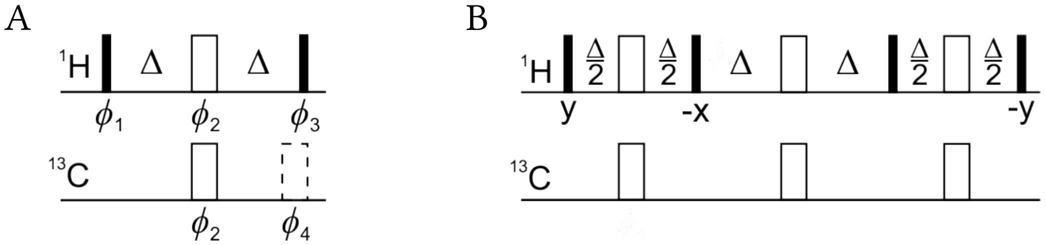

Figure 3.18.: Pulse sequences discussed in the original BIRD publication [175]. Narrow and wide bars correspond to 90° and 180° pulses, respectively. Phases are x unless indicated otherwise. Transfer delays are calibrated to match $\Delta = 1/(2^1 J_{\mathrm{CH}})$. The phases ϕ_1 to ϕ_3 in the original pulse sequence (A) can be set according to [191] to achieve $\mathrm{BIRD}^{\mathrm{d,X}}$ and $\mathrm{BIRD}^{\mathrm{r,X}}$ manipulations. The dashed 180° pulse with phase ϕ_4 can be set to achieve the corresponding $\mathrm{BIRD}^{\mathrm{d}}$ and $\mathrm{BIRD}^{\mathrm{r}}$ manipulations. Originally, $\phi_1 = y$, $\phi_2 = x$ and $\phi_3 = -y$ were proposed. The pulse sequence (B) facilitates a $\mathrm{BIRD}^{\mathrm{d,X}}$ rotation and is said to be less sensitive towards a variation in J couplings.

form

$$U_{\mathrm{BIRD}} = \exp\left(-i\pi 2 I_p^d S_z\right) \tag{3.5}$$

with p either x or y and I^d being ^{1}H magnetization of spins bound to the heteronucleus following the nomenclature of [191]. However, the flip angle only corresponds to 180° if the BIRD delays are matched to the value of the heteronuclear coupling. In the case of delay mismatch magnetization dissipates which causes sensitivity losses. This matter was seemingly addressed in the original publication[175] and the according pulse sequence is depicted in figure 3.18 along with the very basic BIRD filter that allows for various modifications[191] which will be discussed further below. The fidelities of any of these pulse sequence as a function of the magnitude of the heteronuclear coupling J can be assessed just like any 180° rotation. As discussed in section 1.2.3 the degree of spin inversion can be measured by Φ_{PP} $(I_z \rightarrow -I_z)$ or Φ_{UR} can be used to determine if the effective propagator comparable to equation 3.5 is produced. Whereas the former is straightforward, propagator analysis of a two-spin system hides certain subtleties. The fact that the phase factor of a propagator does not affect the final state of the magnetization but plays a major role in pulse sequence design was extensively discussed in [12] for isolated single-spin systems. Allowed phase factors can be determined as follows. Given that

$$\det(e^A) = e^{\mathrm{Tr}(A)} \tag{3.6}$$

and the nuclear spin Hamiltonian is a traceless matrix, the determinant of any unitary single-spin propagator has to yield unity. The same has to hold for propagators with a phase factor $e^{i\phi}$. Following

$$\det(rA) = r^n \det(A) \tag{3.7}$$

with n being the dimension of the matrix,

$$\det(e^{i\phi}U) = e^{i2\phi}\det(U) = 1 \tag{3.8}$$

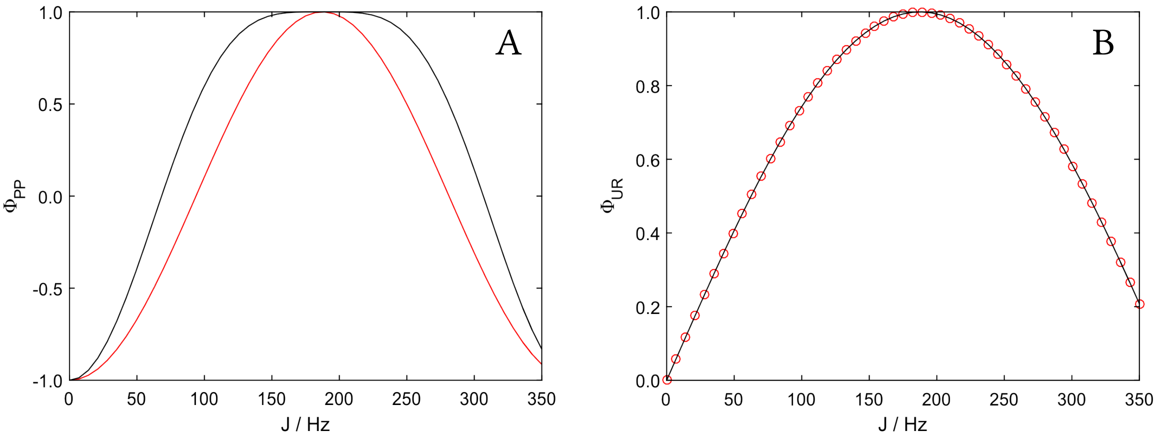

Figure 3.19.: Fidelities of the originally proposed BIRD elements as a function of J were evaluated with respect to spin inversion (A) and synthesis of the desired propagator (B) for the basic sequence depicted in figure 3.18 A (red line in A, red circles in B) and the J-compensated sequence depicted in figure 3.18 B (black line). Delays for magnetization transfer via heteronuclear J couplings were set for a 185 Hz coupling constant.

has to be fulfilled. This is the case if

$$e^{i2\phi} = \cos 2\phi + i \cdot \sin 2\phi = 1 \tag{3.9}$$

is fulfilled. Possible solutions for ϕ are integer multiples of π so that phase factors of ±1 are obtained for single-spin propagators[12]. For two-spin systems, n in equation 3.7 equals 4 so that

$$e^{i4\phi} = \cos 4\phi + i \cdot \sin 4\phi = 1 \tag{3.10}$$

has to hold. Here, solutions for ϕ are integer multiples of $\pi/2$ so that phase factors of ±1 as well as $\pm i$ are allowed. This has to be considered if the rotation properties of BIRD elements are determined in the following. Another peculiarity that is not found at a prominent place in the literature on this topic is that imaginary phase factors can be used to transform a concurrent or even consecutive rotation around axes corresponding to commuting operators into a single bilinear rotation via

$$\exp(-i\pi(I+S)) = -i \cdot \exp(-i\pi 2IS). \tag{3.11}$$

This relation will be a great boon in the following analysis. After the determination of Φ_{PP} for the single-spin operator transformations of both spins individually, the phase factor of the bilinear rotation can be determined from a simple guess. This approach could be used to analyze the rotation properties of the pulse sequences given in figure 3.18. The originally proposed simple BIRD filter thus facilitates a rotation around $2I_yS_y$ with phase factor 1 when the delays are matched to J and $2I_zS_x$ with phase factor $-i$ for $J = 0$. The J-compensated sequence facilitates $2I_xS_y$ with phase factor -1 under the matching condition and $2I_zS_x$ with phase factor $-i$ for $J = 0$. The fidelities of spin inversion according to Φ_{PP} and propagator synthesis according to Φ_{UR} are given in figure 3.19. As far as spin inversion is concerned, the pulse sequence shown in figure 3.18 B indeed provides robustness towards

ϕ_1	ϕ_2	ϕ_3	ϕ_4	$U_{\mathrm{H^r}}$	$e^{i\phi}$	$U_{\mathrm{H^d}}$	$e^{i\phi}$	Descriptor
x	x	x	-	S_x	-1	$2I_yS_y$	1	d,X
x	x	x	x	$\mathbf{1}$	1	$2I_yS_z$	1	d
x	x	x	y	S_z	1	$2I_yS_y + S_y$	1	d
x	x	$-x$	-	$2I_xS_x$	$-i$	$2I_zS_y$	-1	r,X
x	x	$-x$	x	I_x	-1	$2I_zS_z$	-1	r
x	x	$-x$	y	$2I_xS_z$	i	$2I_zS_y + S_y$	-1	r
x	y	x	-	$2I_yS_y$	$-i$	S_x	$-i$	r,X
x	y	x	x	$2I_yS_z$	$-i$	$\mathbf{1}$	i	r
x	y	x	y	I_y	-1	S_z	i	r
x	y	$-x$	-	$2I_zS_y$	i	$2I_xS_x$	1	d,X
x	y	$-x$	x	$2I_zS_z$	i	I_x	$-i$	d
x	y	$-x$	y	I_z	1	$2I_xS_z$	-1	d

Table 3.3.: Known BIRD rotations characterized by their descriptor as introduced in [191] as well as the rotation axes of the effective propagators acting on directly and remotely-bound protons ($U_{\mathrm{H^d}}$ and $U_{\mathrm{H^r}}$, respectively) with their respective phase factors $e^{i\phi}$ as a function of the phases ϕ_1 to ϕ_4.

a variation in J-couplings, but in terms of the bilinear rotation it has the same profile as the simple sequence given in figure 3.18 A. It can therefore not be considered a fully J-compensated bilinear rotation given that a BIRD element also needs to act as a refocusing pulse. An overall robust bilinear rotation operation is thus desirable.

In order to provide the necessary information for a feasibility study by OCT, the propagator analysis was extended to all BIRD variants proposed in [191] and the propagators and phase factors which can serve as input for OCT optimizations are compiled in table 3.3. From an OCT point of view, BIRD filters are J-selective UR 180 pulses which need to maximize Φ_{UR} with $U_{\mathrm{F}} = U_{\mathrm{H^d}}$ for a range of heteronuclear couplings as well as a contribution to Φ_{UR} from $U_{\mathrm{F}} = U_{\mathrm{H^r}}$ for $J = 0$. This can easily be plugged into the GRAPE algorithm to carry out the optimization procedure introduced in [15]. First, SPs are optimized with a rather coarse digitization of 100 μs to define an upper threshold for Φ_{UR} for the hard pulse-delay (HPD) approximation[15, 18]. Ten optimizations with different starting pulses are used to find the optimal sequence for any given overall pulse length between 0.5 and 25 ms incremented in steps of 500 μs. The best sequence of each set will then contribute to the time-optimal pulses (TOP) curve. However, even if protons are assumed to be on resonance, the optimization of BIRD elements is not as straightforward as with other reported transfer elements[15, 18]. Given that BIRD$^{\mathrm{d,X}}$ and BIRD$^{\mathrm{r,X}}$ filters need to manipulate the S spin, the corresponding propagators can not be created without concurrent RF irradiation on both spins. Even BIRD$^{\mathrm{d}}$ and BIRD$^{\mathrm{r}}$ filters require pulses on spin S in cases where ϕ_2 differs from ϕ_4 since this entails occasional composite rotations with a monolinear spin S contribution that can not be created without RF pulses on the S spin. Bearing this in

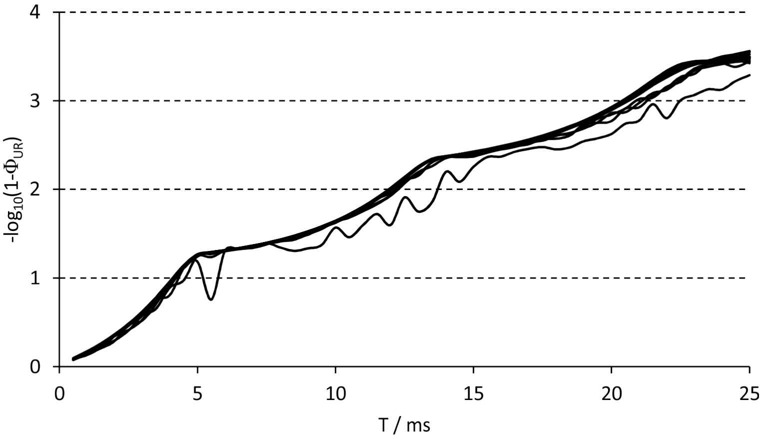

Figure 3.20.: Interpolated TOP curves for the optimizations of BIRD filters as SPs with effective propagators as given in table 3.3. Fidelities are given on a negative logarithmic scale of the error functional $1-\Phi_{\text{UR}}$ to show a rather monotonous increase.

mind, pulse sequences that are tolerant to a typical range of $^{1}J_{\text{CH}}$ couplings of 120-250 Hz could be obtained. The resulting TOP curves for all BIRD variants of table 3.3 are overlaid in figure 3.20. Since all basic BIRD sequences have the same structure, it can be assumed that the underlying mode of action is the same for all BIRD variants and thus the GRAPE algorithm can find similarly optimal solutions in each case. Therefore all TOP curves should lay on top of each other if good convergence is assumed. They more or less do with a single exception of a BIRD$^{\text{r}}$ element where ϕ_2 differs from ϕ_4 (RF controls on spin S needed) and an effective propagator corresponding to unity with an imaginary phase factor has to be created for the directly-bound protons. This particular TOP curve only follows the others up to a first significant dip around 5 ms and then hardly ever reaches the level where all other curves are clustered again. To this remarkable extent, this can not be attributed to convergence issues alone but maybe is due to the fact that spin systems with a range of J-couplings can not be left unstirred to the same extent as demanded by this particular set of target propagators.

The three distinct dips in the majority of the TOP curves in the logarithmic representation are a familiar phenomenon in exploring the limits-type optimization studies, where beyond a certain threshold in pulse length a new family of pulse shapes is made available[12, 22]. Just as phase modulation can create the effect of a second irradiation frequency, BIRD sequences of a certain length can behave as if they match two or more distinct J-couplings.

3.3.2. Hard pulse-delay sequences

The sequences obtained in section 3.3.1 are exclusively compensated against a variation in heteronuclear J-couplings. The next step towards sequences which are robust against J-couplings, offsets and B_1-inhomogeneities is the HPD approximation[15, 18]. Continuous pulse shapes are approximated by a set of hard pulses and evolution delays with varying degrees of complexity. For the basic layout of CLIP/CLAP-RESET HSQC experiments presented in sections 3.2.1 and 3.2.3, a BIRD$^{\mathrm{d}}$ rotation is used to facilitate homonuclear decoupling. The specific pulse sequence according to table 3.3 uses phases ϕ_1 to $\phi_4 = x$ and facilitates a π rotation around the $2I_yS_z$ axis for protons directly-bound to ^{13}C, and the unity operation on remotely-bound protons. Given that the net rotation on ^{13}C amounts to 360°, the pulse sequences can be optimized without RF pulses on ^{13}C. For the optimization of HPD sequences it is necessary to obtain gradients of propagators with respect to time since a set of optimal delays is required in addition to optimal flip angles. They are found more trivially than control derivatives since the time derivative of the exponent in equation 1.60 commutes with the propagator itself so that

$$\frac{\partial U_j}{\partial \Delta t_j} = -i\mathcal{H}_j U_j \tag{3.12}$$

and gradients of Φ_{UR} can be obtained via

$$\frac{\partial \Phi_{\mathrm{UR}}}{\partial \Delta t_j} = -\Re\langle P_j | i\mathcal{H}_j X_j\rangle. \tag{3.13}$$

Again, ten optimizations with different starting pulses are used to find the optimal sequence for any given overall pulse length between 0.5 and 25 ms incremented in steps of 500 μs. The best sequence of each set will then contribute to the TOP curve. Given that the complexity of pulse sequences with a few pulses and delays is very reduced, the hypersurface of Φ_{UR} is heavily jointed so that optimizations using CGs can end up stuck in local extrema very quickly. This is why steepest ascent with constant values for ϵ in equation 1.107 were performed using $\epsilon_{\Delta t} = 10^{-7}$ and $\epsilon_u = 10^{10}$. These values were found semiempirically given that the length of the hard pulses is set to $\Delta t = 0.5$ μs and arbitrary RF amplitude is allowed to facilitate any flip angle while delays are in the range of a few ms. Both values for the two variables were picked to achieve a significant change in the corresponding controls in each iteration so that optimizations can also bypass local extrema[51]. Optimizations were aborted when the change in Φ_{UR} between two iterations was less than 10^{-10}. TOP curves for pulse sequences which facilitate BIRD$^{\mathrm{d}}$ rotations are given in figure 3.21. The continuous pulse shape obtained for the shaped BIRD$^{\mathrm{d}}$ element defines the upper threshold for the achievable fidelities. To provide optimal transfer for J-couplings in the range of 120-250 Hz, conventional BIRD elements need to have delays calibrated to match 185 Hz. If the sequences depicted in figure 3.18 are set up accordingly, the standard BIRD sequence (figure 3.18 A, $T = 5.4$ ms) and the sequence with improved inversion properties (figure 3.18 B, $T = 10.8$ ms), here labeled JC BIRD, both yield fidelities of approximately 0.945 and are included in figure 3.21. HPD sequences with x *p*ulses and y *d*elays are labeled as *xpyd*. The TOP curves can be interpreted rather easily. Up to the length of a conventional BIRD sequence, which corresponds to a *2p1d* sequence, all TOP curves overlap. This threshold marks the first dip in the curve of the SPs which has to correspond to a simple sequence roughly calibrated to match $J = 185$ Hz. Also *3p2d* sequences can not exceed the fidelity of such a simple sequence. The second dip in the TOP curve of SPs marks the point where the sequences are effectively matched to two J-couplings at the same time which lie favorably within the desired range of 120-250 Hz. *4p3d* sequences have the same complexity as the sequence depicted in figure 3.18 B but can

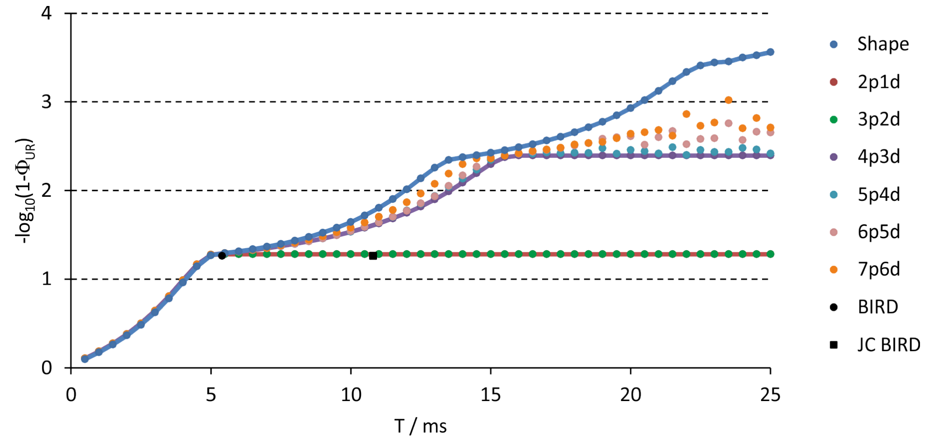

Figure 3.21.: Overlaid TOP curves for the optimizations of BIRD^d elements as HPD sequences with effective propagators corresponding to the sequence with all phases x in table 3.3. The sequences depicted in figure 3.18 A (BIRD) and B (JC BIRD) with delays calibrated to match 185 Hz are inserted as a reference. Fidelities are given on a negative logarithmic scale of the error functional $1-\Phi_{UR}$.

approach the threshold of roughly 0.996 fidelity at overall pulse lengths of about 15 ms but can not improve any further. This fidelity is desirable since it yields Φ_{PP} fidelities of about 0.99. Starting with *5p4d* sequences, the second threshold can be exceeded but at higher pulse lengths the TOP curves starts to scatter and interpolation is no longer meaningful. This can be attributed to convergence issues. The continuous pulse shape obtained for the shaped BIRD^d element defines the upper threshold for the achievable fidelities. To provide optimal transfer for J-couplings in the range of 120-250 Hz, conventional BIRD elements need to have delays calibrated to match 185 Hz. If the sequences depicted in figure 3.18 are set up accordingly, the standard BIRD sequence (figure 3.18 A, T = 5.4 ms) and the sequence with improved inversion properties (figure 3.18 B, T = 10.8 ms), here labeled JC BIRD, both yield fidelities of approximately 0.945 and are included in figure 3.21. HPD sequences with x *p*ulses and y *d*elays are labeled as *xpyd*. The TOP curves can be interpreted rather easily. Up to the length of a conventional BIRD sequence, which corresponds to a *2p1d* sequence, all TOP curves overlap. This threshold marks the first dip in the curve of the SPs which has to correspond to a simple sequence roughly calibrated to match J = 185 Hz. Also *3p2d* sequences can not exceed the fidelity of such a simple sequence. The second dip in the TOP curve of SPs marks the point where the sequences are effectively matched to two J-couplings at the same time which lie favorably within the desired range of 120-250 Hz. *4p3d* sequences have the same complexity as the sequence depicted in figure 3.18 B but can approach the threshold of roughly 0.996 fidelity at overall pulse lengths of about 15 ms but can not improve any further. This fidelity is desirable since it yields Φ_{PP} fidelities of about 0.99. Starting with *5p4d* sequences, the second threshold can be exceeded but at higher pulse lengths the TOP curves starts to scatter and interpolation is no longer meaningful. This can be attributed to convergence issues.

For practical applications, sequences with as little complexity as possible are desirable. Thus, only *4p3d* and *5p4d* sequences are discussed in the following which approach the

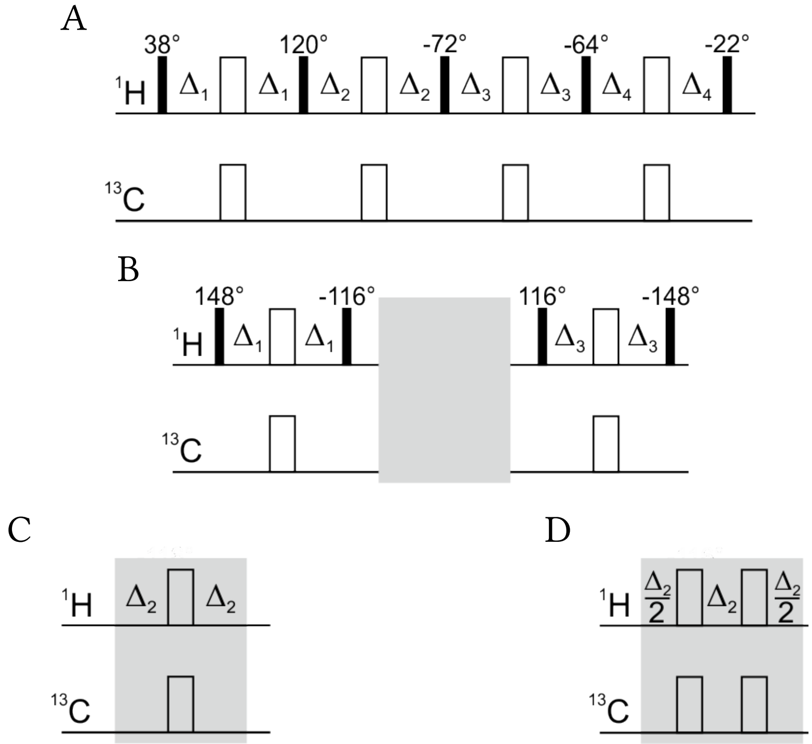

Figure 3.22.: Pulse sequences of COB-BIRD elements. Narrow and wide bars correspond to odd-flip angle and 180° pulses, respectively. Phases are uniformly x. Transfer delays of the *5p4d* sequence (A) are set to Δ_1 = 2.881 ms, Δ_2 = 2.036 ms, Δ_3 = 0.863 ms and Δ_4 = 1.969 ms. The *4p3d* sequence (B) will be transformed into a BIRD^{r,X} element by inserting 180° pulses in the gray box according to (C) and will retain the properties of a BIRD^{d} element by inserting the building block according to (D). Delays are set to $\Delta_1 = \Delta_2 = \Delta_3$ = 2.583 ms. Both delay settings ensure optimal transfer for J = 120-250 Hz.

fidelity of continuous shapes the closest at T = 15.5 ms. The best candidates for both implementations are given in figure 3.22. The analysis of these pulse sequence hold certain subtleties. It has to be noted that phases are uniformly x which will be discussed further below. The sequences can be understood on a first glance from the perspective of the ^{12}C-bound protons, since the sum of all flip angles is either 0° or an integer multiple of 360°. It can easily be proven that pulses with flip angle $\alpha > 180°$ can be replaced by pulses with a flip angle $\alpha - 360°$ to reduce the overall flip angle which will provide an inherent robustness against resonance offsets and B_1-inhomogeneities. In order to compensate transfer elements against resonance offsets, pairs of 180° pulses are inserted in the middle of magnetization transfer periods. However, these additional spin flips count towards the overall rotation. In the case of the *5p4d* sequence (see figure 3.22 A) a total 720° rotation is introduced which corresponds to 0° as far as the balance for the ^{12}C- and ^{13}C-bound protons is concerned. Conversely, the *4p3d* sequence contains an uneven number of delays, so that a total 540° rotation is introduced which corresponds to a net deviation of 180° for the balance of ^{12}C- and ^{13}C-bound protons (see figure 3.22 B). Further, a net rotation is introduced on the carbon spins so that effectively every BIRD^{d} sequence with an odd

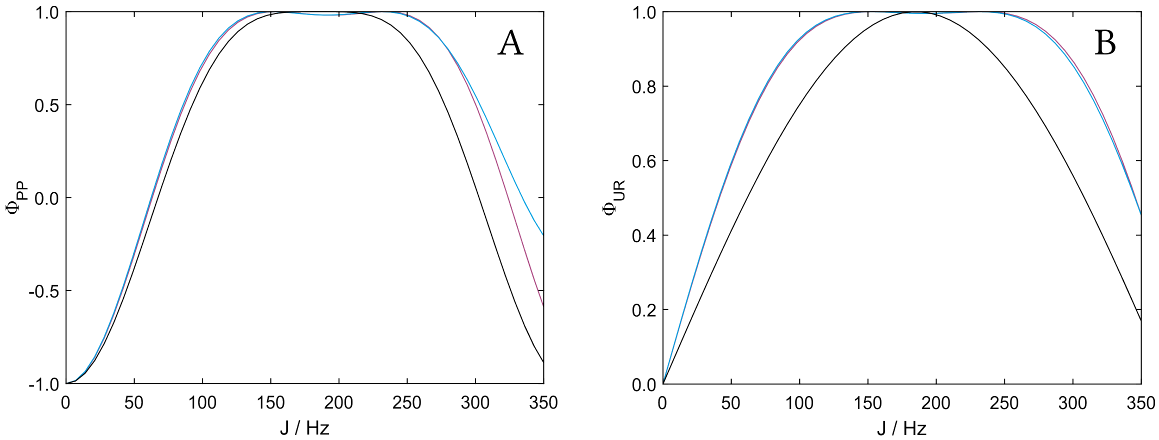

Figure 3.23.: Fidelities of COB-BIRD elements as a function of J were evaluated with respect to spin inversion (A) and synthesis of the desired propagator (B) for the sequence depicted in figure 3.18 B (black) as well as the *5p4d* and *4p3d* COB-BIRD sequences depicted in figure 3.22 (color code according to figure 3.21).

number of delays obtained by the optimizations discussed here, will be transformed into a BIRD^{r,X} sequence as soon as 180° pulses are inserted in the transfer delay according to figure 3.22 C. Such a behavior can be prevented if 180° pulse pairs according to figure 3.22 D are inserted into the middle of a single transfer period. This will ensure the refocusing to chemical shifts while an additional 360° rotation is introduced which corresponds to a net 0° change in the balance of remotely and directly-bound spins. Moreover, this maintenance of the rotation properties is also the reason why all phases have to be purely x (or y for that matter) because the heteronuclear transfer if facilitated by pulses with a mixed phase will be fundamentally impaired as soon as 180° pulses with pure phase are inserted.

Fidelities according to Φ_{PP} and Φ_{UR} of the proposed COB-BIRD elements were evaluated by simulations given in figure 3.23. It becomes clear that not only inversion properties are improved compared to the sequence proposed in [175], but also the overall rotation can be made robust against a variation in heteronuclear J-couplings by both sequences. Within the desired range of J-couplings between 120-250 Hz both sequences provide virtually identical transfer efficiency. Therefore both sequences were tested in a simple proxy setup for CLIP/CLAP-RESET HSQC experiments on a sample of 140 mM sodium acetate-2-^{13}C ($^{1}J_{CH}$ = 125.3 Hz) dissolved in a 1:5 (v/v) mixture of D_2O/DMSO-d_6. Given that ^{13}C-enriched material is used, the HSQC transfer could be replaced by a simple 90° excitation pulse. Further, no homonuclear couplings are active in sodium acetate so that intensities of simple spin echoes can be evaluated after the sign of transversal magnetization was inverted by the BIRD elements. Signals of residual ^{12}C-containing material could have been cycled out using difference spectroscopy[175, 190], but the intensity profiles would be distorted compared to the simulations because the second scan would have full intensity in each case due to the refocusing of heteronuclear couplings by the 180° ^{1}H pulses within the BIRD elements. A comparison between simulated and experimental BIRD^{d} spin echo intensity profiles is given in figure 3.24. The value for J_{eff} has been varied by applying scaling factors

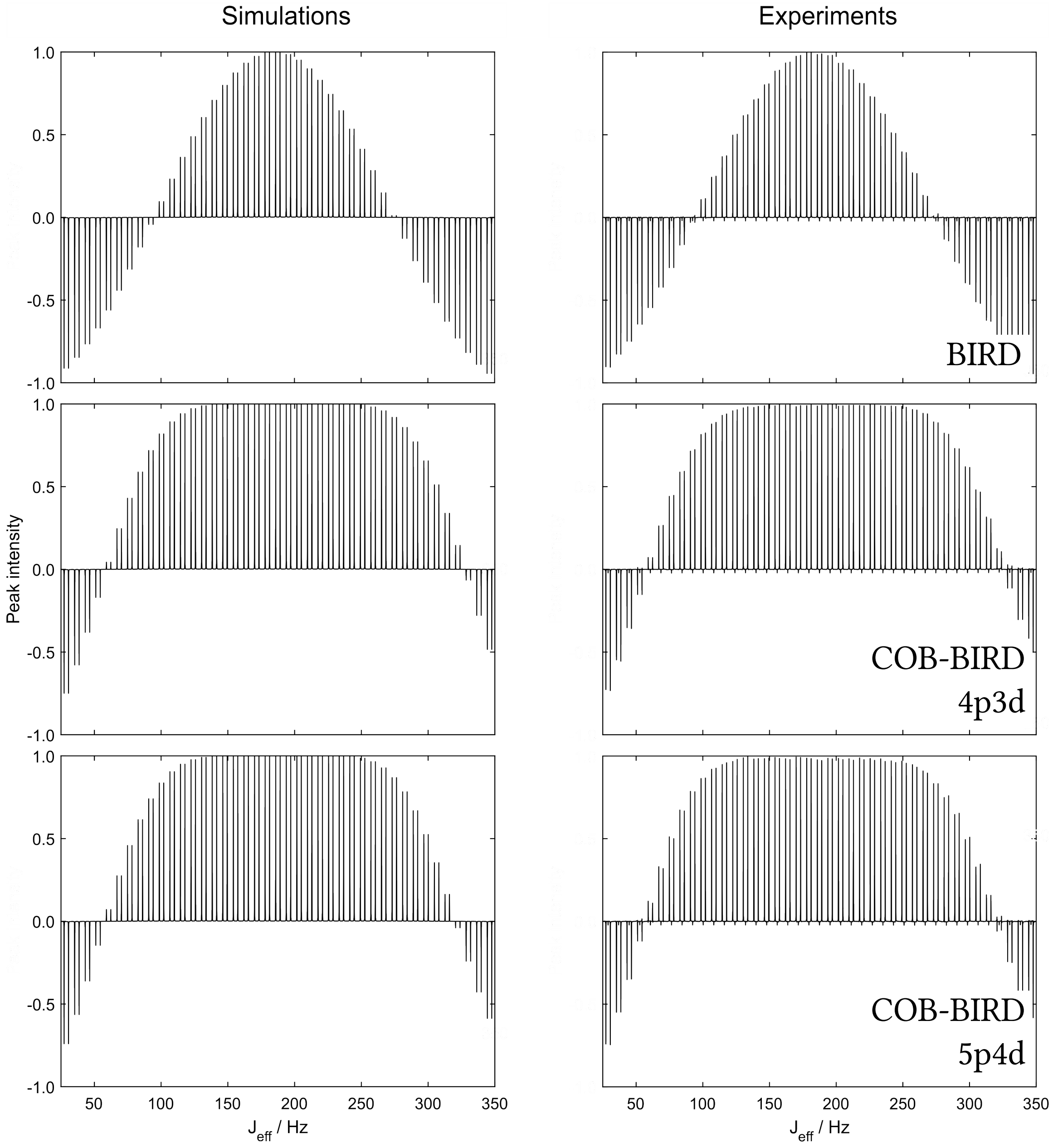

Figure 3.24.: Comparison of simulated (left panel) and experimental (right panels) BIRD^d spin echo intensity profiles. For the conventional BIRD element, the BIRD^d sequence with all phases x was used with delays calibrated to match $^1J_{CH}$ = 185 Hz. The *5p4d* and *4p3d* COB-BIRD sequences with T = 15.5 ms were set up as described in figure 3.22. J_{eff} was varied by varying delays as described in the main text. Signal intensities were normalized to the maximum intensity observed in the observed range of 25-350 Hz.

to delays calibrated to match 185 Hz in the case of conventional BIRD according to

$$\Delta_{\text{eff}} = \frac{J_{\text{eff}}}{2J_{\text{del}} \cdot J_{\text{exp}}} \tag{3.14}$$

with J_{del} = 185 Hz and J_{exp} = 125.3 Hz. Delays for the COB-BIRD sequences given in figure 3.22 were scaled accordingly by $J_{\text{eff}}/J_{\text{exp}}$. For the simulations and experiments 41 values for J_{eff} were sampled between 25 and 350 Hz. Residual anti-phase contributions to the observed signal were removed by a hard 90° pulse on ^{13}C prior to acquisition. Since the length of the sequences varies significantly between the extreme values of J_{eff}, relaxation losses could be observed during preliminary experiments on a sample with a reduced T_2 time due to doping with a paramagnetic relaxation agent. Thus, a variable echo period was appended to the BIRD elements so that the overall relaxation period was kept constant. Signal intensities were normalized to the maximum peak intensity which was achieved across the given range of J-couplings. Further experimental details are given in section 3.4.

All experimental profiles show reasonable agreement with the simulations. Small negative peaks can be observed at the midpoints of each heteronuclear doublet which correspond to signal of the residual ^{12}C-containing material. Since the signal is phased to show the inverted signal of ^{13}C-bound protons with positive intensity and the ^{12}C-bound protons were left untouched by the BIRD$^{\text{d}}$ rotation, the latter appear negative. All intensity profiles are meaningful in the sense of showing maximum intensity either at $J_{\text{eff}} = J_{\text{del}}$ for conventional BIRD or within the optimized range of 120-250 Hz for COB-BIRD while the maximum negative intensity is approached but not reached for the minimum value of J_{eff} = 25 Hz. Further, the profile of the *4p3d* is slightly more homogeneous than for the *5p4d* sequence. This can be attributed in parts to the fact that the latter is using more ^{1}H pulses and is thus more susceptible to B_1-inhomogeneities and miscalibration given that hard pulses were used. Moreover, the inherent structure of the *4p3d* is more advantageous than its *5p4d* counterpart. It has the beneficial symmetry properties described in [29] given that all transfer delays have equal duration and the second half of the sequence is the time and phased-reversed version of the first half. UR pulses with inherent symmetries with respect to the control-amplitudes have also been found to be advantageous in [12]. The most apparent drawback of the COB-BIRD sequences discussed in this section is their rather prolonged overall duration of 15.5 ms which is almost three times as long as a conventional BIRD elements calibrated to match J = 185 Hz. They will be prolonged even further if hard pulses are replaced by SPs which amounts to an additional 2.4 ms for BUBI pulse pairs alone. Thus, the proposed sequence are significantly more prone to the evolution of homonuclear ^{1}H couplings during the transfer element than conventional sequences. They can most definitely not be applied in BIRD-based RT PS acquisition schemes since the losses due to homonuclear couplings would not only accumulate, but the artificial damping due to relaxation during periods of FID interruption would lead to an even more severe line broadening. However, the above-mentioned losses would be constant in each increment of an interferogram-based acquisition scheme, so that RESET-type experiments could benefit from COB-BIRD elements. It is known that if homonuclear couplings impair the efficiency of heteronuclear transfer elements, XY16-cycled CPMG sequences can be used to suppress the couplings amongst the ^{1}H nuclei[176, 223]. Another advantageous aspect of the way the descriptor of the BIRD elements can be manipulated according to the examples given in figure 3.22 is that the need for concurrent shaped odd-flip angle and 180° pulses on ^{1}H and ^{13}C, respectively, is completely bypassed. The rotation properties of BIRD$^{\mathrm{d}}$ and BIRD$^{\mathrm{r}}$ elements with an odd number of delays can be retained if a net rotation of 360° on both spins is facilitated by two 180° pulse pairs in the middle of a single transfer period. At the same time, BIRD$^{\mathrm{d,X}}$ and BIRD$^{\mathrm{r,X}}$ rotations can be obtained from BIRD$^{\mathrm{r}}$ and BIRD$^{\mathrm{d}}$ elements with an odd number of delays, respectively, by inserting single 180° pulse pairs in the middle of each heteronuclear transfer period.

3.3.3. Shaped pulse sequences

Another approach to obtain a degree of heteronuclear J-compensation within magnetization transfer elements which is at least of theoretical interest, is solely based on the timing of adiabatic spin flips and thus SPs acting on ^{13}C [106]. As discussed extensively in chapter 2, the exact time point of inversion during adiabatic sweeps is determined by the chemical shift. In [106] two approaches are presented to solve timing issues with adiabatic pulses during heteronuclear magnetization transfer elements like INEPT and BIRD. Both variants are depicted in figure 3.25 A. Adiabatic sweeps with opposite directions can be used to orchestrate the timing of ^{13}C spin inversion such that optimal heteronuclear transfer for a single value of J is facilitated in a broadband fashion. If adiabatic sweeps with parallel directions are used, a linear correlation between chemical shifts and J couplings can be used to achieve optimal transfer for a wider range of couplings. This section deals with a possibility to obtain pulses from OCT optimizations that aim to facilitate the necessary BIRD rotation for each combination of ν_{S} and J which will be referred to as BIlinear Rotation Decoupling By Optimized Pulses (BIRDBOP) in the following. The basic BIRD pulse sequence modified accordingly is shown in figure 3.25 B.

Before new pulses are designed, the sequences given in figure 3.25 A shall be evaluated with respect to their ^{1}H spin inversion properties as a function of ν_{S} and J. The recipe for optimal pulse lengths T and durations of transfer delays δ given in [106] to correlate a given offset range $\Delta\nu_{\mathrm{S}}$ with a range of J-couplings in BIRD elements assumes

$$T_{\mathrm{opt}} = \frac{1}{4J_{\mathrm{min}}} - \frac{1}{4J_{\mathrm{max}}}. \tag{3.15}$$

For more even numbers $J_{\mathrm{min}} = 125$ Hz and $J_{\mathrm{max}} = 250$ Hz are plugged into equation 3.15 which yields $T_{\mathrm{opt}} = 1$ ms. The optimal delay δ_{opt} can be found via

$$\delta_{\mathrm{opt}} + T_{\mathrm{opt}} = \frac{1}{4J_{\mathrm{min}}} \quad \text{or} \quad \delta_{\mathrm{opt}} - T_{\mathrm{opt}} = \frac{1}{4J_{\mathrm{max}}} \tag{3.16}$$

which equates to $\delta_{\mathrm{opt}} = 3$ ms using the values from above and yields a total duration of 8 ms for this particular BIRD element. Given that the double-sweep layout is used for the purpose of J-compensation, a BIRD$^{\mathrm{d}}$ rotation is obtained. If a BIRD$^{\mathrm{d,X}}$ rotation is desired, the alternatively proposed single-sweep layout can be used[106]. The double-sweep pulse sequence set up as given above using WURST-40 pulses with $T = 1$ ms, $Q = 5$ and a sweep-width $\Delta\nu_{\mathrm{S}} = 40$ kHz was evaluated according to Φ_{PP} in figure 3.26. Adiabatic sweeps with opposed directions were used to create the profile given in figure 3.26 A. It

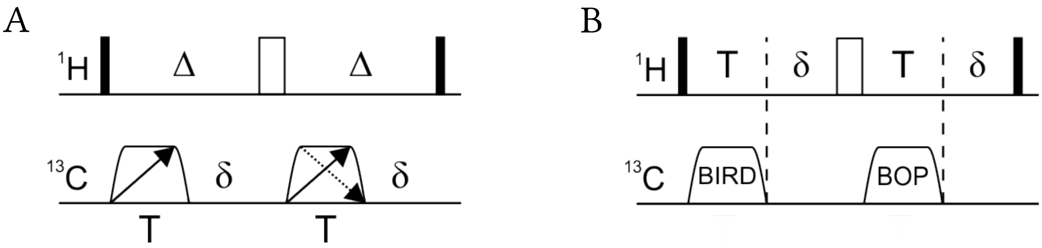

Figure 3.25.: Alternative pulse sequences for J-compensated BIRD elements. Narrow and wide bars correspond to 90° and 180° pulses, respectively. Phases are uniformly x. In (A), trapezoids correspond to adiabatic pulses with pulse length T and sweep directions indicated by diagonal arrows. Transfer delays are calibrated to match $\delta = 1/(2^1J_{CH})$. According to [106] opposite sweep directions (dashed arrow) are employed to provide offset-independent optimal transfer for a single value of J and parallel sweep directions (bold arrows) facilitate a linear correlation between offsets and J. Adiabatic pulses have been replaced by pulse shapes obtained by OCT in (B).

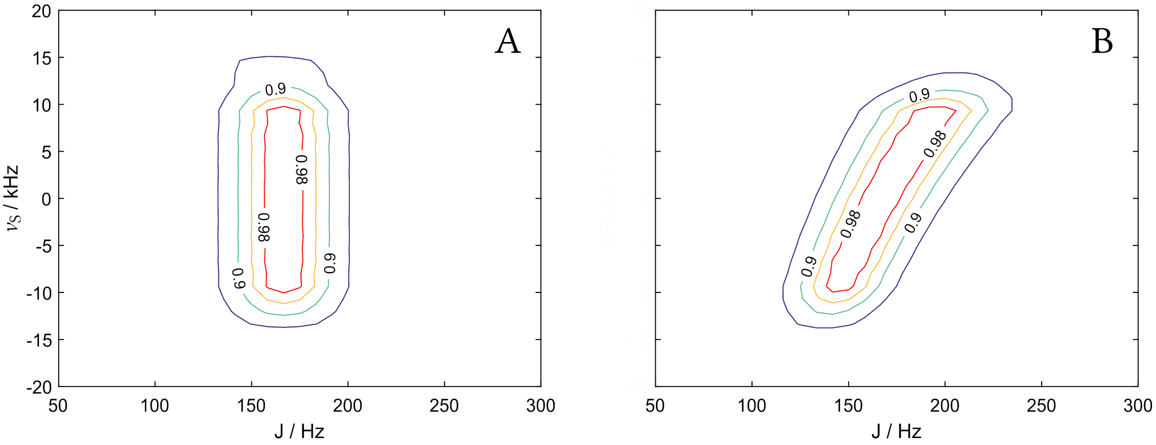

Figure 3.26.: Φ_{PP} fidelities of double-sweep BIRD elements as a function of ν_S and J. ^{1}H spin inversion fidelities according to Φ_{PP} were evaluated using opposed (A) and parallel (B) sweep directions. WURST-40 pulses with T = 1 ms, Q = 5 and a sweep-width $\Delta\nu_S$ = 40 kHz were used in both cases. The delay δ was set to 3 ms. Contour levels are given for Φ_{PP} = 0.8 (blue), 0.9 (green), 0.95 (orange) and 0.98 (red).

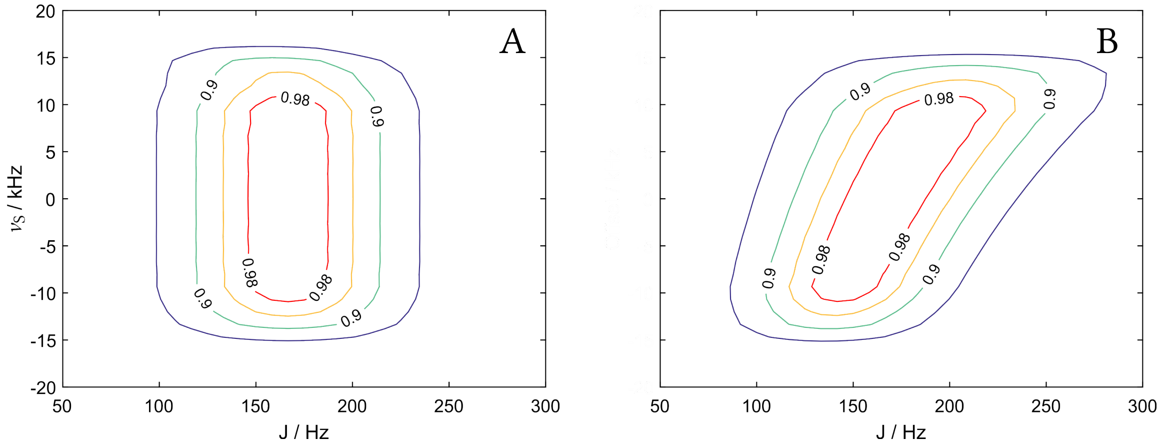

Figure 3.27.: Φ_{UR} fidelities of double-sweep BIRD elements as a function of ν_{S} and J. Fidelities of propagator synthesis according to Φ_{BIRDBOP} (see equation 3.18) were evaluated using opposed (A) and parallel (B) sweep directions. WURST-40 pulses with $T = 1$ ms, $Q = 5$ and a sweep-width $\Delta\nu_{\mathrm{S}} = 40$ kHz were used in both cases. The delay δ was set to 3 ms. Contour levels are given for $\Phi_{\mathrm{PP}} = 0.8$ (blue), 0.9 (green), 0.95 (orange) and 0.98 (red).

can be seen that if an offset ν_{S} is efficiently swept by the adiabatic pulses, efficient transfer is achieved for J-couplings around a single optimal value corresponding to 167 Hz for $\delta = 3$ ms. The profile given in figure 3.26 B was created by employing adiabatic sweeps in parallel directions. The picture is now tilted in a way that a slope of optimal transfer from combinations of low values for ν_{S} and J to combinations of high values is achieved.

In order to analyze this behavior in terms of rotation properties, a Φ_{UR}-like quality factor is necessary that can evaluate the fidelity of a ^{1}H propagator synthesis as a function of ^{13}C pulses. This is highly reminiscent of the BUBI problem[17], where the influence of the effective S spin propagator $U_{\mathrm{eff}}(S)$ had to be separated from the I spin target propagator $U_{\mathrm{F}}(I, J)$ to measure overlap with the effective two-spin propagator $U_{\mathrm{eff}}(I, J, S)$ via

$$\Phi_{\mathrm{BUBI}} = \Re \left\langle U_{\mathrm{F}}(I, J) U_{\mathrm{eff}}(S) \middle| \, U_{\mathrm{eff}}(I, J, S) \right\rangle . \tag{3.17}$$

It might appear as if to apply the BUBI procedure to a BIRD$^{\mathrm{d}}$ element as depicted in figure 3.25 B, the operator $2I_yS_z$ which corresponds to the rotation axis for ^{13}C-bound protons, needs to be deconstructed into the spin I and S component according to equation 3.11 in order to plug it into equation 3.17. However, it was proven in section 3.3.2 that this target propagator can be created without pulses on the S spin and the full bilinear rotation has to contribute to U_{F}. The appropriate quality factor can thus be written as

$$\Phi_{\mathrm{BIRDBOP}} = \Re \left\langle \exp(-i\pi 2I_yS_z) U_{\mathrm{eff}}(S) \middle| U_{\mathrm{eff}}(I, J, S) \right\rangle . \tag{3.18}$$

Equation 3.18 was used to create the profiles given in figure 3.27 using the parameters according to figure 3.26. Since the general pattern of figure 3.26 can be reproduced, Φ_{BIRDBOP} can be assumed to be a valid performance measure for the pulse sequence proposed in figure 3.25 B.

In order to obtain gradients for an optimization, control derivatives with respect to spin S controls have to be calculated from equation 3.18. It becomes evident that the solution has to be obtained in a different way from Φ_{BUBI} since both $U_{\mathrm{eff}}(S)$ and $U_{\mathrm{eff}}(I,J,S)$ are a function of spin S controls. Thus, the product rule has to be applied to equation 3.18 to obtain

$$\begin{aligned}\nabla_{\boldsymbol{u}^{(S)}}\Phi_{\mathrm{BIRDBOP}} = {} & \Re\left\langle U_{\mathrm{F}}(I,J)U_{\mathrm{eff}}(S)\left|\nabla_{\boldsymbol{u}^{(S)}}U_{\mathrm{eff}}(I,J,S)\right.\right\rangle \\ & + \Re\left\langle U_{\mathrm{F}}(I,J)\nabla_{\boldsymbol{u}^{(S)}}U_{\mathrm{eff}}(S)\right|\left.U_{\mathrm{eff}}(I,J,S)\right\rangle . \end{aligned} \tag{3.19}$$

The second addend on the right side of equation 3.19 can be rearranged to fit the shape of the first and to be obtained using the same syntax according to

$$\begin{aligned}\nabla_{\boldsymbol{u}^{(S)}}\Phi_{\mathrm{BIRDBOP}} = {} & \Re\left\langle U_{\mathrm{F}}(I,J)U_{\mathrm{eff}}(S)\left|\nabla_{\boldsymbol{u}^{(S)}}U_{\mathrm{eff}}(I,J,S)\right.\right\rangle \\ & + \Re\left\langle U_{\mathrm{F}}^{\dagger}(I,J)U_{\mathrm{eff}}(I,J,S)\right|\left.\nabla_{\boldsymbol{u}^{(S)}}U_{\mathrm{eff}}(S)\right\rangle . \end{aligned} \tag{3.20}$$

Effective propagators contain the constituents of the pulse sequence from the perspective of spin S or the whole spin system. $U_{\mathrm{eff}}(S)$ is given by

$$U_{\mathrm{eff}}(S) = \left\{U_{\delta}U_{2}U_{\delta}U_{1}\right\}(S) \tag{3.21}$$

with $U_{\delta}(S)$ corresponding to the chemical shift evolution under $\mathcal{H}_{\mathrm{S}}$ according to equation 2.19 besides $U_1(S)$ and $U_2(S)$ corresponding to the effective propagators of the shapes labeled BIRD and BOP in figure 3.25, respectively. They shall be referred to as shape one and two in the following. In both cases, the dynamics of the spin system are exclusively governed by $\mathcal{H}_{\mathrm{S}}$ and $\mathcal{H}_{\mathrm{RF}}^{S}(t)$ according to equation 2.19. For $U_{\mathrm{eff}}(I,J,S)$ the whole pulse sequence as well as the coupling Hamiltonian $\mathcal{H}_{\mathrm{J}}$ has to be taken into account. $\mathcal{H}_{\mathrm{I}}$ can be neglected since the sequence is inherently robust against spin I offsets due to the application of a 180° pulse which is assumed to be perfect. All contributions to $\mathcal{H}$ are used according to their definitions in equation 2.19. This yields

$$U_{\mathrm{eff}}(I,J,S) = \left\{U_{\pi/2}U_{\delta}U_{2}U_{\pi}U_{\delta}U_{1}U_{\pi/2}\right\}(I,J,S). \tag{3.22}$$

Here, $U_{\delta}(I,J,S)$ is governed by $\mathcal{H}_{\mathrm{S}}$ and $\mathcal{H}_{\mathrm{J}}$ besides $U_1(I,J,S)$ and $U_2(I,J,S)$ depending on $\mathcal{H}_{\mathrm{RF}}^{S}(t)$ in addition. $U_{\pi/2}$ and U_{π} correspond to 90° and 180° pulses acting on protons, respectively. Both are assumed to be perfect and are a fixture during the optimizations. When equations 3.21 and 3.21 are plugged into equation 3.20 this yields

$$\begin{aligned}\nabla_{\boldsymbol{u}^{(S)}}\Phi_{\mathrm{BIRDBOP}} = {} & \Re\left\langle U_{\mathrm{F}}(I,J)U_{\mathrm{eff}}(S)\left|\nabla_{\boldsymbol{u}^{(S)}}\left\{U_{\pi/2}U_{\delta}U_{2}U_{\pi}U_{\delta}U_{1}U_{\pi/2}\right\}(I,J,S)\right.\right\rangle \\ & + \Re\left\langle U_{\mathrm{F}}^{\dagger}(I,J)U_{\mathrm{eff}}(I,J,S)\right|\left.\nabla_{\boldsymbol{u}^{(S)}}\left\{U_{\delta}U_{2}U_{\delta}U_{1}\right\}(S)\right\rangle . \end{aligned} \tag{3.23}$$

Depending whether gradients are needed for shape one or shape two the products within each scalar product of the two addends need to be evaluated differently by the product rule. To keep the syntax as before, each factor left of the actual gradient can be cyclically permuted to obtain the master equations for each BIRDBOP shape. The gradient for shape one can be obtained via

$$\begin{aligned}\nabla_{\boldsymbol{u}_1^{(S)}}\Phi_{\mathrm{BIRDBOP}} = {} & \Re\left\langle\left\{U_{\delta}^{\dagger}U_{\pi}^{\dagger}U_{2}^{\dagger}U_{\delta}^{\dagger}U_{\pi/2}^{\dagger}\right\}(I,J,S)U_{\mathrm{F}}(I,J)U_{\mathrm{eff}}(S)\left|\left\{\nabla_{\boldsymbol{u}_1^{(S)}}U_{1}\cdot U_{\pi/2}\right\}(I,J,S)\right.\right\rangle \\ & + \Re\left\langle\left\{U_{\delta}^{\dagger}U_{2}^{\dagger}U_{\delta}^{\dagger}\right\}(S)U_{\mathrm{F}}^{\dagger}(I,J)U_{\mathrm{eff}}(I,J,S)\right|\left.\nabla_{\boldsymbol{u}_1^{(S)}}U_{1}(S)\right\rangle \end{aligned} \tag{3.24}$$

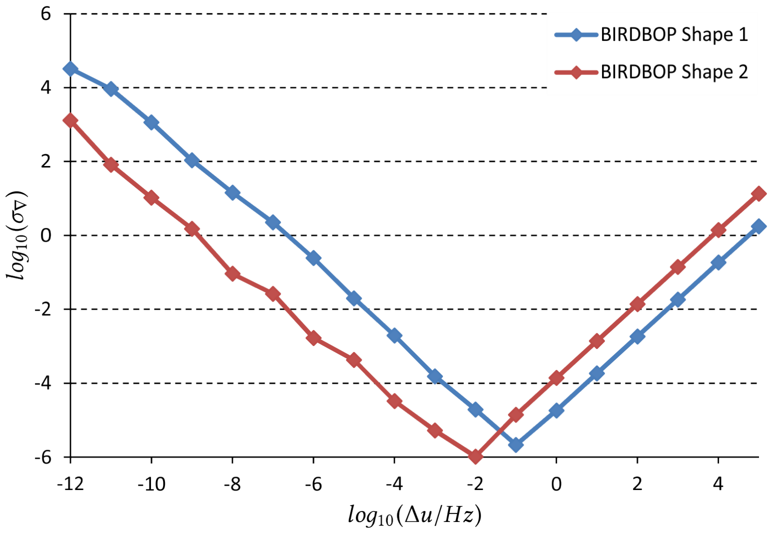

Figure 3.28.: Benchmark of the two master equations for Φ_{BIRDBOP} gradients against a finite difference approximation according to equation 2.60. Both gradients were applied to a randomly generated set of pulses yielding $\Phi_{\text{BIRDBOP}} = 0.169$.

whereas gradients for shape two are given by

$$\begin{aligned}\nabla_{\boldsymbol{u}_2^{(S)}} \Phi_{\text{BIRDBOP}} = {} & \Re \left\langle \left\{ U_\delta^\dagger U_{\pi/2}^\dagger \right\} (I,J,S) U_{\text{F}}(I,J) U_{\text{eff}}(S) \middle| \left\{ \nabla_{\boldsymbol{u}_2^{(S)}} U_2 \cdot U_\pi U_\delta U_1 U_{\pi/2} \right\} (I,J,S) \right\rangle \\ & + \Re \left\langle U_\delta^\dagger (S) U_{\text{F}}^\dagger (I,J) U_{\text{eff}}(I,J,S) \middle| \left\{ \nabla_{\boldsymbol{u}_2^{(S)}} U_2 \cdot U_\delta U_1 \right\} (S) \right\rangle . \end{aligned} \tag{3.25}$$

Both master equations were used to perform a gradient benchmark according to equation 2.60. The resulting gradient errors are depicted in figure 3.28. Just as in figure 2.29, distinct dips in the gradient errors can be observed which were indicative of exact gradients. They can now be used to design BIRDBOP shapes from scratch.

Several optimizations were carried out both starting with randomly-generated pulses as well as using the WURST-40 pulses discussed above as a starting point. Aiming at robustness towards $\Delta\nu_{\text{S}} = 30$ kHz and a variation of J-couplings between 125 and 250 Hz using $B_{1,\text{RMS}} = 10$ kHz, BIRDBOP shapes with $T = 1$ ms could not exceed 94.8% fidelity for any of the tried starting conditions. Fidelity profiles with respect to Φ_{BIRDBOP} and Φ_{PP} for a typically obtained solution are shown in figure 3.29. It becomes apparent that the major improvement compared to the sequences using two adiabatic sweeps is that increased performance is mainly due to a more homogeneous offset profile. J-compensation has only mildly improved and also using WURST-40 pulses as a starting point the J-correlation feature using parallel sweep directions is lost in favor of offset-independent optimal transfer in the proximity of $J = 200$ Hz. Judging the results for BIRDBOP in the context of the TOP curve shown in figure 3.21, the solution lies below the fidelity of a continuous shape with $T = 8$ ms but slightly above a HPD sequence with comparable complexity, namely *2p1d*. Even if HPD sequences of higher complexity are considered, the fidelity of BIRDBOP shapes can not exceed those observed in the TOP curves. It has to be stated that ^{13}C inversion was not demanded from the individual BIRDBOP shapes or the pulse pair as a whole. But even with this reduced set of requirements there is no observable cooperative

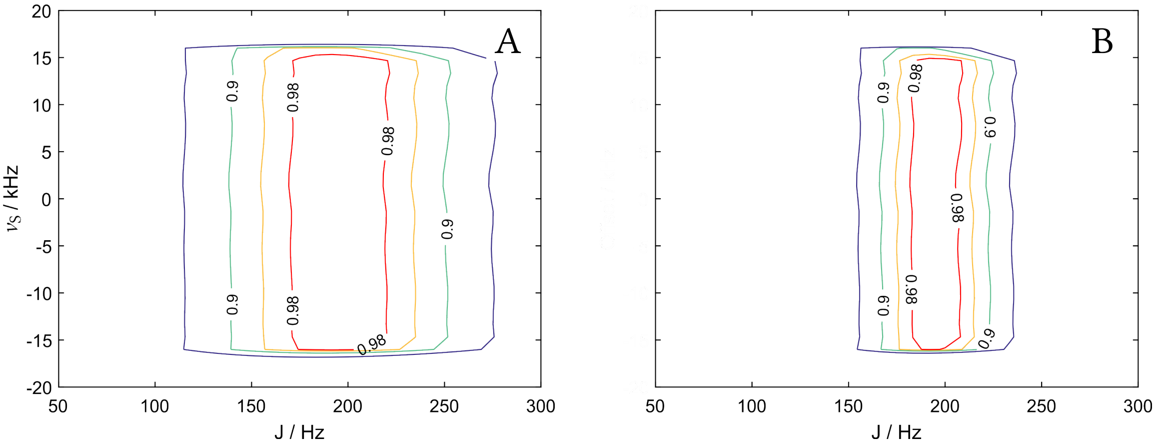

Figure 3.29.: Fidelity profiles of BIRDBOP shapes as a function of ν_S and J. Fidelities of propagator synthesis according to Φ_{BIRDBOP} (A) as well as ^{1}H spin inversion fidelities according to Φ_{PP} (B) were evaluated using two BIRDBOP shapes. The pulse sequence depicted in figure 3.25 B was simulated as a whole. Contour levels are given for both quality factors equal to 0.8 (blue), 0.9 (green), 0.95 (orange) and 0.98 (red).

effect between the individual pulses as described in [40] that would help to provide fidelities exceeding the TOP curve. This case-hardens the claim that pulse sequences which are obtained in section 3.3.2 indeed perform close to the physical maximum and the COB approach is the most effective to obtain pulse sequence elements which are robust against offsets, B_1-inhomogeneities and a variation in heteronuclear J-couplings.

3.4. Materials & methods

Simulations were performed using the MATLAB® software package with self-written scripts and functions (see appendix A.2.2) or code developed during the thesis of Sebastian Ehni[51] as well as modifications of the latter with the following exceptions: The data for the experimental BIRD profiles given in figure 3.24 was processed using a Metabolomics software package provided by the Bruker Biospin GmbH. Adiabatic shapes used in the simulations discussed in sections 3.3.3 were generated using the Shapetool of the Bruker TopSpin® software package.

Spectra shown in figures 3.6 and 3.7 were recorded on a 600 MHz Bruker Avance II+ spectrometer equipped with an inversely detected room temperature BBI probehead using a 500 mM sample of (−)-menthol dissolved in $CDCl_3$. Spectral widths were set to 2 kHz and 10.6 kHz for ^{1}H and ^{13}C, respectively, corresponding to 3.3 ppm and 70 ppm with the carrier frequencies set to 2 and 45 ppm. Data was collected for 512 ms and 6.1 ms in the ^{1}H and ^{13}C dimension, respectively. This corresponds to a data matrix of 2048 × 128 complex data points which was zero-filled to 4096 × 256 points. Homonuclear decoupled FIDs were obtained by the acquisition of 32 chunks of 16 ms per t_2-increment (containing 64 complex points each) combined to an FID with 512 ms effective AQ. Thereby the overall experiment time was increased from 6.9 min to 3 h and 4.5 min.

All other spectra were recorded on a 600 MHz Bruker Avance III spectrometer equipped with an inversely detected ^{1}H,^{13}C,^{15}N-triple-resonance cryogenically cooled TCI probehead. For the CT measurements and comparisons shown in figures 3.9 and 3.10, the constant time delay T was set to 333 ms, corresponding to an evolution of $4/^{2}J_{\mathrm{HH}}$ for a representative coupling of −12 Hz. After correction according to equation 3.4, 310 ms are available for data collection in the ^{1}H dimension. Homonuclear decoupled FIDs were constructed from 31 t_2-increments of 10 ms duration (corresponding to 40 complex points) to yield an overall data matrix of 1240 × 128 complex points which was zero-filled to 2048 × 256 points. The overall experiment time was 3 h and 7.5 min.

For spectra shown in figures 3.12 and 3.13 a mixture of 99.7 mg of ethylvanillin (3-ethoxy-4-hydroxybenzaldehyde), 54 μl of methylpropiolate and 100 μl of triethyl orthoformate (triethoxymethane) were added to 400 μl of DMSO-d_6 to yield 1 M solutions of each component in about 600 μl sample volume. Spectra of this mixture were recorded with spectral widths of 6.6 kHz and 30.2 kHz for ^{1}H and ^{13}C, respectively, corresponding to 11 ppm and 200 ppm with the carrier frequencies set to 5.5 ppm and 100 ppm. Data was collected for 620 ms and 1.9 ms in the ^{1}H and ^{13}C dimension, respectively. This corresponds to data matrices of 8192 × 128 complex time points which were zero-filled to 16384 × 256 points. Homonuclear decoupled FIDs were obtained by the acquisition of 32 chunks of 19.4 ms (256 complex points each) resulting in an AQ of 620 ms. This increased the overall experiment time from 7.5 min to 3 h and 16.3 min. In SP and COB-CLIP/CLAP-RESET experiments all hard pulses were replaced by SPs according to figure 3.11 A and as described in the main text. Using the nomenclature introduced in [12], carbon pulses have been replaced by corresponding BEBOP (37.5 kHz, 10 kHz, 550 μs, ±5%, 1100), BIBOP (37.5 kHz, 10 kHz, 600 μs, ±5%, 1200) and BURBOP-180(37.5 kHz, 10 kHz, 1100 μs, ±5%, 2200) pulses. Correspondingly, proton hard pulses have been replaced in the same manner by BEBOP (10 kHz, 20 kHz, 550 μs, ±20%, 1100), BIBOP (11 kHz, 20 kHz, 100 μs, ±20%, 200) and BURBOP-180(10 kHz, 20 kHz, 600 μs, ±20%, 1200) pulses. In situations with simultaneous RF irradiation on both channels the above-mentioned pulses are combined to BUBI, BEBE$^{\mathrm{tr}}$ and BE$^{\mathrm{tr}}$BE sandwiches and J-compensated as described in [17]. BIRD elements containing SPs also employ concurrent BURBOP-90(10 kHz, 20 kHz, 600 μs, ±20%, 1200) pulses on protons and corresponding BIBOP pulses on carbon (see above) that have not been J-compensated according to the BUBI procedure. All pulse shapes mentioned here were introduced in [15] and [17] except the BURBOP-90 shapes which had to be optimized with parameters chosen equal to the BURBOP-180 on ^{1}H.

Figure 3.14 features subspectra of (−)-menthol and the compound mixture. Subfigures 3.14 A and B were taken from spectra which were rerecorded according to the settings given for figures 3.6 and 3.7. The spectra used in subfigures 3.14 A' and B' were recorded using the same settings and SPs were employed as described for figures 3.12 and 3.13. Subfigures 3.14 C and C' combine subspectra shown in subfigures 3.13 A and A'. Finally, subfigures 3.14 D and D' were obtained from subspectra shown in subfigures 3.13 B and B'.

The aligned sample used in figure 3.15 was prepared using a 30% (w/v) gelatin/D$_2$O gel with 400 mM sucrose. The gel was stretched using a silicone-tube stretching device[228–230] to an extension corresponding to a quadrupolar ^{2}H splitting of the solvent of $\Delta\nu_Q$ = 271 Hz. Homogeneity of the sample was verified using the method described in [231]. Spectral widths for sucrose were set to 2 kHz and 6 kHz for ^{1}H and ^{13}C, respectively, corresponding to 3.3 ppm and 40 ppm with the carrier frequencies set to 4.25 ppm and 75 ppm. Data was collected for 256 ms and 10.6 ms in the ^{1}H and ^{13}C dimension, respectively. This corresponds to data matrices of 1024 × 128 complex time points which were zero-filled to 2048 × 256 points. Homonuclear decoupled FIDs were obtained by the acquisition of 16 chunks of 16 ms (64 complex points each) resulting in an AQ of 256 ms. The overall experiment time was prolonged from an initial 5.9 min to 1 h and 25 min. Isotropic reference spectra on a sample with the same concentration were recorded using the same parameters except that AQs in the ^{1}H dimension were doubled and homonuclear FIDs were obtained from 32 chunks of 16 ms each which yields an AQ of 512 ms.

All two-dimensional experiments were recorded using two scans and 16 dummy scans with a 1 s recovery delay and the first four points were dropped in every FID chunk of homonuclear decoupled spectra to avoid artifacts due to digital-to-analog conversion of the signal. A cosine-squared window function was used for apodization in each case. The temperature was set to 300 K. Delays of heteronuclear magnetization transfer elements such as conventional INEPT and BIRD were calibrated to match $^1J_{\mathrm{CH}} = 145$ Hz. Delays for COB-INEPT were calibrated as described in figure 3.11. All hard and shaped ^{1}H and ^{13}C pulses have been calibrated to a nominal RF amplitude of 20 kHz and 10 kHz, corresponding to pulse lengths of 12.5 and 25 μs, respectively. The processing software to reconstruct PS data was obtained from [214].

Experimental BIRD profiles shown in figure 3.24 were obtained from spectra recorded on a 500 MHz Bruker Avance III HD spectrometer equipped with a CryoProbe Prodigy™using a 140 mM sample of sodium acetate-2-^{13}C dissolved in a 1:5 (v/v) mixture of D_2O/DMSO-d_6. 1D ^{1}H spectra were acquired with spectral widths of 1.5 kHz corresponding to 3 ppm with the carrier frequency set to the methyl resonance at 1.65 ppm. Data was collected for 2.73 s corresponding to 8192 complex data points which were zero-filled to 16384 points. Time-domain data was not apodized prior to FT. The frequency-domain data was then phased and subject to an automated baseline correction procedure. Experiments were recorded using a single scan. The temperature was set to 300 K. The $^1J_{\mathrm{CH}}$ coupling constant of about 125.3 Hz was determined within 0.1 Hz accuracy from a conventional 1D ^{1}H spectrum. To avoid effects of B_1-inhomogeneities and J-couplings during concurrent 180° pulses, BUBI shapes as described above were used. Hard pulses were used for the odd-flip angle rotations. All hard and shaped ^{1}H and ^{13}C pulses have been calibrated to a nominal RF amplitude of 20 kHz and 10 kHz, corresponding to 12.5 and 25 μs pulse length, respectively.

Ethylvanillin, methylpropiolate and triethyl orthoformate were purchased from Alfa Aesar®. Sucrose and (−)-menthol were purchased from Sigma-Aldrich®. Gelatine was purchased from Ewald-Gelatine GmbH. Sodium acetate-2-^{13}C was purchased from Cambridge Isotope Laboratories, Inc. Deuterated solvents were purchased from Eurisotop®. All compounds were used without further purification.

4. Conclusion

The improvement of sensitivity and resolution are main concerns of NMR method development. Suppressing mutual couplings amongst nuclear spins by RF pulses presents itself as an opportunity to achieve both. In this thesis, the optimization of two decoupling scenarios was studied. Numerical optimization algorithms based on OCT but also traditional pulse sequence design were the means to this end.

Heteronuclear decoupling sequences are a fundamental building block in every heteronuclear correlation experiment where resolution and spectral dispersion and sensitivity are of higher importance than the information provided by resonance lines that are split due to heteronuclear couplings between spins, such as standard HSQC or HMQC experiments. Decoupling schemes are needed which provide high decoupled peak intensities paired with low sideband artifact levels for a wide range of resonance offsets. Up until recently it was best-practice to pursue these goals in three steps. First, a robust implementation of spin inversion has to be found which will be repetitively applied with varying phases given by a rationally designed supercycle in a second step. Finally, sideband artifacts arising from recurring periods of effectively free coupling evolution have to be suppressed. Typically, adiabatic bilevel decoupling is the preferred standard implementation to achieve the goals given above. Pulse shapes such as CHIRP, WURST and Hyperbolic Secant (HS) are common inversion elements which are expanded in a supercycle such as M4P5. Bilevel decoupling serves as a scheme to suppress the two most spurious types of sidebands by introducing 180° phase shifts on harmonic and subharmonic sidebands appearing at two distinct frequencies using only four scans. It is thus very specific but thereby extremely efficient and more widely used than the less general accordion technique, which may require more transients to yield comparable sideband levels at a given frequency.

Optimal tracking, a generalized version of the GRAPE algorithm, was presented as an approach that can tackle one inherent source of sidebands of decoupling sequenes which is repetitiveness. Tracking-based decoupling schemes have no inherent source of sidebands at a given frequency since the optimizations result in non-repetitive sequences in all cases. It was shown in this thesis however, that no single tracking-based decoupling sequence can compete with multi-scan approaches such as adiabatic bilevel decoupling in terms of sideband levels. A quality factor was proposed for cooperative decoupling sequences which can compensate their own imperfections by a feedback loop which explicitly facilitates the minimization of temporal signal oscillations. This can further reduce sidebands beyond mere non-repetitiveness. It was shown that for the target parameter set of 40 kHz bandwidth, a mean RF amplitude of 2 kHz and a representative heteronuclear coupling constant of 140 Hz, a set of four decoupling sequences could be obtained which provides sideband amplitudes of about 0.5% across the desired offset range. In other words, decoupling of more than the entire chemical shift range of ^{13}C on a 14.1 T device is facilitated despite an almost 5-fold reduction of RF power dissipation. Put differently, using the same mean RF amplitude the effective bandwidth was more than doubled compared to the gold standard. Conversely, at such reduced RF levels adiabatic decoupling breaks down as soon as the adiabaticity condition is violated. Additional sidebands are introduced which can not be canceled by the same mechanism as bilevel decoupling. Given that the BROCODE sequences presented here are not prone to frequency-specific sidebands, the method described in this thesis can be assumed to be maybe the most general approach to maintain sideband suppression and broadband operation at any given RF level. The efficiency of the BROCODE pulses has been proven by simulations and experiments and further tested on two small molecule examples. It has been shown on a 100:1 mixture of a pesticide molecule and its reactive precursor, that the sideband levels achievable by the BROCODE allow for the unambiguous identification of the minor component at the given dynamic ratio. Even compared to adiabatic bilevel decoupling with RF levels adjusted to fulfill the adiabatic condition, the impurity resonances can quite reliably be identified using the BROCODE. A major benefit of decoupling with reduced mean RF levels is the possibility to extend acquisition periods and gain resolution. On the compound mixture the increased resolution was an additional help in identifying the resonances by splittings due to homonuclear J-couplings. It was shown on the natural compound (+)-borneol that a synergy between BROCODE and LFP can be used to resolve homonuclear splittings to an extent that resonances with identical ^{1}H chemical shifts can be assigned by the analysis of the respective multiplets in HSQC in cases of different ^{13}C chemical shifts. All these benefits could be observed also in cases of unfavorable conditions. The magnitudes of the heteronuclear coupling constants observed in the compound mixture were often higher than the 140 Hz demanded in the optimizations. Further, the extended AQs require repetitive application of the BROCODE pulses, which are PP pulses per design. So each repetition of a given sequence will impair the decoupling performance given that the individual pulses are not designed to be cyclic. Finally, the RF levels were calibrated automatically in the HSQC experiments on the small molecules to test for robustness and general applicability. Given that the BROCODE yielded acceptable decoupling and sideband suppression capabilities nonetheless, it appears to be flexible enough to be a useful tool for a wide range of heteronuclear correlation experiments. Relative sideband amplitudes only appeared to increase when spectra were acquired with higher resolution. This can be attributed to similar effects as with COSY experiments since sidebands can have arbitrary phase and thus negative intensity contributions just like COSY signals which will only gain significant intensity with sufficient resolution.

Despite the availability of static magnetic fields on the order of 23.5 T and multi-dimensional NMR experiments, the resolution in ^{1}H spectroscopy still can pose challenges in terms of signal overlap. Therefore, experimental approaches to collapse homonuclear multiplets were ever sought after. Although homonuclear decoupling approaches were known for a rather long time, most of them were only rediscovered recently during a surge of pure shift (PS) method development. These methods are commonly based on the application of single-spin inversion (SSI) elements to achieve a selection of sub-ensembles of active spins which can in turn be decoupled from the passive spins. Experiments are known which apply SSI elements in indirect dimensions where PS FIDs are recorded as an interferogram or which interrupt the data acquisition for the application of RF pulses to achieve real-time (RT) homonuclear decoupling. SSI elements are available that facilitate sub-ensemble discrimination by slice-selection within the sample (Zangger-Sterk (ZS), with the HOBS experiments as an important off-spring), isotope filtering (BIRD) or statistically (PSYCHE). The benefits and drawbacks of all methods were weighed and matched to a corresponding set of applications in multi-dimensional NMR spectroscopy. ZS and PSYCHE are mostly used in homonuclear correlation experiments whereas the BIRD approach lends itself to HSQC-type experiments. Although the most significant drawback of all PS methods is an inherent loss of sensitivity due to the fact that only a reduced number of spins contribute to the acquired signal, the combination of BIRD and HSQC represents the only known possibility to improve sensitivity and resolution at the same time. However, BIRD can not be applied to HMBC and HSQMBC experiments since it is impossible to distinguish different spins which are remotely-bound to a heteronucleus. Another shortcoming of BIRD is the inability to remove mutual couplings within diastereotopic CH_2 groups whereas ZS and PSYCHE achieve broadband decoupling irrespective of ^{13}C multiplicity. Just as PSYCHE, BIRD can bypass strong coupling effects but can in contrast also be applied during the actual data acquisition. The same holds for HOBS but the latter can not be considered broadband homonuclear decoupling.

In this thesis, HSQC-type experiments were proposed to extract heteronuclear one-bond couplings with highest resolution by combining the CLIP/CLAP approach with BIRD-based homonuclear decoupling. Coupling constants could be extracted from heteronuclear doublets where each component is collapsed to singlets in the case of CH and CH_3 groups under isotropic conditions. Diastereotopic CH_2 groups (and in principle also CH_3 groups under anisotropic conditions) show residual splittings and dispersive line shapes due to unrefocused mutual couplings. It could be shown that in the weak coupling limit, the extraction of heteronuclear couplings is not impaired by this line shape. In general, given that all splittings due to weak homonuclear couplings can readily be removed, cases where strong coupling can not be bypassed are easily recognizable by deviations from the expected line shapes. Splittings caused by geminal couplings could be removed by transforming the BIRD-based PS pseudo-dimension of the interferogram-based experiment into a constant-time (CT) version. In principle, this should also suppress the splittings due to mutual couplings within CH_3 groups under anisotropic conditions. An alternative approach based on a perfect echo fails in the latter case since it is tailored towards decoupling AX spin systems only. The experiments were tested on small organic molecules in isotropic solution as well as in a stretched gel and it could be shown that the accuracy of the extracted couplings benefited from the multiplet reduction in many cases. Particularly in the aligned sample, many artifacts from long-range correlations caused by strong coupling could be suppressed so that more symmetric heteronuclear doublets could be obtained that lead to more reliable couplings and could also prevent the extraction of RDCs with a wrong sign. At the same time, the formation of strong coupling networks among the protons can also render BIRD-based decoupling ineffective. Moreover, a high abundance or magnitude of homonuclear couplings and especially homonuclear RDCs lead to significant deviations of the spins from a PS trajectory so that sideband-like artifacts could be observed. However, they did not significantly affect the line shape of the heteronuclear doublets so that the accuracy of the extracted couplings was not hampered.

The proposed experiments were examined with respect to their robustness towards a variation in heteronuclear couplings, resonance offsets and B_1-inhomogeneities. It could be shown that without the application of broadband pulses and *J*-compensated magnetization transfer elements like COB-INEPT, signal losses greater than 90% have to expected. Still, magnetization losses compared to fully-coupled reference experiments are observed which could be attributed to BIRD elements which are not compensated against a variation of *J*-couplings. It was shown by simulations that none of the sequences proposed in the literature provides a fully *J*-compensated bilinear rotation. After a feasibility study with shaped pulses, BIRD elements were optimized as hard pulse-delay (HPD) sequences and optimal solutions could be found with as little as four pulses and three delays with a total pulse length of 15.5 ms. The resulting transfer elements were tested experimentally using a proxy setup for the proposed HSQC experiments yielding reasonable agreement with the simulations. Further, the usual COB approach was compared to a setup using matched pairs of linear frequency sweeps. Quality factors and gradient functions were derived for a direct optimization of ^{13}C pulses within this particular setup but the results could not compete with the sequences obtained in the systematic study of HPD sequences. Finally, the results for the interferogram-based PS HSQC experiments could not be reproduced with RT BIRD-based homonuclear decoupling. It is now commonly accepted that errors on the coupling constants are introduced, but there is an ongoing debate regarding their very source, whether they are caused by BIRD imperfections or the interruption of the data collection itself.

The methods described in this thesis are not limited to the applications presented herein. BROCODE-type sequences could be scaled and applied to ^{19}F-decoupling of ^{1}H and ^{13}C, which is relevant for NMR of pharmaceuticals but highly challenging due to the enormous chemical shift range of ^{19}F. Optimization algorithms could be modified to aim for cyclic sequences, which would reduce artifacts due to the repetitive application of the BROCODE pulses in experiments where AQ exceeds the individual pulse lengths. Further, when the number of scans recorded for the same experiment exceeds the number of decoupling sequences contributing to a COOP cycle, sidebands could be further reduced by implementing BROCODE pulses which make use of accordion-type averaging.

RESET HSQC-type experiments can not only be used to accurately determine one-bond couplings, but also simplify the correlation of chemical shifts in crowded spectra. Moreover, an experiment to extract the magnitude and sign of $^{2}T_{\mathrm{HH}}$ couplings from collapsed homonuclear multiplets has yet to be developed. Such experiments can benefit from the more robust COB-BIRD elements proposed in this thesis. Given that BIRD filters are also used to orchestrate the evolution of heteronuclear couplings, additional BIRD$^{\mathrm{r}}$ and BIRD$^{\mathrm{d,X}}$ elements could be optimized for use in ω_1-coupled HSQC or heteronuclear *J*-resolved experiments. In summary, the results of this thesis provided several additions to the ever-expanding NMR toolbox in terms of the observation as well as suppression of couplings among nuclear spins.

Bibliography

[1] M. H. Levitt, *Spin Dynamics: Basics of Nuclear Magnetic Resonance*, 2. Edition, Wiley, Chichester, **2008**.

[2] F. J. Dyson, "The Radiation Theories of Tomonaga, Schwinger, and Feynman", *Phys. Rev.* **1949**, *75*, 486–502.

[3] J. Hilgert, K.-H. Neeb, *Structure and geometry of Lie groups*, Springer, New York, NY, **2012**.

[4] R. R. Ernst, G. Bodenhausen, A. Wokaun, *Principles of nuclear magnetic resonance in one and two dimensions*, Clarendon Pr., Oxford, **1987**.

[5] H. Goldstein, C. P. Poole, J. L. Safko, *Klassische Mechanik*, 3., vollst. überarb. und erw. Aufl., Wiley-VCH, Weinheim, **2006**.

[6] D. E. Kirk, *Optimal control theory: an introduction*, Unabridged republication, Dover Publications, Mineola, N.Y., **2004**.

[7] I. Kuprov, Introduction to optimal control theory, part I, University of Southampton, `http://spindynamics.org/Spin-Dynamics---Part-VI---Lecture-06.php`.

[8] M. H. Levitt, R. Freeman, "NMR Population Inversion Using a Composite Pulse", *J. Magn. Reson.* **1979**, *33*, 473–476.

[9] M. H. Levitt, "Composite Pulses", *Prog. NMR Spec.* **1986**, *18*, 61–122.

[10] A. J. Shaka, J. Keeler, "Broadband Spin Decoupling in Isotropic Liquids", *Prog. NMR Spec.* **1987**, *19*, 47–129.

[11] M. A. Janich, R. F. Schulte, M. Schwaiger, S. J. Glaser, "Robust slice-selective broadband refocusing pulses", *J. Magn. Reson.* **2011**, *213*, 126 –135.

[12] K. Kobzar, S. Ehni, T. E. Skinner, S. J. Glaser, B. Luy, "Exploring the limits of broadband 90° and 180° universal rotation pulses", *J. Magn. Reson.* **2012**, *225*, 142 –160.

[13] N. Khaneja, T. Reiss, C. Kehlet, T. Schulte-Herbrüggen, S. J. Glaser, "Optimal control design of coupled spin dynamics: design of NMR pulse sequences by gradient ascent algorithms", *J. Magn. Reson.* **2005**, *172*, 296–305.

[14] T. E. Skinner, N. I. Gershenzon, M. Nimbalkar, W. Bermel, B. Luy, S. J. Glaser, "New strategies for designing robust universal rotation pulses: Application to broadband refocusing at low power", *J. Magn. Reson.* **2012**, *216*, 78 –87.

[15] S. Ehni, B. Luy, "A systematic approach for optimizing the robustness of pulse sequence elements with respect to couplings, offsets, and B_1-field inhomoheneities (COB)", *Magn. Reson. Chem.* **2012**, *50*, S63–S72.

[16] M. Nimbalkar, B. Luy, T. E. Skinner, J. L. Neves, N. I. Gershenzon, K. Kobzar, W. Bermel, S. J. Glaser, “The Fantastic Four: A plug ’n’ play set of optimal control pulses for enhancing NMR spectroscopy”, *J. Magn. Reson.* **2013**, *228*, 16 –31.

[17] S. Ehni, B. Luy, “BEBE^{tr} and BUBI: J-compensated concurrent shaped pulses for ^{1}H-^{13}C experiments”, *J. Magn. Reson.* **2013**, *232*, 7–17.

[18] S. Ehni, B. Luy, “Robust INEPT and refocused INEPT transfer with compensation of a wide range of couplings, offsets, and B_1-field inhomogeneities (COB3)”, *J. Magn. Reson.* **2014**, *247*, 111 –117.

[19] E. L. Hahn, “Spin Echoes”, *Phys. Rev.* **1950**, *80*, 580–594.

[20] T. E. Skinner, T. O. Reiss, B. Luy, N. Khaneja, S. J. Glaser, “Application of optimal control theory to the design of broadband excitation pulses for high-resolution NMR”, *J. Magn. Reson.* **2003**, *163*, 8–15.

[21] T. E. Skinner, T. O. Reiss, B. Luy, N. Khaneja, S. J. Glaser, “Reducing the duration of broadband excitation pulses using optimal control with limited RF amplitude”, *J. Magn. Reson.* **2004**, *167*, 68–74.

[22] K. Kobzar, T. E. Skinner, N. Khaneja, S. J. Glaser, B. Luy, “Exploring the limits of broadband excitation and inversion pulses”, *J. Magn. Reson.* **2004**, *170*, 236 –243.

[23] T. E. Skinner, T. O. Reiss, B. Luy, N. Khaneja, S. J. Glaser, “Tailoring the optimal control cost function to a desired output: application to minimizing phase errors in short broadband excitation pulses”, *J. Magn. Reson.* **2005**, *172*, 17 –23.

[24] T. E. Skinner, K. Kobzar, B. Luy, M. R. Bendall, W. Bermel, N. Khaneja, S. J. Glaser, “Optimal control design of constant amplitude phase-modulated pulses: Application to calibration-free broadband excitation”, *J. Magn. Reson.* **2006**, *179*, 241–249.

[25] N. I. Gershenzon, K. Kobzar, B. Luy, S. J. Glaser, T. E. Skinner, “Optimal control design of excitation pulses that accomodate relaxation”, *J. Magn. Reson.* **2007**, *188*, 330–336.

[26] N. I. Gershenzon, T. E. Skinner, B. Brutscher, N. Khaneja, M. Nimbalkar, B. Luy, S. J. Glaser, “Linear phase slope in pulse design: Application to coherence transfer”, *J. Magn. Reson.* **2008**, *192*, 235 –243.

[27] K. Kobzar, T. E. Skinner, N. Khaneja, S. J. Glaser, B. Luy, “Exploring the limits of broadband excitation and inversion: II. Rf-power optimized pulses”, *J. Magn. Reson.* **2008**, *194*, 58 –66.

[28] T. E. Skinner, N. I. Gershenzon, M. Nimbalkar, S. J. Glaser, “Optimal control design of band-selective excitation pulses that accommodate relaxation and RF inhomogeneity”, *J. Magn. Reson.* **2012**, *217*, 53 –60.

[29] B. Luy, K. Kobzar, T. E. Skinner, N. Khaneja, S. J. Glaser, “Construction of universal rotations from point-to-point transformations”, *J. Magn. Reson.* **2005**, *176*, 179–186.

[30] J. Mao, T. H. Mareci, K. N. Scott, E. R. Andrew, “Selective inversion radiofrequency pulses by optimal control”, *J. Magn. Reson.* **1986**, *70*, 310 –318.

[31] S. Conolly, D. Nishimura, A. Macovski, "Optimal Control Solutions to the Magnetic Resonance Selective Excitation Problem", *IEEE Trans. Med. Imaging* **1986**, *5*, 106–115.

[32] D. Rosenfeld, Y. Zur, "Design of adiabatic selective pulses using optimal control theory", *Magn. Reson. Med.* **1996**, *36*, 401–409.

[33] T. O. Levante, T. Bremi, R. R. Ernst, "Pulse-Sequence Optimization with Analytical Derivatives. Application to Deuterium Decoupling in Oriented Phases", *J. Magn. Reson. A* **1996**, *121*, 167–177.

[34] U. Haeberlen, J. S. Waugh, "Coherent Averaging Effects in Magnetic Resonance", *Physical Review* **1968**, *175*, 453–467.

[35] Z. Tošner, S. J. Glaser, N. Khaneja, N. C. Nielsen, "Effective Hamiltonians by optimal control: Solid-state NMR double-quantum planar and isotropic dipolar recoupling", *J. Chem. Phys.* **2006**, *125*, 184502.

[36] J. L. Neves, B. Heitmann, N. Khaneja, S. J. Glaser, "Heteronuclear decoupling by optimal tracking", *J. Magn. Reson.* **2009**, *201*, 7–17.

[37] J. Keeler, *Understanding NMR Spectroscopy*, 2. Edition, Wiley, **2010**.

[38] S. J. Glaser, M. Braun, German, *European Patent*, EP 2,585,844, **2014**.

[39] M. Braun, S. J. Glaser, "Cooperative pulses", *J. Magn. Reson.* **2010**, *207*, 114–123.

[40] M. Braun, S. J. Glaser, "Concurrently optimized cooperative pulses in robust quantum control: application to broadband Ramsey-type pulse sequence elements", *New J. Phys.* **2014**, *16*, 115002.

[41] I. Kuprov, C. T. Rodgers, "Derivatives of spin dynamics simulations", *J. Chem. Phys.* **2009**, *131*, 234108.

[42] P. de Fouquieres, S. G. Schirmer, S. J. Glaser, I. Kuprov, "Second order gradient ascent pulse engineering", *J. Magn. Reson.* **2011**, *212*, 412–417.

[43] C. Van Loan, "Computing integrals involving the matrix exponential", *IEEE Trans. Automat. Contr.* **1978**, *23*, 395–404.

[44] D. L. Goodwin, I. Kuprov, "Auxiliary matrix formalism for interaction representation transformations, optimal control, and spin relaxation theories", *J. Chem. Phys.* **2015**, *143*, 084113.

[45] K. Aizu, "Parameter Differentiation of Quantum-Mechanical Linear Operators", *J. Math. Phys.* **1963**, *4*, 762.

[46] H. J. Hogben, M. Krzystyniak, G. T. P. Charnock, P. J. Hore, I. Kuprov, "Spinach - A software library for simulation of spin dynamics in large spin systems", *J. Magn. Reson.* **2011**, *208*, 179–194.

[47] J. Nocedal, S. J. Wright, *Numerical optimization*, 2. ed., Springer, New York, NY, **2006**.

[48] D. C. Liu, J. Nocedal, "On the limited memory BFGS method for large scale optimization", *Math. Progr.* **1989**, *45*, 503–528.

[49] D. L. Goodwin, I. Kuprov, “Modified Newton-Raphson GRAPE methods for optimal control of spin systems”, *J. Chem. Phys.* **2016**, *144*, 204107.

[50] M. R. Hestenes, E. Stiefel, “Methods of conjugate gradients for solving linear systems”, *J. Res. Nat. Bur. Stand.* **1952**, *49*, 409–436.

[51] S. Ehni, PhD thesis, Karlsruher Institut für Technologie (KIT), **2013**.

[52] M. R. M. Koos, MA thesis, Karlsruher Institut für Technologie (KIT), **2011**.

[53] I. Kuprov, “Spin system trajectory analysis under optimal control pulses”, *J. Magn. Reson.* **2013**, *233*, 107–112.

[54] S. S. Köcher, T. Heydenreich, S. J. Glaser, “Visualization and analysis of modulated pulses in magnetic resonance by joint time-frequency representations”, *J. Magn. Reson.* **2014**, *249*, 63–71.

[55] F. Bloch, “Recent Developments in Nuclear Induction”, *Phys. Rev.* **1954**, *93*, 944.

[56] A. L. Bloom, J. N. Shoolery, “Effects of Perturbing Radiofrequency Fields on Nuclear Spin Coupling”, *Physical Review* **1955**, *97*, 1261–1265.

[57] W. A. Anderson, R. Freeman, “Influence of a Second Radiofrequency Field on High-Resolution Nuclear Magnetic Resonance Spectra”, *J. Chem. Phys.* **1962**, *37*, 85–103.

[58] W. A. Anderson, F. A. Nelson, “Removal of Residual Splitting in Nuclear Magnetic Double Resonance”, *J. Chem. Phys.* **1963**, *39*, 183.

[59] R. R. Ernst, “Nuclear Magnetic Double Resonance with an Incoherent Radio-Frequency Field”, *J. Chem. Phys.* **1966**, *45*, 3845–3861.

[60] J. B. Grutzner, R. E. Santini, “Coherent broad-band decoupling - An alternative to proton noise decoupling in carbon-13 nuclear magnetic resonance spectroscopy”, *J. Magn. Reson.* **1975**, *19*, 173–187.

[61] V. Basus, P. D. Ellis, H. D. Hill, J. S. Waugh, “Utilization of chirp frequency modulation with 180°-phase modulation for heteronuclear spin decoupling”, *J. Magn. Reson.* **1979**, *35*, 19–37.

[62] R. Freeman, S. P. Kempsell, M. H. Levitt, “Broadband Decoupling and Scaling of Heteronuclear Spin-Spin Interactions in High-Resolution NMR”, *J. Magn. Reson.* **1979**, *35*, 447–450.

[63] R. Freeman, S. P. Kempsell, M. H. Levitt, “Radiofrequency pulse sequences which compensate their own imperfections”, *J. Magn. Reson.* **1980**, *38*, 453–479.

[64] M. H. Levitt, R. Freeman, “Composite pulse decoupling”, *J. Magn. Reson.* **1981**, *43*, 502–507.

[65] M. H. Levitt, R. Freeman, T. Frenkiel, “Broadband Heteronuclear Decoupling”, *J. Magn. Reson.* **1982**, *47*, 328–330.

[66] M. H. Levitt, R. Freeman, T. Frenkiel, “Supercycles for Broadband Heteronuclear Decoupling”, *J. Magn. Reson.* **1982**, *50*, 157–160.

[67] J. S. Waugh, "Systematic Procedure for Constructing Broadband decoupling Sequences", *J. Magn. Reson.* **1982**, *49*, 517–521.

[68] J. S. Waugh, "Theory of Broadband Spin Decoupling", *J. Magn. Reson.* **1982**, *50*, 30–49.

[69] A. J. Shaka, J. Keeler, T. Frenkiel, R. Freeman, "An Improved Sequence for Broadband Decoupling: WALTZ-16", *J. Magn. Reson.* **1983**, *52*, 335–338.

[70] Z. Zhou, R. Kümmerle, X. Qiu, D. Redwine, R. Cong, A. Taha, D. Baugh, B. Winniford, "A new decoupling method for accurate quantification of polyethylene copolymer composition and triad sequence distribution with ^{13}C NMR", *J. Magn. Reson.* **2007**, *187*, 225–233.

[71] A. J. Shaka, P. B. Barker, R. Freeman, "Computer-Optimized Decoupling Scheme for Wideband Applications and Low-Level Operation", *J. Magn. Reson.* **1985**, *64*, 547–552.

[72] A. J. Shaka, C. Lee, A Pines, "Iterative schemes for bilinear operators; application to spin decoupling", *J. Magn. Reson.* **1988**, *77*, 274–293.

[73] L. Braunschweiler, R. R. Ernst, "Coherence transfer by isotropic mixing: Application to proton correlation spectroscopy", *J. Magn. Reson.* **1983**, *53*, 521 –528.

[74] A. J. Shaka, P. B. Barker, C. J. Bauer, R. Freeman, "Cycling sidebands in broadband decoupling", *J. Magn. Reson.* **1986**, *67*, 396 –401.

[75] G. Bodenhausen, D. J. Ruben, "Natural abundance nitrogen-15 NMR by enhanced heteronuclear spectroscopy", *Chem. Phys. Lett.* **1980**, *69*, 185–189.

[76] A. Bax, R. H. Griffey, B. L. Hawkins, "Correlation of proton and nitrogen-15 chemical shifts by multiple quantum NMR", *J. Magn. Reson.* **1983**, *55*, 301–315.

[77] T. Fujiwara, K. Nagayama, "Composite inversion pulses with frequency switching and their application to broadband decoupling", *J. Magn. Reson.* **1988**, *77*, 53–63.

[78] T. Fujiwara, T. Anai, N. Kurihara, K. Nagayama, "Frequency-Switched Composite Pulses for Decoupling Carbon-13 Spins over Ultrabroad Bandwidths", *J. Magn. Reson. A* **1993**, *104*, 103–105.

[79] N. S. Bal, N. Hari, R. Ramachandran, "An Efficient Windowless Sequence for Broadband Heteronuclear Decoupling", *J. Magn. Reson. A* **1994**, *106*, 241–244.

[80] A. Abragam, *Principles of Nuclear Magnetism*, 11. Edition, Oxford University Press, **2007**.

[81] J. Baum, R. Tycko, A. Pines, "Broadband and adiabatic inversion of a two-level system by phase-modulated pulses", *Phys. Rev. A* **1985**, *32*, 3435–3447.

[82] M. S. Silver, R. I. Joseph, C.-N. Chen, V. J. Sank, D. I. Hoult, "Selective population inversion in NMR", *Nature* **1984**, *310*, 681–683.

[83] M. S. Silver, R. I. Joseph, D. I. Hoult, "Highly selective $\pi/2$ and π pulse generation", *J. Magn. Reson.* **1984**, *59*, 347–351.

[84] M. S. Silver, R. I. Joseph, D. I. Hoult, “Selective spin inversion in nuclear magnetic resonance and coherent optics through an exact solution of the Bloch-Riccati equation”, *Phys. Rev. A* **1985**, *31*, 2753–2755.

[85] Z. Starčuk, K. Bartušek, Z. Starčuk, “Heteronuclear Broadband Spin-Flip Decoupling with Adiabatic Pulses”, *J. Magn. Reson. A* **1994**, *107*, 24–31.

[86] M. R. Bendall, “Broadband and Narrowband Spin Decoupling Using Adiabatic Spin Flips”, *J. Magn. Reson. A* **1995**, *112*, 126–129.

[87] J.-M. Böhlen, I. Burghardt, M. Rey, G. Bodenhausen, “Frequency-modulated "Chirp" pulses for broadband inversion recovery in magnetic resonance”, *J. Magn. Reson.* **1990**, *90*, 183–191.

[88] J. M. Böhlen, G. Bodenhausen, “Experimental Aspects of Chirp NMR Spectroscopy”, *J. Magn. Reson. A* **1993**, *102*, 293–301.

[89] R. Fu, G. Bodenhausen, “Ultra-Broadband Decoupling”, *J. Magn. Reson. A* **1995**, *117*, 324–325.

[90] R. Fu, G. Bodenhausen, “Broadband decoupling in NMR with frequency-modulated ’chirp’ pulses”, *Chem. Phys. Lett.* **1995**, *245*, 415–420.

[91] E. Kupče, R. Freeman, “Adiabatic Pulses for Wideband Inversion and Broadband Decoupling”, *J. Magn. Reson. A* **1995**, *115*, 273–276.

[92] E. Kupče, R. Freeman, “Stretched Adiabatic Pulses for Broadband Spin Inversion”, *J. Magn. Reson. A* **1995**, *117*, 246–256.

[93] R. Fu, G. Bodenhausen, “Evaluation of Adiabatic Frequency-Modulated Schemes for Broadband Decoupling in Isotropic Liquids”, *J. Magn. Reson. A* **1996**, *119*, 129–133.

[94] M. R. Bendall, T. E. Skinner, “Calibration of STUD Decoupling to Achieve Selected Sideband Amplitudes”, *J. Magn. Reson. A* **1996**, *120*, 77–87.

[95] E. Kupče, R. Freeman, G. Wider, K. Wüthrich, “Figure of Merit and Cycling Sidebands in Adiabatic Decoupling”, *J. Magn. Reson. A* **1996**, *120*, 264–268.

[96] T. E. Skinner, M. R. Bendall, “Peak Power and Efficiency in Hyperbolic-Secant Decoupling”, *J. Magn. Reson. A* **1996**, *123*, 111–115.

[97] E. Kupče, R. Freeman, “Optimized Adiabatic Pulses for Wideband Spin Inversion”, *J. Magn. Reson. A* **1996**, *118*, 299–303.

[98] R. Tycko, A. Pines, “Iterative schemes for broad-band and narrow-band population inversion in NMR”, *Chem. Phys. Lett.* **1984**, *111*, 462–467.

[99] R. Tycko, A. Pines, J. Guckenheimer, “Fixed point theory of iterative excitation schemes in NMR”, *J. Chem. Phys.* **1985**, *83*, 2775.

[100] H. M. Cho, R. Tycko, A. Pines, J. Guckenheimer, “Iterative Maps for Bistable Excitation of Two-Level Systems”, *Phys. Rev. Lett.* **1986**, *56*, 1905–1908.

[101] T. E. Skinner, M. R. Bendall, “A Phase-Cycling Algorithm for Reducing Sidebands in Adiabatic Decoupling”, *J. Magn. Reson.* **1997**, *124*, 474–478.

[102] M. R. Bendall, T. E. Skinner, "Calibration of STUD+ Parameters to Achieve Optimally Efficient Broadband Adiabatic Decoupling in a Single Transient", *J. Magn. Reson.* **1998**, *134*, 331–349.

[103] S. Zhang, D. G. Gorenstein, "Adiabatic Decoupling Sidebands", *J. Magn. Reson.* **2000**, *144*, 316–321.

[104] R. W. Dykstra, "A method to suppress cycling sidebands in broadband decoupling", *J. Magn. Reson.* **1989**, *82*, 347–351.

[105] E. Kupče, R. Freeman, G. Wider, K. Wüthrich, "Suppression of Cycling Sidebands Using Bi-level Adiabatic Decoupling", *J. Magn. Reson. A* **1996**, *122*, 81–84.

[106] E. Kupče, R. Freeman, "Compensation for Spin-Spin Coupling Effects during Adiabatic Pulses", *J. Magn. Reson.* **1997**, *127*, 36–48.

[107] F. Schilling, L. R. Warner, N. I. Gershenzon, T. E. Skinner, M. Sattler, S. J. Glaser, "Next-Generation Heteronuclear Decoupling for High-Field Biomolecular NMR Spectroscopy", *Angew. Chem. Int. Ed.* **2014**, *53*, 4475–4479.

[108] R. Freeman, *Spin Choreography: Basic Steps in High Resolution NMR*, Überarbeitete Auflage, Oxford University Press, **1999**.

[109] M. A. Smith, H. Hu, A. J. Shaka, "Improved Broadband Inversion Performance for NMR in Liquids", *J. Magn. Reson.* **2001**, *151*, 269–283.

[110] B. Stinson, M. Kuhn, *THE BROCODE*, Simon & Schuster, New York, **2008**.

[111] Absatz von Neonikotinoiden wieder leicht gestiegen, www.proplanta.de, **2015**, `http://www.proplanta.de/Agrar-Nachrichten/Pflanze/Absatz-von-Neonikotinoiden-wieder-leicht-gestiegen_article1448187305.html`.

[112] T. A. Unger, *Pesticide Synthesis Handbook*, Noyes Publications, New Jersey, **1996**.

[113] A. Enthart, J. C. Freudenberger, J. Furrer, H. Kessler, B. Luy, "The CLIP/CLAP-HSQC: Pure Absorptive Spectra for the Measurement of One-Bond Couplings", *J. Magn. Reson.* **2008**, *192*, 314–322.

[114] R. J. Abraham, A. P. Barlow, A. E. Rowan, "Substituent chemical shifts in NMR. Part 4-^{1}H SCS in some 2-substituted norbornanes and bornanes", *Magn. Reson. Chem.* **1989**, *27*, 1074–1084.

[115] W. P. Aue, E. Bartholdi, R. R. Ernst, "Two-dimensional spectroscopy. Application to nuclear magnetic resonance", *J. Chem. Phys.* **1976**, *64*, 2229.

[116] M. Rance, O. W. Sørensen, G. Bodenhausen, G. Wagner, R. R. Ernst, K. Wüthrich, "Improved spectral resolution in COSY ^{1}H NMR spectra of proteins via double quantum filtering", *Biochem. Biophys. Res. Comm.* **1983**, *117*, 479–485.

[117] A. Bax, M. F. Summers, "Proton and carbon-13 assignments from sensitivity-enhanced detection of heteronuclear multiple-bond connectivity by 2D multiple quantum NMR", *J. Am. Chem. Soc.* **1986**, *108*, 2093–2094.

[118] W. Koźmiński, "Simplified Multiplet Pattern HSQC-TOCSY Experiment for Accurate Determination of Long-Range Heteronuclear Coupling Constants", *J. Magn. Reson.* **1999**, *137*, 408–412.

[119] G. Kummerlöwe, S. Schmitt, B. Luy, “Cross-Fitting of Residual Dipolar Couplings”, *The Open Spectrosc. J.* **2010**, *4*, 16–27.

[120] G. A. Morris, R. Freeman, “Enhancement of nuclear magnetic resonance signals by polarization transfer”, *J. Am. Chem. Soc.* **1979**, *101*, 760–762.

[121] B. Baishya, C. L. Khetrapal, “"Perfect echo" INEPT: More efficient heteronuclear polarization transfer by refocusing homonuclear J-coupling interaction”, *J. Magn. Reson.* **2014**, *242*, 143–154.

[122] F. Hallwass, M. Schmidt, H. Sun, A. Mazur, G. Kummerlöwe, B. Luy, A. Navarro-Vázquez, C. Griesinger, U. M. Reinscheid, “Residual Chemical Shift Anisotropy (RCSA): A Tool for the Analysis of the Configuration of Small Molecules”, *Angew. Chem. Int. Ed.* **2011**, *50*, 9487–9490.

[123] P. Tzvetkova, B. Luy, “Q.E.COSY: determining sign and size of small deuterium residual quadrupolar couplings using an extended E.COSY principle”, *Magn. Reson. Chem.* **2016**, *54*, 351–357.

[124] N. Tjandra, A. Bax, “Direct Measurement of Distances and Angles in Biomolecules by NMR in a Dilute Liquid Crystalline Medium”, *Science* **1997**, *278*, 1111–1114.

[125] C. M. Thiele, “Residual Dipolar Couplings (RDCs) in Organic Structure Determination”, *Eur. J. Org. Chem.* **2008**, *2008*, 5673–5685.

[126] G. Kummerlöwe, B. Luy, “Residual dipolar couplings as a tool in determining the structure of organic molecules”, *Trends Anal. Chem.* **2009**, *28*, 483–493.

[127] G. Kummerlöwe, B. Luy, “Residual Dipolar Couplings for the Configurational and Conformational Analysis of Organic Molecules”, *Annu. Rep. NMR Spectrosc.* **2009**, *68*, 193–232.

[128] R. R. Gil, “Constitutional, Configurational, and Conformational Analysis of Small Organic Molecules on the Basis of NMR Residual Dipolar Couplings”, *Angew. Chem. Int. Ed.* **2011**, *50*, 7222–7224.

[129] H. Friebolin, *Ein- und zweidimensionale NMR-Spektroskopie: eine Einführung*, 4., vollst. überarb. und aktualisierte Aufl., Wiley-VCH, Weinheim, **2006**.

[130] I. Tvaroska, F. R. Taravel, “Carbon-Proton Coupling Constants In The Conformational Analysis of Sugar Molecules”, *Adv. Carbohydr. Chem. Biochem.* **1995**, *51*, 15–61.

[131] D. F. Mierke, S. G. Grdadolnik, H. Kessler, “Use of one-bond C^{α}-H^{α} coupling constants as restraints in MD simulations”, *J. Am. Chem. Soc.* **1992**, *114*, 8283–8284.

[132] J. Klages, C. Neubauer, M. Coles, H. Kessler, B. Luy, “Structure Refinement of Cyclosporin A in Chloroform by Using RDCs Measured in a Stretched PDMS-Gel”, *ChemBioChem* **2005**, *6*, 1672–1678.

[133] N. Cramer, S. Helbig, A. Baro, S. Laschat, R. Diestel, F. Sasse, D. Mathieu, C. Richter, G. Kummerlöwe, B. Luy, H. Schwalbe, “Synthesis and Biological Properties of Cylindramide Derivatives: Evidence for Calcium-Dependent Cytotoxicity of Tetramic Acid Lactams”, *ChemBioChem* **2008**, *9*, 2474–2486.

[134] M. U. Kiran, A. Sudhakar, J. Klages, G. Kummerlöwe, B. Luy, B. Jagadeesh, "RDC Enhanced NMR Spectroscopy in Organic Solvent Media: The Importance for the Experimental Determination of Periodic Hydrogen Bonded Secondary Structures", *J. Am. Chem. Soc.* **2009**, *131*, 15590–15591.

[135] C. Gayathri, M. C. de la Fuente, B. Luy, R. R. Gil, A. Navarro-Vázquez, "Probing heterocycle conformation with residual dipolar couplings", *Chem. Commun.* **2010**, *46*, 5879–5881.

[136] S. Weigelt, T. Huber, F. Hofmann, M. Jost, M. Ritzefeld, B. Luy, C. Freudenberger, Z. Majer, E. Vass, J.-C. Greie, L. Panella, B. Kaptein, Q. B. Broxterman, H. Kessler, K. Altendorf, M. Hollósi, N. Sewald, "Synthesis and Conformational Analysis of Efrapeptins", *Chem. Eur. J.* **2011**, *18*, 478–487.

[137] J. C. Freudenberger, P. Spiteller, R. Bauer, H. Kessler, B. Luy, "Stretched Poly(dimethylsiloxane) Gels as NMR Alignment Media for Apolar and Weakly Polar Organic Solvents: An Ideal Tool for Measuring RDCs at Low Molecular Concentrations", *J. Am. Chem. Soc.* **2004**, *126*, 14690–14691.

[138] J. C. Freudenberger, S. Knör, K. Kobzar, D. Heckmann, T. Paululat, H. Kessler, B. Luy, "Stretched Poly(vinyl acetate) Gels as NMR Alignment Media for the Measurement of Residual Dipolar Couplings in Polar Organic Solvents", *Angew. Chem. Int. Ed.* **2004**, *44*, 423–426.

[139] D. Intelmann, G. Kummerlöwe, G. Haseleu, N. Desmer, K. Schulze, R. Fröhlich, O. Frank, B. Luy, T. Hofmann, "Structures of Storage-Induced Transformation Products of the Beer's Bitter Principles, Revealed by Sophisticated NMR Spectroscopic and LC-MS Techniques", *Chem. Eur. J.* **2009**, *15*, 13047–13058.

[140] M. E. García, S. Pagola, A. Navarro-Vázquez, D. D. Phillips, C. Gayathri, H. Krakauer, P. W. Stephens, V. E. Nicotra, R. R. Gil, "Stereochemistry Determination by Powder X-Ray Diffraction Analysis and NMR Spectroscopy Residual Dipolar Couplings", *Angew. Chem. Int. Ed.* **2009**, *48*, 5670–5674.

[141] H. Sun, U. M. Reinscheid, E. L. Whitson, E. J. d'Auvergne, C. M. Ireland, A. Navarro-Vázquez, C. Griesinger, "Challenge of Large-Scale Motion for Residual Dipolar Coupling Based Analysis of Configuration: The Case of Fibrosterol Sulfate A", *J. Am. Chem. Soc.* **2011**, *133*, 14629–14636.

[142] P. Tzvetkova, B. Luy, S. Simova, "Configuration verification via RDCs on the example of a tetra-substituted pyrrolidine ring", *Magn. Reson. Chem.* **2012**, *50*, S92–S101.

[143] G. Kummerlöwe, B. Crone, M. Kretschmer, S. F. Kirsch, B. Luy, "Residual Dipolar Couplings as a Powerful Tool for Constitutional Analysis: The Unexpected Formation of Tricyclic Compounds", *Angew. Chem. Int. Ed.* **2011**, *50*, 2643–2645.

[144] M. Sarfati, P. Lesot, D. Merlet, J. Courtieu, "Theoretical and experimental aspects of enantiomeric differentiation using natural abundance multinuclear nmr spectroscopy in chiral polypeptide liquid crystals", *Chem. Commun.* **2000**, 2069–2081.

[145] L. Ziani, P. Lesot, A. Meddour, J. Courtieu, "Empirical determination of the absolute configuration of small chiral molecules using natural abundance ^{2}H NMR in chiral liquid crystals", *Chem. Commun.* **2007**, 4737–4739.

[146] B. Luy, "Disinction of enantiomers by NMR spectroscopy using chiral orienting media", *J. Indian. Inst. Sci.* **2010**, *192*, 119–132.

[147] R. Berger, J. Courtieu, R. R. Gil, C. Griesinger, M. Köck, P. Lesot, B. Luy, D. Merlet, A. Navarro-Vázquez, M. Reggelin, U. M. Reinscheid, C. M. Thiele, M. Zweckstetter, "Is Enantiomer Assignment Possible by NMR Spectroscopy Using Residual Dipolar Couplings from Chiral Nonracemic Alignment Media?-A Critical Assessment", *Angew. Chem. Int. Ed.* **2012**, *51*, 8388–8391.

[148] P. Nolis, J. F. Espinosa, T. Parella, "Optimum spin-state selection for all multiplicities in the acquisition dimension of the HSQC experiment", *J. Magn. Reson.* **2006**, *180*, 39–50.

[149] P. Tzvetkova, S. Simova, B. Luy, "P.E.HSQC: A simple experiment for simultaneous and sign-sensitive measurement of ($^1J_{\mathrm{CH}}$ + D_{CH}) and ($^2J_{\mathrm{HH}}$ + D_{HH}) couplings", *J. Magn. Reson.* **2007**, *186*, 193–200.

[150] P. Giraudeau, T. Montag, B. Charrier, C. M. Thiele, "Fast access to residual dipolar couplings by single-scan 2D NMR in oriented media", *Magn. Reson. Chem.* **2012**, *50*, S53–S57.

[151] B. Görling, S. Bräse, B. Luy, "HR-HSBC: Measuring heteronuclear one-bond couplings with enhanced resolution", *Magn. Reson. in Chem.* **2012**, *50*, S58–S62.

[152] L. Castañar, J. Saurí, R. T. Williamson, A. Virgili, T. Parella, "Pure In-Phase Heteronuclear Correlation NMR Experiments", *Angew. Chem. Int. Ed.* **2014**, *53*, 8379–8382.

[153] J. Becker, B. Luy, "CLIP-ASAP-HSQC for fast and accurate extraction of one-bond couplings from isotropic and partially aligned molecules", *Magn. Reson. Chem.* **2015**, *53*, 878–885.

[154] K. Kobzar, H. Kessler, B. Luy, "Stretched Gelatin Gels as Chiral Alignment Media for the Discrimination of Enantiomers by NMR spectroscopy", *Angew. Chem. Int. Ed.* **2005**, *44*, 3145–3147.

[155] J. Furrer, M. John, H. Kessler, B. Luy, "*J*-Spectroscopy in the presence of residual dipolar couplings: determination of one-bond coupling constants and scalable resolution", *J. Biomol. NMR* **2007**, *37*, 231–243.

[156] C. M. Thiele, W. Bermel, "Speeding up the measurement of one-bond scalar (^1J) and residual dipolar couplings (^1D) by using non-uniform sampling (NUS)", *J. Magn. Reson.* **2012**, *216*, 134–143.

[157] J. Saurí, L. Castañar, P. Nolis, A. Virgili, T. Parella, "Straightforward measurement of individual ^{1}J(CH) and ^{2}J(HH) in diastereotopic CH_2 groups", *J. Magn. Reson.* **2014**, *242*, 33–40.

[158] J. Farjon, W. Bermel, C. Griesinger, “Resolution enhancement in spectra of natural products dissolved in weakly orienting media with the help oh ^{1}H homonuclear dipolar decoupling during aquisition: Application to ^{1}H-^{13}C dipolar couplings measurements”, *J. Magn. Reson.* **2006**, *180*, 72–82.

[159] W. P. Aue, J. Karhan, R. R. Ernst, “Homonuclear broad band decoupling and two-dimensional J-resolved NMR spectroscopy”, *J. Chem. Phys.* **1976**, *64*, 4226–4227.

[160] P. Sakhaii, W. Bermel, “Improving the sensitivity of conventional spin echo spectra by preservation of initial signal-to-noise ratio”, *J. Magn. Reson.* **2014**, *242*, 220–223.

[161] M. J. Thrippleton, J. Keeler, “Elimination of Zero-Quantum Interference in Two-Dimensional NMR Spectra”, *Angew. Chem. Int. Ed.* **2003**, *42*, 3938–3941.

[162] B. Luy, “Adiabatic z-filtered J-spectroscopy for absorptive homonuclear decoupled spectra”, *J. Magn. Reson.* **2009**, *201*, 18–24.

[163] A. J. Pell, J. Keeler, “Two-dimensional J-spectra with absorption-mode lineshapes”, *J. Magn. Reson.* **2007**, *189*, 293–299.

[164] L. H. Lucas, W. H. Otto, C. K. Larive, “The 2D-J-DOSY Experiment: Resolving Diffusion Coefficients in Mixtures”, *J. Magn. Reson.* **2002**, *156*, 138–145.

[165] J. Cobas, M. Martín-Pastor, “A homodecoupled diffusion experiment for the analysis of complex mixtures by NMR”, *J. Magn. Reson.* **2004**, *171*, 20–24.

[166] A. Bax, A. F. Mahlkopf, J. Smidt, “Homonuclear Broadband-Decoupled Absorption Spectra, with Linewidths Which Are Independent of the Transverse Relaxation Rate”, *J. Magn. Reson.* **1979**, *35*, 167–169.

[167] A. Bax, R. Freeman, “Investigation of complex networks of spin-spin coupling by two-dimensional NMR”, *J. Magn. Reson.* **1981**, *44*, 542–561.

[168] M. Rance, G. Wagner, O. W. Sørensen, K. Wüthrich, R. R. Ernst, “Application of ω_1-decoupled 2D correlation spectra to the study of proteins”, *J. Magn. Reson.* **1984**, *59*, 250–261.

[169] M. Girvin, “Increased Sensitivity of COSY Spectra by Use of Constant-Time t_1 Periods (CT COSY)”, *J. Magn. Reson. A* **1994**, *108*, 99–102.

[170] Y. Xia, G. Legge, K.-Y. Jun, Y. Qi, H. Lee, X. Gao, “IP-COSY, a totally in-phase and sensitive COSY experiment”, *Magn. Reson. Chem.* **2005**, *43*, 372–379.

[171] G. W. Vuister, A. Bax, “Resolution enhancement and spectral editing of uniformly ^{13}C-enriched proteins by homonuclear broadband ^{13}C decoupling”, *J. Magn. Reson.* **1992**, *98*, 428–435.

[172] R. W. Adams, “Pure Shift NMR Spectroscopy”, *eMagRes* **2014**, *3*, 295–310.

[173] K. Zangger, “Pure shift NMR”, *Prog. NMR Spec.* **2015**, *86-87*, 1–20.

[174] L. Castañar, T. Parella, “Broadband ^{1}H homodecoupled NMR experiments: recent developments, methods and applications”, *Magn. Reson. Chem.* **2015**, *53*, 399–426.

[175] J. R. Garbow, D. P. Weitekamp, A. Pines, “Bilinear Rotation Decoupling Of Homonuclear Scalar Interactions”, *Chem. Phys. Lett.* **1982**, *93*, 504–509.

[176] K. Kobzar, B. Luy, “Analyses, extensions and comparison of three experimental schemes for measuring ($^nJ_{CH}$ + D_{CH})-couplings at natural abundance”, *J. Magn. Reson.* **2007**, *186*, 131–141.

[177] P. Sakhaii, W. Bermel, “A different approach to multiplicity-edited heteronuclear single quantum correlation spectroscopy”, *J. Magn. Reson.* **2015**, *259*, 82–86.

[178] C. Griesinger, O. W. Sørensen, R. R. Ernst, “Two-dimensional correlation of connected NMR transitions”, *J. Am. Chem. Soc.* **1985**, *107*, 6394–6396.

[179] O. W. Sørensen, C. Griesinger, R. R. Ernst, “Time reversal of the evolution under scalar spin-spin interactions in NMR. Application for ω_1 decoupling in two-dimensional NOE spectroscopy”, *J. Am. Chem. Soc.* **1985**, *107*, 7778–7779.

[180] H. Oschkinat, A. Pastore, P. Pfändler, G. Bodenhausen, “Two-dimensional correlation of directly and remotely connected transitions by z-filtered COSY”, *J. Magn. Reson.* **1986**, *69*, 559–566.

[181] A. J. Pell, R. A. E. Edden, J. Keeler, “Broadband proton-decoupled proton spectra”, *Magn. Reson. Chem.* **2007**, *45*, 296–316.

[182] K. Zangger, H. Sterk, “Homonuclear Broadband-Decoupled NMR-Spectra”, *J. Magn. Reson.* **1997**, *124*, 486–489.

[183] M. Nilsson, G. A. Morris, “Pure shift proton DOSY: diffusion-ordered ^{1}H spectra without multiplet structure”, *Chem. Commun.* **2007**, 933.

[184] J. A. Aguilar, S. Faulkner, M. Nilsson, G. A. Morris, “Pure Shift ^{1}H NMR: A Resolution of the Resolution Problem?”, *Angew. Chem. Int. Ed.* **2010**, *49*, 3901–3903.

[185] F. Zhang, R. Brüschweiler, “Indirect Covariance NMR Spectroscopy”, *J. Am. Chem. Soc.* **2004**, *126*, 13180–13181.

[186] G. A. Morris, J. A. Aguilar, R. Evans, S. Haiber, M. Nilsson, “True Chemical Shift Correlation Maps: A TOCSY Experiment with Pure Shifts in Both Dimensions”, *J. Am. Chem. Soc.* **2010**, *132*, 12770–12772.

[187] J. J. Koivisto, “Zero-quantum filtered pure shift TOCSY”, *Chem. Commun.* **2013**, *49*, 96–98.

[188] J. A. Aguilar, A. A. Colbourne, J. Cassani, M. Nilsson, G. A. Morris, “Decoupling Two-Dimensional NMR Spectroscopy in Both Dimensions: Pure Shift NOESY and COSY”, *Angew. Chem. Int. Ed.* **2012**, *51*, 6460–6463.

[189] P. Sakhaii, B. Haase, W. Bermel, R. Kerssebaum, G. E. Wagner, K. Zangger, “Broadband homodecoupled NMR spectroscopy with enhanced sensitivity”, *J. Magn. Reson.* **2013**, *233*, 92–95.

[190] J. A. Aguilar, M. Nilsson, G. A. Morris, “Simple Proton Spectra from Complex Spin Systems: Pure Shift NMR Spectroscopy Using BIRD”, *Angew. Chem. Int. Ed.* **2011**, *50*, 9716–9717.

[191] D. Uhrín, T. Liptaj, K. E. Kövér, “Modified BIRD Pulses and Design of Heteronuclear Pulse Sequences”, *J. Magn. Reson. A* **1993**, *101*, 41–46.

[192] P. Sakhaii, B. Haase, W. Bermel, “Experimental access to HSQC spectra decoupled in all frequency dimensions”, *J. Magn. Reson.* **2009**, *199*, 192–198.

[193] P. Sakhaii, B. Haase, W. Bermel, “Broadband homodecoupled heteronuclear multiple bond correlation spectroscopy”, *J. Magn. Reson.* **2013**, *228*, 125–129.

[194] M. Foroozandeh, R. W. Adams, N. J. Meharry, D. Jeannerat, M. Nilsson, G. A. Morris, “Ultrahigh-Resolution NMR Spectroscopy”, *Angew. Chem. Int. Ed.* **2014**, *53*, 6990–6992.

[195] M. Foroozandeh, R. W. Adams, M. Nilsson, G. A. Morris, “Ultrahigh-Resolution Total Correlation NMR Spectroscopy”, *J. Am. Chem. Soc.* **2014**, *136*, 11867–11869.

[196] M. Foroozandeh, R. W. Adams, P. Király, M. Nilsson, G. A. Morris, “Measuring couplings in crowded NMR spectra: pure shift NMR with multiplet analysis”, *Chem. Commun.* **2015**, *51*, 15410–15413.

[197] D. Sinnaeve, M. Foroozandeh, M. Nilsson, G. A. Morris, “A General Method for Extracting Individual Coupling Constants from Crowded ^{1}H NMR Spectra”, *Angew. Chem. Int. Ed.* **2015**, *55*, 1090–1093.

[198] A. Lupulescu, G. L. Olsen, L. Frydman, “Toward single-shot pure-shift solution 1H NMR by trains of BIRD-based homonuclear decoupling”, *J. Magn. Reson.* **2012**, *218*, 141–146.

[199] T. Gullion, D. B. Baker, M. S. Conradi, “New, compensated Carr-Purcell sequences”, *J. Magn. Reson.* **1990**, *89*, 479–484.

[200] L. Paudel, R. W. Adams, P. Király, J. A. Aguilar, M. Foroozandeh, M. J. Cliff, M. Nilsson, P. Sándor, J. P. Waltho, G. A. Morris, “Simultaneously Enhancing Spectral Resolution and Sensitivity in Heteronuclear Correlation NMR Spectroscopy”, *Angew. Chem. Int. Ed.* **2013**, *52*, 11616–11619.

[201] A. Verma, B. Baishya, “Real-time bilinear rotation decoupling in absorptive mode J-spectroscopy: Detecting low-intensity metabolite peak close to high-intensity metabolite peak with convenience”, *J. Magn. Reson.* **2016**, *266*, 51–58.

[202] N. H. Meyer, K. Zangger, “Simplifying Proton NMR Spectra by Instant Homonuclear Broadband Decoupling”, *Angew. Chem. Int. Ed.* **2013**, *52*, 7143–7146.

[203] S. Glanzer, K. Zangger, “Directly Decoupled Diffusion-Ordered NMR Spectroscopy for the Analysis of Compound Mixtures”, *Chem. Eur. J.* **2014**, *20*, 11171–11175.

[204] V. M. R. Kakita, J. Bharatam, “Real-time homonuclear broadband and band-selective decoupled pure-shift ROESY”, *Magn. Reson. Chem.* **2014**, *52*, 389–394.

[205] N. Gubensäk, W. M. F. Fabian, K. Zangger, “Disentangling scalar coupling patterns by real-time SERF NMR”, *Chem. Commun.* **2014**, *50*, 12254–12257.

[206] N. Lokesh, S. R. Chaudhari, N. Suryaprakash, “Quick re-introduction of selective scalar interactions in a pure-shift NMR spectrum”, *Chem. Commun.* **2014**, *50*, 15597–15600.

[207] S. R. Chaudhari, N. Suryaprakash, “J-Edited Pure Shift NMR for the Facile Measurement of $^{n}J_{\mathrm{HH}}$ for Specific Protons”, *ChemPhysChem* **2015**, *16*, 1079–1082.

[208] L. Castañar, P. Nolis, A. Virgili, T. Parella, "Full Sensitivity and Enhanced Resolution in Homodecoupled Band-Selective NMR Experiments", *Chem. Eur. J.* **2013**, *19*, 17283–17286.

[209] J. Ying, J. Roche, A. Bax, "Homonuclear decoupling for enhancing resolution and sensitivity in NOE and RDC measurements of peptides and proteins", *J. Magn. Reson.* **2014**, *241*, 97–102.

[210] R. W. Adams, L. Byrne, P. Király, M. Foroozandeh, L. Paudel, M. Nilsson, J. Clayden, G. A. Morris, "Diastereomeric ratio determination by high sensitivity band-selective pure shift NMR spectroscopy", *Chem. Commun.* **2014**, *50*, 2512–2514.

[211] L. Castañar, P. Nolis, A. Virgili, T. Parella, "Measurement of T_1/T_2 relaxation times in overlapped regions from homodecoupled ^{1}H singlet signals", *J. Magn. Reson.* **2014**, *244*, 30–35.

[212] T. Reinsperger, B. Luy, "Homonuclear BIRD-decoupled spectra for measuring one-bond couplings with highest resolution: CLIP/CLAP-RESET and constant-time-CLIP/CLAP-RESET", *J. Magn. Reson.* **2014**, *239*, 110–120.

[213] M. Ottiger, F. Delaglio, A. Bax, "Measurement of J and Dipolar Couplings from Simplified Two-Dimensional NMR Spectra", *J. Magn. Reson.* **1998**, *131*, 373–378.

[214] R. W. Adams, Reconstruction program for PS data, University of Manchester, `http://nmr.chemistry.manchester.ac.uk/sites/default/files/pshift`.

[215] I. Timári, L. Kaltschnee, A. Kolmer, R. W. Adams, M. Nilsson, C. M. Thiele, G. A. Morris, K. E. Kövér, "Accurate determination of one-bond heteronuclear coupling constants with "pure shift" broadband proton-decoupled CLIP/CLAP-HSQC experiments", *J. Magn. Reson.* **2014**, *239*, 130–138.

[216] A. Fredi, P. Nolis, C. Cobas, G. E. Martin, T. Parella, "Exploring the use of Generalized Indirect Covariance to reconstruct pure shift NMR spectra: Current Pros and Cons", *J. Magn. Reson.* **2016**, *266*, 16–22.

[217] L. Kaltschnee, A. Kolmer, I. Timári, V. Schmidts, R. W. Adams, M. Nilsson, K. E. Kövér, G. A. Morris, C. M. Thiele, ""Perfecting" pure shift HSQC: full homodecoupling for accurate and precise determination of heteronuclear couplings", *Chem. Commun.* **2014**, *50*, 15702–15705.

[218] K. Takegoshi, K. Ogura, K. Hikichi, "A perfect spin echo in a weakly homonuclear J-coupled two spin-$\frac{1}{2}$ system", *J. Magn. Reson.* **1989**, *84*, 611–615.

[219] J. A. Aguilar, M. Nilsson, G. Bodenhausen, G. A. Morris, "Spin echo NMR spectra without J modulation", *Chem. Commun.* **2012**, *48*, 811–813.

[220] B. Baishya, C. L. Khetrapal, K. K. Dey, ""Perfect Echo" HMQC: Sensitivity and resolution enhancement by broadband homonuclear decoupling", *J. Magn. Reson.* **2013**, *234*, 67–74.

[221] J. A. Aguilar, G. A. Morris, A. M. Kenwright, ""Pure shift" ^{1}H NMR, a robust method for revealing heteronuclear couplings in complex spectra", *RSC Adv.* **2014**, *4*, 8278–8282.

[222] S. R. Chaudhari, N. Suryaprakash, "Pure shift NMR approach for fast and accurate extraction of heteronuclear couplings", *RSC Adv.* **2014**, *4*, 15018–15021.

[223] I. Timári, T. Z. Illyés, R. W. Adams, M. Nilsson, L. Szilágyi, G. A. Morris, K. E. Kövér, "Precise Measurement of Long-Range Heteronuclear Coupling Constants by a Novel Broadband Proton-Proton-Decoupled CPMG-HSQMBC Method", *Chem. Eur. J.* **2015**, *21*, 3472–3479.

[224] I. Timári, L. Szilágyi, K. E. Kövér, "PSYCHE CPMG-HSQMBC: An NMR Spectroscopic Method for Precise and Simple Measurement of Long-Range Heteronuclear Coupling Constants", *Chem. Eur. J.* **2015**, *21*, 13939–13942.

[225] N. Marcó, A. Fredi, T. Parella, "Ultra high-resolution HSQC: application to the efficient and accurate measurement of heteronuclear coupling constants", *Chem. Commun.* **2015**, *51*, 3262–3265.

[226] C. M. Thiele, New Methods For Measuring And Orienting Organic Compounds For RDC Structural Analysis, Talk at the EUROMAR Conference, Prague, **2015**.

[227] L. Castañar, J. Saurí, P. Nolis, A. Virgili, T. Parella, "Implementing homo- and heterodecoupling in region-selective HSQMBC experiments", *J. Magn. Reson.* **2014**, *238*, 63–69.

[228] P. W. Kuchel, B. E. Chapman, N. Müller, W. A. Bubb, D. J. Philp, A. M. Torres, "Apparatus for rapid adjustment of the degree of alignment of NMR samples in aqueous media: Verification with residual quadrupolar splittings in ^{23}Na and ^{133}Cs spectra", *J. Magn. Reson.* **2006**, *180*, 256–265.

[229] G. Kummerlöwe, F. Halbach, B. Laufer, B. Luy, "Precise Measurement of RDCs in Water and DMSO Based Gels Using a Silicone Rubber Tube for Tunable Stretching", *The Open Spectrosc. J.* **2008**, *2*, 29–33.

[230] G. Kummerlöwe, E. F. McCord, S. F. Cheatham, S. Niss, R. W. Schnell, B. Luy, "Tunable Alignment for All Polymer Gel/Solvent Combinations for the Measurement of Anisotropic NMR Parameters", *Chem. Eur. J.* **2010**, *16*, 7087–7089.

[231] P. Trigo-Mouriño, C. Merle, M. R. M. Koos, B. Luy, R. R. Gil, "Probing Spatial Distribution of Alignment by Deuterium NMR Imaging", *Chem. Eur. J.* **2013**, *19*, 7013–7019.

List of Figures

List of Tables

A. Appendix

A.1. Benchmark data

In order to quantify the gains in speed by changing the formalism in which the spin dynamics are treated in thesis (see section 2.2.4), a computational benchmark was set. The decoupling sequence obtained in section 2.2.2 was subjected to a linearly increasing number of simple quality factor evaluations under the MATLAB®framework given in appendix A.2.1. Wall clock times were obtained by time stamp commands and Hilbert space computations were compared to their reduced Liouville space counterparts using a Windows® workstation and a Linux machine. Moreover, to assess the reduction in computational efforts under more realistic conditions, the expenditure of time for 1000 iterations of the GRAPE algorithm was measured for optimizations described in section 2.2.2 and compared to examples similar to the ones discussed in [36] and [107]. Time stamps for the latter were obtained after every 50 iterations and data was collected using serial and parallel computation. The data and the respective gain factors deduced from linear fits are compiled in figure A.1. Under MATLAB®, the gain factors show a significant spread between the different machines, which can most likely be attributed to the different hardware architecture. The difference between serial and parallel operation on the same machine seems more peculiar. It appears that either the Hilbert space computations require more overhead, which seems unlikely, or the reduced state space prevents situations where the workload among the different threads is unevenly distributed so that periods of waiting are introduced which would prolong the total duration. In terms of full GRAPE iterations, the gain factors are very similar for serial operation whereas a significant spread is reintroduced upon parallelization. This can be explained by the scale of the problem and the amount of time the optimization actually spends in the parallel fork, which can be correlated with N_{ν_S}. The latter was set to 21 for TRACK[36], 101 for BUSS [107] and 384 for the test pulse in this work. This indicates that the higher the value for N_{ν_S}, the more time is relatively spend in the parallel fork, where the optimization is more significantly sped up by using the state space restriction.

Also in section 2.2.4, the effects of a periodical refreshment of the CG trajectory were explored. For the optimizations leading to the BROCODE, 50 iterations were found to be the optimal period to reset the CG routine. A more frequent reinitialization led to significantly impaired convergence as illustrated in figure A.2. This indicates that at least to some extent the hypersurface of the quality factors is locally quadratic with respect to the control amplitudes.

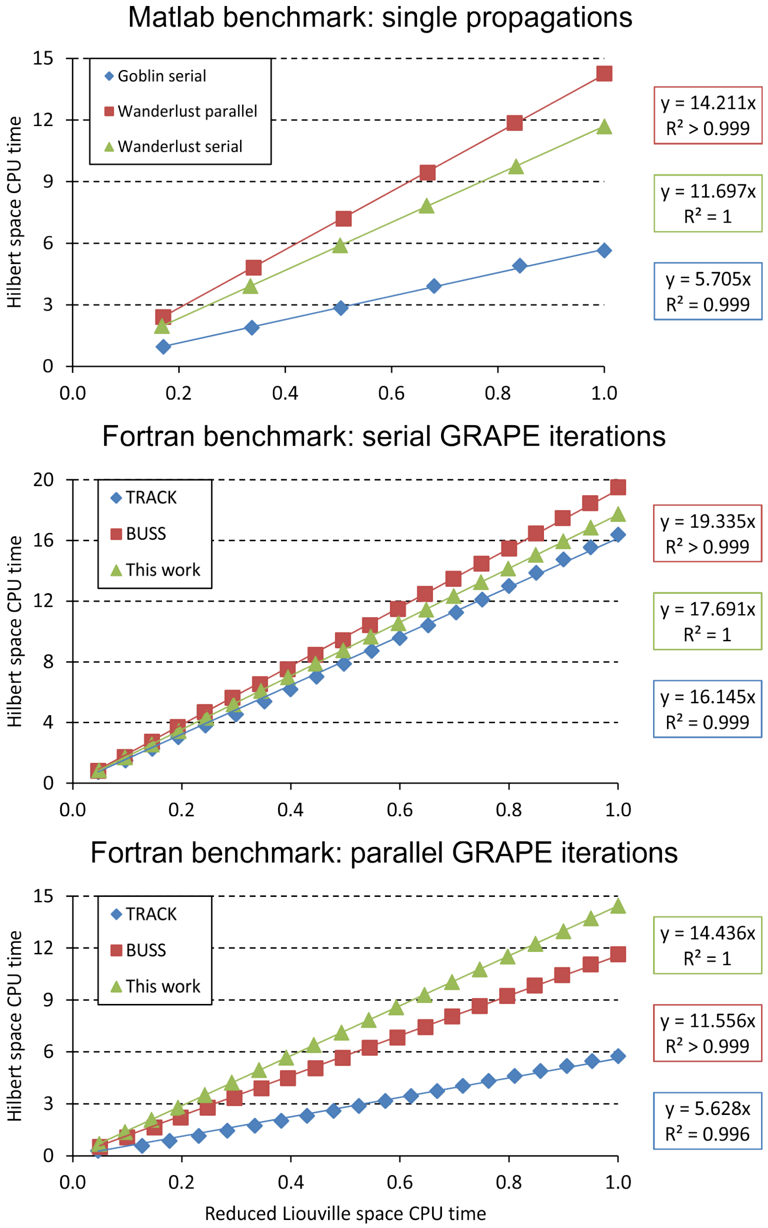

Figure A.1.: Benchmark data for reduced state space vs. conventional Hilbert space computations. The test pulse obtained in section 2.2.2 was used for the MATLAB®benchmark comparing the speed of simple quality factor evaluations. Performance gains were compared between a Windows® workstation (Goblin) and a Linux machine (Wanderlust). The latter was employed to compare the speed of full iterations of the GRAPE algorithm for optimization problems discussed in [36] and [107] with the one in this work using serial as well as parallel computation. All wall clock times were normalized to the slowest reduced Liouville state computation and gains in speed are determined from the slope of linear fits. For reference to the computer pet names and specifications see table 2.6.

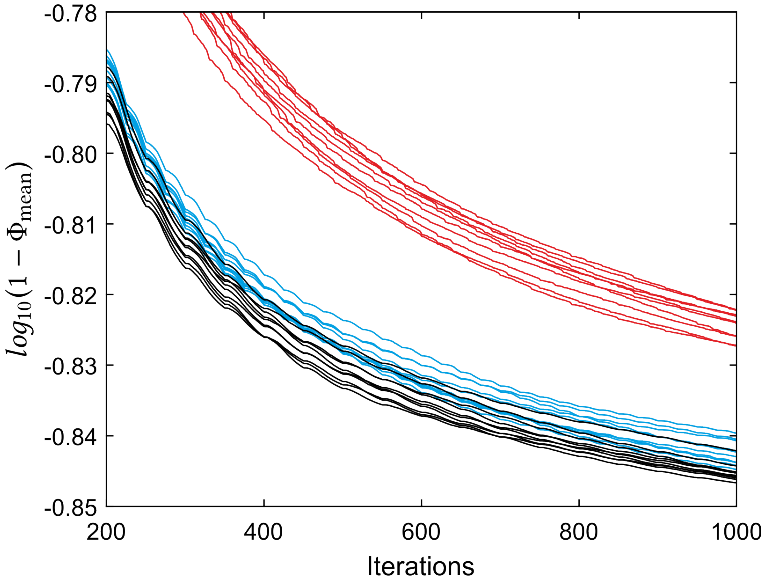

Figure A.2.: Convergence benchmark (spaghetti plots) for different frequencies of CG reinitialization during optimizations of pulse sequences as described in section 2.2.2. The CG trajectory was refreshed after 50 (black), 25 (blue) and 10 (red) iterations. The plot was expanded to the same region as figure 2.30.

A.2. MATLAB source code

A.2.1. Heteronuclear decoupling

Listing A.1: MATLAB® function for parallel simulation of time/frequency-domain data (*fid/spectrum*) and determination of Φ_{mean} (*cost*) of decoupling sequences. Input variable definitions according to sections 1.2.5 and 2.2.4 are: *n_FID* = N, *inc_puls* = M, *ws* = ν_S, *wj* = J, *b1* = $B_{1,\text{rel}}$, *t_dig* = Δt, *xp* = $\boldsymbol{u_x}$ and *yp* = $\boldsymbol{u_y}$. All other variables are only relevant for FID processing.

```
function [fid,spectrum,cost] = parallel_FID(n_FID,inc_puls,ws,wj,b1,t_dig,xp,
    yp,qsin,em,basecor,norm_FT,zf)

%internal prealloc
fid = ones(n_FID+1,1);

%FID
rhossr = [0 0 0 1]';
targetssr = rhossr;

phi = 0;

for i_FID = 1:n_FID
    %dwell time
```

```
    for i_puls = 1:inc_puls
        u_ssr = tf15_reduced_propagator(ws,wj,b1,t_dig(i_puls),...
        xp((i_FID-1)*inc_puls+i_puls),yp((i_FID-1)*inc_puls+i_puls));
        rhossr = u_ssr*rhossr;
    end

    %Kostenfunktion
    checkpointssr = real(targetssr'*rhossr);
    phi = phi + checkpointssr;

    %Spektrum
    fid(i_FID+1) = checkpointssr;
end

%Apodisierung
FT_dummy=fid'.*qsin;
FT_dummy=FT_dummy.*em;

%FT
spectrum=fftshift(fft(FT_dummy,zf));

%Baseline correction
spectrum=spectrum-basecor;

%Norm
spectrum=spectrum/norm_FT;
cost = phi/n_FID;
end
```

Listing A.2: MATLAB®function for parallel simulation of time/frequency-domain data (*fid/spectrum*) and determination of Φ_{COOP} (*cost*) for COOP decoupling sequences. Input variable definitions according to sections 1.2.5 and 2.2.4 are: *ncoop* = N_{COOP}, *n_FID* = N, *inc_puls* = M, *ws* = ν_{S}, *wj* = J, *b1* = $B_{1,\mathrm{rel}}$, *t_dig* = $\boldsymbol{\Delta t}$, *xp* = $\boldsymbol{u_x}$ and *yp* = $\boldsymbol{u_y}$. All other variables are only relevant for FID processing.

```
function [fid,spectrum,cost] = parallel_COOPFID(ncoop,n_FID,inc_puls,...
    ws,wj,b1,t_dig,xp,yp,qsin,em,basecor,norm_FT,zf)

%internal prealloc
fid = ones(n_FID+1,1);

%FID
rhossr_N = zeros(4,n_FID);

for icoop = 1:ncoop
    rhossr = [0 0 0 1]';
```

```
    targetssr = rhossr;

    for i_FID = 1:n_FID
        %dwell time
        for i_puls = 1:inc_puls
            u_ssr = tf15_reduced_propagator(ws,wj,b1,t_dig(i_puls),...
                xp(icoop,(i_FID-1)*inc_puls+i_puls),...
                yp(icoop,(i_FID-1)*inc_puls+i_puls));
            rhossr = u_ssr*rhossr;
        end

        %Propagation
        rhossr_N(:,i_FID) = rhossr_N(:,i_FID)+(1/ncoop)*rhossr;
    end %single FID
end %COOP

%COOP FID
phi_mean = 0;
for i_FID = 1:n_FID
    checkpointssr = targetssr'*rhossr_N(:,i_FID);
    phi_mean = phi_mean + checkpointssr/n_FID;
        fid(i_FID+1) = checkpointssr;
end

%homogenous cost
phi = 0;
for i_FID = 1:n_FID
    checkpointssr = targetssr'*rhossr_N(:,i_FID);
    checkpointssr = 1-(1-checkpointssr)^2-(phi_mean-checkpointssr)^2;
    phi = phi + checkpointssr;
end

%Apodisierung
FT_dummy=fid'.*qsin;
FT_dummy=FT_dummy.*em;

%FT
spectrum=fftshift(fft(FT_dummy,zf));

%Baseline correction
spectrum=spectrum-basecor;

%Norm
spectrum=spectrum/norm_FT;
cost = phi/n_FID;
```

```
end
```

Listing A.3: MATLAB®function for the explicit computation of propagators in a reduced Liouville space. Input variable definitions according to sections 1.2.5 and 2.2.4 are: *ws* = ν_S, *J* identical, *b1* = $B_{1,\text{rel}}$, *timestep* = Δt, *ux* = $u_x(t_j)$ and *uy* = $u_y(t_j)$.

```
function  u  = tf15_reduced_propagator(ws,J,b1,timestep,ux,uy)

u=zeros(4);

%nu plus/minus
nup = sqrt((b1*ux)^2 + (b1*uy)^2 + (ws+(J/2))^2);
num = sqrt((b1*ux)^2 + (b1*uy)^2 + (ws-(J/2))^2);

%Matrix element building blocks a-d (plus/minus);
ap = -((b1*ux)/nup) * sin(pi*nup*timestep);
am = -((b1*ux)/num) * sin(pi*num*timestep);

bp = -((b1*uy)/nup) * sin(pi*nup*timestep);
bm = -((b1*uy)/num) * sin(pi*num*timestep);

cp = -((ws+(J/2))/nup) * sin(pi*nup*timestep);
cm = -((ws-(J/2))/num) * sin(pi*num*timestep);

dp = cos(pi*nup*timestep);
dm = cos(pi*num*timestep);

%Matrix Entries
u(1,1) = ap*am - bp*bm - cp*cm + dp*dm;
u(1,2) = ap*bm + bp*am + cp*dm + dp*cm;
u(1,3) = ap*cm - bp*dm + cp*am - dp*bm;
u(1,4) =-ap*dm - bp*cm + cp*bm + dp*am;

u(2,1) = ap*bm + bp*am - cp*dm - dp*cm;
u(2,2) =-ap*am + bp*bm - cp*cm + dp*dm;
u(2,3) = ap*dm + bp*cm + cp*bm + dp*am;
u(2,4) = ap*cm - bp*dm - cp*am + dp*bm;

u(3,1) = ap*cm + bp*dm + cp*am + dp*bm;
u(3,2) =-ap*dm + bp*cm + cp*bm - dp*am;
u(3,3) =-ap*am - bp*bm + cp*cm + dp*dm;
u(3,4) =-ap*bm + bp*am - cp*dm + dp*cm;

u(4,1) = ap*dm - bp*cm + cp*bm - dp*am;
u(4,2) = ap*cm + bp*dm - cp*am - dp*bm;
u(4,3) =-ap*bm + bp*am + cp*dm - dp*cm;
```

```
u(4,4) = ap*am + bp*bm + cp*cm + dp*dm;

end
```

A.2.2. BIRD filters

Listing A.4: MATLAB® script for the evaluation of Φ_{PP} and Φ_{UR} of HPD BIRD elements discussed in sections 3.3.1 and 3.3.2 as well as simulations of BIRD spin echo intensity profiles.

```
clear;
close all;

%spin system initialization
nspins=2;
a00_basis;

method = 'BIRD';
%BIRD, JCBIRD, 4p3d, 5p4d

n_j = 41;
j_min = 25;
j_max = 350;
j_fix = 125.29; % J_exp
j_del = 185; % J_match

rhoinit = iz(:,:,1);
rhotarget = -iz(:,:,1);
op = 2*iy(:,:,1)*iz(:,:,2);

phi = 0;
colorstyle = 'b';

%Spectra
k = 1024;
dw = 0.000333;
n_FID = 8*k;
SI=16*k;
lb = 1.5;

%Indices
j_index = linspace (j_min, j_max, n_j);
te = ones(1,n_j);
teFID=zeros(n_FID+1,1);
em=zeros(n_FID+1,1);
qsin=zeros(n_FID+1,1);
```

```
spectra = zeros(n_j,SI);
ftindex = linspace(-1/(2*dw),1/(2*dw),SI);

for a = 1:n_FID+1
   qsin(a)=sin(0.5*pi*((a-1)/(n_FID+1)+1))^2;
   em(a)=exp(-pi*lb*(a-1)*dw);
end

h_evo = 2*pi*j_fix*iz(:,:,1)*iz(:,:,2);
u = expm(-1i*h_evo*dw);
u_target = expm(-1i*pi*op);

for i_j = 1:n_j
   rho=rhoinit;
   ueff = eye(2^nspins);

   switch method
       case '4p3d'
%--- 4p3d 2IySz COB 15.5 ms ---
     scaling = j_index(i_j)/j_fix;
     delay1 = 5.1666*1e-3;
     delay2 = 5.1669*1e-3;
     delay3 = 5.1666*1e-3;
     u_pi = expm(-1i*pi*(ix(:,:,1)+ix(:,:,2)));
     flip1 = 2*pi*(148.1455/360);
     flip2 = 2*pi*(-116.2881/360);
     flip3 = 2*pi*(116.2863/360);
     flip4 = 2*pi*(-148.1424/360);

     u_puls = expm(-1i*flip1*ix(:,:,1));
     u_delay = expm(-1i*h_evo*(scaling*delay1/2));
     ueff = u_delay*u_pi*u_delay*u_puls*ueff;

     u_puls = expm(-1i*flip2*ix(:,:,1));
     u_delay = expm(-1i*h_evo*(scaling*delay2/4));
     ueff = u_delay*(-u_pi)*u_delay*u_delay*u_pi*u_delay*u_puls*ueff;

     u_puls = expm(-1i*flip3*ix(:,:,1));
     u_delay = expm(-1i*h_evo*(scaling*delay3/2));
     ueff = u_delay*u_pi*u_delay*u_puls*ueff;

     u_puls = expm(-1i*flip4*ix(:,:,1));
     ueff = u_puls*ueff;

     %CLIP
```

```
     u_clip = expm(-1i*0.5*pi*ix(:,:,2));
     ueff = u_clip*ueff;

       case ’5p4d’
%--- 5p4d 2IySz COB 15.5 ms ---
     scaling = j_index(i_j)/j_fix;
     delay1 = 5.7616*1e-3;
     delay2 = 4.0728*1e-3;
     delay3 = 1.7267*1e-3;
     delay4 = 3.9389*1e-3;
     u_pi = expm(-1i*pi*(ix(:,:,1)+ix(:,:,2)));
     flip1 = 2*pi*(37.6467/360);
     flip2 = 2*pi*(119.8013/360);
     flip3 = 2*pi*(-71.4578/360);
     flip4 = 2*pi*(-63.912/360);
     flip5 = 2*pi*(-22.0815/360);

     u_puls = expm(-1i*flip1*ix(:,:,1));
     u_delay = expm(-1i*h_evo*(scaling*delay1/2));
     ueff = u_delay*u_pi*u_delay*u_puls*ueff;

     u_puls = expm(-1i*flip2*ix(:,:,1));
     u_delay = expm(-1i*h_evo*(scaling*delay2/2));
     ueff = u_delay*u_pi*u_delay*u_puls*ueff;

     u_puls = expm(-1i*flip3*ix(:,:,1));
     u_delay = expm(-1i*h_evo*(scaling*delay3/2));
     ueff = u_delay*u_pi*u_delay*u_puls*ueff;

     u_puls = expm(-1i*flip4*ix(:,:,1));
     u_delay = expm(-1i*h_evo*(scaling*delay4/2));
     ueff = u_delay*u_pi*u_delay*u_puls*ueff;

     u_puls = expm(-1i*flip5*ix(:,:,1));
     ueff = u_puls*ueff;

     %CLIP
     u_clip = expm(-1i*0.5*pi*ix(:,:,2));
     ueff = u_clip*ueff;

       case ’BIRD’
%--- BIRD ---
     vardelay = j_index(i_j)/(2*j_fix*j_del);
     delay = expm(-1i*h_evo*vardelay);
     inv = expm(-1i*pi*(ix(:,:,1)+ix(:,:,2)));
```

```
     puls = expm(-1i*0.5*pi*ix(:,:,1));
     puls2 = expm(-1i*0.5*pi*ix(:,:,1));
     bubi = expm(-1i*(-0.5*pi*ix(:,:,1)+pi*ix(:,:,2)));
     ueff = puls*delay*inv*delay*puls*ueff;

       case 'JCBIRD'
%--- JC BIRD ---
     vardelay = j_index(i_j)/(2*j_fix*j_del);
     u_delay = expm(-1i*h_evo*vardelay);
     u_short = expm(-1i*h_evo*vardelay/2);
     u_x = expm(-1i*0.5*pi*ix(:,:,1));
     u_xm = expm(1i*0.5*pi*ix(:,:,1));
     u_y = expm(-1i*0.5*pi*iy(:,:,1));
     u_ym = expm(1i*0.5*pi*iy(:,:,1));
     u_pi = expm(-1i*pi*(ix(:,:,1)+ix(:,:,2)));
     ueff = u_ym*u_short*u_pi*u_short*u_x*u_delay*u_pi...
         *u_delay*u_xm*u_short*u_pi*u_short*u_y*ueff;

       otherwise
           error('no valid BIRD')
   end

    % ----------- cost -------------------
    if phi == 0
        rho = ueff*rho*ueff';
        norm = real(trace(rhotarget'*rhotarget));
        te(i_j)=real(trace(rhotarget'*rho))/norm;
    elseif phi == 3
        normu = real(trace(u_target'*u_target));
        te(i_j)=real(trace(u_target'*ueff))/normu;
    else
        break
    end

    %---------- peaks ------------------
     rho = ueff*ix(:,:,1)*ueff';
     for j = 1:n_FID+1
         teFID(j) = trace(-ix(:,:,1)'*rho);
         rho = u*rho*u';
     end
     teFID=teFID.*(em.*qsin);
     ft = fftshift(fft(teFID,SI));
     spectra(i_j,:) = ft;
end

```

```
figure;
plot(j_index,te,colorstyle,'Linewidth',0.75);
set(gca,'fontsize',12,'XColor','k','YColor','k','Linewidth',0.75);
set(gca,'YTicklabel',num2str(get(gca,'YTick')','%.1f'));
set(gcf,'color',[1 1 1]);
xlabel('J / Hz');
if phi == 0
    ylabel('\Phi_{PP}');
elseif phi == 3
    ylabel('\Phi_{UR}');
else
    return
end

figure;
entries = find(ftindex > -150 & ftindex < 150);
newftindex = linspace(min(j_index),max(j_index),...
    numel(j_index)*numel(entries));
peaks = reshape(spectra(:,entries)',numel(j_index)*numel(entries),1);
norm = max(real(peaks));
plot(newftindex,real(peaks)/norm,'k','Linewidth',0.75);
axis ([min(newftindex) max(newftindex) -1 1]);
set(gca,'fontsize',12,'XColor','k','YColor','k','Linewidth',0.75);
set(gca,'YTicklabel',num2str(get(gca,'YTick')','%.1f'));
set(gcf,'color',[1 1 1]);
xlabel('J_{eff} / Hz');
ylabel('Peak intensity');
```

Listing A.5: MATLAB® function for the parallel evaluation of Φ_{PP} (*PP*) and Φ_{BIRDBOP} (*UR*) as well as the determination of U_{eff} (*ueff*) according to equation 3.22 of BIRDBOP shapes discussed in section 3.3.3. Input variable definitions are: $wj = J$, $ws = \nu_{\mathrm{S}}$, cell arrays *ix*, *iy* and *iz* correspond to the density operators I_x and S_x, I_y and S_y as well as I_z and S_z, respectively. *zeile1* and *zeile2* correspond to the number of pulse increments of shape one and two, respectively. Other input variables according to section 3.3.3 are: $xp1 = \boldsymbol{u}^{(S)}_{x,1}$, $yp1 = \boldsymbol{u}^{(S)}_{y,1}$, $t\_dig1 = \Delta t_1$, $xp2 = \boldsymbol{u}^{(S)}_{x,2}$, $yp2 = \boldsymbol{u}^{(S)}_{y,2}$ and $t\_dig2 = \Delta t_2$. *uf*, *ux* and *upi* correspond to U_{F}, $U_{\pi/2}$ and U_{π}, respectively.

```
function [UR,PP,ueff] = tf_t14b_sim_bird_shape_jcomp_par(wj,ws,ix,iy,iz,...
    zeile1,zeile2,xp1,yp1,t_dig1,xp2,yp2,t_dig2,uf,ux,upi)

     h_j = 2*pi*wj*iz(:,:,1)*iz(:,:,2);
     h_cs = 2*pi*ws*iz(:,:,1);
     h_evo = h_j+h_cs;

     %Useff puls 1
```

```
    ushape1s = eye(4);
    for j = 1:zeile1
        h_rf = 2*pi*(xp1(j)*ix(:,:,1)+yp1(j)*iy(:,:,1));
        h = h_cs + h_rf;
        u = expm(-1i*h*t_dig1(j));
        ushape1s = u*ushape1s;
    end

    %Ueff puls 1
    ushape1 = eye(4);
    for j = 1:zeile1
        h_rf = 2*pi*(xp1(j)*ix(:,:,1)+yp1(j)*iy(:,:,1));
        h = h_evo + h_rf;
        u = expm(-1i*h*t_dig1(j));
        ushape1 = u*ushape1;
    end

    %Useff puls 2
    ushape2s = eye(4);
    for j = 1:zeile2
        h_rf = 2*pi*(xp2(j)*ix(:,:,1)+yp2(j)*iy(:,:,1));
        h = h_cs + h_rf;
        u = expm(-1i*h*t_dig2(j));
        ushape2s = u*ushape2s;
    end

    %Ueff puls 2
    ushape2 = eye(4);
    for j = 1:zeile2
        h_rf = 2*pi*(xp2(j)*ix(:,:,1)+yp2(j)*iy(:,:,1));
        h = h_evo + h_rf;
        u = expm(-1i*h*t_dig2(j));
        ushape2 = u*ushape2;
    end

    udelay = expm(-1i*h_evo*0.003);
    udelays = expm(-1i*h_cs*0.003);

    useff = udelays*ushape2s*udelays*ushape1s;
    ueff = ux*udelay*ushape2*upi*udelay*ushape1*ux;

    UR = real(trace((uf*useff)'*ueff)/4);
    rho = ueff*iz(:,:,2)*ueff';
    PP = real(trace(-iz(:,:,2)'*rho));
end
```

A.3. Fortran source code

A.3.1. Heteronuclear decoupling - Hilbert space

Listing A.6: Fortran source code for the quality factor evaluation of individual decoupling sequences according to Φ_{mean} in Hilbert space

```fortran
!       2 spins xy      Heterodecoupling                Tony 2012/08
!      phi0 (TRACKING)
!=======================================================================
      ttcost2 = 0d0
      call mcopy(initialrho,rho)
      do k=1,npulses
         call geteigenhamtrack(k)
         call czmul(-1d0,ii,pham(k),work1)
         call expm(duration(k),work1,work1)
         call URUd(work1,rho,rho)
         if (mod(k,Ppdwell) .eq. 0) then
          call mscalp(targetrho,rho,ttcost3)
          ttcost2=ttcost2+ttcost3
         endif
      enddo
      ttcost1 = ttcost1+ttcost2/n_FID
```

Listing A.7: Fortran source code for the gradient evaluation of individual decoupling sequences according to Φ_{mean} in Hilbert space

```fortran
!2 spins xy    Gradient für TRACKING                   Tony 2012/08
!==========================================================================
!-----get single U, same U as with expm(-iH), even with full H (+Sctrl)
           do k=1,npulses            !einzeln alle, voller H
             call geteigenhamtrack(k)
             call VDe(pham(k),k)                 !V=work2, D=work9, e=work8
             call mcopy(work2,optV(k))
             call mcopy(work9,optD(k))
             call mcopy(work8,opte(k))
             call dagger(work2,work3)                  ! Vd
             call mmul(work8,work3,work4)              ! eVd
             call mmul(work2,work4,optG(k))            ! G=U=VeVd
           enddo

!----------initialrho propagieren
         call mcopy(initialrho,prho(1))
         do k=1,npulses         ! Aufmultiplizieren, von rho
           call dagger(optG(k),work2)                 ! Ud
           call mmul(prho(k),work2,prho(k+1))         ! RUd
```

```
           call mmul(optG(k),prho(k+1),prho(k+1))     ! URUd
         enddo

!----------targetrho rückwärts propagieren
         call zeros(plambda(npulses+1))     ! DANGER: comes from npulses+1
         do k=npulses,1,-1
           if (mod(k,Ppdwell) .eq. 0) then
             call madd(targetrho,plambda(k+1),plambda(k+1)) !TRACK
           endif
           call dagger(optG(k),work2)                 ! Ud
           call mmul(plambda(k+1),optG(k),work3)      ! LU
           call mmul(work2,work3,plambda(k))          ! UdLU
         enddo

!---------- exakten grad, basis transformation
         do ictrl=3,nctrl
             call cmul(pii,ctrlham(ictrl),workg1(ictrl)) ! H = 2*pi*H
         enddo
         do k=1,npulses
           call dagger(optG(k),work3)                ! Ud
           call dagger(optV(k),work4)                ! Vd
           call mmul(plambda(k+1),optV(k),work6)     ! L*V
           call mmul(work4,work6,work6)              ! Vd*L*V
           call mmul(work3,optV(k),work7)            ! Ud*V
           call mmul(work4,work7,work8)              ! Vd*Ud*V = work8
           call mmul(work3,optV(k),work7)            ! Ud*V
           call mmul(prho(k),work7,work7)            ! R*Ud*V
           call mmul(work4,work7,work9)              ! Vd*R*Ud*V
           call mmul(prho(k),optV(k),work7)          ! R*V
           call mmul(optG(k),work7,work7)            ! U*R*V
           call mmul(work4,work7,work10)             ! Vd*U*R*Vc

!------------calculate dU/du
           do ictrl=3,nctrl
            call mmul(workg1(ictrl),optV(k),work1)   ! Hctrl*V
            call mmul(work4,work1,work1)             ! Vd*Hctrl*V
            call mpstern(work1,optD(k),work1)        ! U' = Vd*Hctrl*V * D
            call mmul(work1,work8,work7)             ! U' * work8
            call mmul(work8,work7,work7)           ! Ud'=Vd*Ud*V*U'*Vd*Ud*V
            call cmul(-1d0,work7,work7)              ! -Ud'
            call mmul(work10,work7,work5)            ! Vd*U*R*V*-Ud'
            call mmul(work1,work9,work7)             ! U' * V'RU'V
            call madd(work7,work5,work7)             ! (URU)'
            call mmul(work6,work7,work7)             ! Vd*L*V * (URU)'
!-------------imaginäres skalarprodukt
```

```
           call traceim(work7,ttcost)              ! Im(tr{L*(URU)'})
           ttcost=-ttcost*duration(k)              ! -i*<L/R'>*t
           grad2(ictrl,k)=grad2(ictrl,k)-ttcost/n_FID  ! Summe
          enddo
         enddo
```

Listing A.8: Fortran source code for the quality factor evaluation of COOP decoupling sequences according to the full penalty approach in Hilbert space

```
!2 spins xy    COOP-Heterodecoupling           Tony 2012/11/14
!phi0 (TRACKING)                                full penalty
!=================================================================
     !---- init ----
     ttcost2 = 0d0
     do k=1,n_FID
        call zeros(multitarget(k))
     enddo

     !---- propagate ----
     do j=0,ncoop-1
        call mcopy(initialrho,rho)
        do k=j*(npulses/ncoop)+1,(j+1)*npulses/ncoop
         call geteigenhamtrack(k)
         call czmul(-1d0,ii,pham(k),work1)
         call expm(duration(k),work1,work1)
         call URUd(work1,rho,rho)
         if (mod(k,Ppdwell) .eq. 0) then
          call cmul(1d0/ncoop,rho,work1)
          call madd(multitarget(k/Ppdwell-j*n_FID),work1,
    /    multitarget(k/Ppdwell-j*n_FID))
        endif
       enddo !einzelpuls
     enddo !coop

     !---- evaluate ----
     do k=1,n_FID
        call mscalp(targetrho,multitarget(k),ttcost3)  !Target
        call mscalp(coop(10),multitarget(k),ttcost4) !Penalty 2IySz
        ttcost3 = 1d0-(1d0-ttcost3/normrho)**2d0-(ttcost4/normrho)**2d0
        call mscalp(coop(8),multitarget(k),ttcost4) !Penalty 2IySy
        ttcost3=ttcost3-(ttcost4/normrho)**2d0
        call mscalp(coop(11),multitarget(k),ttcost4) !Penalty 2IySx
        ttcost3=ttcost3-(ttcost4/normrho)**2d0
        ttcost2=ttcost2+ttcost3
     enddo
     ttcost1 = ttcost1+ttcost2/n_FID
```

Listing A.9: Fortran source code for the gradient evaluation of COOP decoupling sequences according to the full penalty approach in Hilbert space

```fortran
!2 spins xy     COOP-Heterodecoupling (TRACKING)       Tony 2012/11/14
!phi0 (TRACKING)                                        full penalty
!=====================================================================
!----get single U, same U as with expm(-iH), even with full H (+Sctrl)
         call geteye(work1)
         call mdiv(work1,2d0,work1)
         do k=1,npulses                             !einzeln alle, voller H
           call geteigenhamtrack(k)
           call VDe(pham(k),k)  !V=work2, D=work9, e=work8
           call mcopy(work2,optV(k))
           call mcopy(work9,optD(k))
           call mcopy(work8,opte(k))
           call dagger(work2,work3)                 ! Vd
           call mmul(work8,work3,work4)             ! eVd
           call mmul(work2,work4,optG(k))             ! G=U=VeVd
         enddo

!----------initialrho propagieren
     do k=1,n_FID
         call zeros(multitarget(k))
     enddo

     do j=1,ncoop
      call mcopy(initialrho,prho((j-1)*(npulses/ncoop)+1))
      do k=(j-1)*(npulses/ncoop)+1,j*(npulses/ncoop)
                        ! Aufmultiplizieren von rho
         call dagger(optG(k),work2)                ! Ud
         call mmul(prho(k),work2,prho(k+1))        ! RUd
         call mmul(optG(k),prho(k+1),prho(k+1))    ! URUd
         if (mod(k,Ppdwell) .eq. 0) then
           call cmul(1d0/ncoop,prho(k+1),work1)
           call madd(multitarget(k/Ppdwell-(j-1)*n_FID),work1,
    /  multitarget(k/Ppdwell-(j-1)*n_FID))
         endif
      enddo !einzelpuls
     enddo !coop

!---- time-dependant COOP mixed target operators weighted by cost
     do k=1,n_FID
         call mscalp(targetrho,multitarget(k),ttcost2) !Target
         call cmul((2d0/ncoop)*(1d0-ttcost2/normrho),targetrho,work1)
         call mscalp(coop(10),multitarget(k),ttcost3) !Penalty 2IySz
```

```fortran
         call cmul(-(2d0/ncoop)*ttcost3/normrho,coop(10),work2)
         call madd(work1,work2,work1)
         call mscalp(coop(8),multitarget(k),ttcost3) !Penalty 2IySy
         call cmul(-(2d0/ncoop)*ttcost3/normrho,coop(8),work2)
         call madd(work1,work2,work1)
         call mscalp(coop(11),multitarget(k),ttcost3) !Penalty 2IySx
         call cmul(-(2d0/ncoop)*ttcost3/normrho,coop(11),work2)
         call madd(work1,work2,multitarget(k))
     enddo

!----------targetrho rückwärts propagieren
      do j=ncoop,1,-1
         call zeros(plambda(j*(npulses/ncoop)+1))
        ! DANGER: comes from npulses+1
         do k=j*npulses/ncoop,(j-1)*(npulses/ncoop)+1,-1
        ! rückwärts aufmultplizieren von U
          if (mod(k,Ppdwell) .eq. 0) then
           call madd(multitarget(k/Ppdwell-(j-1)*n_FID),plambda(k+1),
    /     plambda(k+1)) !TRACK
          endif
          call dagger(optG(k),work2)                ! Ud
          call mmul(plambda(k+1),optG(k),work3)      ! LU
          call mmul(work2,work3,plambda(k))         ! UdLU
         enddo
      enddo

!---------- exakten grad, basis transformation
         do ictrl=3,nctrl
             call cmul(pii,ctrlham(ictrl),workg1(ictrl)) ! H = 2*pi*H
         enddo
         do k=1,npulses
           call dagger(optG(k),work3)                ! Ud
           call dagger(optV(k),work4)                ! Vd
           call mmul(plambda(k+1),optV(k),work6)     ! L*V
           call mmul(work4,work6,work6)              ! Vd*L*V
           call mmul(work3,optV(k),work7)            ! Ud*V
           call mmul(work4,work7,work8)              ! Vd*Ud*V = work8
           call mmul(work3,optV(k),work7)            ! Ud*V
           call mmul(prho(k),work7,work7)            ! R*Ud*V
           call mmul(work4,work7,work9)              ! Vd*R*Ud*V
           call mmul(prho(k),optV(k),work7)          ! R*V
           call mmul(optG(k),work7,work7)            ! U*R*V
           call mmul(work4,work7,work10)             ! Vd*U*R*Vc

!------------calculate dU/du
```

```
           do ictrl=3,nctrl
            call mmul(workg1(ictrl),optV(k),work1)   ! Hctrl*V
            call mmul(work4,work1,work1)             ! Vd*Hctrl*V
            call mpstern(work1,optD(k),work1)        ! U' = Vd*Hctrl*V * D
            call mmul(work1,work8,work7)             ! U' * work8
            call mmul(work8,work7,work7)           ! Ud'=Vd*Ud*V*U'*Vd*Ud*V
            call cmul(-1d0,work7,work7)              ! -Ud'
            call mmul(work10,work7,work5)            ! Vd*U*R*V*-Ud'
            call mmul(work1,work9,work7)             ! U' * V'RU'V
            call madd(work7,work5,work7)             ! (URU)'
            call mmul(work6,work7,work7)             ! Vd*L*V * (URU)'
!-------------imaginäres skalarprodukt
            call traceim(work7,ttcost)               ! Im(tr{L*(URU)'})
            ttcost=-ttcost*duration(k)               ! -i*<L/R'>*t
            grad2(ictrl,k)=grad2(ictrl,k)-ttcost/n_FID  ! Summe
           enddo
          enddo
```

Listing A.10: Fortran source code for the quality factor evaluation of COOP decoupling sequences according to the homogenizing approach in Hilbert space

```
!2 spins xy   COOP-Heterodecoupling           Tony 2013/02/06
!phi0 (TRACKING)              <Ix> maximization & homogenisation
!=======================================================================
     !---- init ----
     ttcost2 = 0d0
     do k=1,n_FID
      call zeros(multitarget(k))
     enddo

     !---- propagate ----
     do j=0,ncoop-1
      call mcopy(initialrho,rho)
      do k=j*(npulses/ncoop)+1,(j+1)*npulses/ncoop
       call geteigenhamtrack(k)
       call czmul(-1d0,ii,pham(k),work1)
       call expm(duration(k),work1,work1)
       call URUd(work1,rho,rho)
       if (mod(k,Ppdwell) .eq. 0) then
        call cmul(1d0/ncoop,rho,work1)
        call madd(multitarget(k/Ppdwell-j*n_FID),work1,
   /    multitarget(k/Ppdwell-j*n_FID))
       endif
      enddo !einzelpuls
     enddo !coop

```

```
       !---- evaluate ----
       do k=1,n_FID
        call mscalp(targetrho,multitarget(k),targetmod(k))      !Target
        ttcost2=ttcost2+targetmod(k)/normrho
       enddo

       ttcost4 = ttcost2/n_FID  !mean value
       ttcost2 = 0d0            !reinitialization

       do k=1,n_FID       !maximize & homogenise
        ttcost3 = 1-(1-targetmod(k))**2-(ttcost4-targetmod(k))**2
        ttcost2 = ttcost2+ttcost3
       enddo

       ttcost1 = ttcost1+ttcost2/n_FID
```

Listing A.11: Fortran source code for the gradient evaluation of COOP decoupling sequences according to the homogenizing approach in Hilbert space

```
 !2 spins xy    COOP-Heterodecoupling           Tony 2013/02/06
 !phi0 (TRACKING)               <Ix> maximization & homogenisation
 !=======================================================================
!----get single U, same U as with expm(-iH), even with full H (+Sctrl)
         call geteye(work1)
         call mdiv(work1,2d0,work1)
         do k=1,npulses                              !einzeln alle, voller H
           call geteigenhamtrack(k)
           call VDe(pham(k),k)  !V=work2, D=work9, e=work8
           call mcopy(work2,optV(k))
           call mcopy(work9,optD(k))
           call mcopy(work8,opte(k))
           call dagger(work2,work3)                   ! Vd
           call mmul(work8,work3,work4)               ! eVd
           call mmul(work2,work4,optG(k))               ! G=U=VeVd
         enddo

 !----------initialrho propagieren
 !----------skalarprodukte und mittelwerte berechnen
      do k=1,n_FID
        call zeros(multitarget(k))
      enddo
      ttcost2=0d0

      do j=1,ncoop
       call mcopy(initialrho,prho((j-1)*(npulses/ncoop)+1))
       do k=(j-1)*(npulses/ncoop)+1,j*(npulses/ncoop)
```

```
                       ! Aufmultiplizieren, von rho
        call dagger(optG(k),work2)                 ! Ud
        call mmul(prho(k),work2,prho(k+1))         ! RUd
        call mmul(optG(k),prho(k+1),prho(k+1))     ! URUd
        if (mod(k,Ppdwell) .eq. 0) then
         call cmul(1d0/ncoop,prho(k+1),work1)
         call madd(multitarget(k/Ppdwell-(j-1)*n_FID),work1,
    /    multitarget(k/Ppdwell-(j-1)*n_FID))
        endif
      enddo !einzelpuls
     enddo !coop

!------- evaluate <Ix>
      do k=1,n_FID
       call mscalp(targetrho,multitarget(k),targetmod(k))      !Target
       ttcost2=ttcost2+targetmod(k)/normrho
      enddo

      ttcost4 = ttcost2/n_FID !mean value

!---------Gradientenloops für grad_Ix
       do k=1,n_FID
         call cmul((2d0/ncoop)*(1+ttcost4-2*targetmod(k)),targetrho,
    /    multitarget(k))
       enddo

!----------targetrho rückwärts propagieren
      do j=ncoop,1,-1
        call zeros(plambda(j*(npulses/ncoop)+1))
       ! DANGER: comes from npulses+1
        do k=j*npulses/ncoop,(j-1)*(npulses/ncoop)+1,-1
       ! rückwärts aufmultplizieren von U
         if (mod(k,Ppdwell) .eq. 0) then
          call madd(multitarget(k/Ppdwell-(j-1)*n_FID),plambda(k+1),
    /     plambda(k+1)) !TRACK
         endif
         call dagger(optG(k),work2)                ! Ud
         call mmul(plambda(k+1),optG(k),work3)      ! LU
         call mmul(work2,work3,plambda(k))         ! UdLU
        enddo
      enddo

!---------- exakten grad, basis transformation
        do ictrl=3,nctrl
            call cmul(pii,ctrlham(ictrl),workg1(ictrl)) ! H = 2*pi*H
```

```
         enddo
         do k=1,npulses
           call dagger(optG(k),work3)                ! Ud
           call dagger(optV(k),work4)                ! Vd
           call mmul(plambda(k+1),optV(k),work6)     ! L*V
           call mmul(work4,work6,work6)              ! Vd*L*V
           call mmul(work3,optV(k),work7)            ! Ud*V
           call mmul(work4,work7,work8)              ! Vd*Ud*V = work8
           call mmul(work3,optV(k),work7)            ! Ud*V
           call mmul(prho(k),work7,work7)            ! R*Ud*V
           call mmul(work4,work7,work9)              ! Vd*R*Ud*V
           call mmul(prho(k),optV(k),work7)          ! R*V
           call mmul(optG(k),work7,work7)            ! U*R*V
           call mmul(work4,work7,work10)             ! Vd*U*R*Vc

!------------calculate dU/du
           do ictrl=3,nctrl
            call mmul(workg1(ictrl),optV(k),work1)   ! Hctrl*V
            call mmul(work4,work1,work1)             ! Vd*Hctrl*V
            call mpstern(work1,optD(k),work1)        ! U’ = Vd*Hctrl*V * D
            call mmul(work1,work8,work7)             ! U’ * work8
            call mmul(work8,work7,work7)           ! Ud’=Vd*Ud*V*U’*Vd*Ud*V
            call cmul(-1d0,work7,work7)              ! -Ud’
            call mmul(work10,work7,work5)            ! Vd*U*R*V*-Ud’
            call mmul(work1,work9,work7)             ! U’ * V’RU’V
            call madd(work7,work5,work7)             ! (URU)’
            call mmul(work6,work7,work7)             ! Vd*L*V * (URU)’
!-------------imaginäres skalarprodukt
            call traceim(work7,ttcost)               ! Im(tr{L*(URU)’})
            ttcost=-ttcost*duration(k)               ! -i*<L/R’>*t
            grad2(ictrl,k)=grad2(ictrl,k)-ttcost/n_FID  ! Summe
           enddo
          enddo
```

A.3.2. Heteronuclear decoupling - reduced Liouville space

Listing A.12: Fortran subroutine for the explicit computation of propagators in a reduced Liouville space

```
c------------------------------------------------------------
        subroutine gethamSSR(mout,k)
c------------------------------------------------------------
        IMPLICIT NONE
        include ’octopussi.cmn’
!$omp THREADPRIVATE(/basics/)
        include ’constants.cmn’
```

```
c 2 spins xy SSR

c input         k       intg
c input         mout    pointer to matrix
c input         (implicit=common)       w(1), ctrl, hcp(1)
c output        Matrix mout (saving into array is optional)

        integer mout,i,j,k
        real*8 nup,num,ap,am,bp,bm,cp,cm,dp,dm

c-----> switched to SSR 2014/01/24

        !B1 = B1(iB1) / ux = ctrl(1,k) / uy = ctrl(2,k)
        !J = hcp(1) / w1 = w(1) / t = duration(k)

        nup = dsqrt((B1(iB1)*ctrl(1,k))**2+(B1(iB1)*ctrl(2,k))**2
     /       + (w(1)+(hcp(1)/2))**2 )
        num = dsqrt((B1(iB1)*ctrl(1,k))**2+(B1(iB1)*ctrl(2,k))**2
     /       + (w(1)-(hcp(1)/2))**2 )

         ap = -((B1(iB1)*ctrl(1,k))/nup)*SIN(pi*nup*duration(k))
         am = -((B1(iB1)*ctrl(1,k))/num)*SIN(pi*num*duration(k))

         bp = -((B1(iB1)*ctrl(2,k))/nup)*SIN(pi*nup*duration(k))
         bm = -((B1(iB1)*ctrl(2,k))/num)*SIN(pi*num*duration(k))

         cp = -((w(1)+(hcp(1)/2))/nup)*SIN(pi*nup*duration(k))
         cm = -((w(1)-(hcp(1)/2))/num)*SIN(pi*num*duration(k))

         dp = COS(pi*nup*duration(k))
         dm = COS(pi*num*duration(k))

        wmtrx(1,1,mout) = ap*am - bp*bm - cp*cm + dp*dm
        wmtrx(1,2,mout) = ap*bm + bp*am + cp*dm + dp*cm
        wmtrx(1,3,mout) = ap*cm - bp*dm + cp*am - dp*bm
        wmtrx(1,4,mout) =-ap*dm - bp*cm + cp*bm + dp*am

        wmtrx(2,1,mout) = ap*bm + bp*am - cp*dm - dp*cm
        wmtrx(2,2,mout) =-ap*am + bp*bm - cp*cm + dp*dm
        wmtrx(2,3,mout) = ap*dm + bp*cm + cp*bm + dp*am
        wmtrx(2,4,mout) = ap*cm - bp*dm - cp*am + dp*bm

        wmtrx(3,1,mout) = ap*cm + bp*dm + cp*am + dp*bm
        wmtrx(3,2,mout) =-ap*dm + bp*cm + cp*bm - dp*am
        wmtrx(3,3,mout) =-ap*am - bp*bm + cp*cm + dp*dm
```

```
        wmtrx(3,4,mout) =-ap*bm + bp*am - cp*dm + dp*cm

        wmtrx(4,1,mout) = ap*dm - bp*cm + cp*bm - dp*am
        wmtrx(4,2,mout) = ap*cm + bp*dm - cp*am - dp*bm
        wmtrx(4,3,mout) =-ap*bm + bp*am + cp*dm - dp*cm
        wmtrx(4,4,mout) = ap*am + bp*bm + cp*cm + dp*dm

         return
         end
```

Listing A.13: Fortran subroutine for the explicit computation of exact propagator derivatives in a reduced Liouville space

```
c-------------------------------------------------------------
        subroutine getgradSSR(dux,duy,k)
c-------------------------------------------------------------
        IMPLICIT NONE
        include 'octopussi.cmn'
!$omp THREADPRIVATE(/basics/)
        include 'constants.cmn'
c 2 spins xy SSR

c input         k       intg
c input         dux,duy pointers to matrices
c input         (implicit=common)       w(1), ctrl, hcp(1)
c output        matrices dU/dux & dU/duy

        integer dux,duy,i,j,k
        real*8 nup,num,ap,am,bp,bm,cp,cm,dp,dm
        real*8 dnup,dnum,dap,dam,dbp,dbm,dcp,dcm,ddp,ddm
        !dcp deleted from cmn block (integer nspins x nspins)
        real*8 element1,element2,element3,element4

c-----> switched to SSR 2014/01/24

        !B1 = B1(iB1) / ux = ctrl(1,k) / uy = ctrl(2,k)
        !J = hcp(1) / w1 = w(1) / t = duration(k)

c-----> basic matrix elements

        nup = dsqrt((B1(iB1)*ctrl(1,k))**2+(B1(iB1)*ctrl(2,k))**2
     /       + (w(1)+(hcp(1)/2))**2 )
        num = dsqrt((B1(iB1)*ctrl(1,k))**2+(B1(iB1)*ctrl(2,k))**2
     /       + (w(1)-(hcp(1)/2))**2 )

         ap = -((B1(iB1)*ctrl(1,k))/nup)*SIN(pi*nup*duration(k))
```

```
         am = -((B1(iB1)*ctrl(1,k))/num)*SIN(pi*num*duration(k))

         bp = -((B1(iB1)*ctrl(2,k))/nup)*SIN(pi*nup*duration(k))
         bm = -((B1(iB1)*ctrl(2,k))/num)*SIN(pi*num*duration(k))

         cp = -((w(1)+(hcp(1)/2))/nup)*SIN(pi*nup*duration(k))
         cm = -((w(1)-(hcp(1)/2))/num)*SIN(pi*num*duration(k))

         dp = COS(pi*nup*duration(k))
         dm = COS(pi*num*duration(k))

c-----> dU/dux

        dnup = (B1(iB1)**2)*ctrl(1,k)/nup
        dnum = (B1(iB1)**2)*ctrl(1,k)/num

        dap = ((B1(iB1)*SIN(pi*nup*duration(k))
     /  *(ctrl(1,k)*dnup-nup))/nup**2)
     /  -pi*duration(k)*B1(iB1)*ctrl(1,k)
     /  *COS(pi*duration(k)*nup)*dnup/nup

        dam = ((B1(iB1)*SIN(pi*num*duration(k))
     /  *(ctrl(1,k)*dnum-num))/num**2)
     /  -pi*duration(k)*B1(iB1)*ctrl(1,k)
     /  *COS(pi*duration(k)*num)*dnum/num

        dbp = ((B1(iB1)*ctrl(2,k)*SIN(pi*duration(k)*nup)*dnup)/nup**2)
     /  -pi*duration(k)*B1(iB1)*ctrl(2,k)
     /  *COS(pi*duration(k)*nup)*dnup/nup

        dbm = ((B1(iB1)*ctrl(2,k)*SIN(pi*duration(k)*num)*dnum)/num**2)
     /  -pi*duration(k)*B1(iB1)*ctrl(2,k)
     /  *COS(pi*duration(k)*num)*dnum/num

        dcp = (((hcp(1)+2*w(1))*SIN(pi*duration(k)*nup)*dnup)/(2*nup**2))
     /  -pi*duration(k)*(hcp(1)+2*w(1))
     /  *COS(pi*duration(k)*nup)*dnup/(2*nup)

        dcm = (((-hcp(1)+2*w(1))*SIN(pi*duration(k)*num)*dnum)/(2*num**2))
     /  - pi*duration(k)*(-hcp(1)+2*w(1))
     /  *COS(pi*duration(k)*num)*dnum/(2*num)

        ddp = -pi*duration(k)*SIN(pi*duration(k)*nup)*dnup
        ddm = -pi*duration(k)*SIN(pi*duration(k)*num)*dnum

```

```
c-----> Matrix entries

        !Row 1
        element1 = dap*am+ap*dam
        element2 = dbp*bm+bp*dbm
        element3 = dcp*cm+cp*dcm
        element4 = ddp*dm+dp*ddm
        wmtrx(1,1,dux) = element1-element2-element3+element4

        element1 = dap*bm+ap*dbm
        element2 = dbp*am+bp*dam
        element3 = dcp*dm+cp*ddm
        element4 = ddp*cm+dp*dcm
        wmtrx(1,2,dux) = element1+element2+element3+element4

        element1 = dap*cm+ap*dcm
        element2 = dbp*dm+bp*ddm
        element3 = dcp*am+cp*dam
        element4 = ddp*bm+dp*dbm
        wmtrx(1,3,dux) = element1-element2+element3-element4

        element1 = dap*dm+ap*ddm
        element2 = dbp*cm+bp*dcm
        element3 = dcp*bm+cp*dbm
        element4 = ddp*am+dp*dam
        wmtrx(1,4,dux) = -element1-element2+element3+element4

        !Row 2
        element1 = dap*bm+ap*dbm
        element2 = dbp*am+bp*dam
        element3 = dcp*dm+cp*ddm
        element4 = ddp*cm+dp*dcm
        wmtrx(2,1,dux) = element1+element2-element3-element4

        element1 = dap*am+ap*dam
        element2 = dbp*bm+bp*dbm
        element3 = dcp*cm+cp*dcm
        element4 = ddp*dm+dp*ddm
        wmtrx(2,2,dux) = -element1+element2-element3+element4

        element1 = dap*dm+ap*ddm
        element2 = dbp*cm+bp*dcm
        element3 = dcp*bm+cp*dbm
        element4 = ddp*am+dp*dam
        wmtrx(2,3,dux) = element1+element2+element3+element4
```

```

        element1 = dap*cm+ap*dcm
        element2 = dbp*dm+bp*ddm
        element3 = dcp*am+cp*dam
        element4 = ddp*bm+dp*dbm
        wmtrx(2,4,dux) = element1-element2-element3+element4

        !Row 3
        element1 = dap*cm+ap*dcm
        element2 = dbp*dm+bp*ddm
        element3 = dcp*am+cp*dam
        element4 = ddp*bm+dp*dbm
        wmtrx(3,1,dux) = element1+element2+element3+element4

        element1 = dap*dm+ap*ddm
        element2 = dbp*cm+bp*dcm
        element3 = dcp*bm+cp*dbm
        element4 = ddp*am+dp*dam
        wmtrx(3,2,dux) = -element1+element2+element3-element4

        element1 = dap*am+ap*dam
        element2 = dbp*bm+bp*dbm
        element3 = dcp*cm+cp*dcm
        element4 = ddp*dm+dp*ddm
        wmtrx(3,3,dux) = -element1-element2+element3+element4

        element1 = dap*bm+ap*dbm
        element2 = dbp*am+bp*dam
        element3 = dcp*dm+cp*ddm
        element4 = ddp*cm+dp*dcm
        wmtrx(3,4,dux) = -element1+element2-element3+element4

        !Row 4
        element1 = dap*dm+ap*ddm
        element2 = dbp*cm+bp*dcm
        element3 = dcp*bm+cp*dbm
        element4 = ddp*am+dp*dam
        wmtrx(4,1,dux) = element1-element2+element3-element4

        element1 = dap*cm+ap*dcm
        element2 = dbp*dm+bp*ddm
        element3 = dcp*am+cp*dam
        element4 = ddp*bm+dp*dbm
        wmtrx(4,2,dux) = element1+element2-element3-element4

```

```fortran
        element1 = dap*bm+ap*dbm
        element2 = dbp*am+bp*dam
        element3 = dcp*dm+cp*ddm
        element4 = ddp*cm+dp*dcm
        wmtrx(4,3,dux) = -element1+element2+element3-element4

        element1 = dap*am+ap*dam
        element2 = dbp*bm+bp*dbm
        element3 = dcp*cm+cp*dcm
        element4 = ddp*dm+dp*ddm
        wmtrx(4,4,dux) = element1+element2+element3+element4

c-----> dU/duy

        dnup = (B1(iB1)**2)*ctrl(2,k)/nup
        dnum = (B1(iB1)**2)*ctrl(2,k)/num

        dap = ((B1(iB1)*ctrl(1,k)*sin(pi*duration(k)*nup)*dnup)/nup**2)
     /  -pi*duration(k)*B1(iB1)*ctrl(1,k)
     /  *cos(pi*duration(k)*nup)*dnup/nup

        dam = ((B1(iB1)*ctrl(1,k)*sin(pi*duration(k)*num)*dnum)/num**2)
     /  -pi*duration(k)*B1(iB1)*ctrl(1,k)
     /  *cos(pi*duration(k)*num)*dnum/num

        dbp = ((B1(iB1)*sin(pi*nup*duration(k))
     /  *(ctrl(2,k)*dnup-nup))/nup**2)
     /  -pi*duration(k)*B1(iB1)*ctrl(2,k)
     /  *cos(pi*duration(k)*nup)*dnup/nup

        dbm = ((B1(iB1)*sin(pi*num*duration(k))
     /  *(ctrl(2,k)*dnum-num))/num**2)
     /  -pi*duration(k)*B1(iB1)*ctrl(2,k)
     /  *cos(pi*duration(k)*num)*dnum/num

        dcp = (((hcp(1)+2*w(1))*sin(pi*duration(k)*nup)*dnup)/(2*nup**2))
     /  -pi*duration(k)*(hcp(1)+2*w(1))
     /  *cos(pi*duration(k)*nup)*dnup/(2*nup)

        dcm = (((-hcp(1)+2*w(1))*sin(pi*duration(k)*num)*dnum)/(2*num**2))
     /  -pi*duration(k)*(-hcp(1)+2*w(1))
     /  *cos(pi*duration(k)*num)*dnum/(2*num)

        ddp = -pi*duration(k)*sin(pi*duration(k)*nup)*dnup
        ddm = -pi*duration(k)*sin(pi*duration(k)*num)*dnum
```

```

c-----> Matrix entries

        !Row 1
        element1 = dap*am+ap*dam
        element2 = dbp*bm+bp*dbm
        element3 = dcp*cm+cp*dcm
        element4 = ddp*dm+dp*ddm
        wmtrx(1,1,duy) = element1-element2-element3+element4

        element1 = dap*bm+ap*dbm
        element2 = dbp*am+bp*dam
        element3 = dcp*dm+cp*ddm
        element4 = ddp*cm+dp*dcm
        wmtrx(1,2,duy) = element1+element2+element3+element4

        element1 = dap*cm+ap*dcm
        element2 = dbp*dm+bp*ddm
        element3 = dcp*am+cp*dam
        element4 = ddp*bm+dp*dbm
        wmtrx(1,3,duy) = element1-element2+element3-element4

        element1 = dap*dm+ap*ddm
        element2 = dbp*cm+bp*dcm
        element3 = dcp*bm+cp*dbm
        element4 = ddp*am+dp*dam
        wmtrx(1,4,duy) = -element1-element2+element3+element4

        !Row 2
        element1 = dap*bm+ap*dbm
        element2 = dbp*am+bp*dam
        element3 = dcp*dm+cp*ddm
        element4 = ddp*cm+dp*dcm
        wmtrx(2,1,duy) = element1+element2-element3-element4

        element1 = dap*am+ap*dam
        element2 = dbp*bm+bp*dbm
        element3 = dcp*cm+cp*dcm
        element4 = ddp*dm+dp*ddm
        wmtrx(2,2,duy) = -element1+element2-element3+element4

        element1 = dap*dm+ap*ddm
        element2 = dbp*cm+bp*dcm
        element3 = dcp*bm+cp*dbm
        element4 = ddp*am+dp*dam
```

```
        wmtrx(2,3,duy) = element1+element2+element3+element4

        element1 = dap*cm+ap*dcm
        element2 = dbp*dm+bp*ddm
        element3 = dcp*am+cp*dam
        element4 = ddp*bm+dp*dbm
        wmtrx(2,4,duy) = element1-element2-element3+element4

        !Row 3
        element1 = dap*cm+ap*dcm
        element2 = dbp*dm+bp*ddm
        element3 = dcp*am+cp*dam
        element4 = ddp*bm+dp*dbm
        wmtrx(3,1,duy) = element1+element2+element3+element4

        element1 = dap*dm+ap*ddm
        element2 = dbp*cm+bp*dcm
        element3 = dcp*bm+cp*dbm
        element4 = ddp*am+dp*dam
        wmtrx(3,2,duy) = -element1+element2+element3-element4

        element1 = dap*am+ap*dam
        element2 = dbp*bm+bp*dbm
        element3 = dcp*cm+cp*dcm
        element4 = ddp*dm+dp*ddm
        wmtrx(3,3,duy) = -element1-element2+element3+element4

        element1 = dap*bm+ap*dbm
        element2 = dbp*am+bp*dam
        element3 = dcp*dm+cp*ddm
        element4 = ddp*cm+dp*dcm
        wmtrx(3,4,duy) = -element1+element2-element3+element4

        !Row 4
        element1 = dap*dm+ap*ddm
        element2 = dbp*cm+bp*dcm
        element3 = dcp*bm+cp*dbm
        element4 = ddp*am+dp*dam
        wmtrx(4,1,duy) = element1-element2+element3-element4

        element1 = dap*cm+ap*dcm
        element2 = dbp*dm+bp*ddm
        element3 = dcp*am+cp*dam
        element4 = ddp*bm+dp*dbm
        wmtrx(4,2,duy) = element1+element2-element3-element4
```

```

       element1 = dap*bm+ap*dbm
       element2 = dbp*am+bp*dam
       element3 = dcp*dm+cp*ddm
       element4 = ddp*cm+dp*dcm
       wmtrx(4,3,duy) = -element1+element2+element3-element4

       element1 = dap*am+ap*dam
       element2 = dbp*bm+bp*dbm
       element3 = dcp*cm+cp*dcm
       element4 = ddp*dm+dp*ddm
       wmtrx(4,4,duy) = element1+element2+element3+element4

        return
        end
```

Listing A.14: Fortran source code for the quality factor evaluation of individual decoupling sequences according to Φ_{mean} in a reduced Liouville space

```
 !       2 spins xy SSR     Heterodecoupling          Tony 2014/01/24
 !       phi0 (TRACKING)
 ! =======================================================================
     ttcost2 = 0d0
     call vcopy(initialrho,rho)

     do k=1,npulses
      call gethamSSR(work1,k) !SSR
      call mvmul(work1,rho,rhoout)
      call vcopy(rhoout,rho)
      if (mod(k,Ppdwell) .eq. 0) then
       ttcost3=wvctr(4,1,rho)
       ttcost2=ttcost2+ttcost3
      endif
     enddo
     ttcost1 = ttcost1+ttcost2/n_FID
```

Listing A.15: Fortran source code for the gradient evaluation of individual decoupling sequences according to Φ_{mean} in a reduced Liouville space

```
!2 spins xy SSR   Gradient für TRACKING                     Tony 2014/01/27
!==========================================================================
!----------initialrho propagieren
        call vcopy(initialrho,prho(1))
        do k=1,npulses
          call gethamSSR(work1,k)
          call mvmul(work1,prho(k),prho(k+1))
```

```
        enddo

!----------targetrho rückwärts propagieren
        call zerovec(plambda(npulses+1))     ! DANGER: comes from npulses+1
        do k=npulses,1,-1      ! rückwärts aufmultplizieren von U
          if (mod(k,Ppdwell) .eq. 0) then
            call vadd(initialrho,plambda(k+1),plambda(k+1)) !TRACK
          endif
          call gethamSSR(work1,k)
          call mtrans(work1,work2)
          call mvmul(work2,plambda(k+1),plambda(k))
        enddo

!----------explicit gradients
        do k=1,npulses
           call getgradSSR(work1,work2,k)
           call mvmul(work1,prho(k),rho)
           call vscalp(plambda(k+1),rho,ttcost)
           grad2(1,k)=grad2(1,k)+ttcost/n_FID
           call mvmul(work2,prho(k),rho)
           call vscalp(plambda(k+1),rho,ttcost)
           grad2(2,k)=grad2(2,k)+ttcost/n_FID
        enddo
```

Listing A.16: Fortran source code for the quality factor evaluation of COOP decoupling sequences according to the homogenizing approach in a reduced Liouville space

```
!2 spins xy SSR        COOP-Heterodecoupling          Tony 2014/02/20
!phi0 (TRACKING)               <Ix> maximization & homogenisation
!=====================================================================
      !---- init ----
      ttcost2 = 0d0
      do k=1,n_FID
       call zerovec(multitarget(k))
      enddo

      !---- propagate ----
      do j=0,ncoop-1
       call vcopy(initialrho,rho)
       do k=j*(npulses/ncoop)+1,(j+1)*npulses/ncoop
      call gethamSSR(work1,k) !SSR
      call mvmul(work1,rho,rhoout)
      call vcopy(rhoout,rho)
        if (mod(k,Ppdwell) .eq. 0) then
         call cvmul(1d0/ncoop,rho,work10)
         call vadd(multitarget(k/Ppdwell-j*n_FID),work10,
```

```
   /    multitarget(k/Ppdwell-j*n_FID))
       endif
      enddo !einzelpuls
     enddo !coop

     !---- evaluate ----
     do k=1,n_FID
      targetmod(k)=wvctr(4,1,multitarget(k))          !Target
      ttcost2=ttcost2+targetmod(k)
     enddo

     ttcost4 = ttcost2/n_FID  !mean value
     ttcost2 = 0d0            !reinitialization

     do k=1,n_FID      !maximize & homogenise
      ttcost3 = 1-(1-targetmod(k))**2-(ttcost4-targetmod(k))**2
      ttcost2 = ttcost2+ttcost3
     enddo

     ttcost1 = ttcost1+ttcost2/n_FID
```

Listing A.17: Fortran source code for the gradient evaluation of COOP decoupling sequences according to the homogenizing approach in a reduced Liouville space

```
!2 spins xy   SSR     COOP-Heterodecoupling           Tony 2014/02/28
!phi0 (TRACKING)              <Ix> maximization & homogenisation
!=======================================================================
!----------initialrho propagieren
    do k=1,n_FID
      call zerovec(multitarget(k))
    enddo
    ttcost2=0d0

    do j=1,ncoop
     call vcopy(initialrho,prho((j-1)*(npulses/ncoop)+1))
     do k=(j-1)*(npulses/ncoop)+1,j*(npulses/ncoop)
                      ! Aufmultiplizieren, von rho
         call gethamSSR(work1,k)
         call mvmul(work1,prho(k),prho(k+1))
       if (mod(k,Ppdwell) .eq. 0) then
        call cvmul(1d0/ncoop,prho(k+1),work10)
        call vadd(multitarget(k/Ppdwell-(j-1)*n_FID),work10,
   /    multitarget(k/Ppdwell-(j-1)*n_FID))
       endif
     enddo !einzelpuls
    enddo !coop
```

```

!------- evaluate <Ix>
      do k=1,n_FID
       targetmod(k)=wvctr(4,1,multitarget(k))          !Target
       ttcost2=ttcost2+targetmod(k)
      enddo

      ttcost4 = ttcost2/n_FID !mean value

       do k=1,n_FID
         call cvmul((2d0/ncoop)*(1+ttcost4-2*targetmod(k)),initialrho,
    /    multitarget(k))
       enddo

!----------targetrho rückwärts propagieren
      do j=ncoop,1,-1
        call zerovec(plambda(j*(npulses/ncoop)+1))
       ! DANGER: comes from npulses+1
        do k=j*npulses/ncoop,(j-1)*(npulses/ncoop)+1,-1
       ! rückwärts aufmultplizieren von U
         if (mod(k,Ppdwell) .eq. 0) then
          call vadd(multitarget(k/Ppdwell-(j-1)*n_FID),plambda(k+1),
    /     plambda(k+1)) !TRACK
         endif
          call gethamSSR(work1,k)
          call mtrans(work1,work2)
          call mvmul(work2,plambda(k+1),plambda(k))
        enddo
      enddo

!----------explicit gradients
        do k=1,npulses
           call getgradSSR(work1,work2,k)
           call mvmul(work1,prho(k),rho)
           call vscalp(plambda(k+1),rho,ttcost)
           grad2(1,k)=grad2(1,k)+ttcost/n_FID
           call mvmul(work2,prho(k),rho)
           call vscalp(plambda(k+1),rho,ttcost)
           grad2(2,k)=grad2(2,k)+ttcost/n_FID
        enddo
```

The computation of quality factors and gradients can be further simplified if decoupling is demanded after each increment of the pulse sequence.

Listing A.18: Fortran source code for the quality factor evaluation of individual decoupling sequences according to Φ_{mean} in a reduced Liouville space

```
!       2 spins xy SSR     Heterodecoupling          Tony 2014/05/26
!       phi0 (TRACKING)                       CONTINUOUS
! =======================================================================
    ttcost2 = 0d0
    call vcopy(initialrho,rho)

    do k=1,npulses
     call gethamSSR(work1,k) !SSR
     call mvmul(work1,rho,rhoout)
     call vcopy(rhoout,rho)
      ttcost3=wvctr(4,1,rho)
      ttcost2=ttcost2+ttcost3
    enddo
    ttcost1 = ttcost1+ttcost2/npulses
```

Listing A.19: Fortran source code for the gradient evaluation of individual decoupling sequences according to Φ_{mean} in a reduced Liouville space

```
!2 spins xy SSR   Gradient für TRACKING                     Tony 2014/05/26
! CONTINOUS decoupling throughout FID
!==========================================================================
!----------initialrho propagieren
        call vcopy(initialrho,prho(1))
        do k=1,npulses
          call gethamSSR(work1,k)
          call mvmul(work1,prho(k),prho(k+1))
        enddo

!----------targetrho rückwärts propagieren
        call zerovec(plambda(npulses+1))     ! DANGER: comes from npulses+1
        do k=npulses,1,-1      ! rückwärts aufmultplizieren von U
          call vadd(initialrho,plambda(k+1),plambda(k+1)) !TRACK
          call gethamSSR(work1,k)
          call mtrans(work1,work2)
          call mvmul(work2,plambda(k+1),plambda(k))
        enddo

!----------explicit gradients
        do k=1,npulses
           call getgradSSR(work1,work2,k)
           call mvmul(work1,prho(k),rho)
           call vscalp(plambda(k+1),rho,ttcost)
           grad2(1,k)=grad2(ictrl,k)+ttcost/npulses
           call mvmul(work2,prho(k),rho)
           call vscalp(plambda(k+1),rho,ttcost)
           grad2(2,k)=grad2(ictrl,k)+ttcost/npulses
```

```
          enddo
```

Listing A.20: Fortran source code for the quality factor evaluation of COOP decoupling sequences according to the homogenizing approach in a reduced Liouville space

```
!2 spins xy SSR        COOP-Heterodecoupling           Tony 2014/05/27
!phi0 (TRACKING) <Ix> maximization & homogenisation CONTINUOUS
!=====================================================================
      !---- init ----
      ttcost2 = 0d0
      do k=1,npulses/ncoop
       call zerovec(multitarget(k))
      enddo

      !---- propagate ----
      do j=0,ncoop-1
       call vcopy(initialrho,rho)
       do k=j*(npulses/ncoop)+1,(j+1)*npulses/ncoop
         call gethamSSR(work1,k) !SSR
         call mvmul(work1,rho,rhoout)
         call vcopy(rhoout,rho)
         call cvmul(1d0/ncoop,rho,work10)
         call vadd(multitarget(k-j*npulses/ncoop),work10,
    /    multitarget(k-j*npulses/ncoop))
       enddo !einzelpuls
      enddo !coop

      !---- evaluate ----
      do k=1,npulses/ncoop
       targetmod(k)=wvctr(4,1,multitarget(k))          !Target
       ttcost2=ttcost2+targetmod(k)
      enddo

      ttcost4 = ttcost2/(npulses/ncoop)        !mean value
      ttcost2 = 0d0                            !reinitialization

      do k=1,npulses/ncoop     !maximize & homogenise
       ttcost3 = 1-(1-targetmod(k))**2-(ttcost4-targetmod(k))**2
       ttcost2 = ttcost2+ttcost3
      enddo

      ttcost1 = ttcost1+ttcost2/(npulses/ncoop)
```

Listing A.21: Fortran source code for the gradient evaluation of COOP decoupling sequences according to the homogenizing approach in a reduced Liouville space

```
 !2 spins xy   SSR     COOP-Heterodecoupling           Tony 2014/05/27
 !phi0 (TRACKING) <Ix> maximization & homogenisation CONTINOUS
 !========================================================================
 !----------initialrho propagieren
     do k=1,npulses/ncoop
       call zerovec(multitarget(k))
     enddo
     ttcost2=0d0

     do j=1,ncoop
      call vcopy(initialrho,prho((j-1)*(npulses/ncoop)+1))
      do k=(j-1)*(npulses/ncoop)+1,j*(npulses/ncoop)
                       ! Aufmultiplizieren, von rho
         call gethamSSR(work1,k)
         call mvmul(work1,prho(k),prho(k+1))
         call cvmul(1d0/ncoop,prho(k+1),work10)
         call vadd(multitarget(k-(j-1)*(npulses/ncoop)),work10,
    /    multitarget(k-(j-1)*(npulses/ncoop)))
      enddo !einzelpuls
     enddo !coop

!------- evaluate <Ix>
      do k=1,npulses/ncoop
       targetmod(k)=wvctr(4,1,multitarget(k))          !Target
       ttcost2=ttcost2+targetmod(k)
      enddo

      ttcost4 = ttcost2/(npulses/ncoop) !mean value

       do k=1,npulses/ncoop
         call cvmul((2d0/ncoop)*(1+ttcost4-2*targetmod(k)),initialrho,
    /    multitarget(k))
       enddo

!----------targetrho rückwärts propagieren
      do j=ncoop,1,-1
        call zerovec(plambda(j*(npulses/ncoop)+1))
       ! DANGER: comes from npulses+1
        do k=j*npulses/ncoop,(j-1)*(npulses/ncoop)+1,-1
       ! rückwärts aufmultplizieren von U
          call vadd(multitarget(k-(j-1)*(npulses/ncoop)),plambda(k+1),
    /     plambda(k+1)) !TRACK
          call gethamSSR(work1,k)
          call mtrans(work1,work2)
          call mvmul(work2,plambda(k+1),plambda(k))
```

```
         enddo
       enddo

 !----------explicit gradients
         do k=1,npulses
            call getgradSSR(work1,work2,k)
            call mvmul(work1,prho(k),rho)
            call vscalp(plambda(k+1),rho,ttcost)
            grad2(1,k)=grad2(1,k)+ttcost/(npulses/ncoop)
            call mvmul(work2,prho(k),rho)
            call vscalp(plambda(k+1),rho,ttcost)
            grad2(2,k)=grad2(2,k)+ttcost/(npulses/ncoop)
         enddo
```

A.3.3. BIRD filters

Listing A.22: Fortran source code for the quality factor evaluation of BIRD elements as continuous shapes or HPD sequences

```
c! 2 spins xy    exact    hard pulse delay              2013.11.20, SE
c! d(phi3)/dt   (d_p_d)*nincrm
c! shape TR 2014.09.30
c! ======================================================================
        call geteye(work1)
        do k=1,npulses
          call geteigenham(k)
          call czmul(-duration(k),ii,phamm,work3)
          call expm(1d0,work3,work4)
          call mmul(work4,work1,work2)             !(Uj+1*Uj...U1)
          call mcopy(work2,work1)
        enddo
        if(jpattern(1,iJ).eq.0)then                 !J=0
          call dagger(unitary1(1),work2)
        elseif(jpattern(1,iJ).eq.1)then             !Jcomp
          call dagger(unitary1(2),work2)
        endif
        call mmul(work2,work1,work2)               !(Uf+ * Uj...U1)
        call trace(work2,ttcost2)                  !Re(Tr{(Uf+ * Uj...U1)})
        ttcost1=ttcost1+ttcost2/normuni
        endif
```

Listing A.23: Fortran source code for the gradient evaluation of BIRD elements as continuous shapes

```
c! 2 spins xy    exact    UR BIRD shape         2014.09.30
c! =========================================================
            call geteye(work1)
```

```
do k=1,npulses ! einzeln alle, voller H
  call geteigenham(k)                       ! H= 2pi*v*Ii
  call VDe(phamm,k)                 ! V=work2, D=wor9, e=work8
  call mcopy(work2,optV(k))
  call mcopy(work9,optD(k))
  call dagger(work2,work3)
  call mmul(work8,work3,work4)
  call mmul(work2,work4,optG(k)) ! G=U=VeVd
enddo
! ------------vorwärts: multiply U---------
call geteye(prho(1))
do k=1,npulses
  call mmul(optG(k),prho(k),prho(k+1))
enddo
! ------------rückwärts: multiply from U_F+
if(jpattern(1,iJ).eq.0)then                 ! J = 0
  call dagger(unitary1(1),plambda(npulses+1))
elseif(jpattern(1,iJ).eq.1)then             ! Jcomp
  call dagger(unitary1(2),plambda(npulses+1))
endif
do k=npulses,1,-1 ! rückwärts aufmultplizieren von U_F
  call mmul(plambda(k+1),optG(k),plambda(k))! LD (lambda dagger)
enddo
do ictrl=1,nctrl
  call cmul(pii,ctrlham(ictrl),workg1(ictrl))
enddo
do k=1,npulses                      ! calc grad
  call mmul(prho(k),plambda(k+1),work1)     ! UiUf
  call dagger(optV(k),work2)
  call mmul(work1,optV(k),work1)
  call mmul(work2,work1,work1)              ! V'*UiUf*V
  call mtrans(work1,work1)                  ! (V'*UiUf*V).'
  do ictrl=1,nctrl
    call mmul(workg1(ictrl),optV(k),workg2(ictrl))  ! I*V
    call mmul(work2,workg2(ictrl),workg2(ictrl))    ! V'*I*V
    call mpstern(workg2(ictrl),optD(k),workg2(ictrl))!(V'*I*V).*D
    call mpstern(workg2(ictrl),work1,workg2(ictrl))
    ! (V'*I*V).*D.* (V'*UiUf*V).'
    call sumsumim(workg2(ictrl),ttcost) ! imag(sum(sum( " )))
    ttcost=ttcost*duration(k) ! imag(sum(sum( ")))*timestep
    grad2(ictrl,k)=grad2(ictrl,k)+ttcost/normuni
  enddo
enddo
```

Listing A.24: Fortran source code for the gradient evaluation of BIRD elements as HPD sequences

```
c! 2 spins xy    exact    hard pulse delay            2013.11.20, SE
c! d(phi3)/dt   (d_p_d)*nincrm
c! ===================================================================
            call geteye(work1)
            do k=1,npulses ! einzeln alle, voller H
              call geteigenham(k)                       ! H= 2pi*v*Ii
              call VDe(phamm,k)                ! V=work2, D=wor9, e=work8
              call mcopy(work2,optV(k))
              call mcopy(work9,optD(k))
              call dagger(work2,work3)
              call mmul(work8,work3,work4)
              call mmul(work2,work4,optG(k)) ! G = U = V*e*V'
            enddo
            ! -------------vorwärts: multiply U---------
            call geteye(prho(1))
            do k=1,npulses
              call mmul(optG(k),prho(k),prho(k+1))
            enddo
            ! -------------rückwärts: multiply from U_F+
            if(jpattern(1,iJ).eq.0)then                 ! J = 0
              call dagger(unitary1(1),plambda(npulses+1))
            elseif(jpattern(1,iJ).eq.1)then             ! Jcomp
              call dagger(unitary1(2),plambda(npulses+1))
            endif
            do k=npulses,1,-1 ! rückwärts aufmultplizieren von U_F
              call mmul(plambda(k+1),optG(k),plambda(k))! LD (lambda dagger)
            enddo
            do ictrl=1,nctrl
              call cmul(pii,ctrlham(ictrl),workg1(ictrl))
            enddo
            do k=2,npulses,2                            ! calc grad
              call mmul(prho(k),plambda(k+1),work1)     ! UiUf
              call dagger(optV(k),work2)
              call mmul(work1,optV(k),work1)
              call mmul(work2,work1,work1)              ! V'*UiUf*V
              call mtrans(work1,work1)                  ! (V'*UiUf*V).'
              do ictrl=1,nctrl
                call mmul(workg1(ictrl),optV(k),workg2(ictrl))  ! I*V
                call mmul(work2,workg2(ictrl),workg2(ictrl))    ! V'*I*V
                call mpstern(workg2(ictrl),optD(k),workg2(ictrl))!(V'*I*V).*D
                call mpstern(workg2(ictrl),work1,workg2(ictrl))
                ! (V'*I*V).*D.* (V'*UiUf*V).'
```

```
                call sumsumim(workg2(ictrl),ttcost) !imag(sum(sum( " )))
                ttcost=ttcost*duration(k) !imag(sum(sum( ")))*timestep
                grad2(ictrl,k)=grad2(ictrl,k)+ttcost/normuni
              enddo
            enddo
            ! ------------- grad------------------------
            do k=1,npulses,2 ! dU/dt=d(exp(-iHt)/dt=-iH*exp(-iHt)
              call geteigenham(k)                     ! H= 2pi*v*Ii
              call czmul(1d0,ii,phamm,work1)    ! i*Hj
              call mmul(work1,prho(k+1),work2)        ! i*Hj*Uj...U1
              call mmul(plambda(k+1),work2,work3) !U_F+..Uj+1*i*Hj *Uj...U1
              call trace(work3,ttcost)                ! Re(Tr("))
              grad2(1,k)=grad2(1,k)-ttcost/normuni      ! -Re(Tr("))/norm
            enddo
```

Listing A.25: Fortran source code for the quality factor evaluation of BIRD elements as BIRDBOP shapes

```
! 2 spins xy            BUBI-Cost UR BIRD auf Spin 1
! phi3b BIRDBOP                                                 2015.02.24 TR
! ========================================================================
c call get...ham91(ipulse,k)
c ipulse = 1 -> pulse 1 /// ipulse = 3 -> pulse 2
        ttcost5 = 0.003 !BIRD delay

        !Ueff Pulse 1
        call geteye(work1)
        do k=1,npulses
          call getfullham91(1,k)        !yields phamm
          call czmul(-duration(k),ii,phamm,work2)
          call expm(1d0,work2,work3)
          call mmul(work3,work1,work2)
          call mcopy(work2,work1)
        enddo

        !USeff Pulse 1
        call geteye(work2)
        do k=1,npulses
          call getsham91(1,k)
          call czmul(-duration(k),ii,phamm,work3)
          call expm(1d0,work3,work4)
          call mmul(work4,work2,work3)
          call mcopy(work3,work2)
        enddo

        !Ueff Pulse 2
```

```
        call geteye(work3)
        do k=1,npulses
          call getfullham91(3,k)
          call czmul(-duration(k),ii,phamm,work4)
          call expm(1d0,work4,work5)
          call mmul(work5,work3,work4)
          call mcopy(work4,work3)
        enddo

        !USeff Pulse 2
        call geteye(work4)
        do k=1,npulses
          call getsham91(3,k)
          call czmul(-duration(k),ii,phamm,work5)
          call expm(1d0,work5,work6)
          call mmul(work6,work4,work5)
          call mcopy(work5,work4)
        enddo

        !H
        call cmul(pii*w(1),Iz(1),work5) !H_cs
        call cmul(pii*hcp(1),IzSz,work6) !H_J
        call madd(work5,work6,work7)    !H_evo

        !U_delay
        call czmul(ttcost5,ii,work7,work6)
        call expm(-1d0,work6,work7)

        !U_delays
        call czmul(ttcost5,ii,work5,work6)
        call expm(-1d0,work6,work5)

        !USeff
        call mmul(work5,work2,work8)
        call mmul(work4,work8,work8)
        call mmul(work5,work8,work8)

        !Ueff
        call czmul(-0.5*pi,ii,Ix(2),work2)
        call expm(1d0,work2,work5)      !90° x
        call czmul(-pi,ii,Ix(2),work2)
        call expm(1d0,work2,work6)      !180° x

        call mmul(work1,work5,work9)
        call mmul(work7,work9,work9)
```

```
        call mmul(work6,work9,work9)
        call mmul(work3,work9,work9)
        call mmul(work7,work9,work9)
        call mmul(work5,work9,work9)

        !Cost
        call mmul(unitary,work8,work1)
        call dagger(work1,work2)
        call mmul(work2,work9,work1)
        call trace(work1,ttcost2)

        ttcost1=ttcost1+ttcost2/normuni
```

Listing A.26: Fortran source code for the gradient evaluation of BIRD elements as BIRDBOP shapes

```
! 2 spins xy            BUBI-Cost UR BIRD auf Spin 1
! phi3b BIRDBOP                                         2015.02.24 TR
! ======================================================================
c call get...ham91(ipulse,k)
c ipulse = 1 -> pulse 1 /// ipulse = 3 -> pulse 2
        ttcost4 = 0.003 !BIRD delay

c!--------------------- SHAPE 1 ---------------------
c!----------- linke Seite der Produktregel ----------
c!--- <Ud’Upi’U2’Ud’Ux’*Uf*USeff|grad(U1eff)*Ux> ----

        !U(I,S,J)j für Puls 1
        do k=1,npulses
          call getfullham91(1,k)
          call VDe(phamm,k)
          call mcopy(work2,optV(k))
          call mcopy(work9,optD(k))
          call dagger(work2,work3)
          call mmul(work8,work3,work4)  ! U = V*e*V’
          call mmul(work2,work4,optG(k))! G = nicht aufmultiplizierte U
        enddo

        !USeff --------------------------------------
        !Puls 1
        call geteye(work1)
        do k=1,npulses
          call getsham91(1,k)
          call czmul(-duration(k),ii,phamm,work2)
          call expm(1d0,work2,work3)
          call mmul(work3,work1,work2)
```

```
          call mcopy(work2,work1)
        enddo

        !Puls 2
        call geteye(work2)
        do k=1,npulses
          call getsham91(3,k)
          call czmul(-duration(k),ii,phamm,work3)
          call expm(1d0,work3,work4)
          call mmul(work4,work2,work3)
          call mcopy(work3,work2)
        enddo

        !U_delayS
        call cmul(pii*w(1),Iz(1),work5)
        call czmul(ttcost4,ii,work5,work6)
        call expm(-1d0,work6,work7)

        !USeff
        call mmul(work7,work1,work3)
        call mmul(work2,work3,work3)
        call mmul(work7,work3,work9)

        !UBIRD' ----------------------------------
        !U_delay
        call cmul(pii*hcp(1),IzSz,work6)
        call madd(work5,work6,work7)
        call czmul(ttcost4,ii,work7,work6)
        call expm(-1d0,work6,work7)
        call dagger(work7,work7)

        !90° x
        call czmul(-0.5*pi,ii,Ix(2),work2)
        call expm(1d0,work2,work5)
        call dagger(work5,work5)

        !180° x
        call czmul(-pi,ii,Ix(2),work2)
        call expm(1d0,work2,work6)
        call dagger(work6,work6)

        !Ueff(I,S,J) für Puls2
        call geteye(work2)
        do k=1,npulses
          call getfullham91(3,k)
```

```
        call czmul(-duration(k),ii,phamm,work3)
        call expm(1d0,work3,work4)
        call mmul(work4,work2,work3)
        call mcopy(work3,work2)
      enddo
      call dagger(work2,work2)

      !UBIRD’*UF*USeff --------------------------
      call mmul(unitary,work9,work1)
      call mmul(work5,work1,work1)
      call mmul(work7,work1,work1)
      call mmul(work2,work1,work1)
      call mmul(work6,work1,work1)
      call mmul(work7,work1,work1)
      call dagger(work1,work1)

      !vorwärts von 90°x
      call dagger(work5,prho(1))
      !zurueckdaggern da oben 90°x’ gebraucht wurde
      do k=1,npulses
        call mmul(optG(k),prho(k),prho(k+1))
      enddo

      !rückwärts von (UBIRD’*UF*USeff)+
      call mcopy(work1,plambda(npulses+1))
      do k=npulses,1,-1 ! rückwärts aufmultplizieren von U
        call mmul(plambda(k+1),optG(k),plambda(k)) ! LD (lambda dagger)
      enddo

          ! ------------- grad
          do ictrl=1,2
            call cmul(pii,ctrlham(ictrl),workg1(ictrl))
          enddo
          do k=1,npulses                              ! calc grad
            call mmul(prho(k),plambda(k+1),work1)     ! UiUf
            call dagger(optV(k),work2)
            call mmul(work1,optV(k),work1)
            call mmul(work2,work1,work1)              ! V’*UiUf*V
            call mtrans(work1,work1)                  ! (V’*UiUf*V).’
            do ictrl=1,2
             call mmul(workg1(ictrl),optV(k),workg2(ictrl))  ! I*V
             call mmul(work2,workg2(ictrl),workg2(ictrl)) !V’*I*V
             call mpstern(workg2(ictrl),optD(k),workg2(ictrl))!(V’*I*V).*D
             call mpstern(workg2(ictrl),work1,workg2(ictrl))
             ! (V’*I*V).*D.* (V’*UiUf*V).’
```

```
              call sumsumim(workg2(ictrl),gradg(ictrl)) !imag(sum(sum(")))
              gradg(ictrl)=gradg(ictrl)*duration(k)
              ! imag(sum(sum(")))*timestep
              grad2(ictrl,k)=grad2(ictrl,k)+gradg(ictrl)/normuni
             enddo
           enddo

c!-------------------- SHAPE 1 --------------------
c!---------- rechte Seite der Produktregel ----------
c!-------- <Ud'U2'Ud'*Uf'*Ueff|grad(U1Seff)> --------

        !U(S) für Puls 1
        do k=1,npulses
          call getsham91(1,k)
          call VDe(phamm,k)
          call mcopy(work2,optV(k))
          call mcopy(work9,optD(k))
          call dagger(work2,work3)
          call mmul(work8,work3,work4)  ! U = V*e*V'
          call mmul(work2,work4,optG(k))! G = nicht aufmultiplizierte U
        enddo

        !Ueff ------------------------------------
        !Puls 1
        call geteye(work1)
        do k=1,npulses
          call getfullham91(1,k)
          call czmul(-duration(k),ii,phamm,work2)
          call expm(1d0,work2,work3)
          call mmul(work3,work1,work2)
          call mcopy(work2,work1)
        enddo

        !Puls 2
        call geteye(work2)
        do k=1,npulses
          call getfullham91(3,k)
          call czmul(-duration(k),ii,phamm,work3)
          call expm(1d0,work3,work4)
          call mmul(work4,work2,work3)
          call mcopy(work3,work2)
        enddo

        !U_delay
        call cmul(pii*w(1),Iz(1),work5)
```

```
      call cmul(pii*hcp(1),IzSz,work6)
      call madd(work5,work6,work7)
      call czmul(ttcost4,ii,work7,work6)
      call expm(-1d0,work6,work7)

      !90° x
      call czmul(-0.5*pi,ii,Ix(2),work3)
      call expm(1d0,work3,work3)

      !180° x
      call czmul(-pi,ii,Ix(2),work4)
      call expm(1d0,work4,work4)

      !Ueff
      call mmul(work1,work3,work8)
      call mmul(work7,work8,work8)
      call mmul(work4,work8,work8)
      call mmul(work2,work8,work8)
      call mmul(work7,work8,work8)
      call mmul(work3,work8,work8)

      !UBIRD'-------------------------
      !USeff für Puls2
      call geteye(work2)
      do k=1,npulses
        call getsham91(3,k)
        call czmul(-duration(k),ii,phamm,work3)
        call expm(1d0,work3,work4)
        call mmul(work4,work2,work3)
        call mcopy(work3,work2)
      enddo
      call dagger(work2,work2)

      !U_delays
      call czmul(ttcost4,ii,work5,work6)
      call expm(-1d0,work6,work5)
      call dagger(work5,work5)

      !UBIRD'*UF'*Ueff -----------------
      call dagger(unitary,work1)
      call mmul(work1,work8,work9)
      call mmul(work5,work9,work9)
      call mmul(work2,work9,work9)
      call mmul(work5,work9,work9)
      call dagger(work9,work1)
```

```fortran

    !vorwärts von 1
    call geteye(prho(1))
    do k=1,npulses
      call mmul(optG(k),prho(k),prho(k+1))
    enddo

    !rückwärts von (UBIRD’*UF’*Ueff)+
    call mcopy(work1,plambda(npulses+1))
    do k=npulses,1,-1 ! rückwärts aufmultplizieren von U
      call mmul(plambda(k+1),optG(k),plambda(k)) ! LD (lambda dagger)
    enddo
      do k=1,npulses                                ! calc grad
        call mmul(prho(k),plambda(k+1),work1)      ! UiUf
        call dagger(optV(k),work2)
        call mmul(work1,optV(k),work1)
        call mmul(work2,work1,work1)                ! V’*UiUf*V
        call mtrans(work1,work1)                    ! (V’*UiUf*V).’
        do ictrl=1,2
          call mmul(workg1(ictrl),optV(k),workg2(ictrl))  ! I*V
          call mmul(work2,workg2(ictrl),workg2(ictrl))    ! V’*I*V
          call mpstern(workg2(ictrl),optD(k),workg2(ictrl))!(V’*I*V).*D
          call mpstern(workg2(ictrl),work1,workg2(ictrl))
          ! (V’*I*V).*D.* (V’*UiUf*V).’
          call sumsumim(workg2(ictrl),gradg(ictrl))! imag(sum(sum(")))
          gradg(ictrl)=gradg(ictrl)*duration(k)
          ! imag(sum(sum(")))*timestep
          grad2(ictrl,k)=grad2(ictrl,k)+gradg(ictrl)/normuni
        enddo
      enddo

c!--------------------- SHAPE 2 ---------------------
c!----------- linke Seite der Produktregel ----------
c!----- <Ud’Ux’*Uf*USeff|grad(U2eff)*UpiUdU1Ux> -----

    !U(I,S,J)j für Puls 2
    do k=1,npulses
      call getfullham91(3,k)
      call VDe(phamm,k)
      call mcopy(work2,optV(k))
      call mcopy(work9,optD(k))
      call dagger(work2,work3)
      call mmul(work8,work3,work4)  ! U = V*e*V’
      call mmul(work2,work4,optG(k))! G = nicht aufmultiplizierte U
    enddo
```

```

        !USeff --------------------------------------
        !Puls 1
        call geteye(work1)
        do k=1,npulses
          call getsham91(1,k)
          call czmul(-duration(k),ii,phamm,work2)
          call expm(1d0,work2,work3)
          call mmul(work3,work1,work2)
          call mcopy(work2,work1)
        enddo

        !Puls 2
        call geteye(work2)
        do k=1,npulses
          call getsham91(3,k)
          call czmul(-duration(k),ii,phamm,work3)
          call expm(1d0,work3,work4)
          call mmul(work4,work2,work3)
          call mcopy(work3,work2)
        enddo

        !U_delayS
        call cmul(pii*w(1),Iz(1),work5)
        call czmul(ttcost4,ii,work5,work6)
        call expm(-1d0,work6,work7)

        !USeff
        call mmul(work7,work1,work3)
        call mmul(work2,work3,work3)
        call mmul(work7,work3,work9)

        !UBIRD’ -----------------------------------
        !U_delay
        call cmul(pii∗hcp(1),IzSz,work6)
        call madd(work5,work6,work7)
        call czmul(ttcost4,ii,work7,work6)
        call expm(-1d0,work6,work7)
        call dagger(work7,work7)

        !90° x
        call czmul(-0.5∗pi,ii,Ix(2),work2)
        call expm(1d0,work2,work5)
        call dagger(work5,work5)

```

```
    !UBIRD -----------------------------------
    !180° x
    call czmul(-pi,ii,Ix(2),work2)
    call expm(1d0,work2,work6)

    !Ueff(I,S,J) für Puls1
    call geteye(work2)
    do k=1,npulses
      call getfullham91(1,k)
      call czmul(-duration(k),ii,phamm,work3)
      call expm(1d0,work3,work4)
      call mmul(work4,work2,work3)
      call mcopy(work3,work2)
    enddo

    !UBIRD'*UF*USeff -------------------------
    call mmul(unitary,work9,work1)
    call mmul(work5,work1,work1)
    call mmul(work7,work1,work1)
    call dagger(work1,work1)

    !UBIRD ------------------------------------
    call dagger(work5,work5) !90°x zurückdaggern
    call dagger(work7,work7) !delay zurückdaggern
    call mmul(work2,work5,work3)
    call mmul(work7,work3,work3)
    call mmul(work6,work3,work3)

    !vorwärts von UBIRD
    call mcopy(work3,prho(1))
    do k=1,npulses
      call mmul(optG(k),prho(k),prho(k+1))
    enddo

    !rückwärts von (UBIRD'*UF*USeff)+
    call mcopy(work1,plambda(npulses+1))
    do k=npulses,1,-1 ! rückwärts aufmultplizieren von U
      call mmul(plambda(k+1),optG(k),plambda(k)) ! LD (lambda dagger)
    enddo

        ! ------------- grad
        do ictrl=1,2
          call cmul(pii,ctrlham(ictrl),workg1(ictrl+2))
        enddo
        do k=1,npulses                              ! calc grad
```

```
              call mmul(prho(k),plambda(k+1),work1)     ! UiUf
              call dagger(optV(k),work2)
              call mmul(work1,optV(k),work1)
              call mmul(work2,work1,work1)              ! V’*UiUf*V
              call mtrans(work1,work1)                  ! (V’*UiUf*V).’
              do ictrl=3,4
                call mmul(workg1(ictrl),optV(k),workg2(ictrl))  ! I*V
                call mmul(work2,workg2(ictrl),workg2(ictrl))    ! V’*I*V
                call mpstern(workg2(ictrl),optD(k),workg2(ictrl))!(V’*I*V).*D
                call mpstern(workg2(ictrl),work1,workg2(ictrl))
                ! (V’*I*V).*D.* (V’*UiUf*V).’
                call sumsumim(workg2(ictrl),gradg(ictrl)) ! imag(sum(sum(")))
                gradg(ictrl)=gradg(ictrl)*duration(k)
                ! imag(sum(sum(")))*timestep
                grad2(ictrl,k)=grad2(ictrl,k)+gradg(ictrl)/normuni
              enddo
            enddo

c!--------------------- SHAPE 2 ---------------------
c!---------- rechte Seite der Produktregel ----------
c!--------- <Ud’*Uf’*Ueff|grad(U2Seff)UdU1> ---------

        !U(S) für Puls 1
        do k=1,npulses
          call getsham91(3,k)
          call VDe(phamm,k)
          call mcopy(work2,optV(k))
          call mcopy(work9,optD(k))
          call dagger(work2,work3)
          call mmul(work8,work3,work4)  ! U = V*e*V’
          call mmul(work2,work4,optG(k))! G = nicht aufmultiplizierte U
        enddo

        !Ueff --------------------------------------
        !Puls 1
        call geteye(work1)
        do k=1,npulses
          call getfullham91(1,k)
          call czmul(-duration(k),ii,phamm,work2)
          call expm(1d0,work2,work3)
          call mmul(work3,work1,work2)
          call mcopy(work2,work1)
        enddo

        !Puls 2
```

```
        call geteye(work2)
        do k=1,npulses
          call getfullham91(3,k)
          call czmul(-duration(k),ii,phamm,work3)
          call expm(1d0,work3,work4)
          call mmul(work4,work2,work3)
          call mcopy(work3,work2)
        enddo

        !U_delay
        call cmul(pii*w(1),Iz(1),work5)
        call cmul(pii*hcp(1),IzSz,work6)
        call madd(work5,work6,work7)
        call czmul(ttcost4,ii,work7,work6)
        call expm(-1d0,work6,work7)

        !90° x
        call czmul(-0.5*pi,ii,Ix(2),work3)
        call expm(1d0,work3,work3)

        !180° x
        call czmul(-pi,ii,Ix(2),work4)
        call expm(1d0,work4,work4)

        !Ueff
        call mmul(work1,work3,work8)
        call mmul(work7,work8,work8)
        call mmul(work4,work8,work8)
        call mmul(work2,work8,work8)
        call mmul(work7,work8,work8)
        call mmul(work3,work8,work8)

        !UBIRD'-------------------------
        !U_delays
        call czmul(ttcost4,ii,work5,work6)
        call expm(-1d0,work6,work5)
        call dagger(work5,work5)

        !UBIRD'*UF'*Ueff ------------------
        call dagger(unitary,work1)
        call mmul(work1,work8,work9)
        call mmul(work5,work9,work9)
        call dagger(work9,work1)

        !UBIRD----------------------------
```

```
        !USeff für Puls1
        call geteye(work2)
        do k=1,npulses
          call getsham91(1,k)
          call czmul(-duration(k),ii,phamm,work3)
          call expm(1d0,work3,work4)
          call mmul(work4,work2,work3)
          call mcopy(work3,work2)
        enddo

        !UBIRD-----------------------------
        call dagger(work5,work5) !delay zurückdaggern
        call mmul(work5,work2,work2)

        !vorwärts von UBIRD
        call mcopy(work2,prho(1))
        do k=1,npulses
          call mmul(optG(k),prho(k),prho(k+1))
        enddo

        !rückwärts von (UBIRD’*UF’*Ueff)+
        call mcopy(work1,plambda(npulses+1))
        do k=npulses,1,-1 ! rückwärts aufmultplizieren von U
          call mmul(plambda(k+1),optG(k),plambda(k)) ! LD (lambda dagger)
        enddo
            do k=1,npulses                              ! calc grad
              call mmul(prho(k),plambda(k+1),work1)     ! UiUf
              call dagger(optV(k),work2)
              call mmul(work1,optV(k),work1)
              call mmul(work2,work1,work1)              ! V’*UiUf*V
              call mtrans(work1,work1)                  ! (V’*UiUf*V).’
              do ictrl=3,4
                call mmul(workg1(ictrl),optV(k),workg2(ictrl))  ! I*V
                call mmul(work2,workg2(ictrl),workg2(ictrl))    ! V’*I*V
                call mpstern(workg2(ictrl),optD(k),workg2(ictrl))!(V’*I*V).*D
                call mpstern(workg2(ictrl),work1,workg2(ictrl))
                ! (V’*I*V).*D.* (V’*UiUf*V).’
                call sumsumim(workg2(ictrl),gradg(ictrl)) ! imag(sum(sum(")))
                gradg(ictrl)=gradg(ictrl)*duration(k)
                ! imag(sum(sum(")))*timestep
                grad2(ictrl,k)=grad2(ictrl,k)+gradg(ictrl)/normuni
              enddo
            enddo
```

A.4. CT-SP-CLIP/CLAP-RESET HSQC

If CT versions of the more robust SP (see figure 3.11 B) or COB-CLIP/CLAP-RESET HSQC experiments (see figure 3.11 C) are to be recorded, the PS pseudo-dimension depicted in figure 3.8 needs to be made more robust. If all hard pulses are replaced with corresponding broadband shapes as described in section 3.2.3, the pulse sequence shown in figure A.3 is obtained.

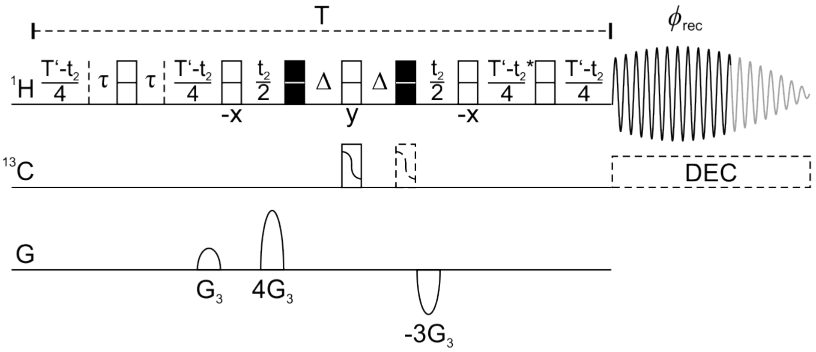

Figure A.3.: Pulse sequence for a CT pseudo-dimension of SP/COB-CLIP/CLAP-RESET HSQC experiments. Rectangular 90° and 180° pulses have been replaced by shaped pulses according to their function depicted in figure 3.11 A. Phases are x unless indicated otherwise. For the acquisition of CLAP spectra, ϕ_{rec} has to be changed to y, $-y$, $-y$, y. Heteronuclear transfer delays are calibrated to match $\Delta = 1/(2^1J_{\text{CH}})$. If the dashed 180° pulse is omitted and broadband heteronuclear decoupling is applied during acquisition, CT versions of more robust fully decoupled RESET HSQC experiment can be obtained. The delay τ is set to AQ/4n with n being the number of data chunks. Decremented CT delays have to be corrected from the overall evolution period T according to equation 3.4. Delays marked with an asterisk allow for the compensation of phase distortions introduced by dropping points at the beginning of each FID chunk. Graphic taken and modified from [212].

A.5. Bruker pulse programs

Listing A.27: CPD program for decoupling using the BROCODE

```
bilev "l31=(nsdone+ds)%4+1"
jump to l31
1 pcpd:sp11:0 pl=sp11
  jump to 1
2 pcpd:sp12:0 pl=sp12
  jump to 2
3 pcpd:sp13:0 pl=sp13
  jump to 3
4 pcpd:sp14:0 pl=sp14
  jump to 4
```

Listing A.28: Pulse program for CLIP-RESET HSQC experiments

```
; CLIP_RESET_hsqcetgp
;
;based on hsqcetgp
;avance-version (09/04/17)
;HSQC
;2D H-1/X correlation via double inept transfer
;phase sensitive using Echo/Antiecho-TPPI gradient selection
;clip pulse before aquisition
;
;$CLASS=HighRes
;$DIM=2D
;$TYPE=
;$SUBTYPE=
;$COMMENT=

#include <Avance.incl>
#include <Grad.incl>
#include <Delay.incl>

"p2=p1*2"
"p4=p3*2"
"d4=1s/(cnst2*4)"
"d11=30m"

#   ifdef LABEL_CN
"p22=p21*2"
#   else
#   endif /*LABEL_CN*/

```

```
"acqt0=0"

"d0=3u"
"d10=3u"
"in0=inf1/2"
"in10=inf2/2"

"DELTA1=d4-p16-de+p1*2/PI-8u-p3"
"DELTA2=in0/2-p16-d16"
"DELTA3=in0-p16-d16"
"DELTA4=in0/2-(dw*2*cnst4)-p16-d16"

#   ifdef LABEL_CN
"DELTA=p16+d16+larger(p2,p22)+d0*2"
#   else
"DELTA=p16+d16+p2+d0*2"
#   endif /*LABEL_CN*/

1 ze
  d11
2 d1
3 (p1 ph1)
  d4 pl2:f2
  (center (p2 ph1) (p4 ph6):f2 )
  d4 UNBLKGRAD
  (p1 ph2) (p3 ph3):f2
  d10
#   ifdef LABEL_CN
  (center (p2 ph5) (p22 ph1):f3 )
#   else
  (p2 ph5)
#   endif /*LABEL_CN*/
  d10
  p16:gp1*EA
  d16
  (p4 ph4):f2
  DELTA
  (ralign (p1 ph1) (p3 ph5):f2 )
  d4
  (center (p2 ph1) (p4 ph1):f2 )
  4u
  p16:gp2
  DELTA1
  4u
  (p3 ph8):f2
```

```

  ;;;;; Pure-Shift Pseudo-Dimension ;;;;;
  d0
  DELTA2
  p16:gp3
  d16
  (p2 ph1):f1
  DELTA3
  p16:gp4
  d16
  (p1 ph1):f1 ;BIRDd
  d4*2
  (center (p2 ph1) (p4 ph1):f2 )
  d4*2
  (ralign (p1 ph1) (p4 ph1):f2 )
  DELTA4
  p16:gp5
  d16 BLKGRAD
  d0

  go=2 ph31
  d1 mc #0 to 2
    F1QF( caldel(d0, +in0) )
    F2EA(calgrad(EA), caldel(d10, +in10) & calph(ph3, +180) & calph(ph6,
   +180) & calph(ph31, +180))
exit

ph1=0
ph2=1
ph3=0 2
ph4=0 0 0 0 2 2 2 2
ph5=0 0 2 2
ph6=0
ph8=0 2
ph31=0 2 0 2 2 0 2 0

;pl1 : f1 channel - power level for pulse (default)
;pl2 : f2 channel - power level for pulse (default)
;pl3 : f3 channel - power level for pulse (default)
;pl12: f2 channel - power level for CPD/BB decoupling
;p1 : f1 channel -  90 degree high power pulse
;p2 : f1 channel - 180 degree high power pulse
;p3 : f2 channel -  90 degree high power pulse
;p4 : f2 channel - 180 degree high power pulse
;p16: homospoil/gradient pulse
```

```
;p22: f3 channel - 180 degree high power pulse
;p28: f1 channel - trim pulse
;d0 : incremented delay (2D)                  [3 usec]
;d1 : relaxation delay; 1-5 * T1
;d4 : 1/(4J)XH
;d11: delay for disk I/O                            [30 msec]
;d16: delay for homospoil/gradient recovery
;cnst2: = J(XH)
;cnst4: = Points dropped by AU program
;inf1: 1/SW(X) = 2 * DW(X)
;in0: 1/(2 * SW(X)) = DW(X)
;nd0: 2
;NS: 1 * n
;DS: >= 16
;td1: number of experiments
;FnMODE: echo-antiecho
;cpd2: decoupling according to sequence defined by cpdprg2
;pcpd2: f2 channel - 90 degree pulse for decoupling sequence

;use gradient ratio:    gp 1 : gp 2
;                         80 : 20.1    for C-13
;                         80 :  8.1    for N-15
;use gradient ratio:    gp 3 : gp 4 : gp 5
;                         1 : 4 : 3
;for z-only gradients:
;gpz1: 80%
;gpz2: 20.1% for C-13, 8.1% for N-15
;gpz3: n*1 %
;gpz4: n*4 %
;gpz5: n*3 %

;use gradient files:
;gpnam1: SMSQ10.100
;gpnam2: SMSQ10.100
;gpnam3: SMSQ10.100
;gpnam4: SMSQ10.100
;gpnam5: SMSQ10.100

;preprocessor-flags-start
;LABEL_CN: for C-13 and N-15 labeled samples start experiment with
;             option -DLABEL_CN (eda: ZGOPTNS)
;preprocessor-flags-end

;$Id: hsqcetgp,v 1.5.4.1 2011/02/24 17:26:40 ber Exp $
```

Listing A.29: Pulse program for CLAP-RESET HSQC experiments

```
; CLAP_RESET_hsqcetgp
;
;based on hsqcetgp
;avance-version (09/04/17)
;HSQC
;2D H-1/X correlation via double inept transfer
;phase sensitive using Echo/Antiecho-TPPI gradient selection
;
;$CLASS=HighRes
;$DIM=2D
;$TYPE=
;$SUBTYPE=
;$COMMENT=

#include <Avance.incl>
#include <Grad.incl>
#include <Delay.incl>

"p2=p1*2"
"p4=p3*2"
"d4=1s/(cnst2*4)"
"d11=30m"

#   ifdef LABEL_CN
"p22=p21*2"
#   else
#   endif /*LABEL_CN*/

"acqt0=0"

"d0=3u"
"d10=3u"
"in0=inf1/2"
"in10=inf2/2"

"DELTA1=d4-p16-de+p1*2/PI-8u"
"DELTA2=in0/2-p16-d16"
"DELTA3=in0-p16-d16"
"DELTA4=in0/2-(dw*2*cnst4)-p16-d16"

#   ifdef LABEL_CN
"DELTA=p16+d16+larger(p2,p22)+d0*2"
#   else
```

```
"DELTA=p16+d16+p2+d0*2"
#   endif /*LABEL_CN*/

1 ze
  d11
2 d1
3 (p1 ph1)
  d4 pl2:f2
  (center (p2 ph1) (p4 ph6):f2 )
  d4 UNBLKGRAD
  (p1 ph2) (p3 ph3):f2
  d10
#   ifdef LABEL_CN
  (center (p2 ph5) (p22 ph1):f3 )
#   else
  (p2 ph5)
#   endif /*LABEL_CN*/
  d10
  p16:gp1*EA
  d16
  (p4 ph4):f2
  DELTA
  (ralign (p1 ph1) (p3 ph5):f2 )
  d4
  (p2 ph1)
  4u
  p16:gp2
  DELTA1
  4u

  ;;;;; Pure-Shift Pseudo-Dimension ;;;;;
  d0
  DELTA2
  p16:gp3
  d16
  (p2 ph1):f1
  DELTA3
  p16:gp4
  d16
  (p1 ph1):f1 ;BIRDd
  d4*2
  (center (p2 ph1) (p4 ph1):f2 )
  d4*2
  (ralign (p1 ph1) (p4 ph1):f2 )
  DELTA4
```

```
  p16:gp5
  d16 BLKGRAD
  d0

  go=2 ph31
  d1 mc #0 to 2
    F1QF( caldel(d0, +in0) )
    F2EA(calgrad(EA), caldel(d10, +in10) & calph(ph3, +180) & calph(ph6,
   +180) & calph(ph31, +180))
exit

ph1=0
ph2=1
ph3=0 2
ph4=0 0 0 0 2 2 2 2
ph5=0 0 2 2
ph6=0
ph31=1 3 1 3 3 1 3 1

;pl1 : f1 channel - power level for pulse (default)
;pl2 : f2 channel - power level for pulse (default)
;pl3 : f3 channel - power level for pulse (default)
;pl12: f2 channel - power level for CPD/BB decoupling
;p1 : f1 channel -  90 degree high power pulse
;p2 : f1 channel - 180 degree high power pulse
;p3 : f2 channel -  90 degree high power pulse
;p4 : f2 channel - 180 degree high power pulse
;p16: homospoil/gradient pulse
;p22: f3 channel - 180 degree high power pulse
;p28: f1 channel - trim pulse
;d0 : incremented delay (2D)                  [3 usec]
;d1 : relaxation delay; 1-5 * T1
;d4 : 1/(4J)XH
;d11: delay for disk I/O                             [30 msec]
;d16: delay for homospoil/gradient recovery
;cnst2: = J(XH)
;cnst4: = Points dropped by AU program
;inf1: 1/SW(X) = 2 * DW(X)
;in0: 1/(2 * SW(X)) = DW(X)
;nd0: 2
;NS: 1 * n
;DS: >= 16
;td1: number of experiments
;FnMODE: echo-antiecho
;cpd2: decoupling according to sequence defined by cpdprg2
```

```
;pcpd2: f2 channel - 90 degree pulse for decoupling sequence

;use gradient ratio:    gp 1 : gp 2
;                         80 : 20.1    for C-13
;                         80 :  8.1    for N-15
;use gradient ratio:    gp 3 : gp 4 : gp 5
;                         1 : 4 : 3
;for z-only gradients:
;gpz1: 80%
;gpz2: 20.1% for C-13, 8.1% for N-15
;gpz3: n*1 %
;gpz4: n*4 %
;gpz5: n*3 %

;use gradient files:
;gpnam1: SMSQ10.100
;gpnam2: SMSQ10.100
;gpnam3: SMSQ10.100
;gpnam4: SMSQ10.100
;gpnam5: SMSQ10.100

;preprocessor-flags-start
;LABEL_CN: for C-13 and N-15 labeled samples start experiment with
;             option -DLABEL_CN (eda: ZGOPTNS)
;preprocessor-flags-end

;$Id: hsqcetgp,v 1.5.4.1 2011/02/24 17:26:40 ber Exp $
```

Listing A.30: Pulse program for SP-CLIP-RESET HSQC experiments

```
;SP_CLIP_RESET_hsqcetgp
;
;based on hsqcetgp,v 1.5.2.1 2011/02/24
;HSQC
;2D H-1/X correlation via double inept transfer
;phase sensitive using Echo/Antiecho-TPPI gradient selection
;clip pulse before aquisition
;
;$CLASS=HighRes
;$DIM=2D
;$TYPE=
;$SUBTYPE=
;$COMMENT=

#include <Avance.incl>
#include <Grad.incl>
```

```
#include <Delay.incl>
#include<Sysconf.incl>

"d11=30m"
"acqt0=0"
"d4=1s/(cnst2*4)"

"d0=3u"
"d10=3u"
"in0=inf1/2"
"in10=inf2/2"

"DELTA=p16+d16+p26+d0*2"
"DELTA1=d4-p16-4u-p3"
"DELTA2=in0/2-p16-d16"
"DELTA3=in0-p16-d16"
"DELTA4=in0/2-(dw*2*cnst4)-p16-d16"

1 ze
  d11
2 d1
3 (p21:sp21 ph1):f1             ;zx
  d4
  (p22:sp22 ph1):f1     (p22:sp23 ph1):f2       ;URx180 BIBOP
  d4 UNBLKGRAD
  (p21:sp24 ph1):f1     (p21:sp25 ph3):f2       ;yz z-y
  d10
  (p26:sp26 ph5):f1
  d10
  p16:gp1*EA
  d16
  (p27:sp27 ph4):f2
  DELTA
  (p21:sp28 ph1):f1     (p21:sp29 ph4):f2       ;z-y yz
  d4
  (p22:sp22 ph1):f1     (p22:sp23 ph1):f2       ;URx180 BIBOP
  p16:gp2
  DELTA1
  4u pl2:f2
  (p3 ph8):f2

  ;;;;; Pure-Shift Pseudo-Dimension ;;;;;
  d0
  DELTA2
  p16:gp3
```

```
  d16
  (p22:sp22 ph1):f1
  DELTA3
  p16:gp4
  d16
  (p22:sp30 ph1):f1 ;BIRDd
  d4*2
  (p22:sp22 ph1):f1     (p22:sp23 ph1):f2       ;URx180 BIBOP
  d4*2
  (p22:sp30 ph1):f1     (p22:sp23 ph1):f2 ;URx90 BIBOP
  DELTA4
  p16:gp5
  d16 BLKGRAD
  d0

  go=2 ph31
  d1 mc #0 to 2
    F1QF(caldel(d0, +in0) )
    F2EA(calgrad(EA), caldel(d10, +in10) & calph(ph3, +180) & calph(ph6, +180) & calph(ph31, +180))
exit

ph1=0
ph2=1
ph3=0 2
ph4=0 0 2 2
ph5=0 0 0 0 2 2 2 2
ph6=0
ph8=0 2
ph31=0 2 2 0

;pl1 : f1 channel - power level for pulse (default)
;pl2 : f2 channel - power level for pulse (default)
;pl3 : f3 channel - power level for pulse (default)
;pl12: f2 channel - power level for CPD/BB decoupling
;p1 : f1 channel -  90 degree high power pulse
;p2 : f1 channel - 180 degree high power pulse
;p3 : f2 channel -  90 degree high power pulse
;p4 : f2 channel - 180 degree high power pulse
;p16: homospoil/gradient pulse
;p21 : 550u excitation pulses
;p22 : 600u UR and Inversion pulses
;p26 : 100u Inversion pulse
;p27 : 1100u UR pulse

```

```
;spnam21 : jc01_BEBOP_zx_550u_BW10_RF20_pm20_Hc0.99997119.pul
;spnam22 : jc02_BURBOP_x_600u_BW10_RF20_pm20_matched.pul
;spnam24 : jc04_BEBOP_yz_550u_BW10_RF20_pm20_matched.pul
;spnam26 : jc06_BIBOP_z-z_100u_BW11_RF20_pm20_Hc0.99966724.pul
;spnam28 : jc08_BEBOP_z-y_550u_BW10_RF20_pm20_matched.pul
;spnam30 : UR90x_600u_BW10_RF20_pm20_Hc0.999959.bruker

;spnam23 : jc03_BIBOP_600u_BW37.5_RF10_pm5_matched.pul
;spnam25 : jc05_BEBOP_zy_550u_BW37.5_RF10_pm5_matched.pul
;spnam27 : jc07_BURBOP_y_1100u_BW37.5_RF10_pm5_Hc0.999876221.pul
;spnam29 : jc09_BEBOP_-yz_550u_BW37.5_RF10_pm5_matched.pul

;sp21 : 20 kHz Rf Amplitude
;sp22 : 20 kHz Rf Amplitude
;sp24 : 20 kHz Rf Amplitude
;sp26 : 20 kHz Rf Amplitude
;sp28 : 20 kHz Rf Amplitude
;sp30 : 20 kHz Rf Amplitude

;sp23 : 10 kHz Rf Amplitude
;sp25 : 10 kHz Rf Amplitude
;sp27 : 10 kHz Rf Amplitude
;sp29 : 10 kHz Rf Amplitude

;d0 : incremented delay (2D)                   [3 usec]
;d1 : relaxation delay; 1-5 * T1
;d4 : 1/(4J)XH
;d11: delay for disk I/O                             [30 msec]
;d16: delay for homospoil/gradient recovery
;cnst2: = J(XH)
;cnst4: = Points dropped by AU program
;inf1: 1/SW(X) = 2 * DW(X)
;in0: 1/(2 * SW(X)) = DW(X)
;nd0: 2
;NS: 2 * n
;DS: >= 16
;td1: number of experiments
;FnMODE: echo-antiecho
;cpd2: decoupling according to sequence defined by cpdprg2
;pcpd2: f2 channel - 90 degree pulse for decoupling sequence

;use gradient ratio:    gp 1 : gp 2
;                         80 : 20.1    for C-13
;                         80 :  8.1    for N-15
;use gradient ratio:    gp 3 : gp 4 : gp 5
```

```
;                          1 : 4 : 3
;for z-only gradients:
;gpz1: 80%
;gpz2: 20.1% for C-13, 8.1% for N-15
;gpz3: n*1 %
;gpz4: n*4 %
;gpz5: n*3 %

;use gradient files:
;gpnam1: SMSQ10.100
;gpnam2: SMSQ10.100
;gpnam3: SMSQ10.100
;gpnam4: SMSQ10.100
;gpnam5: SMSQ10.100

;preprocessor-flags-start

;$Id: hsqcetgp,v 1.5.2.1 2011/02/24 17:27:48 ber Exp $
```

Listing A.31: Pulse program for SP-CLAP-RESET HSQC experiments

```
;SP_CLAP_RESET_hsqcetgp
;
;based on hsqcetgp,v 1.5.2.1 2011/02/24
;HSQC
;2D H-1/X correlation via double inept transfer
;phase sensitive using Echo/Antiecho-TPPI gradient selection
;
;$CLASS=HighRes
;$DIM=2D
;$TYPE=
;$SUBTYPE=
;$COMMENT=

#include <Avance.incl>
#include <Grad.incl>
#include <Delay.incl>
#include<Sysconf.incl>

"d11=30m"
"acqt0=0"
"d4=1s/(cnst2*4)"

"d0=3u"
"d10=3u"
"in0=inf1/2"
```

```
"in10=inf2/2"

"DELTA=p16+d16+p26+d0*2"
"DELTA1=d4-p16-4u"
"DELTA2=in0/2-p16-d16"
"DELTA3=in0-p16-d16"
"DELTA4=in0/2-(dw*2*cnst4)-p16-d16"

1 ze
  d11
2 d1
3 (p21:sp21 ph1):f1             ;zx
  d4
  (p22:sp22 ph1):f1     (p22:sp23 ph1):f2       ;URx180 BIBOP
  d4 UNBLKGRAD
  (p21:sp24 ph1):f1     (p21:sp25 ph3):f2       ;yz z-y
  d10
  (p26:sp26 ph5):f1
  d10
  p16:gp1*EA
  d16
  (p27:sp27 ph4):f2
  DELTA
  (p21:sp28 ph1):f1     (p21:sp29 ph4):f2       ;z-y yz
  d4
  (p22:sp22 ph1):f1     ;URx180
  p16:gp2
  DELTA1
  4u

  ;;;;; Pure-Shift Pseudo-Dimension ;;;;;
  d0
  DELTA2
  p16:gp3
  d16
  (p22:sp22 ph1):f1
  DELTA3
  p16:gp4
  d16
  (p22:sp30 ph1):f1 ;BIRDd
  d4*2
  (p22:sp22 ph1):f1     (p22:sp23 ph1):f2       ;URx180 BIBOP
  d4*2
  (p22:sp30 ph1):f1     (p22:sp23 ph1):f2 ;URx90 BIBOP
  DELTA4
```

```
  p16:gp5
  d16 BLKGRAD
  d0

  go=2 ph31
  d1 mc #0 to 2
    F1QF(caldel(d0, +in0) )
    F2EA(calgrad(EA), caldel(d10, +in10) & calph(ph3, +180) & calph(ph6, +180) & calph(ph31, +180))
exit

ph1=0
ph2=1
ph3=0 2
ph4=0 0 2 2
ph5=0 0 0 0 2 2 2 2
ph6=0
ph8=0 2
ph31=1 3 3 1

;pl1 : f1 channel - power level for pulse (default)
;pl2 : f2 channel - power level for pulse (default)
;pl3 : f3 channel - power level for pulse (default)
;pl12: f2 channel - power level for CPD/BB decoupling
;p1 : f1 channel -  90 degree high power pulse
;p2 : f1 channel - 180 degree high power pulse
;p3 : f2 channel -  90 degree high power pulse
;p4 : f2 channel - 180 degree high power pulse
;p16: homospoil/gradient pulse
;p21 : 550u excitation pulses
;p22 : 600u UR and Inversion pulses
;p26 : 100u Inversion pulse
;p27 : 1100u UR pulse

;spnam21 : jc01_BEBOP_zx_550u_BW10_RF20_pm20_Hc0.99997119.pul
;spnam22 : jc02_BURBOP_x_600u_BW10_RF20_pm20_matched.pul
;spnam24 : jc04_BEBOP_yz_550u_BW10_RF20_pm20_matched.pul
;spnam26 : jc06_BIBOP_z-z_100u_BW11_RF20_pm20_Hc0.99966724.pul
;spnam28 : jc08_BEBOP_z-y_550u_BW10_RF20_pm20_matched.pul
;spnam30 : UR90x_600u_BW10_RF20_pm20_Hc0.999959.bruker

;spnam23 : jc03_BIBOP_600u_BW37.5_RF10_pm5_matched.pul
;spnam25 : jc05_BEBOP_zy_550u_BW37.5_RF10_pm5_matched.pul
;spnam27 : jc07_BURBOP_y_1100u_BW37.5_RF10_pm5_Hc0.999876221.pul
;spnam29 : jc09_BEBOP_-yz_550u_BW37.5_RF10_pm5_matched.pul
```

```

;sp21 : 20 kHz Rf Amplitude
;sp22 : 20 kHz Rf Amplitude
;sp24 : 20 kHz Rf Amplitude
;sp26 : 20 kHz Rf Amplitude
;sp28 : 20 kHz Rf Amplitude
;sp30 : 20 kHz Rf Amplitude

;sp23 : 10 kHz Rf Amplitude
;sp25 : 10 kHz Rf Amplitude
;sp27 : 10 kHz Rf Amplitude
;sp29 : 10 kHz Rf Amplitude

;d0 : incremented delay (2D)                  [3 usec]
;d1 : relaxation delay; 1-5 * T1
;d4 : 1/(4J)XH
;d11: delay for disk I/O                             [30 msec]
;d16: delay for homospoil/gradient recovery
;cnst2: = J(XH)
;cnst4: = Points dropped by AU program
;inf1: 1/SW(X) = 2 * DW(X)
;in0: 1/(2 * SW(X)) = DW(X)
;nd0: 2
;NS: 2 * n
;DS: >= 16
;td1: number of experiments
;FnMODE: echo-antiecho
;cpd2: decoupling according to sequence defined by cpdprg2
;pcpd2: f2 channel - 90 degree pulse for decoupling sequence

;use gradient ratio:    gp 1 : gp 2
;                         80 : 20.1    for C-13
;                         80 :  8.1    for N-15
;use gradient ratio:    gp 3 : gp 4 : gp 5
;                         1 : 4 : 3
;for z-only gradients:
;gpz1: 80%
;gpz2: 20.1% for C-13, 8.1% for N-15
;gpz3: n*1 %
;gpz4: n*4 %
;gpz5: n*3 %

;use gradient files:
;gpnam1: SMSQ10.100
;gpnam2: SMSQ10.100
```

```
;gpnam3: SMSQ10.100
;gpnam4: SMSQ10.100
;gpnam5: SMSQ10.100

;preprocessor-flags-start

;$Id: hsqcetgp,v 1.5.2.1 2011/02/24 17:27:48 ber Exp $
```

Listing A.32: Pulse program for COB-CLIP-RESET HSQC experiments

```
;COB_CLIP_RESET_hsqcetgp
;
;based on hsqcetgp,v 1.5.2.1 2011/02/24
;HSQC
;2D H-1/X correlation via double inept transfer
;phase sensitive using Echo/Antiecho-TPPI gradient selection
;clip pulse before aquisition
;
;$CLASS=HighRes
;$DIM=2D
;$TYPE=
;$SUBTYPE=
;$COMMENT=

#include <Avance.incl>
#include <Grad.incl>
#include <Delay.incl>
#include<Sysconf.incl>

"d11=30m"
"acqt0=0"
"d4=1s/(cnst2*4)"

"d20=d5*0.001469"
"d21=d5*0.00213465"
"d22=d5*0.0003938"

"d0=3u"
"d10=3u"
"in0=inf1/2"
"in10=inf2/2"

"DELTA=p16+d16+p26+d0*2"
"DELTA1=d5*0.001469-p16-4u-p3"
"DELTA2=in0/2-p16-d16"
"DELTA3=in0-p16-d16"
```

```
"DELTA4=in0/2-(dw*2*cnst4)-p16-d16"

1 ze
  d11
2 d1
3 (p21:sp21 ph1):f1             ;zx
  d20
  (p22:sp22 ph1):f1     (p22:sp23 ph1):f2       ;URx180 BIBOP
  d20 UNBLKGRAD
  (p30:sp30 ph1):f1             ;URx242  ;p1*2.7 ph1
  d21
  (p22:sp22 ph1):f1     (p22:sp23 ph1):f2       ;URx180 BIBOP
  d21
  (p30:sp31 ph1):f1             ;URx65  ;p1*0.72 ph1
  d22
  (p22:sp22 ph1):f1     (p22:sp23 ph1):f2       ;URx180 BIBOP
  d22
  (p21:sp24 ph1):f1     (p21:sp25 ph3):f2       ;yz z-y
  d10
  (p26:sp26 ph5):f1
  d10
  p16:gp1*EA
  d16
  (p27:sp27 ph4):f2
  DELTA
  (p21:sp28 ph1):f1     (p21:sp29 ph4):f2       ;z-y yz
  d22
  (p22:sp22 ph1):f1     (p22:sp23 ph1):f2       ;URx180 BIBOP
  d22
  (p30:sp31 ph1):f1             ;URx65  ;p1*0.72 ph1
  d21
  (p22:sp22 ph1):f1     (p22:sp23 ph1):f2       ;URx180 BIBOP
  d21
  (p30:sp30 ph1):f1             ;URx242  ;p1*2.7 ph1
  d20
  (p22:sp22 ph1):f1     (p22:sp23 ph1):f2       ;URx180 BIBOP
  p16:gp2
  DELTA1 BLKGRAD
  4u
  (p3 ph8):f2

  ;;;;; Pure-Shift Pseudo-Dimension ;;;;;
  d0
  DELTA2
  p16:gp3
```

```
  d16
  (p22:sp22 ph1):f1
  DELTA3
  p16:gp4
  d16
  (p22:sp30 ph1):f1 ;BIRDd
  d4*2
  (p22:sp22 ph1):f1     (p22:sp23 ph1):f2       ;URx180 BIBOP
  d4*2
  (p22:sp32 ph1):f1     (p22:sp23 ph1):f2 ;URx90 BIBOP
  DELTA4
  p16:gp5
  d16 BLKGRAD
  d0

  go=2 ph31
  d1 mc #0 to 2
    F1QF(caldel(d0, +in0) )
    F2EA(calgrad(EA), caldel(d10, +in10) & calph(ph3, +180) & calph(ph6, +180) & calph(ph31, +180))
exit

ph1=0
ph2=1
ph3=0 2
ph4=0 0 2 2
ph5=0 0 0 0 2 2 2 2
ph6=0
ph8=0 2
ph31=0 2 2 0

;pl1 : f1 channel - power level for pulse (default)
;pl2 : f2 channel - power level for pulse (default)
;pl3 : f3 channel - power level for pulse (default)
;pl12: f2 channel - power level for CPD/BB decoupling
;p1 : f1 channel -  90 degree high power pulse
;p2 : f1 channel - 180 degree high power pulse
;p3 : f2 channel -  90 degree high power pulse
;p4 : f2 channel - 180 degree high power pulse
;p16: homospoil/gradient pulse

;p21 : 550u excitation pulses
;p22 : 600u UR and Inversion pulses
;p26 : 100u Inversion pulse
;p27 : 1100u UR pulse
```

```
;p30 : 200u odd UR pulses

;spnam21 : jc01_BEBOP_zx_550u_BW10_RF20_pm20_Hc0.99997119.pul
;spnam22 : jc02_BURBOP_x_600u_BW10_RF20_pm20_matched.pul
;spnam24 : jc04_BEBOP_yz_550u_BW10_RF20_pm20_matched.pul
;spnam26 : jc06_BIBOP_z-z_100u_BW11_RF20_pm20_Hc0.99966724.pul
;spnam28 : jc08_BEBOP_z-y_550u_BW10_RF20_pm20_matched.pul
;spnam30 : jc10_BURBOP_x242.8833deg_200u_BW10_RF20_pm20_Hc0.9997027.pul
;spnam31 : jc11_BURBOP_x65.3166deg_200u_BW10_RF20_pm10_Hc0.9998099.pul
;spnam32 : UR90x_600u_BW10_RF20_pm20_Hc0.999959.bruker

;spnam23 : jc03_BIBOP_600u_BW37.5_RF10_pm5_matched.pul
;spnam25 : jc05_BEBOP_zy_550u_BW37.5_RF10_pm5_matched.pul
;spnam27 : jc07_BURBOP_y_1100u_BW37.5_RF10_pm5_Hc0.999876221.pul
;spnam29 : jc09_BEBOP_-yz_550u_BW37.5_RF10_pm5_matched.pul

;sp21 : 20 kHz Rf Amplitude
;sp22 : 20 kHz Rf Amplitude
;sp24 : 20 kHz Rf Amplitude
;sp26 : 20 kHz Rf Amplitude
;sp28 : 20 kHz Rf Amplitude
;sp30 : 20 kHz Rf Amplitude
;sp31 : 20 kHz Rf Amplitude
;sp32 : 20 kHz Rf Amplitude

;sp23 : 10 kHz Rf Amplitude
;sp25 : 10 kHz Rf Amplitude
;sp27 : 10 kHz Rf Amplitude
;sp29 : 10 kHz Rf Amplitude

;d0 : incremented delay (2D)                  [3 usec]
;d1 : relaxation delay; 1-5 * T1
;d4 : 1/(4J)XH
;d5: = d5=1 (for J=120-250Hz, Delay Scaling Factor)
;d11: delay for disk I/O                             [30 msec]
;d16: delay for homospoil/gradient recovery
;cnst2: = J(XH)
;cnst4: = Points dropped by AU program
;infl: 1/SW(X) = 2 * DW(X)
;in0: 1/(2 * SW(X)) = DW(X)
;nd0: 2
;NS: 2 * n
;DS: >= 16
;td1: number of experiments
;FnMODE: echo-antiecho
```

```
;cpd2: decoupling according to sequence defined by cpdprg2
;pcpd2: f2 channel - 90 degree pulse for decoupling sequence

;use gradient ratio:    gp 1 : gp 2
;                         80 : 20.1    for C-13
;                         80 :  8.1    for N-15
;use gradient ratio:    gp 3 : gp 4 : gp 5
;                         1 : 4 : 3
;for z-only gradients:
;gpz1: 80%
;gpz2: 20.1% for C-13, 8.1% for N-15
;gpz3: n*1 %
;gpz4: n*4 %
;gpz5: n*3 %

;use gradient files:
;gpnam1: SMSQ10.100
;gpnam2: SMSQ10.100
;gpnam3: SMSQ10.100
;gpnam4: SMSQ10.100
;gpnam5: SMSQ10.100

;preprocessor-flags-start

;$Id: hsqcetgp,v 1.5.2.1 2011/02/24 17:27:48 ber Exp $
```

Listing A.33: Pulse program for COB-CLAP-RESET HSQC experiments

```
;COB_CLAP_RESET_hsqcetgp
;
;based on hsqcetgp,v 1.5.2.1 2011/02/24
;HSQC
;2D H-1/X correlation via double inept transfer
;phase sensitive using Echo/Antiecho-TPPI gradient selection
;
;$CLASS=HighRes
;$DIM=2D
;$TYPE=
;$SUBTYPE=
;$COMMENT=

#include <Avance.incl>
#include <Grad.incl>
#include <Delay.incl>
#include<Sysconf.incl>

```

```
"d11=30m"
"acqt0=0"
"d4=1s/(cnst2*4)"

"d20=d5*0.001469"
"d21=d5*0.00213465"
"d22=d5*0.0003938"

"d0=3u"
"d10=3u"
"in0=inf1/2"
"in10=inf2/2"

"DELTA=p16+d16+p26+d0*2"
"DELTA1=d5*0.001469-p16-4u"
"DELTA2=in0/2-p16-d16"
"DELTA3=in0-p16-d16"
"DELTA4=in0/2-(dw*2*cnst4)-p16-d16"

1 ze
  d11
2 d1
3 (p21:sp21 ph1):f1             ;zx
  d20
  (p22:sp22 ph1):f1   (p22:sp23 ph1):f2       ;URx180 BIBOP
  d20 UNBLKGRAD
  (p30:sp30 ph1):f1             ;URx242  ;p1*2.7 ph1
  d21
  (p22:sp22 ph1):f1   (p22:sp23 ph1):f2       ;URx180 BIBOP
  d21
  (p30:sp31 ph1):f1             ;URx65  ;p1*0.72 ph1
  d22
  (p22:sp22 ph1):f1   (p22:sp23 ph1):f2       ;URx180 BIBOP
  d22
  (p21:sp24 ph1):f1   (p21:sp25 ph3):f2       ;yz z-y
  d10
  (p26:sp26 ph5):f1
  d10
  p16:gp1*EA
  d16
  (p27:sp27 ph4):f2
  DELTA
  (p21:sp28 ph1):f1   (p21:sp29 ph4):f2       ;z-y yz
  d22
  (p22:sp22 ph2):f1   ;URx180
```

```
  d22
  (p30:sp31 ph2):f1             ;URx65  ;p1*0.72 ph1
  d21
  (p22:sp22 ph2):f1     ;URx180
  d21
  (p30:sp30 ph2):f1             ;URx242  ;p1*2.7 ph1
  d20
  (p22:sp22 ph2):f1     ;URx180
  p16:gp2
  DELTA1 BLKGRAD
  4u

  ;;;;; Pure-Shift Pseudo-Dimension ;;;;;
  d0
  DELTA2
  p16:gp3
  d16
  (p22:sp22 ph1):f1
  DELTA3
  p16:gp4
  d16
  (p22:sp30 ph1):f1 ;BIRDd
  d4*2
  (p22:sp22 ph1):f1     (p22:sp23 ph1):f2       ;URx180 BIBOP
  d4*2
  (p22:sp32 ph1):f1     (p22:sp23 ph1):f2 ;URx90 BIBOP
  DELTA4
  p16:gp5
  d16 BLKGRAD
  d0

  go=2 ph31
  d1 mc #0 to 2
    F1QF(caldel(d0, +in0) )
    F2EA(calgrad(EA), caldel(d10, +in10) & calph(ph3, +180) & calph(ph6,
    +180) & calph(ph31, +180))
exit

ph1=0
ph2=1
ph3=0 2
ph4=0 0 2 2
ph5=0 0 0 0 2 2 2 2
ph6=0
ph31=1 3 3 1
```

```

;pl1 : f1 channel - power level for pulse (default)
;pl2 : f2 channel - power level for pulse (default)
;pl3 : f3 channel - power level for pulse (default)
;pl12: f2 channel - power level for CPD/BB decoupling
;p1 : f1 channel -  90 degree high power pulse
;p2 : f1 channel - 180 degree high power pulse
;p3 : f2 channel -  90 degree high power pulse
;p4 : f2 channel - 180 degree high power pulse
;p16: homospoil/gradient pulse

;p21 : 550u excitation pulses
;p22 : 600u UR and Inversion pulses
;p26 : 100u Inversion pulse
;p27 : 1100u UR pulse
;p30 : 200u odd UR pulses

;spnam21 : jc01_BEBOP_zx_550u_BW10_RF20_pm20_Hc0.99997119.pul
;spnam22 : jc02_BURBOP_x_600u_BW10_RF20_pm20_matched.pul
;spnam24 : jc04_BEBOP_yz_550u_BW10_RF20_pm20_matched.pul
;spnam26 : jc06_BIBOP_z-z_100u_BW11_RF20_pm20_Hc0.99966724.pul
;spnam28 : jc08_BEBOP_z-y_550u_BW10_RF20_pm20_matched.pul
;spnam30 : jc10_BURBOP_x242.8833deg_200u_BW10_RF20_pm20_Hc0.9997027.pul
;spnam31 : jc11_BURBOP_x65.3166deg_200u_BW10_RF20_pm10_Hc0.9998099.pul
;spnam32 : UR90x_600u_BW10_RF20_pm20_Hc0.999959.bruker

;spnam23 : jc03_BIBOP_600u_BW37.5_RF10_pm5_matched.pul
;spnam25 : jc05_BEBOP_zy_550u_BW37.5_RF10_pm5_matched.pul
;spnam27 : jc07_BURBOP_y_1100u_BW37.5_RF10_pm5_Hc0.999876221.pul
;spnam29 : jc09_BEBOP_-yz_550u_BW37.5_RF10_pm5_matched.pul

;sp21 : 20 kHz Rf Amplitude
;sp22 : 20 kHz Rf Amplitude
;sp24 : 20 kHz Rf Amplitude
;sp26 : 20 kHz Rf Amplitude
;sp28 : 20 kHz Rf Amplitude
;sp30 : 20 kHz Rf Amplitude
;sp31 : 20 kHz Rf Amplitude
;sp32 : 20 kHz Rf Amplitude

;sp23 : 10 kHz Rf Amplitude
;sp25 : 10 kHz Rf Amplitude
;sp27 : 10 kHz Rf Amplitude
;sp29 : 10 kHz Rf Amplitude

```

```
;d0 : incremented delay (2D)                  [3 usec]
;d1 : relaxation delay; 1-5 * T1
;d4 : 1/(4J)XH
;d5: = d5=1 (for J=120-250Hz, Delay Scaling Factor)
;d11: delay for disk I/O                             [30 msec]
;d16: delay for homospoil/gradient recovery
;cnst2: = J(XH)
;cnst4: = Points dropped by AU program
;inf1: 1/SW(X) = 2 * DW(X)
;in0: 1/(2 * SW(X)) = DW(X)
;nd0: 2
;NS: 2 * n
;DS: >= 16
;td1: number of experiments
;FnMODE: echo-antiecho
;cpd2: decoupling according to sequence defined by cpdprg2
;pcpd2: f2 channel - 90 degree pulse for decoupling sequence

;use gradient ratio:    gp 1 : gp 2
;                         80 : 20.1    for C-13
;                         80 :  8.1    for N-15
;use gradient ratio:    gp 3 : gp 4 : gp 5
;                         1 : 4 : 3
;for z-only gradients:
;gpz1: 80%
;gpz2: 20.1% for C-13, 8.1% for N-15
;gpz3: n*1 %
;gpz4: n*4 %
;gpz5: n*3 %

;use gradient files:
;gpnam1: SMSQ10.100
;gpnam2: SMSQ10.100
;gpnam3: SMSQ10.100
;gpnam4: SMSQ10.100
;gpnam5: SMSQ10.100

;preprocessor-flags-start

;$Id: hsqcetgp,v 1.5.2.1 2011/02/24 17:27:48 ber Exp $
```

Conventional CLIP/CLAP-RESET HSQC experiments have to be modified as given below to obtain CT versions of the according spectra where all heteronuclear doublet components are collapsed to singlets irrespective of the ^{13}C multiplicity.

Listing A.34: Pulse program building block for CT-CLIP/CLAP-RESET HSQC experiments

```
"in0=inf1/2"
"in10=inf2/2"
"in20=in0/2"

"DELTA2=in0/2"
"DELTA3=in0/2+p16+d16+2*d0"
"DELTA4=dw*2*cnst4"

"d21=d19-DELTA2-DELTA3-6*p2-2*d0-4*d4-DELTA4-p16-d16"
"d20=d21/4"

  ;;;;; CT Pure-Shift Pseudo-Dimension ;;;;;
  d20
  DELTA2
  (p2 ph1):f1
  DELTA3
  d20
  p16:gp3
  d16
  (p2 ph7):f1
  d0
  p16:gp4
  d16
  (p1 ph1):f1 ;BIRDr
  d4*2
  (center (p2 ph2) (p4 ph1):f2 )
  d4*2
  (ralign (p1 ph1) (p4 ph1):f2 )
  p16:gp5*-1
  d16 BLKGRAD
  d0
  (p2 ph7):f1
  d20
  DELTA4
  (p2 ph1):f1
  d20

  go=2 ph31
  d1 mc #0 to 2
    F1QF( caldel(d0, +in0) & caldel(d20, -in20) )
    F2EA(calgrad(EA), caldel(d10, +in10) & calph(ph3, +180) & calph(ph6, +180) & calph(ph31, +180))
exit

ph1=0
```

```
ph2=1
ph3=0 2
ph4=0 0 0 0 2 2 2 2
ph5=0 0 2 2
ph6=0
ph7=2
ph8=0 2
ph31=0 2 0 2 2 0 2 0

;d19: d19 = T  (constant time period) = n/J(HH)geminal
;d20: Decremented delay (CT)
;d21: Available AQ for pure-shift FID
```

The modifications of the SP/COB-CLIP/CLAP-RESET HSQC pulse sequences to obtain the CT experiments described in appendix A.4 are given below.

Listing A.35: Pulse program building block for CT-SP/COB-CLIP/CLAP-RESET HSQC experiments

```
"in0=inf1/2"
"in10=inf2/2"
"in20=in0/2"

"DELTA2=in0/2"
"DELTA3=in0/2+p16+d16+2*d0"
"DELTA4=dw*2*cnst4"

"d21=d19-DELTA2-DELTA3-7*p22-2*d0-4*d4-DELTA4-p16-d16"
"d20=d21/4"

  ;;;;; CT Pure-Shift Pseudo-Dimension ;;;;;
  d20
  DELTA2
  (p22:sp22 ph1):f1
  DELTA3
  d20
  p16:gp3
  d16
  (p22:sp22 ph7):f1
  d0
  p16:gp4
  d16
  (p22:sp30 ph1):f1 ;BIRDr
  d4*2
  (p22:sp22 ph2):f1     (p22:sp23 ph2):f2       ;URx180 BIBOP
  d4*2
  (p22:sp30 ph1):f1     (p22:sp23 ph1):f2 ;URx90 BIBOP
```

```
  p16:gp5*-1
  d16 BLKGRAD
  d0
  (p22:sp22 ph7):f1
  d20
  DELTA4
  (p22:sp22 ph1):f1
  d20
  go=2 ph31
  d1 mc #0 to 2
    F1QF( caldel(d0, +in0) & caldel(d20, -in20) )
    F2EA(calgrad(EA), caldel(d10, +in10) & calph(ph3, +180) & calph(ph6,
   +180) & calph(ph31, +180))
exit

ph1=0
ph2=1
ph3=0 2
ph4=0 0 0 0 2 2 2 2
ph5=0 0 2 2
ph6=0
ph7=2
ph8=0 2
ph31=0 2 0 2 2 0 2 0

;d19: d19 = T  (constant time period) = n/J(HH)geminal
;d20: Decremented delay (CT)
;d21: Available AQ for pure-shift FID
```

B. List of Abbreviations

AHT	Average Hamiltonian Theory	21
AQ	acquisition time	II
BASH	Band-Selective Homonuclear	117
BEBE$^{\text{tr}}$	Broadband Excitation and time-reversed Broadband Excitation	126
BE$^{\text{tr}}$BE	time-reversed Broadband Excitation and Broadband Excitation	126
BEBOP	Broadband Excitation By Optimized Pulses	17
BFGS	Broyden-Fletcher-Goldfarb-Shanno	29
BIBOP	Broadband Inversion By Optimized Pulses	17
BIP	Broadband Inversion Pulse	65
BIRD	BIlinear Rotation Decoupling	112
BIRDBOP	BIlinear Rotation Decoupling By Optimized Pulses	147
BROCODE	BROadband COoperative DEcoupling	94
BUBI	Broadband Universal Broadband Inversion	126
BURBOP	Broadband Universal Rotation By Optimized Pulses	17
BUSS	Broadband Uniform Sideband Suppression	53
caWURST	constant-adiabaticity WURST	47
CG	conjugate gradient	29
CLAP-HSQC	CLean Anti-Phase-HSQC	118
CLIP-HSQC	CLean In-Phase-HSQC	95
COB	Couplings, Offsets, B_1-deviation	126
COSY	COrrelation SpectroscopY	102
CPD	Composite Pulse Decoupling	37
CPMG	Carr-Purcell-Meiboom-Gill	125
CSA	Chemical Shift Anisotropy	4
CT	constant-time	111
CTP	coherence transfer pathway	112
CW	continuous-wave	36
DIPSI	Decoupling In the Presence of Scalar Interactions	43

DMSO	dimethyl sulfoxide	
DOSY	Diffusion-Ordered SpectroscopY	111
DQF-COSY	Double-Quantum-Filtered COSY	102
E.COSY	Exclusice COrrelation SpectroscopY	112
ECO	Eliminate Cycling Oscillations	51
FID	free induction decay	36
FRPRMN	Fletcher-Reeves-Polak-Ribière-minimization	30
FT	Fourier transform	I
FWHM	full width at half maximum	33
GARP	Globally optimized Alternating-phase Rectangular Pulses	41
GRAPE	GRadient Ascent Pulse Engineering	20
HMBC	Heteronuclear Multiple-Bond Correlation	105
HMQC	Heteronuclear Multiple-Quantum Correlation	43
HOBS	Homodecoupled Band-Selective	117
HPD	hard pulse-delay	139
HS	Hyperbolic Secant	46
HSQC	Heteronuclear Single-Quantum Correlation	43
HSQMBC	Heteronuclear Single-Quantum Multiple-Bond Correlation	136
ICEBERG	Inherent Coherence Evolution optimized Broadband Excitation Resulting in constant phase Gradients	25
INEPT	Insensitive Nuclei Enhanced by Polarization Transfer	108
IPAP	In-Phase Anti-Phase	118
L-BFGS	limited-memory BFGS	29
LFP	linear forward-prediction	98
MRI	Magnetic Resonance Imaging	30
NMR	Nuclear Magnetic Resonance	I
NOE	Nuclear Overhauser Enhancement	109
NOESY	Nuclear Overhauser Enhancement SpectroscopY	114
OCT	Optimal Control Theory	I
PE-INEPT	perfect echo INEPT	108
PFG	pulsed field gradient	
PP	point-to-point	16
ppm	parts per million	I
PS	pure shift	112

PSYCHE	Pure Shift Yielded by CHirp Excitation	114
RCSA	Residual Chemical Shift Anisotropy	I
RDC	Residual Dipolar Coupling	I
RESET	Reducing nuclEar Spin multiplicitiEs to singuleTs	114
RF	radio frequency	I
RMS	root mean square	82
ROESY	Rotating frame nuclear Overhauser Enhancement SpectroscopY	116
RQC	Residual Quadrupolar Coupling	I
RT	real-time	116
S/A	signal to artifact	II
S/N	signal to noise	24
SP	shaped pulse	24
SSI	single-spin inversion	112
STFT	short-time Fourier transform	33
STUD	Sech/Tanh Universal Decoupling	46
SUSAN	Spin decoupling employing Ultra-broadband-inversion sequences generated via Simulated ANnealing	44
TMS	Tetramethylsilane	
TOCSY	TOtal Correlation SpectroscopY	43
TOP	time-optimal pulses	139
TPPI	Time-Proportional Phase Incrementation	
UR	universal rotation	16
WALTZ	Wideband, Alternating-phase, Low-power Technique for Zero-residual-splitting	41
WURST	Wideband, Uniform Rate, and Smooth Truncation	46
ZS	Zangger-Sterk	113

C. Lebenslauf

Nicht verfügbar in der elektronischen Version.

D. Danksagung

Am Ende aber nicht zuletzt gilt es, alle die Personen zu würdigen, die mich bei der Anfertigung dieser Arbeit betreut, unterstützt, beeinflusst oder ermutigt und aufgemuntert haben. Mein besonderer Dank gilt...

...Prof. Dr. Burkhard Luy für die Aufnahme in seinen Arbeitskreis, die herausfordernden Projekte, bei denen er mich sowohl unterstützt aber auch meinen eigenen Weg hat gehen lassen, und die Geduld bei der Lehre der NMR-Spektroskopie.

...PD Dr. Claudia Muhle-Goll für ihren unermüdlichen Einsatz bei der Organisation des Bioanalytik-Praktikums und anderer Belange des Arbeitskreises.

...Dr. Pavleta Tzvetkova für ihr selbstloses Engagement, den Sprektrometerfuhrpark zu warten und zu pflegen.

...Prof. Dr. Mirko Bunzel und seinen Mitarbeitern für die Möglichkeit, das 500 MHz Avance III HD Spektrometer am Institut für Organische Chemie nutzen zu dürfen.

...Anni Barwig, Pinar Sancar und Janine Moritz für die stets reibungslose Abwicklung von Verwaltungsangelegenheiten.

...Dr. Larissa Kaufmann, Dr. Gudrun Knedlitschek, Samira Junge und Dagmar Klimmek, die mir als Administration der internationalen Graduiertenschule *BioInterFaces in Technology and Medicine* (BIF-TM) beim erfolgreichen Durchlaufen des Programms mit Rat und Tat zur Seite standen.

...Prof. Dr. Ralf Mikut und Dr. Stephan Grage für ihre Bereitschaft, als Mitglieder meines *Thesis Advisory Committee* (TAC) zu fungieren und zum Gelingen meiner Arbeit beizutragen.

...Dr. Ralph Adams und Dr. Aitor Moreno für ihre Hilfe bei der Einarbeitung in die Programmierung und Prozessierung von PS-Experimenten.

...Prof. Dr. Katalin Kövér, Prof. Dr. Gareth Morris, Prof. Dr. Christina Thiele und ihren Mitarbeitern für das Einverständnis, das homonuklear entkoppelte CLIP-HSQC-Experiment parallel zu publizieren.

...Prof. Dr. Steffen Glaser und Dr. Franz Schilling für die Kooperation im Bereich der kooperativen Entkopplungssequenzen und dem gesamten Arbeitskreis Glaser für den schönen Besuch in München.

...Dr. Wolfgang Bermel für die Hilfe im Bereich der Implementierung der BROCODE-Sequenzen und die vielen tiefgehenden Einblicke in die Pulsprogrammierung.

...Prof. Dr. Ilya Kuprov und seinen Mitarbeitern für die Unterstützung bei den ersten Gehversuchen in Spinach und die vielen inspirierenden Diskussionen auf QUAINT workshops und anderen Konferenzen.

...Dr. Sebastian Ehni für die theoretische und praktische Einarbeitung und seine Bereitschaft, mich in jedem Aspekt meiner Arbeit zu unterstützen, selbst als Alumnus.

...den "Nordlichtern": Dipl.-Chem. Johanna Becker, Dr. Benjamin Görling, Dipl.-Chem. Martin Koos und Dipl.-Phys. David Schulze Sünninghausen für die schöne Zeit im Viererbüro, die schmackhaften Mahlzeiten und die musikalische Bereicherung in allen Tonlagen.

...der "Kommune 401": Dipl.-Chem. Philipp Eisenmann, Dipl.-Chem. Thomas Gloge, Marika Kromke, Dipl.-Chem. Malin Reller und Rebecca Rothenberger für die schöne Zeit und die erhellenden Tischgespräche nach meiner "Rückkehr in den Süden".

...den zahlreichen Bachelor-, Master- und Vertieferstudenten, die ihren Ehrgeiz und Eifer in unseren Arbeitskreis eingebracht haben. Insbesondere Kai Müller, der für mich Programmierarbeiten und Optimierungen durchgeführt hat.

...Dr. Julian Bär, Dipl.-Chem. Christoph Kaub, Dipl.-Chem. Frank Kuhn, Dr. Jan Müller, Dipl.-Chem. Kai Pahnke, Dr. Alexander Quick, Dr. Lukas Schwab und Dr. Alexander Zellner dafür, dass sie den Weg von Studienbeginn bis Promotion (fast) von Anfang bis (fast) zum Ende zusammen mit mir bestritten haben.

...Dr. Tobias Brunner, Dr. Lennart Brütsch, Dr. Meike Gotthardt, Dr. Dimitri Merger, Dr. Judith Schäfer, Dr. Franziska Völcker und Dr. Theresa Wagner für die vielen unterhaltsamen gemeinsamen Mittagessen.

...Dr. Sabrina Conrad, Mirijam Lehmann, Dr. Joachim Reimer, Dr. Meike Zellner und den zahllosen anderen Personen, die in dieser Liste fehlen, für die schöne gemeinsame Zeit während Studium und/oder Promotion.

...Anneke und Vico für ihre Liebe, die Wärme und das Licht. Ich widme diese Arbeit Euch.